Dynamics of a Photoswitch: Norbornadiene and Quadricyclane

Performed by

Joseph C. Cooper

of

New College

In partial fulfilment of the degree of

Doctor of Philosophy

in the

Physical and Theoretical Chemistry Laboratory

of the

University of Oxford

Under the supervision of

Prof. Adam Kirrander

2020-2024

Contents

List of Figures

List of Tables

List of Abbreviations

- **ADC(2)** — Second-order algebraic diagrammatic correction
- **AIMS** — Ab initio multiple spawning
- **CASSCF** — Complete active space self-consistent field
- **CASPT2** — Complete active space second-order perturbation theory
- **CC2** — Coupled cluster singles, and perturbative doubles
- **CC3** — Coupled cluster singles, doubles, and perturbative triples
- **CI** — Conical intersection
- **FC** — Franck–Condon (region)
- **FCF** — Franck–Condon Factor
- **FSSH** — Fewest switches surface hopping
- **FWHM** — Full-width-at-half-maximum
- **HF** — Hartree–Fock
- **IP** — Ionisation potential
- **LIIC** — Linear interpolation in internal coordinates
- **LR** — Linear-response
- **MECI** — Minimum energy conical intersection
- **MRCI** — Multi-reference configuration interaction (singles and doubles)
- **MRCI+Q** — MRCI with Davidson correction
- **NACME** — Non-adiabatic coupling matrix element
- **NBD** — Norbornadiene
- **NTO** — Natural transition orbital
- **QC** — Quadricyclane
- **PES** — Photo-electron spectroscopy
- **(R/X)MS** — (Rotated/Extended) multi-state
- **TRPES** — Time-resolved photo-electron spectroscopy
- **UED** — Ultrafast electron diffraction
- **(X)FEL** — (X-ray) free-electron laser
- **(X)UV** — (Extreme) ultraviolet

List of Publications

1. K. D. Borne, J. C. Cooper, M. N. R. Ashfold, J. Bachmann, S. Bhattacharyya, R. Boll, M. Bonanomi, M. Bosch, C. Callegari, M. Centurion, M. Coreno, B. F. E. Curchod, M. B. Danailov, A. Demidovich, M. Di Fraia, B. Erk, D. Faccialà, R. Feifel, R. J. G. Forbes, C. S. Hansen, D. M. P. Holland, R. A. Ingle, R. Lindh, L. Ma, H. G. McGhee, S. B. Muvva, J. P. F. Nunes, A. Odate, S. Pathak, O. Plekan, K. C. Prince, P. Rebernik, A. Rouzée, A. Rudenko, A. Simoncig, R. J. Squibb, A. S. Venkatachalam, C. Vozzi, P. M. Weber, A. Kirrander, and D. Rolles, *Ultrafast electronic relaxation pathways of the molecular photoswitch quadricyclane*, *Nat. Chem.*, **16**, 2024, 1–7.

2. J. C. Cooper, D. M. P. Holland, R. A. Ingle, M. Bonanomi, D. Faccialà, N. De Oliveira, A. R. Abid, J. Bachmann, S. Bhattacharyya, K. Borne, M. Bosch, M. Centurion, K. Chen, R. J. G. Forbes, H. V. S. Lam, A. Odate, A. Rudenko, A. S. Venkatachalam, C. Vozzi, E. Wang, P. M. Weber, M. N. R. Ashfold, A. Kirrander, and D. Rolles, *Valence shell electronically excited states of norbornadiene and quadricyclane*, *J. Chem. Phys.*, 2024, **160**, 064305

3. N. Goff, M. Simmermacher, E. Fasshauer, T. Northey, A. Moreno Carrascosa, L. Ma, H. Yong, B. Stankus, A. Odate, X. Xu, W. Du, K. Acheson, J. C. Cooper, D. Ratner, M. Liang, R. Forbes, M. Minitti, A. Kirrander, and P. Weber, *High-intensity x-ray scattering reveals core electron dynamics*, Under review in *Nature*

4. J. C. Cooper and Adam Kirrander, *Electronic structure of norbornadiene and quadricyclane*, Under review in *Phys. Chem. Chem. Phys.*

5. J. C. Cooper, C. Brown, J. Kára, and Adam Kirrander, *Dynamics of norbornadiene*, *Submitted*

6. J. C. Cooper and Adam Kirrander, *Ultrafast observables in norbornadiene*, *In preparation*

7. J. C. Cooper and Adam Kirrander, *Dynamics of quadricyclane*, *In preparation*

Acknowledgements

Before we get to the sappy stuff, I want to thank the people for slightly more tangible things. Firstly, thank you to Kurtis and Daniel for such a fantastic collaboration. Communicating across continents is never easy, but we got there in the end. Thank you to Mike and David, for being such inspiring models of scientific rigour, as well as understanding the struggles of a slightly overwhelmed PhD student. Thank you to Jakub and Cameron for providing such good ideas and for your hard work. Finally, thank you to Adam, Jakub, Lauren and Mats for your diligence in proof-reading — I shudder to think how many em-dashes would have been used without your help. Now, onto the sentimentality.

Firstly, thank you to my family. Dad, Mum, Sam and Rachel, thank you for all of your support, especially for providing the only real times during my PhD when I switched off. Suffolk, Sicily and the Île de Ré were all beautiful experiences and left me recharged and ready to try again.

To Peter and Julie, for your endless hospitality, both this and the other side of the pond. As of my writing this, Pinellas is bracing for impact, but I cannot wait to be back.

To all of my friends. I have not been the most fantastic communicator these past few years, but knowing you are all there for me has been a constant comfort. In the future, when I will be *slightly* more financially compensated, I will endeavour to turn my very occasional texts into very frequent visits.

To the Room 234 lot, for one of the most rewarding and exciting periods of my life. Specifically, thank you to Jon, for your friendship and willingness to continually explain why time does not really matter in a molecular dynamics simulation.

To our little lunch crew here in Oxford, for providing a relaxing distraction every day at noon sharp, whether discussing politics, philosophy, or food classification schemes.

To the Kirrander group, for providing such a wonderful and exciting environment to work in. The breadth of interests and knowledge in the group is staggering, and I cannot imagine I would have learned half as much in any other environment. Aside from the boring work stuff, thank you to Kyle for your humour, companionship and for introducing me to the wonders of a good *.vimrc*, Mats for your relentless positivity and encouragement, Andrés for teaching me Spanish swear words, Eirik for not laughing *every* time I say a Norwegian name, and Jakub for challenging my Arsenal-red-tinted glasses.

To Adam, for your continual support, guidance, and encouragement, even in the face of my refusal to work on the same project for more than a week at a time. Thank you for not questioning why I needed to install and learn a new electronic structure package every two and a half weeks, and for guiding me back to the path whenever needed.

Finally, thank you to Lauren.

Abstract

This thesis comprehensively investigates the molecular photoswitch of norbornadiene and quadricyclane, spanning electronic structure, non-adiabatic dynamics and ultrafast experimental observables. The theoretical results are closely linked to state-of-the-art experimental results, both of already-completed and future experiments. These molecules display promise as molecular solar thermal (MOST) systems, which capture, store and release solar energy. Norbornadiene and quadricyclane access the same intersection after photo-excitation, offering a unique opportunity to study a photochemical reaction through the same conical intersection from two different starting geometries.

We show a full multi-configurational exploration of the valence potential energy surfaces, with specific emphasis on the topography of the S_1/S_0 conical intersection. The surface hopping dynamics of norbornadiene is then performed with four electronic structure models (CASSCF and XMS-CASPT2 with two active spaces), and the dynamics is compared to the CASSCF(2,2) surface hopping of quadricyclane, affording a greater understanding of the potential energy surfaces and the dynamics itself. Both molecules display a rapid (sub-100 fs) decay, and different electronic structure methods show notably different quantum yields. The pre-conical intersection motion is the principal arbiter of the dynamical outcome, with minor contributions from conical intersection topography, a feature we posit is common in photoswitches. These dynamics are used to predict x-ray scattering patterns and time-resolved photo-electron spectra, allowing for suggestions for realistic potential experiments and critical examination of the experimental methods.

A complete, novel assignment of the static absorption and photo-electron spectra of the two molecules is presented, and finally, the results of an ultrafast time-resolved photo-electron spectroscopy experiment are explained via surface hopping/RMS-CASPT2 simulations. The dynamics simultaneously excites Rydberg and valence states, with notably faster dynamics on the latter, and fully explains the observed bipartite nature of the experimental signal.

This study provides a computationally feasible model that entirely elucidates the ultrafast dynamics of the norbornadiene/quadricyclane system, offering a framework to improve the design for MOST and photoswitch applications. Additionally, this system remains a target of future ultrafast experiments, inevitably requiring correct and reliable simulations for their interpretation. More generally, this system is an excellent example of photoswitch systems, showing quick, coherent, and simple dynamics with complex outcomes.

— 1 —

Introduction

Photochemistry, as the name implies, is the reaction of molecules following absorption of light. It is the process at the heart of vision,[8] photosynthesis,[8,9] atmospheric chemistry,[10,11] bioluminescence,[12] photocatalysis[13–15] and photochemical rearrangements.[16,17] Understanding photochemical reactions is also critical for designing novel technologies, such as solar energy harvesting,[18–20] molecular motors,[21–23] light-activated drugs,[24,25] and photoswitch devices.[26–28]

In Fig. 1.1, we show a schematic of a photochemical reaction: the reaction of norbornadiene (NBD) into quadricyclane (QC), the subject of this thesis. The wavepacket initially resides in the ground state equilibrium, but is then excited by UV light. The wavepacket is now non-stationary, rapidly evolving on the excited state surface until it finds the conical intersection, where the two electronic states are degenerate. Here, the coupling between the states is strong, and the wavepacket transfers to the ground state. Interestingly, this particular system has two potential energy wells, separated by a large barrier, and either can be accessed from the conical intersection. The deeper minimum, where the wavepacket starts, corresponds to NBD and the shallower to QC.

Until now, we have only mentioned the possibility of non-radiative, singlet-to-singlet decay — otherwise known as internal conversion. Of course, other decay processes, such as intersystem-crossing, fluorescence, and phosphorescence, are all possible, but the system we study shows dynamics on the sub-100 fs femtosecond time-scale, too fast to allow any other process. Finally, we mention that we concentrate on the gas phase, precluding collisional or solvent-induced decay.

Photochemistry offers a unique advantage in studying chemical reactions; modern ultrafast lasers allow measurements on the timescale of nuclear motion, watching the chemical transformations as they unfold.[1,29–31] These invariably rely on the pump-probe technique, which we cover more in Chapter 4. Unfortunately, the experimental observation of photochemistry is exceptionally challenging. Not only are the motions of nuclei extremely fast, occurring on the femtosecond timescale, but the experiments project the high-dimensionality dynamics onto a comparatively low-dimensional observable, making the interpretation of the experimental signal often so challenging it necessitates theoretical input. As such, computational simulations are indispensable tools for studying photochemistry.

Simulation of non-adiabatic dynamics

Photochemical simulation requires non-adiabatic dynamics, which describes the coupled motion of electrons and nuclei. To perform this, we almost always separate the two, propagating a nuclear wavefunction (covered in Chapter 2) on the potential energy surfaces of the electrons (covered in Chapter 3). Crucially, these simulations must allow the nuclear wavefunction to transfer between electronic states, covering the critical non-adiabatic decay processes. In prin-

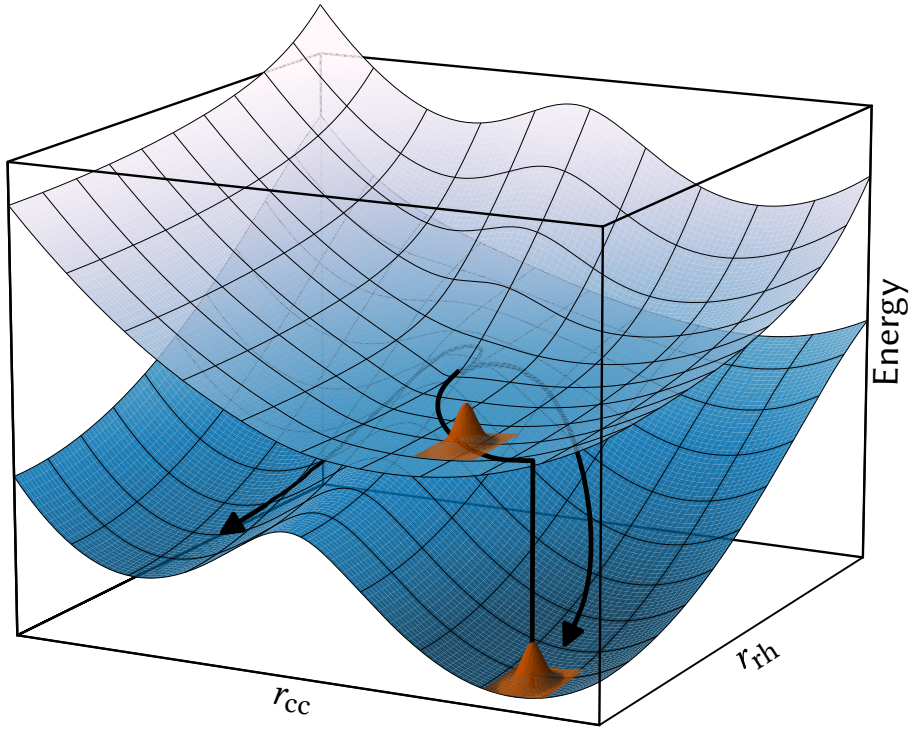

Figure 1.1: Schematic of the photochemical reaction of norbornadiene and quadricyclane. Upon excitation to the upper state, the wavepacket towards the conical intersection, transferring to the ground state and falling into either of the two wells. These are the two isomers: norbornadiene (right, where the wavepacket starts) and quadricyclane (left). On the ground state surface, these two geometries are separated by a large potential energy barrier, and so do not interconvert. The two coordinates, r_{cc} and r_{rh}, are discussed in more detail in Chapter 5.

ciple, the dynamics of both the electrons and nuclei should be solved quantum mechanically. Unfortunately, full quantum calculations scale exponentially with the system size, and are entirely unfeasible for the systems we study in this thesis without significant approximation.

For electrons, the particles are so light that all methods, of which there is a surplus, will treat the electrons fully quantum mechanically. These are challenging calculations, and we often must make significant approximations to reduce the calculation time. The particular challenge of photochemistry is describing all important electronic states correctly and without significant biases, generally leading to costly and time-consuming calculations. This is especially true near conical intersections, which require multi-configurational calculations that invariably involve human-selected *active spaces*. Understanding these calculations, and how to balance accuracy and computational efficiency, is often the primary factor in whether a photochemical simulation is correct.

On the other hand, the nuclei are much heavier and can be described, at least qualitatively, using Newtonian mechanics. In doing this, we represent the nuclear wavefunction with an ensemble of point particles, propagating them individually according to Newton's laws. The trajectories represent plausible dynamics paths, modelling the spread of the wavepacket and allowing for processes such as wavepacket splitting. This reduces the computational time from exponential to linear, but in doing so, we lose the ability to describe nuclear quantum effects such as tunnelling or wavepacket interference.

Ideally, we would use the best methods available to simulate both the electrons and nuclei. But, given the intense scaling of these procedures and the finite computational resources and time scales of our projects, this is almost always impossible. We must, therefore, balance the levels of approximation to provide a reasonable model for the system at hand, aiming for the best results within a given timeframe. It is common, for example, to compromise our description of the nuclei, reducing their computational cost, to get a slightly better electronic simulation, or vice versa.

However, using approximations introduces errors. To validate these models and understand whether they can be used more generally, we can compare their results with either higher-level methods or experimental observations. Unfortunately, high-level quantum calculations are often unfeasible for larger systems, leaving experimental validation as a crucial step in ensuring the reliability of the simulations. The system studied in this thesis is on the cusp of our current computational ability, just small enough to find some convergence while showing qualities of much larger systems. As such, we explore both paradigms, using careful comparisons to higher-level theory and experimental validation to benchmark our predictions.

As mentioned, this project focuses on a single photochemical system, aiming to achieve as complete an understanding of the dynamics as possible. We then contextualise the results in the broader scheme of photochemistry, aiming to find and explore essential features that might be more general phenomena. From here, we strive to combine our findings with experiments to elucidate and validate as much as possible of these complex dynamics. In doing this, we also consider the possible extent of experimental validation, and whether current experiments can hope to challenge the results of our dynamics simulations.

Norbornadiene and quadricyclane

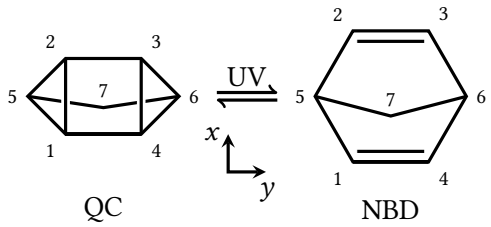

Figure 1.2: The reaction of quadricyclane (QC, left) and norbornadiene (NBD, right) can be driven with UV light. NBD converts its two C=C bonds to form a highly-strained four-carbon ring at the base of QC, gaining ≈ 1 eV of energy.

This thesis focuses on norbornadiene (NBD) and quadricyclane (QC), a quintessential example of a molecular photoswitch. These are a class of molecule that isomerises after absorption of light, storing a binary state with the system's current geometry (i.e. isomer). Photoswitches have many potential uses, from light harvesting,[18,20] logic devices,[26,28,32] molecular motors,[22] data storage,[33,34] super-resolution microscopy,[35,36] photopharmacology,[24,25,37] and bio- and smart-molecules.[38] From a purely photochemical point of view, these systems are targets for ultrafast experiments for three primary reasons: firstly, they show fast, coherent dynamics with localised structural changes, allowing for an in-depth study of a single process. Secondly, the two isomers provide two different starting geometries and, hence, two potential experiments, allowing a much better understanding of the potential energy surfaces involved. Thirdly, and most practically, the overall structure of the molecule is preserved in both isomers. This is useful both theoretically, as it simplifies the electronic structure, and experimentally, as it

allows scattering experiments to track the dynamics across the entire photochemical reaction, unlike in photodissociation.

NBD and QC are shown schematically in Fig. 1.2. Upon electronic excitation, NBD (right, Fig. 1.2) breaks the two double bonds to perform a retro-[2+2]-cyclo-addition, forming the eponymous four-carbon ring at the base of QC (left, Fig. 1.2), and vice versa. We have already shown a schematic of the potential energy surfaces in Fig. 1.1, with an example reaction after photoexcitation from NBD. The key features of a photoswitch are apparent in this model: two ground-state isomers separated by a large barrier, and a conical intersection that allows the dynamics to form either. After photoexcitation, the wavepacket can then find and become 'trapped' in one of the potential energy wells, storing the state of the system.

Due to the strain of the ring, QC has a ground state energy approximately 1 eV higher than NBD, as implied in Fig. 1.1. Practically, this makes the NBD/QC system a promising candidate for molecular solar thermal (MOST) systems[18–20,39,40] Simply, after reacting with sunlight, NBD forms QC, storing energy that can later be released as heat via a catalytic back reaction. These systems represent a credible alternative to solar cells for applications such as domestic heating. Interestingly, QC has also been researched for rocket propulsion, illustrating the high energy storage density.[41–43]

Aside from being of practical interest, NBD and QC are attractive for theoretical purposes, with quick, limited phase-space dynamics proceeding through a single conical intersection. It is a clear example of a [2+2]-cyclo-addition, a fundamental element of photochemistry.[44,45] However, the two ethylenic moieties are held together by the backbone of the molecule, limiting their conformational freedom, which leads to both theoretical and experimental simplification. As mentioned earlier, the two different isomers also afford two different starting conditions and, hence, two different sets of dynamics through the same conical intersection. This has made NBD and QC a target for modern ultrafast experimental techniques[30,46,47]. In particular, the system can be studied by scattering experiments,[30,46] as the motion is not hydrogenic, and photo-electron spectroscopy[47], as the molecule displays strong Rydberg features[1,48] and a low ionisation potential.[1,2]

Before we move on, we should temper our expectations slightly. The NBD/QC system is exceptionally complex, and the unsubstituted variant we cover in this thesis lacks the properties necessary for practical engineering. Further, we only consider gas-phase molecules, whereas practical applications will almost certainly be in the condensed phase.

Most of the absorption to unsubstituted NBD and QC is to Rydberg states at energies above 6 eV. These are not the states used in practical systems, as they show slow and incoherent dynamics. The most critical state for practical applications is the low-lying reactive valence state. In unsubstituted NBD, this state only absorbs light weakly and at approximately 5.25 eV, where there is little actinic flux.[2,49,50] Additionally, excitation of NBD does not form significant amounts of QC, at least in the long time limit,[20] making the reaction inefficient.

Engineering this system is a highly active area of research.[18–20,40,51–55] This is achieved by substitution, with primary goals of increasing both the efficiency of the conversion reaction and the amount of energy stored as a function of total molecular mass. Finally, the substitutions aim to energetically lower and strengthen the absorption to the reactive valence state, along with removing the effects of the Rydberg states.

That said, the simplicity of the system we study allows for a more in-depth understanding of the reaction, and even in its unsubstituted form, the NBD/QC system provides critical insights into the principles governing molecular photoswitches. As such, we present two separate studies of this system. The first is a valence-only model, where we aim to elucidate the fundamental dynamics of the system as well as our understanding of molecular photoswitches and photochemistry in general. This also connects strongly with the potential design and

modification of the system for photoswitch and MOST applications, which utilise the low-lying valence states, explicitly avoiding the Rydberg states.

In the second part, we consider the Rydberg states. The reason for this is twofold: firstly, molecular Rydberg states are of fundamental photochemical interest.[48,56–58] Secondly, as mentioned earlier, NBD and QC are the targets of ultrafast experiments, which are easier to perform when exciting the higher cross-section Rydberg states. The second half of this thesis thus focuses on the Rydberg states to connect both with already completed and future experiments.

Reader's guide to the thesis

The remainder of this thesis is split into three parts. In Part I, we go through the theory used in the remainder of the work, starting with the non-adiabatic dynamics. First, Chapter 2 covers the complete quantum picture and discusses the most critical regions of the potential energy surfaces: the conical intersections. After that, we include a survey of the important non-adiabatic dynamics methods we will use in our work and discuss some practical details involved in simulation. Chapter 3 covers electronic structure theory. As this topic is well-understood, we only cover the methods used in this thesis, which all come from multi-configurational quantum chemistry. Finally, given our desire to strongly link to experiments, Chapter 4 discusses the theory of three separate experimental observables: x-ray and electron scattering and photo-electron spectroscopy. These provide excellent probes of electronic structure and dynamics, each shedding a slightly different light on the underlying molecules.

The following two parts concentrate on the photochemistry of the NBD/QC system. Part II is a self-contained, consistent analysis of the valence states. Chapter 5 starts by presenting an exploration of the electronic structure, taken from Ref. 4, where we evaluate the static picture of the photochemistry of the system, looking at important features of the potential energy surfaces. In this chapter, we identify four electronic structure models suitable for non-adiabatic dynamics simulations, benchmark them against higher-level methods, and evaluate all important regions of the potential energy surfaces.

After that, we move to the valence dynamics of NBD in Chapter 6, which makes up Ref. 5. We use the same initial conditions for four sets of surface hopping dynamics using the aforementioned electronic structure methods. This study covers a multitude of different areas. First, it serves as a valuable approach for understanding the driving forces of the dynamics of NBD. As we use four well-understood potentials, we can ascribe outcomes of the dynamics to specific features on the potential energy surfaces, also possibly guiding chemical substitution on these systems for potential applications. Extending this, it is an intriguing study of the interplay of potential energy surfaces and dynamics, and how significant the effects can be from relatively minor changes in the potentials. The efficiency of the electronic structure also allows for well-converged simulations with few approximations, testing the non-adiabatic dynamics algorithms themselves. Finally, this system presents a fascinating case study of dynamics through conical intersections. The electronic structure methods show relatively similar local conical intersection topography but different dynamics before their passage, leading to distinct outcomes.

Chapter 7 makes a quick detour to predictions of ultrafast experimental observables from the NBD dynamics, which will be part of Ref. 6. In this chapter, we use our different ensembles as four sets of plausible dynamics, comparing their predicted x-ray scattering patterns and photo-electron spectra. This leads to direct suggestions for future experiments, the assignment of separate signals within the predictions, and a more general discussion about which dynamical variables are deducible from such measurements. For the latter, having a deep understanding of the underlying dynamics gives context to the features of the signals.

We round off Part II with the valence dynamics of QC in Chapter 8, primarily to give an alternative view of the dynamics on the potential energy surfaces. This is taken from Ref. 7. We make extensive comparisons to the NBD dynamics, using almost identical analysis, contextualising and confirming the results of the previous sections.

The final part of the thesis, Part III, presents a couple of investigations that directly bridge theory and experiments. Chapter 9 explores the static absorption and photo-electron spectra of both NBD and QC, taken from Ref. 2. While this work may not directly align with the rest of the thesis, as it primarily focuses on the high-lying Rydberg states, it is crucial for conducting future experiments on NBD. This work was carried out in close collaboration with David Holland and Mike Ashfold, and led to a final assignment of the excitation spectrum of this molecule.

The final results in the thesis are shown in Chapter 10, which presents a theoretical study of the dynamics of QC following excitation at 200 nm, considering both Rydberg and valence state excitation, taken from Ref. 1. This work is connected to a time-resolved photo-electron spectroscopy experiment performed at the FERMI free-electron laser in Trieste, in collaboration with the group of Daniel Rolles, and aims to explain the signals observed in the experiment.

Here, we must emphasise that the work in this final chapter was carried out *before* all of the other work presented in this thesis and, therefore, does not use the full range of methods presented in the earlier valence-only chapters. To simultaneously describe the Rydberg manifold *and* the valence states was a particularly challenging task, leading to our use of RMS-CASPT2, a new variant of electronic structure theory. Later, we found that this method does not describe the valence states particularly well, leading to somewhat flawed dynamics when held against the benchmark of our later work. However, the overall picture of the photochemical dynamics remains unchanged, and the qualitative agreement with the experiment is still good. This does stress an underlying theme of this work, in that ultrafast experiments are not necessarily sensitive to all of the subtleties of the dynamics, and agreement between theoretical and experimental results does *not* guarantee that the underlying dynamics is exactly the same.

— I —

Methods & Theory

— 2 —

Dynamics

First, we explore non-adiabatic dynamics, the theory of coupled nuclear and electronic motion. We start at a fairly low level, first deriving the fully quantum equation of motion from the time-dependent Schrödinger equation. To solve this equation, we partition our wavefunction into two sections: a nuclear and an electronic part. In this chapter, we are concerned with the nuclei's motion on the electrons' potential energy surfaces, so we leave a more in-depth discussion of electronic structure theory to Chapter 3.

Using the partitioning, we can find relatively simple-looking equations of motion for the nuclei. Unfortunately, solving these equations for molecules is computationally intensive, requiring integration over the nuclear configuration space, which scales exponentially with the number of degrees of freedom.[59,60] This is challenging even for small molecules, but for the molecules we consider in this thesis, it is effectively impossible without significant approximation.

As such, we use classical approximations, where we approximate the entire wavepacket as the sum of a series of classical trajectories.[61–63] Unlike the quantum equations, Newtonian mechanics is exceptionally computationally efficient, requiring only information about the trajectory's exact position and momentum, removing the need to integrate over all space. However, classical approximations cannot describe nuclear quantum effects, such as tunnelling or zero-point energies, and, thus, will never fully recover the quantum picture. In this thesis, the method we focus on most is surface hopping, a very popular approach, but we also cover classical Ehrenfest dynamics and ab initio multiple spawning.

All the methods discussed are explicitly non-adiabatic, allowing nuclear motion to induce transitions between different electronic states. For this, the most critical regions of the potential energy surface are *conical intersections*, where two electronic states are degenerate. As these are so crucial to the work of this thesis, we review them in some detail, including a relatively simple classification scheme.

Here, we have explicitly *not* included any coupling to an external field. While the processes we model in this thesis are pump-probe experiments that start *and* end with this coupling, we treat these interactions as extremely fast. This allows us to use the results of the observable calculations (shown in Chapter 4) as uncoupled from the main dynamics, and all dynamics in this thesis will be propagated 'field-free'.

2.1 — Non-adiabatic Dynamics

Chemistry, being a subject concerned with the very small, is a naturally quantum mechanical discipline. Quantum mechanics, which first came from the work of Schrödinger and

Heisenberg[64,65], is founded on a single equation — the time-dependent Schrödinger equation[i]

$$i\frac{\partial}{\partial t}\Psi(\mathscr{R},t) = \hat{H}\Psi(\mathscr{R},t). \tag{2.1}$$

In this equation, i is the imaginary unit, t is time, and $\hat{H}$ is the Hamiltonian operator of our system. $\Psi(\mathscr{R},t)$, known as the wavefunction, is the central element of quantum theory, and is dependent on the coordinates of the system, $\mathscr{R}$.

The Hamiltonian operator $\hat{H}$ also has a set of eigenstates $\{\Psi_i(\mathscr{R},t)\}$ and eigenvalues $\{E_i\}$, which are defined by the time-independent Schrödinger equation

$$\hat{H}\Psi_i(\mathscr{R}) = E_i\Psi_i(\mathscr{R}). \tag{2.2}$$

These form a complete (orthonormal) basis over Hilbert space.

As we deal with molecules in an idealised gas phase, well separated from any other molecules, we make a natural approximation; the Hamiltonian of our system only consists of the kinetic and potential energy operators for the isolated molecule. This is written

$$\begin{aligned}\hat{H} &= \hat{T}_\mathrm{n} + \hat{T}_\mathrm{e} + \hat{V}_\mathrm{ee} + \hat{V}_\mathrm{nn} + \hat{V}_\mathrm{en} \\ &= -\sum_\alpha \frac{1}{2M_\alpha}\nabla_\alpha^2 - \sum_i \frac{1}{2}\nabla_i^2 + \sum_{i,j}\frac{1}{r_{ij}} + \sum_{\alpha,\beta}\frac{Z_\alpha Z_\beta}{r_{\alpha\beta}} - \sum_{i,\alpha}\frac{Z_\alpha}{r_{i\alpha}},\end{aligned} \tag{2.3}$$

with $r_{AB} = |\boldsymbol{r}_A - \boldsymbol{r}_B|$ the distance between particles A and B, ∇_A the gradient operator for particle A, and $\hat{T}$ and $\hat{V}$ indicating kinetic and potential energy operators, respectively.

In a general case, we could consider a total wavefunction containing all of the nuclear and electronic degrees of freedom, denoted previously as $\mathscr{R}$. Unfortunately, this is very challenging computationally, and thus, we make a distinction between electron (denoted with $\boldsymbol{r}$) and nuclear ($\boldsymbol{R}$) coordinates. Mathematically, we partition the Hamiltonian into two terms as

$$\hat{H} = \hat{T}_\mathrm{n} + \underbrace{\hat{T}_\mathrm{e} + \hat{V}_\mathrm{ee} + \hat{V}_\mathrm{nn} + \hat{V}_\mathrm{en}}_{\hat{H}^\mathrm{el}}, \tag{2.4}$$

where we call $\hat{H}^\mathrm{el}$ the *electronic Hamiltonian*. Using this as the Hamiltonian in Eq. (2.2), we can find the eigenvalues $\left\{E_m^\mathrm{el}(\boldsymbol{R})\right\}$, the nuclear-position-dependent potential energy surfaces of the electrons, and their corresponding orthonormal electronic wavefunctions $\{\psi_m(\boldsymbol{r};\boldsymbol{R})\}$. The wavefunctions have a parametric dependence on $\boldsymbol{R}$, denoted by the semicolon. We shall leave all discussion of how to calculate these quantities until Chapter 3. The electronic eigenstates are often called the adiabatic states and correspond to the limit of a system with no nuclear motion. In this thesis, we only consider singlet electronic states, which we shall label S_n, with the ground state given the label $n = 0$, the first excited $n = 1$, etc.

We expand the total time-dependent wavefunction using the Born–Huang ansatz,[66,67]

$$\Psi(\boldsymbol{r},\boldsymbol{R},t) = \sum_m \chi_m(\boldsymbol{R},t)\psi_m(\boldsymbol{r};\boldsymbol{R}), \tag{2.5}$$

where $\psi_m(\boldsymbol{r};\boldsymbol{R})$ is an electronic eigenstate containing the electronic degrees of freedom, and $\chi_m(\boldsymbol{R},t)$ a nuclear wavefunction, which contains all of the time-dependence. This is an expansion of the wavefunction into a basis of electronic states, and as long as the sum over m is

[i] In this thesis we use atomic units, where $\hbar = m_\mathrm{e} = e = 4\pi\epsilon_0 = 1$. For indexing, we shall use i, j for electrons, α, β for nuclei and m, n for electronic states throughout this thesis. We shall also use the $\hat{}$ symbol for operators, boldface text for vector quantities, and italic for scalar (and magnitudes of vector quantities).

not truncated, this representation is exact. Here, we also note that we shall assume that the electronic wavefunctions are real, with all phase information in the nuclear wavefunctions.

The nuclear wavefunctions $\{\chi_m(\boldsymbol{R},t)\}$ are state-specific, defining the current state of the nuclei on a given electronic state. We define the square norm

$$P_m(t) = \int_{-\infty}^{\infty} |\chi_m(\boldsymbol{R},t)|^2 \mathrm{d}\boldsymbol{R}$$

as the population on electronic state m, and normalise such that

$$\sum_m P_m(t) = 1. \tag{2.6}$$

Combining Eqs. (2.1) and (2.5), we can find equations of motion for the nuclear wavefunctions

$$i\frac{\partial}{\partial t}\chi_n(\boldsymbol{R},t) = \left[\hat{T}_\mathrm{n} + E_n^\mathrm{el}\right]\chi_n(\boldsymbol{R},t) - \sum_\alpha \frac{1}{2M_\alpha}\sum_m K_{nm}^\alpha \chi_m(\boldsymbol{R},t), \tag{2.7}$$

with the couplings

$$K_{nm}^\alpha(\boldsymbol{R}) = \underbrace{\int_{-\infty}^{\infty}\psi_n^*(\boldsymbol{r};\boldsymbol{R})\nabla_\alpha^2\psi_m(\boldsymbol{r};\boldsymbol{R})\mathrm{d}\boldsymbol{r}}_{g_{nm}^\alpha(\boldsymbol{R})} + 2\underbrace{\int_{-\infty}^{\infty}\psi_n^*(\boldsymbol{r};\boldsymbol{R})\nabla_\alpha\psi_m(\boldsymbol{r};\boldsymbol{R})\mathrm{d}\boldsymbol{r}}_{\boldsymbol{d}_{nm}^\alpha(\boldsymbol{R})}\cdot\nabla_\alpha. \tag{2.8}$$

The nuclear wavefunction $\chi_n(\boldsymbol{R},t)$ evolves as a function of time according to two separate terms: a pseudo-Hamiltonian $\left[\hat{T}_n + E_m^\mathrm{el}\right]$ consisting of the nuclear kinetic energy and the adiabatic potential energy surface of state m, and a coupling term $\sum_\alpha \frac{1}{2M_\alpha}\sum_m K_{nm}$. For the nuclear wavefunction $\chi_n(\boldsymbol{R},t)$, the two terms imply quite different dynamics, with the first implying unitary propagation on state n, without changing the norm of $\chi_n(\boldsymbol{R},t)$. The second term, on the other hand, allows for the interaction with other electronic states, generally allowing for the population of state m to change.

The two coupling terms g_{nm}^α and $\boldsymbol{d}_{nm}^\alpha$ are of crucial importance and thus worth further discussion. The former, g_{nm}^α, is known as the *scalar coupling* and is often neglected,[68,69] while the latter, $\boldsymbol{d}_{nm}^\alpha$, is known as the *non-adiabatic coupling* and plays a crucial role in non-adiabatic dynamics.[ii] It is a vector (in nuclear space) between two states. For real electronic wavefunctions, the diagonal elements $\boldsymbol{d}_{nn}^\alpha = 0$ due to the anti-hermicity of the gradient operator ∇. For the non-diagonal elements, we can use Hellmann-Feynman theorem to find

$$\boldsymbol{d}_{nm}^\alpha(\boldsymbol{R}) = \frac{1}{E_m^\mathrm{el} - E_n^\mathrm{el}}\int_{-\infty}^{\infty}\psi_n^*(\boldsymbol{r};\boldsymbol{R})\left(\nabla_\alpha\hat{H}^\mathrm{el}\right)\psi_m(\boldsymbol{r};\boldsymbol{R})\mathrm{d}\boldsymbol{r}, \tag{2.9}$$

giving the characteristic inverse energy-difference scaling of the non-adiabatic coupling.[67]

In regions where K_{nm}^α is small (for all m and α), Eq. (2.7) reduces to

$$i\frac{\partial}{\partial t}\chi_n(\boldsymbol{R},t) \approx \left[\hat{T}_\mathrm{n} + E_n^\mathrm{el}\right]\chi_n(\boldsymbol{R},t). \tag{2.10}$$

This is often called the Born-Oppenheimer approximation, describing unitary evolution on a single state. This can be alternatively derived by considering an initial ansatz of

$$\Psi(\boldsymbol{r},\boldsymbol{R},t) \approx \chi_n(\boldsymbol{R},t)\psi_n(\boldsymbol{r};\boldsymbol{R}) \tag{2.11}$$

[ii] There are *many* different naming conventions for these quantities. We choose this particular one as the term *non-adiabatic coupling* in practical electronic structure theory almost always refers to the single-derivative term $\boldsymbol{d}_{nm}^\alpha$. Referring to the combination K_{nm}^α as non-adiabatic couplings is also common. As we neglect the term g_{nm}^α in this thesis, the only difference is a factor of two and the ∇_α operator. We also mention that the neglecting of the scalar coupling is primarily performed for computational, not principled, purposes.

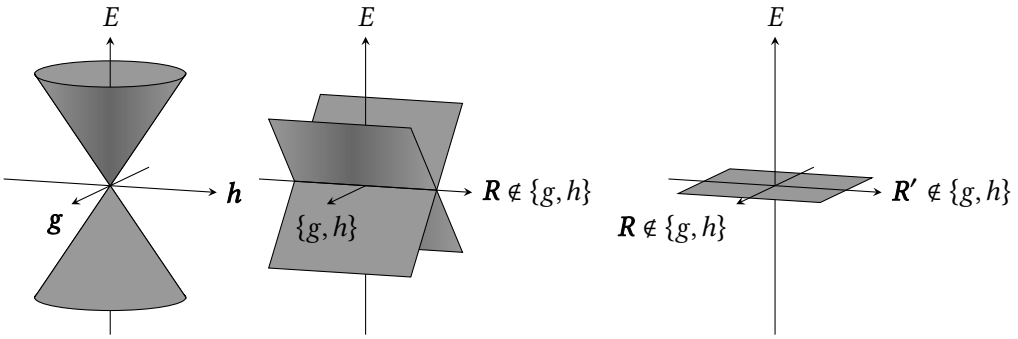

Figure 2.1: Energy of the conical intersection in different coordinate planes, with R_X at the origin. Left: the branching-plane, where the double cone can be seen. Middle: one branching and one seam coordinate, where the energy gap increases along g but not along $\boldsymbol{R}$. Right: two seam coordinates, there the energy gap is zero. For simplicity, $\Delta\overline{H}(\boldsymbol{R})$ is set to 0.

for some n, insertion into Eq. (2.1), and neglecting the diagonal scalar coupling term g^{α}_{nn}, which can be considered as a correction to the adiabatic potential energy surface E^{el}_n.

We now have two separate equations, Eqs. (2.7) and (2.10), which describe the motion of the nuclei. The question remains: which shall we use? Clearly, Eq. (2.10) is identical to Eq. (2.7) when $K^{\alpha}_{nm} = 0$. We can see from Eq. (2.9) that the non-adiabatic couplings will be small when the state m is energetically separated from all other states. There is no population transfer between states in this approximation, and the dynamics is known as *adiabatic*.

When $K^{\alpha}_{nm} \neq 0$, there will be differences between the two frameworks. The wavepacket will transfer between the states, especially in regions with low energy separation, and we call this dynamics *non-adiabatic*. The coupling allows for complicated photochemical processes and is epitomised by our next topic, conical intersections.

2.2 — Conical Intersections

It is now useful to investigate points where electronic states are degenerate – that is, regions where $E^{\mathrm{el}}_n(\boldsymbol{R}) - E^{\mathrm{el}}_m(\boldsymbol{R}) = 0$ and, by Eq. (2.9), $\boldsymbol{d}^{\alpha}_{nm}(\boldsymbol{R})$ is singular. As discussed earlier, such regions play a key role in non-adiabatic dynamics. We can gain some intuition by taking the simplest possible model, a two-state system. A generic Hamiltonian for this system can be written as

$$\boldsymbol{H}_{2\mathrm{s}}(\boldsymbol{R}) = \begin{pmatrix} H_{11}(\boldsymbol{R}) & H_{12}(\boldsymbol{R}) \\ H^{*}_{12}(\boldsymbol{R}) & H_{22}(\boldsymbol{R}) \end{pmatrix}. \tag{2.12}$$

The potential energy surfaces are found by diagonalisation, returning

$$E_{\pm}(\boldsymbol{R}) = \frac{H_{11}(\boldsymbol{R}) + H_{22}(\boldsymbol{R})}{2} \pm \sqrt{\left(\frac{H_{11}(\boldsymbol{R}) - H_{22}(\boldsymbol{R})}{2}\right)^2 + |H_{12}(\boldsymbol{R})|^2} \tag{2.13}$$

$$= \overline{H}(\boldsymbol{R}) \pm \sqrt{(\Delta H(\boldsymbol{R}))^2 + |H_{12}(\boldsymbol{R})|^2}. \tag{2.14}$$

For a degeneracy, i.e. when $E_{+}(\boldsymbol{R}) = E_{-}(\boldsymbol{R}) = \overline{H}(\boldsymbol{R})$, the radical must equal zero, which only occurs when both the energy difference $\Delta H(\boldsymbol{R})$ and the Hamiltonian coupling $|H_{12}(\boldsymbol{R})|$ equal zero. Generically, this requires two separate degrees of freedom in $\boldsymbol{R}$ and means that pseudo-one-dimensional systems, such as diatomics in the limit of no rotational or translation coupling, do not have degeneracies.

We can also approximate the quantities around the degenerate geometry $\boldsymbol{R}_\mathrm{X}$ using a simple first-order Taylor expansion as

$$\overline{H}(\boldsymbol{R}) \approx \overline{H}(\boldsymbol{R}_\mathrm{X}) + \nabla\overline{H}(\boldsymbol{R}_\mathrm{X}) \cdot \Delta\boldsymbol{R} \tag{2.15}$$

$$\Delta H(\boldsymbol{R}) \approx \nabla\left(\Delta H\right)_{\boldsymbol{R}_\mathrm{X}} \cdot \Delta\boldsymbol{R} \tag{2.16}$$

$$|H_{12}|(\boldsymbol{R}) \approx \nabla\left(|H_{12}|\right)_{\boldsymbol{R}_\mathrm{X}} \cdot \Delta\boldsymbol{R}, \tag{2.17}$$

where $\Delta\boldsymbol{R} = \boldsymbol{R} - \boldsymbol{R}_\mathrm{X}$, ∇ is the gradient operator in $\boldsymbol{R}$ and the subscript indicates evaluation at $\boldsymbol{R}_\mathrm{X}$. To break the degeneracy, we need either $\Delta H(\boldsymbol{R})$ or $|H_{12}(\boldsymbol{R})|$ to become non-zero, which only happens when the displacement has non-zero projection along one of the two vectors $\nabla\left(\Delta H\right)_{\boldsymbol{R}_\mathrm{X}} \equiv \boldsymbol{g}$ and $\nabla\left(|H_{12}|\right)_{\boldsymbol{R}_\mathrm{X}} \equiv \boldsymbol{h}$. These two coordinates, known as the difference gradient ($\boldsymbol{g}$) and the Hamiltonian coupling ($\boldsymbol{h}$), together form the *branching-plane*. This linear approximation leads to the two potentials being conical around the degeneracy. The other $N_\mathrm{c} - 2$ coordinates, while they might change the average energy $\overline{H}(\boldsymbol{R})$ do not separate the two states (at least to first-order), and are known as the *seam* or *intersection-space*. The conical intersection is therefore a $(N_\mathrm{c} - 2)$-dimensional manifold within the total N_c-dimensional space.

In Fig. 2.1, we show a schematic example of a conical intersection in three different slices of configuration space. On the left, we show the two states in both branching-plane coordinates, and the characteristic double cone can be easily seen. In the centre, we show one branching-plane coordinate and one seam coordinate, noticing that the states only separate along the former, and the right-hand plot shows the states in two seam coordinates. Here, we can only see one state, as they are degenerate.

Conical intersections (and the surrounding regions) are essential to photo-dynamics due to the strength of the coupling. Near a degenerate point, population will readily transfer between two adiabatic states. In the next section, we move to a characterisation scheme, but here it is worth mentioning the geometric phase effect. When a wavepacket moves in a closed loop around a conical intersection, there will be an additional term of π in the wavefunction phase.[67,70] Hence, conical intersections can influence dynamics even when the wavepacket does not explicitly feel the coupling in the conical intersection. These effects are important in simple chemical reactions,[71–73] but require a higher-level treatment of the dynamics than we consider in this thesis, and so we mention them only for completeness.

Characterisation of Conical Intersections

Due to their importance, there are many classification schemes for conical intersections.[74–78] In general, we use these to provide a simplified understanding of the nature of these points and how the potential energy surfaces look in the vicinity. It is well known that the local topography of conical intersections can have a strong effect on the coupling rate,[76,79–86] and so we show the follow the work of Fdez. Galván et al.,[78] who provide a simple, robust framework.

First, we use two new coordinates, $\tilde{\boldsymbol{g}}$ and $\tilde{\boldsymbol{h}}$, such that

$$\begin{gathered}\tilde{\boldsymbol{g}} = \boldsymbol{g}\cdot\cos(\beta) + \boldsymbol{h}\cdot\sin(\beta), \quad \tilde{\boldsymbol{h}} = -\boldsymbol{g}\cdot\sin(\beta) + \boldsymbol{h}\cdot\cos(\beta), \\ \beta = \frac{1}{2}\tan^{-1}\left(\frac{2\boldsymbol{g}\cdot\boldsymbol{h}}{\boldsymbol{g}\cdot\boldsymbol{g} - \boldsymbol{h}\cdot\boldsymbol{h}}\right).\end{gathered} \tag{2.18}$$

This is an orthogonalisation of the two branching-plane coordinates and is derived from a unitary rotation of the electronic states at the point of intersection.[78] As the two original states are degenerate, so are the new states, and they constitute an equivalent set of eigenstates for

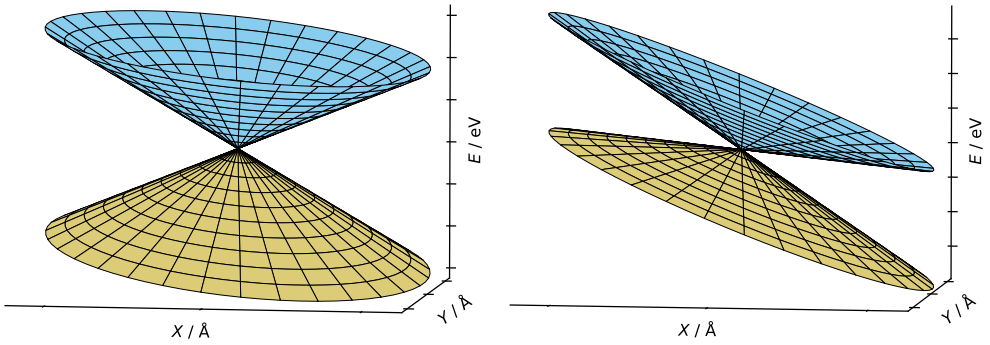

Figure 2.2: Example of a peaked (left) and sloped (right) intersection. The former is a local minimum on the excited state, guiding excited state trajectories to the high-coupling region. The latter is not a local minimum and is less likely to be encountered in excited state dynamics.

the electronic wavefunction. Further, we are free to normalise these vectors, which we shall call X and Y, as

$$X = \frac{\tilde{\boldsymbol{g}}}{|\tilde{\boldsymbol{g}}|}, \quad Y = \frac{\tilde{\boldsymbol{h}}}{|\tilde{\boldsymbol{h}}|}. \tag{2.19}$$

Displacements in the branching-plane can now be written as (x, y), corresponding to the projection along X and Y, respectively. Finally, we introduce the sum-gradient coordinate,

$$\boldsymbol{s} = \frac{1}{2}(\nabla E_i + \nabla E_j), \tag{2.20}$$

the overall tilt of the intersection, which is invariant to the rotation of electronic states. From here, we define four parameters: the intersection pitch and asymmetry

$$\delta = \sqrt{\frac{1}{2}\left(\tilde{\boldsymbol{g}} \cdot \tilde{\boldsymbol{g}} + \tilde{\boldsymbol{h}} \cdot \tilde{\boldsymbol{h}}\right)}, \quad \Delta = \frac{\tilde{\boldsymbol{g}} \cdot \tilde{\boldsymbol{g}} - \tilde{\boldsymbol{h}} \cdot \tilde{\boldsymbol{h}}}{\tilde{\boldsymbol{g}} \cdot \tilde{\boldsymbol{g}} + \tilde{\boldsymbol{h}} \cdot \tilde{\boldsymbol{h}}}, \tag{2.21}$$

which quantify the overall energy scale and the difference in energy separations in the orthogonal axes, respectively. As the choice of β in Eq. (2.18) is unique up to an arbitrary phase of $\frac{\pi}{2}$, we choose the value such that $\Delta \geq 0$. Next, we have the relative tilt and tilt-heading

$$\sigma = \frac{1}{\delta}\sqrt{(\boldsymbol{s} \cdot X)^2 + (\boldsymbol{s} \cdot Y)^2}, \quad \theta_s = \tan^{-1}\left(\frac{\boldsymbol{s} \cdot X}{\boldsymbol{s} \cdot Y}\right), \tag{2.22}$$

which are the projection of the sum=gradient on the branching-plane and the tilt angle, respectively. Together, these parameters allow for a linear approximation of energies in the branching-plane as

$$E^{\pm}(r, \theta) = E(\boldsymbol{R}_X) + \delta r\left(\sigma \cos(\theta - \theta_s) \pm \sqrt{1 + \Delta \cos(2\theta)}\right), \tag{2.23}$$

using the standard definition of polar coordinates as

$$r = \sqrt{x^2 + y^2}, \quad \theta = \tan^{-1}\left(\frac{y}{x}\right). \tag{2.24}$$

Equation (2.23) provides a reasonable approximation for the energies in the branching-plane. Importantly, the quantities used in this approximation, i.e. electronic gradients and non-adiabatic couplings, are readily available from electronic structure calculations.

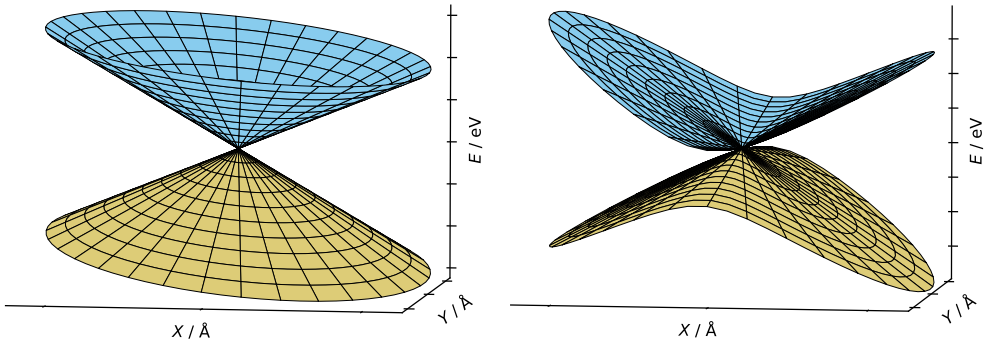

Figure 2.3: Example of a single-path (left) and bifurcating (right) intersection. To understand the difference, we can imagine the potential energy along a constant-radius circle around the degeneracy. The former would only show one minimum on the ground state, and thus can only form one product. The latter would have two clear minima, allowing for the formation of two isomers.

Fdez. Galván et al. also provided a useful two-number analysis of the local topography of the conical intersection.[78] Starting with the overall slope parameter P, defined as

$$P = \frac{\sigma}{1-\Delta^2}\left(1 - \Delta\cos\left(2\theta_s\right)\right), \tag{2.25}$$

with $P < 1$ indicating a peaked and $P > 1$ a sloped intersection. This distinction is shown in Fig. 2.2, with peaked intersections (left panel) being local minima (maxima) on the upper (lower) state. Peaked intersections are generally associated with much faster upper-to-lower state decays due to the wavepacket being funnelled towards the region of high coupling.[79–81] Contrastingly, sloped intersections (Fig. 2.2, right panel) are not a local minimum and so do not give rise to such fast decays.

The second parameter B defines the number of minima on the ground state and is given by

$$B = \left(\frac{\sigma}{2\Delta}\right)^{\frac{2}{3}}\left(\sqrt[3]{(1+\Delta)\cos^2\left(\theta_s\right)} + \sqrt[3]{(1-\Delta)\sin^2\left(\theta_s\right)}\right), \tag{2.26}$$

with Δ defined in Eq. (2.21). When $B > 1$, we have a 'single-path' intersection, and with $B < 1$, a 'bifurcating' intersection. This quality is best understood through an example, given in Fig. 2.3. For the single-path intersection (left panel), if one were to plot the energy as a function of θ on the ground state surface, there would only be one minimum. Taking the example of a photochemical reaction, dynamics through a single-path intersection should only form one product — the structure at the bottom of the single minimum. Bifurcating intersections (Fig. 2.3, right panel) show two distinct minima on the lower surface. A photochemical reaction could potentially form two different products, giving the 'bifurcating' moniker.

Both P and B are continuous parameters, and values near the bordering value of one indicate less extreme examples. In this thesis, we are particularly interested in peaked and bifurcating intersections, which return fast, two-product dynamics — an essential for molecular photoswitches.

2.3 — Mixed-Quantum-Classical Approaches

While the quantum mechanical equations of Eqs. (2.7) and (2.10) are simple-looking equations, their solution requires integration over the entirety of coordinate space, which scales exponentially with the number of dimensions. This is possible for a handful of dimensions, but as we

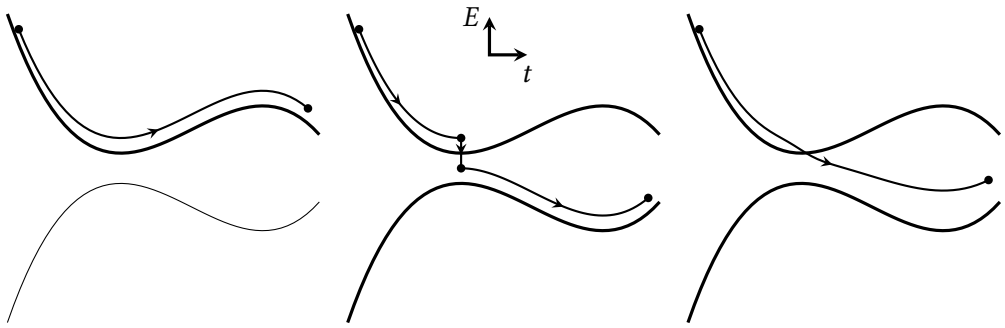

Figure 2.4: Schematic of the different mixed-quantum-classical approaches. Born–Oppenheimer dynamics only exists on one state, ignoring the coupling region. Surface hopping can 'hop' from one state to another, evolving according to its current active state. Ehrenfest dynamics propagate on an averaged potential, leading to incorrect behaviour at divergences.

move towards more complex molecules, such as those we study here, the explicit integration becomes impossible to perform computationally. As such, we must move to approximations.

In this thesis, the most pertinent method of solving Eqs. (2.7) and (2.10) relies on classical approximations. Generically, we approximate our wavefunction as

$$\Psi(\boldsymbol{r}, \boldsymbol{R}, t) \approx \sum_{u}^{N_{\text{tr}}} w_u \sum_{m} c_m^u(t)\, \delta(\boldsymbol{R} - \boldsymbol{R}_u(t))\, \psi_m(\boldsymbol{r}; \boldsymbol{R}) \tag{2.27}$$

where u enumerates the N_{tr} trajectories, which are represented as delta functions centred at $\boldsymbol{R}_u(t)$, the moving centre of the trajectory. Each of these trajectories has a given set of coefficients $c_m(t)$, which is state-specific, and weight w_u. For simplicity, we will just set $w_u = \frac{1}{N_{\text{tr}}}$, equally weighting the trajectories.

The state coefficients form an 'electronic wavefunction' for each trajectory, allowing us to generalise the notion of population as

$$P_m(t) = \frac{1}{N_{\text{tr}}} \sum_{u}^{N_{\text{tr}}} |c_m^u(t)|^2,$$

with a similar normalisation as in Eq. (2.6). As we shall see later, there are two main types of electronic wavefunction: the single-set and multi-set formalisms. In a single-set formalism, the wavefunction is only on one state at a time, and $c_m^u = \delta_{mi}$. There is no such restriction in the multi-set formalism, and the wavefunction can be on multiple states at a time.

Generally, these trajectories are propagated classically. In short, that means that the nuclear position $\boldsymbol{R}_u(t)$ obeys Newton's equations, i.e.

$$\boldsymbol{M}\ddot{\boldsymbol{R}}_u(t) = \boldsymbol{F}_u(\boldsymbol{R}_u(t)), \tag{2.28}$$

where $\ddot{\boldsymbol{R}}_u(t)$, $\boldsymbol{M}$, and $\boldsymbol{F}_u(\boldsymbol{R}_u(t))$ are the acceleration vector, mass matrix, and force vector of trajectory u, respectively. These are generally represented in cartesian coordinate space, enumerating them over x, y, and z for each atom — a total of $3N_{\text{atoms}}$ degrees of freedom. We integrate these equations in time with a finite time-step (Δt), usually using a symplectic algorithm like velocity-Verlet. A key feature of classical dynamics is the preservation of the total energy of the trajectory, also ensuring that the total energy expectation value of the wavefunction is conserved.

The integration of Eq. (2.28) is far simpler than (e.g.) Eq. (2.7), as the equation is entirely local — it only contains terms from the trajectory point. This allows the propagation of dynamics 'on-the-fly', updating the position and calculating the energy for each new time-step.

As the mass is constant, the only thing which changes in different trajectory-based methods is the evaluation of the force. In the simplest method, Born–Oppenheimer dynamics, we assume that the sum over m in Eq. (2.27) can be truncated to only one state, as described in Eqs. (2.10) and (2.11). Then, we can write the force as the gradient of a single potential energy surface at the trajectory centre, or

$$\boldsymbol{F}(\boldsymbol{R}_u(t)) = -\nabla E_i(\boldsymbol{R}_u(t)). \tag{2.29}$$

We will call this state the 'active state' and always denote it by i. We show a representative example in Fig. 2.4, where the trajectory, located on the upper state, moves along the potential classically, never crossing to the other state. We can immediately see the Achilles heel of Born–Oppenheimer dynamics: the lack of description of non-adiabatic coupling. This specific trajectory would be trapped on the upper surface and unable to transfer to another state. There are cases where this behaviour is perfectly acceptable — for example, pure ground state dynamics such as a protein in an aqueous environment — but it is entirely inappropriate for photo-chemistry, where coupling is critical.

Ehrenfest Dynamics

Ehrenfest dynamics is the simplest method for mixed-quantum-classical dynamics, and can be readily derived from quantum-mechanical equations. To begin, we use a multi-set formalism for the electronic wavefunction, beginning with the ansatz for the wavefunction:

$$\Psi^{\mathrm{Ehr}}(\boldsymbol{r},\boldsymbol{R},t) = \psi^{\mathrm{Ehr}}(\boldsymbol{r},t)\chi(\boldsymbol{R},t) = \left(\sum_m c_m(t)\psi_m(\boldsymbol{r};\boldsymbol{R})\right)\chi(\boldsymbol{R},t), \tag{2.30}$$

The wavefunction is split into a nuclear and electronic part, which both depend on time, and neither are state-specific. The Ehrenfest coefficients $c_m(t)$ hold the information about the makeup of the Ehrenfest electronic wavefunction $\psi^{\mathrm{Ehr}}(\boldsymbol{r},t)$, which we will represent in the basis of adiabatic states, again normalised as $\sum_m |c_m|^2 = 1$.

From this and Eq. (2.1), we can derive two coupled equations of motion[61,87]:

$$i\frac{\partial}{\partial t}\psi^{\mathrm{Ehr}}(\boldsymbol{r},t) = \left[\hat{T}_{\mathrm{e}} + \int_{-\infty}^{\infty}\chi^*(\boldsymbol{R},t)\hat{V}_{\mathrm{tot}}(\boldsymbol{r},\boldsymbol{R})\chi(\boldsymbol{R},t)\mathrm{d}\boldsymbol{R}\right]\psi^{\mathrm{Ehr}}(\boldsymbol{r},t) \tag{2.31}$$

$$i\frac{\partial}{\partial t}\chi(\boldsymbol{R},t) = \left[\hat{T}_{\mathrm{n}} + \int_{-\infty}^{\infty}\psi^{\mathrm{Ehr}*}(\boldsymbol{r},t)\hat{H}^{\mathrm{el}}(\boldsymbol{r},\boldsymbol{R})\psi^{\mathrm{Ehr}}(\boldsymbol{r},t)\mathrm{d}\boldsymbol{r}\right]\chi(\boldsymbol{R},t). \tag{2.32}$$

Definitions of operators can be found in Eqs. (2.3) and (2.4), and we have used $\hat{V}_{\mathrm{tot}}(\boldsymbol{r},\boldsymbol{R}) = \hat{V}_{\mathrm{ee}}(\boldsymbol{r}) + \hat{V}_{\mathrm{en}}(\boldsymbol{r},\boldsymbol{R}) + \hat{V}_{\mathrm{nn}}(\boldsymbol{R})$, making explicit the dependencies. These equations are a mean-field approximation, where the electronic and nuclear wavefunctions evolve in effective potentials derived from each other's energy expectation values. This is due to the second terms on the right-hand sides of Eqs. (2.31) and (2.32), where the propagation of the electronic (nuclear) wavefunction is mediated by the integration over the entirety of the nuclear (electronic) wavefunction.

Until now, this is a fully quantum set of equations. We will now take the classical limit, setting the nuclear density to

$$|\chi(\boldsymbol{R},t)|^2 = \delta(\boldsymbol{R} - \boldsymbol{R}_u(t)). \tag{2.33}$$

Eventually, we will sum over many individual trajectories, all denoted by u, and so we will also use a trajectory-specific set of coefficients $c_m^u(t)$ that define a trajectory-specific Ehrenfest

wavefunction $\psi_u^{\mathrm{Ehr}}(\boldsymbol{r}, \boldsymbol{R}_u, t)$, which now explicitly depends on $\boldsymbol{R}_u$ (as the nuclear wavefunction is localised). Finally, we shall not show the time-dependence of $\boldsymbol{R}_u$ for concision.

The classical limit[iii] of the nuclear force for trajectory u is given by

$$\boldsymbol{F}(\boldsymbol{R}_u, t) = -\nabla\left(\int_{-\infty}^{\infty} \psi_u^{\mathrm{Ehr}*}(\boldsymbol{r}, \boldsymbol{R}_u, t)\hat{H}_{\mathrm{el}}(\boldsymbol{r}, \boldsymbol{R}_u)\psi_u^{\mathrm{Ehr}}(\boldsymbol{r}, \boldsymbol{R}_u, t)\mathrm{d}\boldsymbol{r}\right) \tag{2.34}$$

$$= -\sum_m |c_m^u(t)|^2 \nabla E_m(\boldsymbol{R}_u) - \sum_{m\neq n} c_m^{u\,*}(t)\, c_n^u(t)\; \boldsymbol{d}_{mn}(\boldsymbol{R}_u) \cdot (E_n(\boldsymbol{R}_u) - E_m(\boldsymbol{R}_u)), \tag{2.35}$$

where we have also used Eqs. (2.9) and (2.30), and we use $\boldsymbol{d}_{mn}(\boldsymbol{R})$ to indicate the coupling across all atoms. For the electronic equation Eq. (2.31), we can derive

$$i\frac{\partial}{\partial t}\psi^{\mathrm{Ehr}}(\boldsymbol{r}, \boldsymbol{R}_u, t) = \left[\hat{T}_{\mathrm{e}} + V_{\mathrm{tot}}(\boldsymbol{R}_u)\right]\psi^{\mathrm{Ehr}}(\boldsymbol{r}, \boldsymbol{R}_u, t) = \hat{H}^{\mathrm{el}}(\boldsymbol{R}_u)\psi^{\mathrm{Ehr}}(\boldsymbol{r}, \boldsymbol{R}_u, t) \tag{2.36}$$

where $V_{\mathrm{tot}}(\boldsymbol{R}_u)$ and $\hat{H}^{\mathrm{el}}(\boldsymbol{R}_u)$ are the potential and electronic Hamiltonian evaluated at nuclear position $\boldsymbol{R}_u$. Alternatively, we can find an equation of motion for the coefficients $c_m^u(t)$ as

$$\frac{\mathrm{d}c_n^u(t)}{\mathrm{d}t} = -i\, c_n^u(t)\, E_n(\boldsymbol{R}_u) - \sum_m c_m^u(t)\, \boldsymbol{d}_{nm}(\boldsymbol{R}_u) \cdot \dot{\boldsymbol{R}}_u. \tag{2.37}$$

To summarise, we now have an equation that gives the classical force for a classical point particle, and an equation that derives the change in the electronic wavefunction for those trajectories. Putting these together, we can create an *classical Ehrenfest trajectory*, which takes a given initial state defined by a set of nuclear geometries $\boldsymbol{R}_u(t=0)$ and velocities $\dot{\boldsymbol{R}}_u(t=0)$, and a set of electronic coefficients $c_m^u(t=0)$, and propagates it forward in time. In a simulation, we will run many of these to simulate the spread of the nuclear wavefunction.

To calculate observables for the ensemble, we simply sum the observables for each trajectory. To give a simple but critical example, the classical Ehrenfest populations are given by

$$P_m^{\mathrm{Ehr}}(t) = \frac{1}{N_{\mathrm{tr}}}\sum_u^{N_{\mathrm{tr}}} |c_m^u(t)|^2. \tag{2.38}$$

Finally, we turn to Eqs. (2.31) and (2.34), which gives a particularly nice way of understanding Ehrenfest dynamics: propagation on an averaged potential energy surface (shown here for the classical case)

$$E^{\mathrm{Ehr}}(\boldsymbol{R}_u, t) = \int_{-\infty}^{\infty} \psi^{\mathrm{Ehr}*}(\boldsymbol{r}, \boldsymbol{R}_u, t)\hat{H}_{\mathrm{el}}(\boldsymbol{r}, \boldsymbol{R}_u)\psi^{\mathrm{Ehr}}(\boldsymbol{r}, \boldsymbol{R}_u, t)\mathrm{d}\boldsymbol{r} = \sum_m |c_m(t)|^2 E_m(\boldsymbol{R}_u) \tag{2.39}$$

We show this schematically in the rightmost panel of Fig. 2.4. This also belies the crucial flaw of classical Ehrenfest — the wavefunction ansatz (and average potential energy surface) implies total electronic coherence, leading to incorrect asymptotic behaviour. Ehrenfest dynamics is a useful theoretical method, as it provides a simple framework and can be rigorously derived from quantum-mechanical equations. However, due to over-coherence issues, Ehrenfest trajectories are generally used with additional 'decoherence' algorithms, which we will cover later.

Surface Hopping

Surface hopping, at its simplest, can be considered a non-adiabatic extension of Born–Oppenheimer dynamics, where we allow the active state i to change throughout the dynamics. Clearly, how

[iii] We do not go into the details here as it is covered well elsewhere.[61,87]

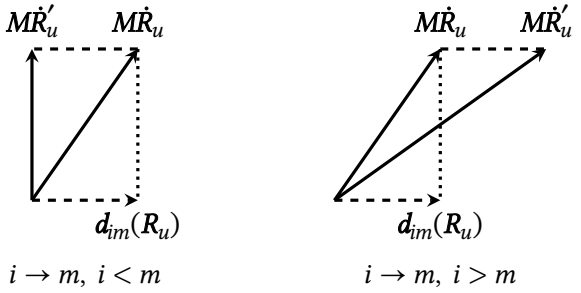

Figure 2.5: Re-scaling in surface hopping, for a hop from states i to m. Left: hop to a higher state. The component of old momentum $M\dot{\boldsymbol{R}}_u$ along the coupling $\boldsymbol{d}_{im}(\boldsymbol{R}_u)$ is re-scaled, producing a new momentum $M\dot{\boldsymbol{R}}'_u$ and a lower kinetic energy to adjust for the higher potential energy. Right: hop to a lower state. The same process is followed, except the kinetic energy is increased to compensate for lower potential energy.

the active state is chosen is critically important. We show this schematically in Fig. 2.4 (middle panel), which shows an example surface hopping trajectory. Initially, the trajectory propagates on the upper state, but in the coupling region, it can 'hop' to the lower state, where it then propagates further.

We will first introduce the industry standard algorithm: Tully's fewest switches surface hopping (FSSH).[62,88] In this, we perform a dual propagation. Firstly, we propagate a single-state wavefunction, written as

$$\Psi^{\mathrm{SS}}(\boldsymbol{r}, \boldsymbol{R}, t) = \sum_m \psi_m(\boldsymbol{r}; \boldsymbol{R})\, \delta(\boldsymbol{R} - \boldsymbol{R}_u(t))\, \delta_{im} = \psi_i(\boldsymbol{r}; \boldsymbol{R})\, \delta(\boldsymbol{R} - \boldsymbol{R}_u(t)). \tag{2.40}$$

As in Eq. (2.33), we have used a delta-function for the nuclear wavefunction. This ansatz is used for two purposes: firstly, this state is used to propagate the nuclear dynamics, as in Born–Oppenheimer molecular dynamics (see Eq. (2.29)). Secondly, all observables from the trajectories are calculated using this wavefunction.

Simultaneously, we propagate an Ehrenfest electronic wavefunction, starting with the initial ansatz in Eq. (2.30). As detailed in that section, we can calculate the electronic coefficients using Eq. (2.37), propagating the Ehrenfest coefficients along a classical trajectory. Here, we stress that this is not the same as classical Ehrenfest dynamics, as we are using the single-state force.

The key to this dual propagation is to use the Ehrenfest electronic wavefunction to decide the active state i. For FSSH, this is performed using a stochastic sampling at each time-step. First, the probability of hopping from state i to state m is calculated using the equation

$$\mathscr{P}^u_{im}(t) = \max\left(0, \frac{-2\mathrm{Re}\left(\boldsymbol{d}_{im}(\boldsymbol{R}_u) \cdot \dot{\boldsymbol{R}}_u\, c^{u\,*}_m(t)\, c^u_i(t)\right) \Delta t}{|c^u_i(t)|^2}\right), \tag{2.41}$$

where Δt is the time-step. If a uniform random number $0 \leq \zeta \leq 1$ fulfils the condition

$$\sum_{n<m} \mathscr{P}^u_{in}(t) < \zeta < \sum_{n \leq m} \mathscr{P}^u_{in}(t), \tag{2.42}$$

the hop is accepted, and we change the active state to m.

We then use a process called re-scaling, depicted schematically in Fig. 2.5, to change the velocity of the trajectory such that the total energy is conserved in the hopping process. If the total energy can only be conserved by negative kinetic energies, then the hop is 'frustrated' and abandoned. In this case, the component that would have been re-scaled is sometimes

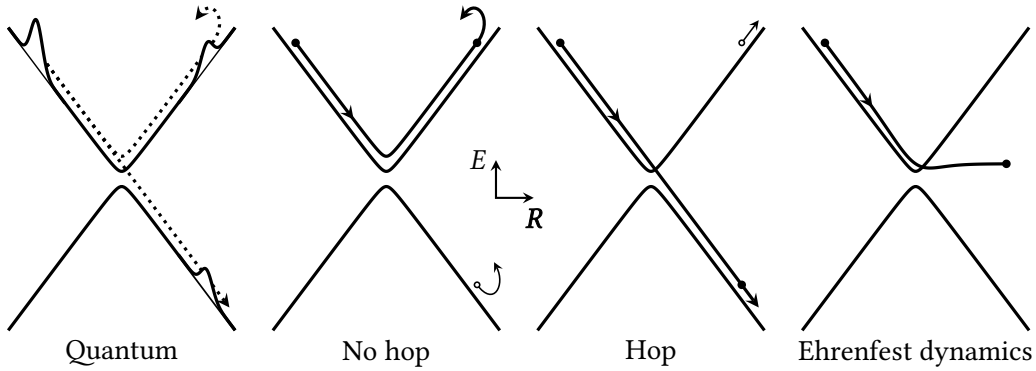

Figure 2.6: Decoherence. For a simple avoided crossing, the quantum wavepacket will split and decohere, with the lower state wavepacket moving further right and the upper state wavepacket being reflected. In surface hopping, if the trajectory does not hop, it will be pushed back towards the crossing, while a hopping trajectory will continue away from the crossing. With no decoherence, the Ehrenfest populations on the other state (represented with unfilled circles) will behave non-physically. A pure Ehrenfest trajectory will feel the force from both states, leading to no overall force, unlike either of the correct options.

'reflected', i.e. multiplied by minus one. In practice, we only re-scale the component of the momentum that lies along the non-adiabatic coupling vector.[62,63]

As in Ehrenfest dynamics, we generally run an ensemble of surface hopping trajectories to model the spatial extent of the wavepacket. As mentioned before, we derive all observables from the single-state ansatz, e.g. for population

$$P_m^{\mathrm{SS}}(t) = \frac{1}{N_{\mathrm{tr}}} \sum_{u}^{N_{\mathrm{tr}}} \delta_{i_u m}, \tag{2.43}$$

where we have used the somewhat clumsy i_u to indicate the active state of trajectory u (which is time-dependent). We also have an Ehrenfest wavefunction, and thus, we can calculate Ehrenfest populations *à la* Eq. (2.38). The Ehrenfest populations are often referred to as the *quantum* populations and the single-state populations as the *classical* populations.

Decoherence Corrections

Unfortunately, surface hopping and classical Ehrenfest dynamics inherently lack any decoherence. This is a generic problem, but here we show a particularly vivid example: a simple avoided crossing system, as shown schematically in Fig. 2.6. Considering first the fully quantum picture in the left panel, the wavepacket will approach the conical intersection, interact with the coupling region (where the wavepacket will be coherent), and then split into two separate wavepackets, one on each state. Here, the wavepacket decoheres, and the dynamics of the two branches are no longer the same — the wavepacket on the upper state will be reflected towards the intersection, while the wavepacket on the lower state will be pushed further away.

For surface hopping, the trajectory approaches the crossing located entirely on one state, as in the quantum picture. When it reaches the coupling region, it will either hop or stay on the same surface — schematically designated in the middle two panels of Fig. 2.6. After the crossing, the single-state electronic wavefunction $|\psi_i\rangle$ is located entirely on one state, while the Ehrenfest electronic wavefunction, defined by the coefficients $\{c_m\}$, is coherently spread across both states. As there is no coupling between the states in this region, the Ehrenfest electronic wavefunction will stay like this until the next coupling region (cf. Eq. (2.37)).

As in the wavefunction case, if the active state remains the upper, and the trajectory returns to the coupling region. If it hops, the trajectory then will be forced away from the coupling region. Either way, the portion of the Ehrenfest wavefunction not on the active state will behave non-physically by 'moving uphill'. When the trajectory next reaches a coupling region, there will be a spurious interference between the two states. We also have a similar issue in the pure Ehrenfest dynamics case, shown on the right of Fig. 2.6. If the two states' populations are similar, then the force on the classical trajectory, given by Eq. (2.34), is like neither of the individual states, and neither of the correct cases is seen.

The root of the decoherence problem in surface hopping is the dual propagation of wavefunctions. When there happen to be situations when the two electronic wavefunctions are not the same, then there will always be some degree of non-physical behaviour. This is known as the *internal consistency* problem[88] — a correct surface hopping simulation will have

$$P_m^{\mathrm{Ehr}}(t) \approx P_m^{\mathrm{SS}}(t).$$

These effects have led to the (sometimes contentious) topic of decoherence corrections. Simply, these attempt to find some additional way of correcting the simple surface hopping picture to remove the non-physical behaviour of the Ehrenfest populations.

The most commonly used method is the *energy-based decoherence* (EDC) correction,[88–90] which corrects the Ehrenfest wavefunction to resemble the single-state wavefunction. To do this, the Ehrenfest coefficients[iv] on all non-active states are exponentially decayed away using

$$\begin{gathered} c'_m(t) = c_m(t)\exp\left(-\Delta t \tau_{im}^{-1}\right), \quad c'_i(t) = c_i(t)\left(\sum_{m\neq i}\frac{1-|c'_m(t)|^2}{|c_i(t)|^2}\right)^{\frac{1}{2}}, \\ \tau_{im} = \frac{1}{|E_m - E_i|}\left(1+\frac{C}{E_{\mathrm{kin}}}\right) \end{gathered} \tag{2.44}$$

where the prime indicates the corrected coefficients, Δt the time-step, C is a constant usually set to the value of 0.1 $\mathrm{E_h}$, and τ_{im} is the decoherence time between states i and m. The corrected coefficients are then used at the start of the next step. Taking the example in Fig. 2.6, the energy-based decoherence correction would remove the Ehrenfest populations on the non-active state and, hence, the non-physical behaviour. We note that this method was originally applied to classical Ehrenfest dynamics in a slightly modified manner.[89,90]

The energy-based decoherence method can be controversial, as the decoherence lifetime is calculated in a somewhat ad hoc manner, which can not be derived from underlying quantum theories.[91] It is, however, used in almost all modern surface hopping calculations, as it has effectively no computational cost and gives at least qualitatively correct results, an improvement on plain fewest switches surface hopping. Alternative methods also exist, with the augmented fewest switches algorithm[63,91] and mapping inspired approaches[92–94] both available. The former involves propagating additional auxiliary trajectories to calculate the decoherence rate, so it is not often used, while the latter has only recently been introduced.

Frozen Gaussians

Here, we very briefly cover the most common method of improving on mixed-quantum-classical methods, namely frozen Gaussian methods.[87,95–97] These use fixed-width Gaussian functions to model the nuclear wavepacket, which are usually propagated using classical or semi-classical equations of motion for the central phase-space coordinate.

[iv] Occasionally this is implemented to the Ehrenfest populations. Practically, this attaches a factor of two to the decay rate and does not normally make a great deal of difference.

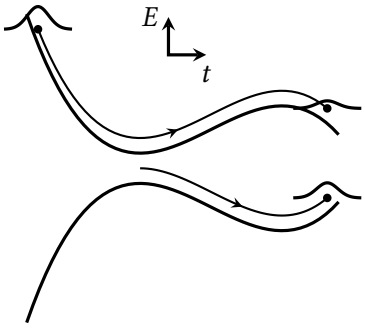

Figure 2.7: Example of ab initio multiple spawning. The constant width (frozen) Gaussian approximates the nuclear wavefunction and is propagated according to the classical dynamics of the centre. In coupling regions, a new Gaussian can be spawned, which travels according to its centre. These Gaussians can transfer population, indicated by the changing heights of the Gaussians.

An intriguing aspect of these methods is that the frozen Gaussians form a basis in which the full Schrödinger equation is solved, as given in Eq. (2.7). Therefore, the dynamics can, *in principle*, be converged to the correct quantum answer, in the limit of a complete basis and no algorithmic approximations. Unfortunately, this is seldom achievable, as the number of trajectories would be far too large for any practical calculation.

In this thesis, we use a simple variant, ab initio multiple spawning (AIMS),[97,98] with a schematic example shown in Fig. 2.7. This method resembles surface hopping, as each frozen Gaussian is propagated according to a single-state classical trajectory. In regions with large non-adiabatic couplings, we 'spawn' a new frozen Gaussian on the non-populated state and propagate it independently. The two Gaussians can then interact, transferring population between each other, and the new frozen Gaussian is also free to spawn new frozen Gaussians, leading to a steadily increasing number of basis functions. The finer details of AIMS are not particularly important to this thesis, and are covered elsewhere.[97]

2.4 — Initial Conditions

For both frozen Gaussian and mixed-quantum-classical dynamics methods, a trajectory requires an initial condition: a set of electronic coefficients, nuclear positions and momenta. The outcome of the dynamics is significantly affected by all three of these factors, so finding the correct set of initial conditions is extremely important for good-quality dynamics.

Generally, as we are trying to simulate photo-dynamics, we try to simulate the excitation process from the wavefunction's ground electronic state. To perform this, we first need a representation of the nuclear wavefunction $\chi(\boldsymbol{R})$ in phase-space. The simplest way to do this is using the Wigner quasi-probability distribution, defined (in one dimension) as

$$W(R,P) = \frac{1}{\pi}\int_{-\infty}^{\infty} \chi^*(R+s)\chi(R-s)\exp(2iPs)\,\mathrm{d}s, \tag{2.45}$$

where P and R indicate momentum and position displacements from the minimum. The most common distribution to use is the Wigner transform of the ground-state N_{dim}-dimensional harmonic oscillator, which has the simple form

$$W(\boldsymbol{R},\boldsymbol{P}) = \prod_i^{N_{\mathrm{dim}}} \frac{1}{\pi}\exp\left(\frac{-2}{\omega_i}\left(\frac{P_i^2}{2m_i} + \frac{1}{2}m_i\omega_i^2 R_i^2\right)\right), \tag{2.46}$$

where m_i, ω_i are the mass and angular frequency of mode i, $\boldsymbol{R} = (R_1, \ldots, R_{N_{\text{dim}}})$ and $\boldsymbol{P} = (P_1, \ldots, P_{N_{\text{dim}}})$. This assumes that all modes are orthogonal, and is usually performed in the vibrational normal mode basis.

This method has two issues: first, it assumes a harmonic oscillator and, thus, does not deal with anharmonicity (or multiple minima) in the ground state potential, and second, we use Cartesian normal modes, which do not describe rotational coordinates well. As such, it is also common to use full ground state (Born–Oppenheimer) dynamics simulations, with the potentials calculated using electronic structure theory.[99,100] These can more adequately deal with these restrictions, although they generally lack a good description of nuclear quantum effects (such as the zero-point energy). The most high-level techniques currently employed use a molecular dynamics simulation coupled to a 'quantum thermostat' to better approximate nuclear quantum effects.[99,101,102] Either way, the molecular dynamics simulations will approximate a ground state distribution within the limit of long simulation time, following the ergodic hypothesis, and thus, we can sample random points in time.

From whichever distribution we have chosen, we sample N_{sa} points with phase-space coordinates $(\boldsymbol{R}_u, \boldsymbol{P}_u)$, and for each point calculate the transition energies E^u_{mz} and transition dipole moments

$$\mu^u_{mz} = \int_{-\infty}^{\infty} \psi^*_m(\boldsymbol{r}; \boldsymbol{R}_u) \hat{\mu}(\boldsymbol{r}) \psi_z(\boldsymbol{r}; \boldsymbol{R}_u) \mathrm{d}\boldsymbol{r}$$

for a set of final electronic states indexed by z. We can then calculate the relative probability of the point u being excited into state z from state m as

$$p^u_{mz} = \frac{\mathscr{W}(E^u_{mz})}{E_{mz}} \left|\mu^u_{mz}\right|^2, \tag{2.47}$$

where $\mathscr{W}(E)$ is an energetic window function (which models the energy spread of the excitation pulse).

For each transition, we generate a uniform random number $0 < \zeta < 1$, and the initial condition is accepted if $\zeta < p^u_{mz}/\max(p^u)$, normalising the probability to the maximum of the ensemble. We then use the accepted initial condition u to start a trajectory localised on state z (e.g. for surface hopping $|c^u_m(t=0)|^2 = \delta_{mz}$ and z as the active state). As an additional benefit, we can calculate the photo-absorption spectra via the nuclear ensemble approximation 'for free',[100,103,104] by using the formula

$$\sigma^{\text{NEA}}(E) \propto \sum_z \sum_u^{N_{\text{sa}}} E^u_{mz} \left|\mu^u_{mz}\right|^2 g(E, E^u_{mz}), \tag{2.48}$$

where $\sigma^{\text{NEA}}(E)$ is the absorption spectrum. $g(E, E^u_{mz})$ is a function (usually a Gaussian or Lorentzian) centred at E^u_{mz} introducing a phenomenological broadening.

When simulating experiments, we have to match the window function W(E) to the experiment's excitation process. Generally, this will involve a comparison of experimental and predicted absorption spectra, shifting the excitation window function to better match the region of the spectrum excited in the experiment rather than the absolute energies of the experimental pump-probe experiment. This practice is somewhat controversial, but can help mitigate some of the errors that occur when one uses an electronic structure method that does not describe the transition energies particularly well.

— 3 —

Electronic Structure Theory

Almost all previously derived equations require separating the system into two parts. In this section, we deal with electronic structure theory, which concerns itself with the electronic part, solving the electronic time-independent Schrödinger equation[i]

$$\hat{H}^{\mathrm{el}}|\psi_m\rangle = E_m|\psi_m\rangle, \tag{3.1}$$

which was defined in Eqs. (2.2) and (2.4) earlier. Electronic structure theory aims to calculate the electronic energies, E_m, and wavefunctions, $|\psi_m\rangle$. As the goal of this work is to describe non-adiabatic dynamics and conical intersections, we are interested in methods which allow the calculation of more than one electronic state, as well as analytical calculations of the gradients $\nabla_\alpha E_m = \langle\psi_m|\nabla_\alpha \hat{H}|\psi_m\rangle$ and non-adiabatic couplings $\boldsymbol{d}^\alpha_{mn} = \langle\psi_m|\nabla_\alpha|\psi_n\rangle$. We shall not show any of the details of the calculations of these quantities; instead, we will focus on the qualitative differences in the wavefunctions and potential energies of the methods.

In contrast to the nuclei, the electrons are very light, and so *only* fully quantum solutions to the Schrödinger equation give reasonable answers. Additionally, except for the most straightforward cases, the solution of these equations is a numerical procedure, where the solution must be found through optimisation. Unfortunately, the *correct* result, which we will later see is called full-CI, scales exponentially with the system size.

The central problem of modern electronic structure theory is chiefly electron correlation. In this thesis, we use the definition

$$P(\boldsymbol{r}_1, \boldsymbol{r}_2) \neq \frac{1}{2}\rho(\boldsymbol{r}_1)\,\rho(\boldsymbol{r}_2)\,, \tag{3.2}$$

where we have defined the two-electron density as[105]

$$P(\boldsymbol{r}_1, \boldsymbol{r}_2) = \langle\psi_i|\hat{\rho}(\boldsymbol{r}_1, \boldsymbol{r}_2)|\psi_j\rangle, \text{ with } \hat{\rho}(\boldsymbol{r}_1, \boldsymbol{r}_2) = \frac{1}{2}\sum_{i,j\neq i}^{N_\mathrm{e}} \delta(\boldsymbol{r}_1 - \boldsymbol{r}_i)\,\delta\big(\boldsymbol{r}_2 - \boldsymbol{r}_j\big) \tag{3.3}$$

and the one-electron density as[105]

$$\rho(\boldsymbol{r}_1) = \langle\psi_i|\hat{\rho}(\boldsymbol{r}_1)|\psi_j\rangle, \text{ with } \hat{\rho}(\boldsymbol{r}_1) = \sum_{i}^{N_\mathrm{e}} \delta(\boldsymbol{r}_1 - \boldsymbol{r}_i)\,. \tag{3.4}$$

In short, the position of one electron affects the position of another. Correlation comes in two distinct forms, Fermi and Coulomb, which arise from different effects. Fermi correlation is the manifestation of the Pauli exclusion principle, stating that two electrons with the same

[i] In the following, we will use the Dirac notation, implicitly including the dependence of these energies and wavefunctions on the nuclear position $\boldsymbol{R}$.

spin cannot exist in the same position. As we shall see, all of the methods we cover here deal with this essentially perfectly. The second type, Coulomb correlation, arises from the electron-electron repulsion interaction, acting to decrease the system's energy by increasing the inter-electronic separation. This is much harder to calculate and, in general, can only be perfectly calculated in the simplest of systems.

Inside Coulomb correlation, there are two other common distinctions: static and dynamic correlation. Defining these can be difficult, as they arise from the same physical interaction (electron-electron repulsion). We shall use a working definition, where we use static correlation to mean 'qualitative' correlation (i.e. the wavefunction is qualitatively wrong without it) and dynamic correlation to mean 'quantitative' correlation (i.e. the wavefunction is only quantitatively wrong without it). In this thesis, static correlation is particularly important around areas of electronic degeneracy, such as conical intersections. Thus, to describe photodynamics, we will need a robust way to deal with it. On top of that, dynamic correlation refines a picture that is already approximately correct.

We begin by looking at Hartree–Fock, the 'worst acceptable method', and forms the basis of all other methods. Hartree–Fock accounts for Fermi correlation, but does not account for Coulomb correlation. Next, we discuss configuration interaction, defining the brute force correct answer and some practical algorithms to approximate it. After, we move to multi-configurational calculations, which are generalised versions of Hartree–Fock that make qualitative improvements, generally giving static correlation, and then briefly cover multi-reference perturbation theory, which is a highly effective method to add dynamic correlation to multi-configurational wavefunctions.

3.1 — Hartree–Fock

As it is the basis of almost all electronic structure, we first cover the Hartree–Fock method.[105–107] This approach is straightforward, often giving qualitatively correct wavefunctions, and is frequently used as a starting point for the calculation of higher-level methods.

First, we describe the electronic wavefunction as a single Slater determinant (labelled ϕ)

$$|\psi^{\mathrm{HF}}\rangle = |\phi\rangle, \quad \langle \boldsymbol{x}_1, \boldsymbol{x}_2, \ldots |\phi\rangle = \frac{1}{\sqrt{N_e!}} \begin{vmatrix} \varphi_1(\boldsymbol{x}_1) & \varphi_2(\boldsymbol{x}_1) & \cdots \\ \varphi_1(\boldsymbol{x}_2) & \varphi_2(\boldsymbol{x}_2) & \\ \vdots & & \ddots \end{vmatrix}, \tag{3.5}$$

where $\boldsymbol{x}_i = (\boldsymbol{r}_i, s_i)$ is the combined position and spin coordinate of electron i, N_e is the number of electrons, and the functions φ_q are molecular spin-orbitals. Using this wavefunction, we solve for the energy self-consistently such that the overall energy of the wavefunction is minimised (i.e. variationally).

The anti-symmetry of the determinant causes the function to obey the Pauli principle, and the value of the wavefunction tends to zero at $\boldsymbol{x}_i = \boldsymbol{x}_j$. This leads to the key strength of Hartree–Fock theory: we model Fermi correlation. However, the single Slater determinant does not allow any Coulomb correlation, so Hartree–Fock gives a higher energy than the correct one.

While Hartree–Fock theory has issues, the results are generally qualitatively good, except around conical intersections or dissociation limits. The next section covers ways to add dynamic correlation to Hartree–Fock, improving its qualitative accuracy. In the following section, we discuss adding static correlation and improving its description around conical intersections.

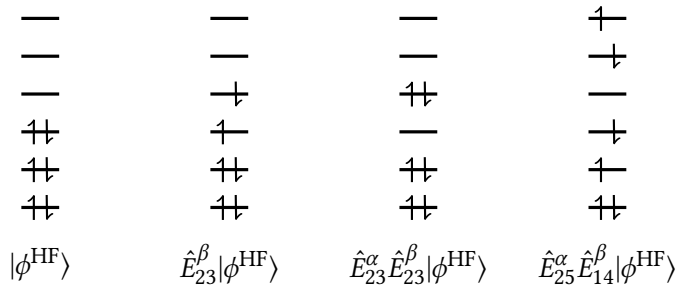

Figure 3.1: Example of excited configurations reachable in an SRCISD calculation. The superscript α, β indicates whether the excitation operator acts on alpha or beta spins.

3.2 — Configuration Interaction

As we shall see, configuration interaction (CI) is a conceptually simple but very powerful way to improve the results of a Hartree–Fock calculation.[105,108] In general, a CI wavefunction is written

$$|\psi^{\mathrm{CI}}\rangle = \sum_{i \in D} c_i |\phi_i\rangle, \tag{3.6}$$

where the CI wavefunction $|\psi^{\mathrm{CI}}\rangle$ is formed as the weighted sum of the set D of Slater determinants $|\phi_i\rangle$. Configuration interaction, like Hartree–Fock, is a variational theory; we aim to find the minimum energy solution for the equation

$$\hat{H}^{\mathrm{el}}|\psi^{\mathrm{CI}}\rangle = E^{\mathrm{CI}}|\psi^{\mathrm{CI}}\rangle, \tag{3.7}$$

with the set of weights $\{c_i\}$ often called the CI vector.

Configuration interaction calculations are popular due to their simplicity; they are easy to implement, understand, and calculate properties for. They also give a hierarchy of improvement in the expansion of D — due to the variational optimisation, adding configurations will always provide a better wavefunction. With that, we will discuss three methods to construct the set D.

A special example of CI is when D contains all possible configurations which preserve the number of electrons and the spin- and space-symmetry. This is called full configuration interaction (FCI), representing a brute-force solution to the Schrödinger equation in a particular basis.[105,108] This method addresses both Fermi and Coulomb correlation and is of such importance that the most common definition of correlation energy,

$$E^{\mathrm{corr}} = E^{\mathrm{FCI}} - E^{\mathrm{HF}}, \tag{3.8}$$

is defined as the difference between the FCI and Hartree–Fock energies.

The issue with full CI is simple: the number of Slater determinants in D scales as

$$N_{\mathrm{SD}} = \binom{N_{\mathrm{o}}}{n_\uparrow}\binom{N_{\mathrm{o}}}{n_\downarrow} \tag{3.9}$$

where N_{o} indicates the number of orbitals and $n_\uparrow$ and $n_\downarrow$ the number of spin-up and spin-down electrons respectively. For $n_\uparrow = n_\downarrow = N_{\mathrm{o}}$, this is a scaling of $\mathcal{O}(N_{\mathrm{o}}^{-1}4^{N_{\mathrm{o}}})$, and increases exponentially. For all but the very smallest systems ($N_{\mathrm{e}} = n_\uparrow + n_\downarrow \approx N_{\mathrm{o}} < 20$), full-CI is not computationally feasible.

The simplest approximate method for constructing D is *single-reference* configuration interaction (SRCI).[105] In this, the configurations are generated by applying excitation operators $\hat{E}_{ia}$ to a reference determinant, usually a Hartree–Fock wavefunction. The calculation is limited

in the number of excitation operators applied, with the calculation most often being truncated at only single- and double-excitations (SRCISD). This can be written as

$$|\psi^{\mathrm{SRCISD}}\rangle = c_0|\phi^{\mathrm{HF}}\rangle + \sum_{i,a} c_{ia}|\phi_{ia}\rangle + \sum_{ij,ab} c_{ijab}|\phi_{ijab}\rangle, \tag{3.10}$$

where $|\phi_{ij\ldots ab\ldots}\rangle = \hat{E}_{ia}\hat{E}_{jb}\ldots|\phi^{\mathrm{HF}}\rangle$[ii] represents the configuration[iii] consisting of an n-tuple excitation from the HF reference, and $c_{ij\ldots ab\ldots}$ its weight. We illustrate this process schematically in Fig. 3.1. Unfortunately, the quality of an SRCISD calculation is strongly related to the quality of the original reference, and it cannot reliably improve a Hartree–Fock calculation which is not already qualitatively correct.

A useful generalisation of this is *multi-reference* configuration interaction (MRCI).[105,109] In this case, the excitation operators are applied to a set of reference Slater determinants $R = \left\{\phi^{\xi}\right\}$, which should already recover much of the static correlation. Truncating at only singles- and doubles, the generalisation is thus

$$|\psi^{\mathrm{MRCISD}}\rangle = \sum_{\xi\in R} c_0^{\xi}|\phi^{\xi}\rangle + \sum_{i,a,\xi\in R} c_{ia}^{\xi}|\phi_{ia}^{\xi}\rangle + \sum_{ij,ab,\xi\in R} c_{ijab}^{\xi}|\phi_{ijab}^{\xi}\rangle, \tag{3.11}$$

where $|\phi_{ij\ldots ab\ldots}^{\xi}\rangle = \hat{E}_{ia}\hat{E}_{jb}\ldots|\phi^{\xi}\rangle$ is n-tuple excitation from the reference determinant ξ and $c_{ij\ldots ab\ldots}^{\xi}$ its coefficient. We will cover the choice of the reference set in the chapter on multi-configurational self-consistent field theory below. Multi-reference configuration interaction improves significantly on its single-reference cousin, especially when the original reference is good. Unfortunately, the number of variational parameters (i.e. $c_{ij\ldots ab\ldots}^{\xi}$) can be large, making MRCI an expensive method.

We mention the internally contracted formalism, which requires that $c_{ij\ldots ab\ldots}^{\xi}$ is the same for each ξ. This leads to the total number of variational parameters being similar to the single-reference case. While it appears to be a reasonably significant approximation, it does seem to give reasonable results.

One glaring fault of both of these methods is their lack of size-consistency.[110–112] Briefly, if two non-interacting subsystems A and B are considered, then a calculation performed on the subsystems separately or together should return the same result. When calculating separately, both $|\psi_A^{\mathrm{SRCISD}}\rangle$ and $|\psi_B^{\mathrm{SRCISD}}\rangle$ will contain up to double excitations, which leads to effective quadruple excitations upon combination. If the calculation were performed with the two systems together, then the combined wavefunction $|\psi_{A+B}^{\mathrm{SRCISD}}\rangle$ will only contain double excitations. Thus, the two calculations contain different configurations, giving different energies.

This issue has led to the superseding of SRCI by coupled-cluster techniques. In MRCI, however, it is not obvious how to generalise the coupled cluster methods to multiple reference configurations.[113,114] Therefore, there exist several *ad hoc* strategies, sometimes called Davidson corrections, which aim to correct the MRCI energy.[109,110] In the MRCISD case, they are often denoted by adding a '+Q' to the end of the truncation. In this thesis, we use the renormalised Davidson correction,[109]

$$E^{\mathrm{MRCI+Q}} = E^{\mathrm{MRCISD}} + \frac{1-c_0^2}{2c_0^2-1}\left(E^{\mathrm{MRCISD}} - E^0\right), \tag{3.12}$$

where $c_0^2 = \sum_{\zeta\in R}(c_0^{\zeta})^2$ is the reference weight and E^0 is the reference energy. Unfortunately, this correction only affects the energy. All molecular properties which depend on the wavefunction

[ii] We use a, b, c to represent virtual orbitals

[iii] We use configuration here to indicate either Slater determinants or spin-adapted combinations thereof.

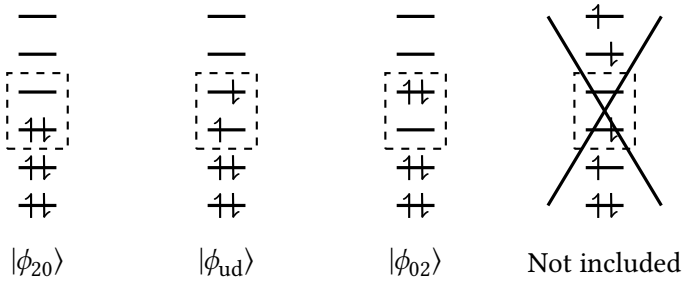

Figure 3.2: Example of configurations allowable in CASSCF calculation, in this case, a (2,2) active space (denoted by the dashed box). The subscripts on the determinants describe the occupation of orbitals inside the active space. The final configuration excites both from and to orbitals outside of this active space (either is sufficient) and is not included in the configuration expansion.

(e.g. dipole moments, scattering, etc.) are unaffected by this correction, and the size-consistency issues are not easily fixable. Additionally, properties that depend on the potential energy surfaces, such as the gradient and frequencies, can no longer be calculated analytically. While it is possible to use numerical differentiation, this requires at least $6N_{\mathrm{at}} - 11$ calculations per point and is generally not feasible in a dynamics simulation.

In this section, we showed only single-state variants of these methods. In CI, finding more than one energy from Eq. (3.7) is relatively easy, giving multiple sets of coefficients, one for each state. Equally important is that the calculation of gradients and non-adiabatic couplings is relatively simple, as well as observable quantities such as dipole moments or the scattering patterns discussed in Section 4.2.

3.3 — Multi-configurational Self-consistent Field

We previously mentioned that MRCI gives good wavefunctions if its reference is statically correlated. To find that reference, we use a method that combines configuration interaction and Hartree–Fock, the multi-configurational self-consistent field (MCSCF) method.[115–117] Like Hartree–Fock, MCSCF only really gives qualitative accuracy (i.e. is not dynamically correlated), but unlike Hartree–Fock, it can be used to give good wavefunctions when static correlation is needed.[iv]

The ansatz for multi-configurational self-consistent field is

$$|\psi^{\mathrm{MCSCF}}\rangle = \sum_{i \in D} c_i |\phi_i\rangle, \tag{3.13}$$

which looks identical to the CI ansatz in Eq. (3.6). The difference is that *both* the coefficients $\{c_i\}$ and the orbitals $\{\varphi_q\}$ which make up the configurations are varied. As in CI, MCSCF is variational, and one varies both parameters until the overall energy is minimised. This is normally done in an iterative process, where a CI procedure is first performed, followed by an orbital optimisation step similar to a Hartree–Fock calculation. The new orbitals are then fed back into the CI procedure, and so on, until both the orbitals and the coefficients are converged. For the same set D, the additional flexibility in this method leads to lower energies than configuration interaction and, hence, better wavefunctions.

The most common variant of MCSCF is the complete active space self-consistent field (CASSCF) method.[115–117] In this method, a subset of orbitals (the active space) is chosen, and

[iv] To be clear, MCSCF can give dynamical correlation in the limit of having many determinants, just as in CI. Often, it is used with comparatively small numbers of determinants, primarily recovering static correlation.

a full-CI calculation is performed within this space, which limits the number of orbitals to ≈ 14. Active spaces are usually denoted by (m, n), where m is the number of electrons and n is the number of orbitals in the active space. This process is depicted schematically in Fig. 3.2 for the simplest case, the (2,2) active space.

While this nomenclature is useful, more important than the number of orbitals in the active space is their nature. The orbitals must be adequate to describe the qualitative chemistry of the molecule,[118] for instance, if one is describing a bond-breaking process, the active space should include configurations where electrons are in either the bonding or anti-bonding orbital. This gives the wavefunction the flexibility to describe the electronic density as the bond stretches, giving a good description of the states at all points of the reaction.

CASSCF calculations can also be performed in a state-averaged (SA) manner.[119,120] In this, we calculate N_s individual states from the CI procedure and average them, creating the state-averaged energy as

$$E_{SA} = \sum_{\gamma}^{N_s} w_\gamma E_\gamma, \tag{3.14}$$

where E_γ is the energy of state γ and w_γ the weight, generally set to $\frac{1}{N_s}$, equally weighting all of the states. The variational procedure then optimises this state-averaged energy.

This is a cheap and flexible method for describing systems where more than one state is required, but it is notoriously tricky in its application,[109,118] as there are many parameters (size of active space, choice of orbitals, number of states) which all affect the results significantly. Consequently, SA-CASSCF calculations are often plagued by bias, where different states or geometries are described with different quality. This can lead to qualitatively incorrect potential energy surfaces, such as predicting the wrong ordering of states or crossings far away from their correct positions.

It is, however, a cheap and flexible method to describe multiple states. It allows for the calculation of properties such as gradients and non-adiabatic couplings,[78] observables such as those covered in section Chapter 4,[121] and different spin-manifolds, all with relatively simple implementations. Critically, it is ideal for calculating conical intersections, as it considers both states equally in the calculation. All in all, this means that SA-CASSCF is the workhorse for non-adiabatic dynamics, even if the potential energy surfaces often lack dynamic correlation.

To fix this, we often base dynamically correlated treatments on a base of SA-CASSCF. This includes MRCI, and the topic of the next section, multi-reference perturbation theory.

3.4 — Multi-reference Perturbation Theory

There are often cases where a relatively cheap, dynamically correlated multi-configurational method capable of describing multiple states is needed — particularly in the case of non-adiabatic dynamics. Simulations of dynamics require good potentials, especially at conical intersections, but also efficient calculations, as one will perform many calculations.

While CASSCF often provides good-quality wavefunctions, it often lacks a proper treatment of dynamic correlation. We have already covered one statically and dynamically correlated method — MRCI — but this method is very expensive. For dynamcis, the most commonly used method is multi-state second-order complete active space perturbation theory (MS-CASPT2)[122], and its 'extended' (XMS-CASPT2)[123] and 'rotated' (RMS-CASPT2)[124,125] cousins. These are quasi-degenerate extensions of standard perturbations theory applied on a basis of multiple reference Slater determinants. Aside from (X/R)MS-CASPT2, there are a host of other similar algorithms, all with their own barely intelligible string of letters and numbers, but they are not as often used nor as significantly developed.[126,127]

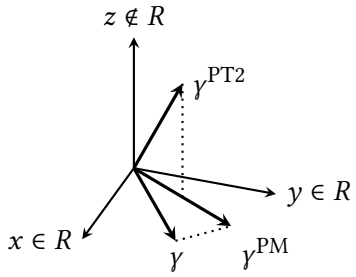

Figure 3.3: Schematic description of the three different states from a (X/R)MS-CASPT2 calculations. The original reference state γ comes from an SA-CASSCF calculation and is located in the xy-plane, representing the reference space R. The MS-CASPT2 state γ^{PT2} has a non-zero projection onto the z-axis, representing the perturbation space. Projecting γ^{PT2} down to the xy-plane (and re-normalising) gives the perturbation-modified state γ^{PM}, which is not necessarily the same as the original state γ.

The detailed theory of MS-CASPT2 is quite involved, so we will only give a cursory description, but the differences between individual standard, rotated, and extended variants are both easy to understand and result in significant differences. We begin a MS-CASPT2 calculation with a SA-CASSCF calculation, which returns a set R of N_{s} states. We then find the expectation value of the Fock operator

$$f_{pq}^{\gamma} = h_{pq} + \sum_{rs} D_{rs}^{\gamma} \left[(pq|rs) - \frac{1}{2} (pr|qs) \right], \tag{3.15}$$

where D_{rs}^{γ} is the one-electron density matrix element (in the SA-CASSCF molecular orbital basis) for state γ and orbitals r and s, and $(\cdot|\cdot)$ the electron-electron repulsion integral in Chemist's notation.[105] This operator is *state-specific*, applying to the state γ.

From here, we generate an effective Hamiltonian matrix $\hat{H}^{\mathrm{eff}}$. The actual procedure for doing this involves solving for the first-order perturbatively-corrected wavefunction, which introduces effective single and double excitations in a perturbative manner. We do not cover this as it is quite involved, and covered well elsewhere.[127,128] After finding $\hat{H}^{\mathrm{eff}}$, it is symmetrised and diagonalised, receiving the MS-CASPT2 energies.

This diagonalisation will generally mix the states, describing the rotation of the original CASSCF states into the new MS-CASPT2 states. We can also simply rotate the CASSCF states (without applying the perturbation) to retrieve the perturbation-modified (PM-CASSCF) states[128], which serve as zeroth-order approximations to the MS-CASPT2 states and allow easy calculation of properties. This rotation is shown schematically in Fig. 3.3.

MS-CASPT2 has been shown to give excellent results, especially for excitation energies. This is primarily due to the state-specific Fock operator, which allows for a tailored description for each state. The most obvious improvement is that it can alter the CASSCF states. For example, in systems with non-physical mixing of states at the SA-CASSCF level, MS-CASPT2 can separate two states, allowing for a much better qualitative description. Unfortunately, there are issues with MS-CASPT2. If we perform a unitary transformation of the CASSCF states before calculating the Fock operators, the state-specific Fock operators will be different and, thus, so will the MS-CASPT2 energies. This is not usually an issue but becomes essential around conical intersections, where any linear combination of the two degenerate states is also an eigenstate of the Hamiltonian. MS-CASPT2, however, gives different energies upon mixing, leading to incorrect descriptions around conical intersections.

To fix this, extended MS-CASPT2 (XMS-CASPT2) was developed. Here, we use a state-averaged Fock operator, which can be found by taking the definition of the Fock operator in

Eq. (3.15) and replacing the state-specific one-electron density matrix with the state-averaged density matrix, given as

$$D_{rs}^{\mathrm{SA}} = \sum_{\gamma \in R} w_\gamma D_{rs}^{\gamma}, \tag{3.16}$$

where w_γ is the weight of state γ. After that, the calculation proceeds almost identically to the MS-CASPT2 calculation, and we generate and diagonalise an effective Hamiltonian, which includes the perturbation. Again, the initial SA-CASSCF states are intermixed into the final XMS-CASPT2 states, and a set of PM-CASSCF states can be generated.

The main benefit of XMS-CASPT2 is a much better wavefunction near electronic degeneracies, as the state-specific Fock operator is invariant to unitary transformations of the CASSCF states. Unfortunately, we no longer have the state-specific Fock operator, so XMS-CASPT2 is known not to provide excitation energies as accurately as MS-CASPT2.

The final (and most recent) alteration was rotated MS-CASPT2 (RMS-CASPT2). This method combines the benefits of both methods, using a state-averaged Fock operator to retrieve an intermediate set of states but then a state-specific Fock operator (like in MS-CASPT2) to generate the energies. In principle, this leads to the advantages of both methods, namely, good excitation energies while maintaining smooth potential energy surfaces around the conical intersections. As this is a new method, the benchmarking performed on RMS-CASPT2 is not as complete as it is on XMS- or MS-CASPT2, and it is unclear whether it provides a better overall result than its predecessors.

Overall, the (X/R)MS-CASPT2 methods provide a robust description for both strongly and weakly correlated systems and are flexible enough to deal with both excited and ground states. Furthermore, they are often computationally affordable, especially compared to similar methods such as MRCI, and have been implemented in various programs. They are particularly efficient in their internally contracted forms. Recently, gradient and non-adiabatic coupling implementations have become available,[123,129] which makes them applicable for non-adiabatic dynamics simulations — in fact, they are often considered among the best methods available. Finally, the PM-CASSCF wavefunctions allow for cheap calculation of molecular properties, which, while approximate, usually give acceptable results.

— 4 —

Observables

In this chapter, we cover the theory and calculation of three different ultrafast experimental observables, summarised as

$$\begin{aligned} A + \hbar\omega &\rightarrow A + \hbar\omega' && \text{(x-ray scattering)} \\ A + e^- &\rightarrow A + e^- && \text{(electron scattering)} \\ A + \hbar\omega &\rightarrow A^+ + e^- && \text{(photo-ionisation).} \end{aligned}$$

The first process, x-ray scattering, involves the incident photon $\hbar\omega$ colliding with a target A, changing its momentum. We then measure this change, giving information about the target A. This thesis focuses entirely on non-resonant processes when the photon is of sufficiently high energy, generally in the hard x-ray regime. The second process is a variant of the first: electron scattering, where instead of an x-ray photon the scattering particle is a high-energy electron. Thankfully, this has very similar physics to x-ray scattering; we will describe both in a similar framework.

Finally, we have photo-ionisation, where the molecule absorbs the incident photon, and an electron is ejected. We use this technique in photo-electron spectroscopy, which uses a laser to ionise a molecule and measure the kinetic energy of the departing electron. This allows the measurement of the energy differences between the neutral and ionic energy manifolds.

These three methods are leading methods for ultrafast experiments,[1,31,31,47,48,130–141] as they can be readily extended down to the femtosecond regime of time-resolution. This is due to the advent of new light-sources, such as free-electron lasers (FELs)[1,135,142] and their x-ray cousins (XFELs),[143–145] as well as a host of other new photonic breakthroughs.[137,145–148]

These three methods are also complementary. Scattering provides mainly spatial information, helping understand the locations of the particles in the molecule. In contrast, spectroscopy probes the energy of the wavepacket on the potential surfaces. Together, these methods offer a more comprehensive understanding of the wavepacket than either one alone.

4.1 — Time-resolved Measurements

Before we get into the details of each technique, we will quickly discuss the basics of time-resolved measurements and create a framework to calculate observables for time-resolved wavefunctions.

The workhorse of ultrafast photochemistry is the *pump-probe* technique, depicted schematically in Fig. 4.1. The sample is first irradiated by a *pump* pulse, which moves the molecule to an excited electronic state. For simplicity, we will set the time of excitation to be $t = 0$. A second pulse, called the *probe* pulse, then measures the sample, giving information about the state of the sample at time t after excitation. This has led to the term 'molecular movie', envisioning the separate times as individual frames.[29] While somewhat quixotic, this analogy neatly summarises the goal of ultrafast experiments.

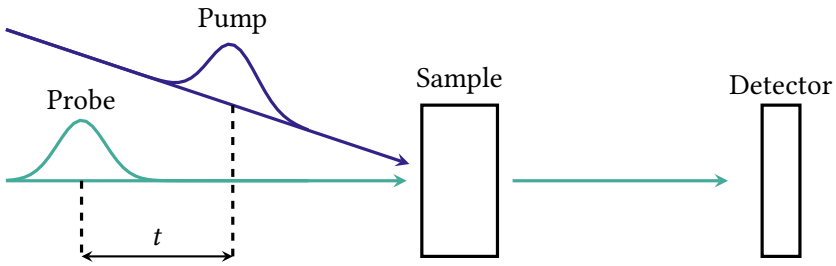

Figure 4.1: Schematic diagram of pump-probe experiment. The pump pulse (indigo) hits the sample, exciting the molecule. At time t later, the probe pulse (green) hits the sample, measuring its state, and then is recorded on the detector. In this thesis, t is in the femtosecond (10^{-15} s) range.

Each technique in this thesis is primarily an electronic observable, corresponding to matrix elements that are integrals over electronic coordinates. In that sense, we can use the Born–Huang representation to define a generic cross-section as

$$\begin{aligned}\sigma(t) &= \sum_{m,n} \int_{-\infty}^{\infty} \chi_m^*(\boldsymbol{R},t) \left[\int_{-\infty}^{\infty} \psi_m^*(\boldsymbol{r};\boldsymbol{R}) \hat{O} \psi_n(\boldsymbol{r};\boldsymbol{R}) \mathrm{d}\boldsymbol{r} \right] \chi_n(\boldsymbol{R},t) \mathrm{d}\boldsymbol{R} \\ &= \sum_{m,n} \int_{-\infty}^{\infty} \chi_m^*(\boldsymbol{R},t) O_{mn}(\boldsymbol{R}) \chi_n(\boldsymbol{R},t) \mathrm{d}\boldsymbol{R}\end{aligned} \tag{4.1}$$

where σ is the cross-section of the process and $\hat{O}$ is the characteristic operator of the process with $O_{mn}(\boldsymbol{R}) = \int_{-\infty}^{\infty} \psi_m^*(\boldsymbol{r};\boldsymbol{R}) \hat{O} \psi_n(\boldsymbol{r};\boldsymbol{R}) \mathrm{d}\boldsymbol{r}$ its electronic matrix element. As mentioned, we are using these equations to model a pseudo-instantaneous interaction, which only occurs at time t. In Chapter 7, we shall introduce how to include energy/time uncertainty into the measurement. The equations are also somewhat generic; they account for static and dynamic measurements and can be used for all electronic observables.

Since we will be working extensively with classical trajectories, we shall also explicitly describe the special case of the nuclear wavefunction represented as a sum of point functions,

$$\sigma(t) = \frac{1}{N_{\mathrm{tr}}} \sum_{u}^{N_{\mathrm{tr}}} \sum_{m,n} c_m^{u\,*}(t) c_n^u(t) O_{mn}\left(\boldsymbol{R}_u(t)\right). \tag{4.2}$$

Here, the sum is both over the N_{tr} trajectories and electronic states, and c_m^u is the coefficient for the electronic state m and trajectory u (e.g. $c_m^u(t) = \delta_{mi_u}$ for a surface hopping trajectory).

In each of the next sections, we will describe a different observable, and how to calculate the electronic matrix elements $O_{mm}(\boldsymbol{R})$. As in the previous chapter, we will use the Dirac notation, with $O_{mn}(\boldsymbol{R}) = \langle \psi_m | \hat{O} | \psi_n \rangle$, remembering the implicit parametric dependence on $\boldsymbol{R}$.

4.2 — X-ray Scattering

We first consider the most basic case of x-ray scattering, the scattering of a free particle. This is given by the *Thomson cross-section*

$$\frac{\mathrm{d}\sigma_{\mathrm{Th}}}{\mathrm{d}\Omega} = P \left(\frac{e^2 Z^2}{4\pi\epsilon_0 m c^2} \right)^2, \tag{4.3}$$

with P the polarisation factor, e the elementary charge, Z and m the charge and mass of the particle, ϵ_0 the permittivity of free space, and c the speed of light. The Thomson cross-section

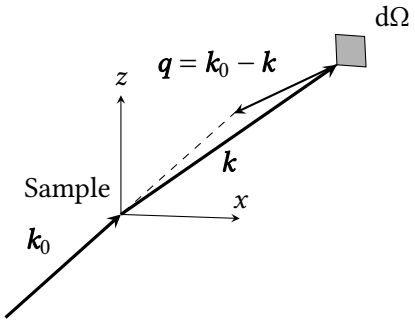

Figure 4.2: Scattering detection geometry. The incoming photon (labelled $\boldsymbol{k}_0$) travels along y, strikes the sample (at the origin), and scatters. The scattered photon (with momentum $\boldsymbol{k}$) is measured by a detector, with the number of photons detected in a small solid angle dΩ proportional to the differential scattering cross-section. Each solid angle is characterised by its momentum transfer $\boldsymbol{q} = \boldsymbol{k}_0 - \boldsymbol{k}$. Elastic scattering events have $|\boldsymbol{k}| = |\boldsymbol{k}_0|$ while inelastic do not. For a rotationally-averaged experiment, the signal only depends on the magnitude of the momentum transfer, q, which can be related to the angle of deviation by Eq. (4.6).

is negligible for any particle except electrons due to the m^{-2} scaling, and so x-ray scattering is (to an excellent approximation) described purely by photon-electron interactions. We will not describe the details of polarisation effects on the scattering, as they are well covered elsewhere.[149]

We now move to molecules, where the scattering pattern is formed of the interference of the scattering of all of the N_e electrons. If we measure all scattered photons, we measure the *two-electron x-ray scattering* matrix element[149,150],

$$O^{\mathrm{x,t}}_{mn} = \frac{\mathrm{d}\sigma_\mathrm{Th}}{\mathrm{d}\Omega}\langle\psi_m|\hat{L}^\dagger\hat{L}|\psi_n\rangle \equiv \frac{\mathrm{d}\sigma_\mathrm{Th}}{\mathrm{d}\Omega}\Lambda_{mn}. \tag{4.4}$$

$\hat{L}$ is the scattering operator,[149,150] given in the position representation by

$$\hat{L} = \sum_i^{N_\mathrm{e}} e^{i\boldsymbol{q}\cdot\boldsymbol{r}_i}, \tag{4.5}$$

where $\boldsymbol{q}$ is the momentum transfer vector. This is the change in momentum of the scattered photon relative to the initial photon, $\boldsymbol{q} = \boldsymbol{k} - \boldsymbol{k}_0$, depicted schematically in Fig. 4.2. The magnitude of the momentum transfer q is given by

$$q = 2\boldsymbol{k}\sin\left(\frac{\theta}{2}\right), \tag{4.6}$$

with θ the scattering angle. Before we move on, we note that the definition of the scattering operator uses the first Born approximation,[65,151] where the x-ray only interacts once with the sample, and Eqs. (4.4) and (4.6) use the Waller–Hartree approximation,[152] where the initial and scattered photons have the same wavelength, i.e. $|\boldsymbol{k}| = |\boldsymbol{k}_0|$. These are both excellent approximations, especially at lower momentum transfers.[150,153]

We have been entirely generic in considering both the diagonal and off-diagonal elements of Eq. (4.4). The diagonal elements give the *total scattering* and include all scattering events starting from the same state.[149,153] The off-diagonal elements pertain to the coherent-mixed scattering signal, which can only be measured when the wavefunction displays electronic coherence.[154] This quantity is not relevant to this work, so we will concentrate on the diagonal elements Λ_{mm}, but still maintain the generality of the equations.

As mentioned, total scattering does not distinguish between events that change the scattered photon energy. If we can measure scattered photon energies, as may be experimentally feasible soon, we can distinguish between two types of scattering: elastic and inelastic.

Elastic scattering, where the energy of the photon does not change, uses the diagonal one-electron x-ray scattering matrix elements

$$O_{mm}^{\mathrm{x,e}} = \frac{\mathrm{d}\sigma_{\mathrm{Th}}}{\mathrm{d}\Omega}\langle\psi_m|\hat{L}^\dagger|\psi_m\rangle\langle\psi_m|\hat{L}|\psi_m\rangle = \frac{\mathrm{d}\sigma_{\mathrm{Th}}}{\mathrm{d}\Omega}|L_{mm}|^2. \tag{4.7}$$

The inelastic scattering, where the energy does change, is given by the sum over the off-diagonal one-electron x-ray scattering matrix elements

$$O_{mm}^{\mathrm{x,ine}} = \frac{\mathrm{d}\sigma_{\mathrm{Th}}}{\mathrm{d}\Omega}\sum_{f\neq m}\langle\psi_m|\hat{L}^\dagger|\psi_f\rangle\langle\psi_f|\hat{L}|\psi_m\rangle = \frac{\mathrm{d}\sigma_{\mathrm{Th}}}{\mathrm{d}\Omega}\sum_{f\neq m}|L_{mf}|^2. \tag{4.8}$$

This is the sum of several individual transitions, each with matrix element L_{mf}. In the limit of perfect energy resolution, all of these would be individually detectable with an x-ray energy shift equal to the transition energy $E_{mf} = E_f - E_m$. Here, we will only consider the sum of all inelastic transitions, sometimes called the 'net inelastic'. Using Eq. (4.4) and the completeness of the electronic states $\{\psi_m\}$, we can write

$$\Lambda_{mm} = \sum_f \langle\psi_m|\hat{L}^\dagger|\psi_f\rangle\langle\psi_f|\hat{L}|\psi_m\rangle = \sum_f |L_{mf}|^2, \tag{4.9}$$

indicating that the total scattering (Eq. (4.4)) is the sum of the elastic and inelastic terms (Eqs. (4.7) and (4.8)), as expected. Both elastic and inelastic use the Thomson cross-section, as before.

Assuming our wavefunctions are real-valued, we can use the definition of the scattering operator (Eq. (4.5)) to derive formulae for the evaluation of these elements as

$$|L_{mn}(\boldsymbol{q})|^2 = \iint_{-\infty}^{\infty} \rho_{mn}(\boldsymbol{r}_1)\,\rho_{mn}(\boldsymbol{r}_2)\,e^{i\boldsymbol{q}\cdot(\boldsymbol{r}_2-\boldsymbol{r}_1)}\mathrm{d}\boldsymbol{r}_1\mathrm{d}\boldsymbol{r}_2 \tag{4.10}$$

$$\Lambda_{mn}(\boldsymbol{q}) = 2\iint_{-\infty}^{\infty} P_{mn}(\boldsymbol{r}_1,\boldsymbol{r}_2)e^{i\boldsymbol{q}\cdot(\boldsymbol{r}_2-\boldsymbol{r}_1)}\mathrm{d}\boldsymbol{r}_1\mathrm{d}\boldsymbol{r}_2 + N_{\mathrm{e}}\delta_{mn}. \tag{4.11}$$

The one-electron scattering matrix element is the double Fourier transform of the product of two one-electron densities [105,149]

$$\rho_{mn}(\boldsymbol{r}) = \langle\psi_m|\hat{\rho}(\boldsymbol{r})|\psi_n\rangle, \text{ with } \hat{\rho}(\boldsymbol{r}) = \sum_i^{N_{\mathrm{e}}}\delta(\boldsymbol{r}-\boldsymbol{r}_i),$$

and the two-electron scattering matrix element is the double Fourier transform of the two-electron density [105,149]

$$P_{mn}(\boldsymbol{r}_1,\boldsymbol{r}_2) = \langle\psi_m|\hat{\rho}(\boldsymbol{r}_1,\boldsymbol{r}_2)|\psi_n\rangle, \text{ with } \hat{\rho}(\boldsymbol{r}_1,\boldsymbol{r}_2) = \frac{1}{2}\sum_{i,j\neq i}^{N_{\mathrm{e}}}\delta(\boldsymbol{r}_1-\boldsymbol{r}_i)\,\delta\big(\boldsymbol{r}_2-\boldsymbol{r}_j\big),$$

and a constant term equal to the number of electrons.

As a quick aside, we can see that the two different scattering terms are almost identical, except in elastic scattering, we use the *classical* two-particle density

$$P_{mn}^{\mathrm{c}}(\boldsymbol{r}_1,\boldsymbol{r}_2) = \frac{1}{2}\rho_{mn}(\boldsymbol{r}_1)\,\rho_{mn}(\boldsymbol{r}_2),$$

, as defined in Eq. (3.2).[155] This quantity is the mean-field cousin of the two-particle density and is completely uncorrelated. Here, we mention that the two quantities have slightly different integrals[155] with

$$\iint_{-\infty}^{\infty} P_{mm}(\boldsymbol{r}_1, \boldsymbol{r}_2)\mathrm{d}\boldsymbol{r}_1\mathrm{d}\boldsymbol{r}_2 = \frac{N_\mathrm{e}^2 - N_\mathrm{e}}{2} \tag{4.12}$$

$$\iint_{-\infty}^{\infty} P^\mathrm{c}_{mm}(\boldsymbol{r}_1, \boldsymbol{r}_2)\mathrm{d}\boldsymbol{r}_1\mathrm{d}\boldsymbol{r}_2 = \frac{N_\mathrm{e}^2}{2}. \tag{4.13}$$

The former reflects the number of unique electron pairs in the system, while the latter, as a mean-field quantity, includes the density from when $\boldsymbol{r}_1$ and $\boldsymbol{r}_2$ are the same electron. We note here that these quantities are the same ones introduced at the beginning of Chapter 3, and x-ray scattering is a promising means to directly measure electron correlation and bonding effects.[156,157]

Although *in principle* one could calculate the inelastic scattering by converging the sum over f in Eq. (4.8), this is an extremely difficult task[158]. Even though L_{mf} is only non-zero when m and f are connected by a single-electron excitation (as $\hat{L}$ is a one-electron operator), this includes both excited states and ionised states, where the electron in the continuum is still interacting with the system. A far simpler way to calculate the net inelastic scattering is to rearrange Eq. (4.9) to find

$$\sum_{f\neq m} |L_{mf}|^2 = \left[\sum_f |L_{mf}|^2\right] - |L_{mm}|^2 = \Lambda_{mm} - |L_{mm}|^2, \tag{4.14}$$

merely subtracting the elastic scattering from the total.

Implicit in this section is the assumption that we detect all photons with equal probability. If this is not the case, and we have a detector which only detects within a certain window, then the sum over inelastic transitions in Eq. (4.9) is truncated, and we do not measure all scattering events. Thankfully, transitions with significant energy changes, which would fall outside the detection window, generally occur at higher momentum transfer, which we often do not measure experimentally.[158]

Rotational Averaging

Hitherto, the Fourier pair $(\boldsymbol{r}, \boldsymbol{q})$ have been vectors, and all scattering signals have all of the information about the alignment of the molecules. In actual gas-phase experiments, the molecules are not aligned, and to calculate a scattering pattern comparable with experiment, we must average over all possible rotational orientations of the molecule.[149,150,155i] This is notoriously hard to do numerically,[161,162] so we re-derive the equations to produce rotationally averaged quantities.[149,163,164] As a result, we will Fourier transform over two scalar quantities (r_{12}, q),[ii] the electron-electron distance and the momentum transfer magnitude, respectively.

Starting first with total scattering, the density we now use is the radial pair-distribution function[155] $\Gamma_{mn}(r_{12})$, which can be found as

$$\Gamma_{mn}(r_{12}) = \int P_{mn}(\boldsymbol{r}_{12}, \boldsymbol{S})\, r_{12}^2 \mathrm{d}\boldsymbol{\Omega}\mathrm{d}\boldsymbol{S}, \tag{4.15}$$

[i] In a pump-probe experiment, molecules are preferentially excited when their transition dipole moment is along the polarisation axis of the pump pulse, introducing a $\cos^2$ alignment,[159,160] but we do not consider that here.

[ii] We use the sub-scripted r_{12} as the electron-electron distance to connect with the language of explicitly correlated electronic structure.

transforming our coordinates to $\boldsymbol{S} = \frac{1}{2}(\boldsymbol{r}_1 + \boldsymbol{r}_2)$, $\boldsymbol{r}_{12} = \boldsymbol{r}_2 - \boldsymbol{r}_1$. $\boldsymbol{\Omega}$ indicates the solid angle of $\boldsymbol{r}_{12}$ and the integration is over all of $\boldsymbol{S}$ and $\boldsymbol{\Omega}$. We can perform the same manipulation using the classical two-electron density $P^{\mathrm{c}}_{mm}(\boldsymbol{r}_1, \boldsymbol{r}_2)$ to get the classical radial pair-distribution function $\Gamma^{\mathrm{c}}_{mn}(r_{12})$.[155]

We can calculate the rotationally averaged diagonal one- and two-electron scattering matrix elements as

$$|L_{mm}(q)|^2 = 2\int_0^\infty \Gamma^{\mathrm{c}}_{mm}(r_{12})\,\mathrm{sinc}\,(qr_{12})\,\mathrm{d}r_{12} \tag{4.16}$$

$$\Lambda_{mm}(q) = 2\int_0^\infty \Gamma_{mm}(r_{12})\,\mathrm{sinc}\,(qr_{12})\,\mathrm{d}r_{12} + N_{\mathrm{e}}, \tag{4.17}$$

where $\mathrm{sinc}\,(qr_{12}) = \frac{\sin(qr_{12})}{qr_{12}}$ is the zeroth-order spherical Bessel function.

For completeness, we mention the reverse process, the *sine transform*. Reversing Eqs. (4.16) and (4.17), we can find

$$\Gamma^{\mathrm{c}}_{mm}(r_{12}) = \frac{r_{12}}{\pi}\int_0^\infty |L_{mm}(q)|^2\, q\,\sin\,(qr_{12})\,\mathrm{d}q \tag{4.18}$$

$$\Gamma_{mm}(r_{12}) = \frac{r_{12}}{\pi}\int_0^\infty (\Lambda_{mm} - N_{\mathrm{e}})\, q\,\sin\,(qr_{12})\,\mathrm{d}q. \tag{4.19}$$

In principle, this can be used to directly find the pair-distribution functions, but it is more commonly used to measure interatomic distances.[46] This hinges on the fact that the core electrons of any atom are held closely to the nuclei; thus, a peak in the pair-distribution function appears at the interatomic distance. When applying this to experimental data, we are generally constrained by the experimentally measured momentum-transfer range. In most experiments performed currently, we measure approximately $0.5 \leq q/\ \text{Å}^{-1} \leq 10$ *or worse*. This leads to most experimental sine-transforms having fairly poor spatial-resolution.

The technical details of calculating the scattering matrix elements are covered briefly in Appendix A.

Electron Scattering

Here, we briefly mention electron scattering, only covering the more pertinent rotationally averaged picture. Firstly, the electron scattering off a free particle with charge Z is the Rutherford cross-section[149]

$$Z\frac{\mathrm{d}\sigma_{\mathrm{Ru}}}{\mathrm{d}\Omega} = Z\frac{4}{a_0^2 q^4}, \tag{4.20}$$

where a_0 is the Bohr radius and q is the momentum transfer[iii]. While this may seem a small change to the Thomson cross-section (Eq. (4.3)), the effects are quite large. The Rutherford cross-section does not have the m^{-2} scaling of the Thomson cross-section, and thus, electrons scatter non-negligibly off of both electrons and nuclei. This leads to additional terms in the scattering signal not present in x-ray-based measurements. Additionally, we notice a q^{-4} scaling.

As we now must also consider nuclei, we use a modified scattering operator,[149] which gives

$$\hat{\xi} = \sum_i^{N_{\mathrm{e}}} e^{i\boldsymbol{q}\cdot\boldsymbol{r}_i} - \sum_\alpha^{N_{\mathrm{at}}} Z_\alpha e^{i\boldsymbol{q}\cdot\boldsymbol{R}_\alpha}, \tag{4.21}$$

[iii] s is often used instead of q for electron scattering. For consistency, we do not change here.

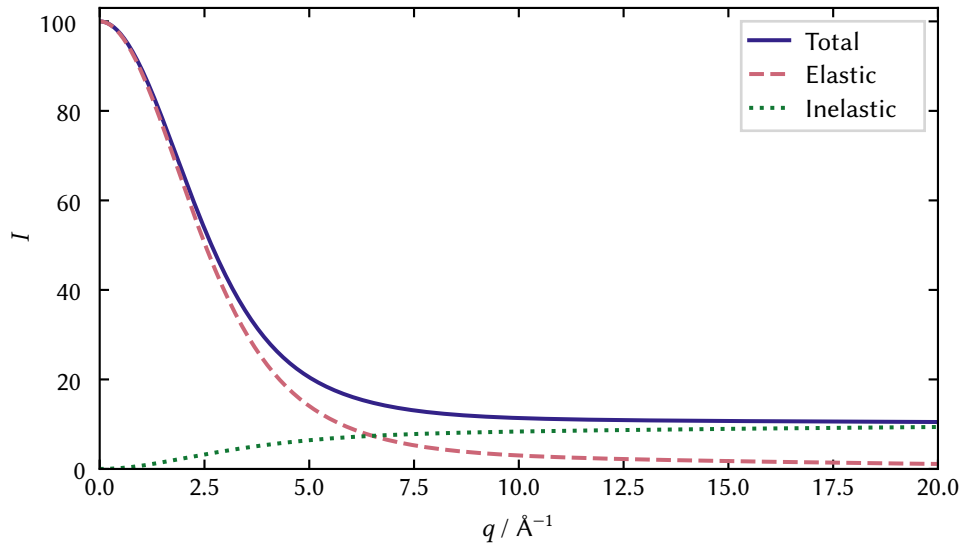

Figure 4.3: Rotationally-averaged x-ray scattering components for hydrogen fluoride, calculated with HF/aug-cc-pVQZ. The total and elastic scattering give values of $N_e^2 = 100$ at $q = 0$, while the inelastic scattering starts at 0. As q increases, the inelastic scattering increases to its asymptotic value of $N_e = 10$, while the elastic scattering decays to 0. The total scattering thus also goes to $N_e = 10$. I represents the scattering in units of the Thomson cross-section.

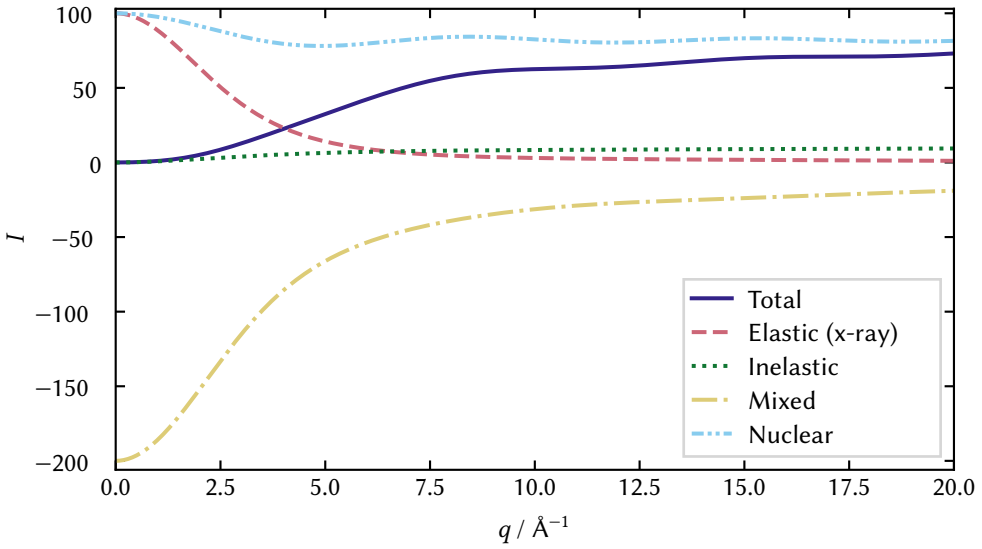

Figure 4.4: Separated electron scattering contributions for hydrogen fluoride, calculated with HF/aug-cc-pVQZ. The mixed nuclear/electronic cross-term gives a value of $-2N_e^2$ at $q = 0$, while the elastic (x-ray) and nuclear each equal N_e^2, adding together to cancel the mixed scattering. The total scattering is the sum of all other scattering types shown in the figure. The elastic (x-ray) scattering is combined with the nuclear and mixed terms to retrieve the elastic electron scattering, which is then combined with the inelastic to return the total electron scattering, shown as the solid indigo line. I represents the scattering in units of the Rutherford cross-section.

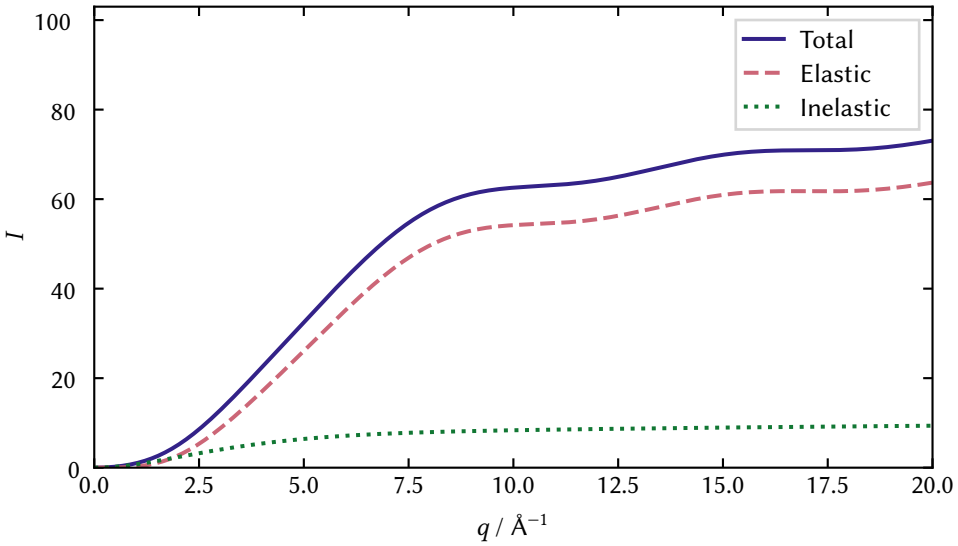

Figure 4.5: Electron scattering components for hydrogen fluoride, calculated with HF/aug-cc-pVQZ. All three forms of scattering start at 0, rising as q increases. The oscillatory structure is much more present than in x-ray scattering. I represents the scattering in units of the Rutherford cross-section.

with $\boldsymbol{R}_\alpha$ and Z_α the position and charge of atom α. From this, we can calculate

$$|\xi_{mn}(q)|^2 = |L_{mn}(q)|^2 + \delta_{mn}\left[\sum_{\alpha,\beta} Z_\alpha Z_\beta \operatorname{sinc}\left(qR_{\alpha\beta}\right) - 2\sum_{\alpha}\int_0^\infty Z_\alpha \Pi_\alpha(R_{i\alpha}) \operatorname{sinc}(qR_{i\alpha})\,\mathrm{d}R_{i\alpha}\right] \tag{4.22}$$

$$\Xi_{mn}(q) = \Lambda_{mn}(q) + \delta_{mn}\sum_{\alpha,\beta} Z_\alpha Z_\beta \operatorname{sinc}\left(qR_{\alpha\beta}\right) - 2\sum_{\alpha}\int_0^\infty Z_\alpha \Pi_\alpha(R_{i\alpha}) \operatorname{sinc}(qR_{i\alpha})\,\mathrm{d}R_{i\alpha}, \tag{4.23}$$

where $R_{i\alpha}$ is the distance between an electron and the nucleus α, and $\Pi_\alpha(R_{i\alpha})$ is the electron radial distribution function from the nucleus, the probability of finding an electron at a given distance from nucleus α. The purely nuclear term gives direct information about the distances between the nuclei, unmodulated by any electron distributions. On the other hand, the mixed-electron-nuclear term comes from the cross-terms in the self-product of $\hat{\xi}$ and relates the positions of the nuclei to the positions of the electrons. Again, the calculation of these matrix elements is covered in Appendix A.

The Qualitative Picture

To gain a qualitative understanding of the x-ray scattering matrix elements, we plot the three types of scattering (total, elastic and inelastic) in Fig. 4.3. Most important are the limiting values at small and large q. At small momentum transfer, the limits are

$$\begin{aligned} \lim_{q\to 0} |L_{mn}(q)|^2 &= 0 \text{ for } m \neq n \\ \lim_{q\to 0} |L_{mm}(q)|^2 &= N_\mathrm{e}^2 \\ \lim_{q\to 0} \Lambda_{mm} &= N_\mathrm{e}^2. \end{aligned} \tag{4.24}$$

While there is no inelastic scattering at zero momentum transfer, the elastic and total scattering are proportional to the number of electrons squared. For large momentum transfers,

$$\begin{aligned} \lim_{q\to\infty} \sum_{n\neq m} |L_{mn}(q)|^2 &= N_\mathrm{e} \\ \lim_{q\to\infty} |L_{mm}(q)|^2 &= 0 \\ \lim_{q\to\infty} \Lambda_{mm} &= N_\mathrm{e}. \end{aligned} \tag{4.25}$$

At infinite momentum transfer, the story is flipped, and only the inelastic scattering contributes to the total signal.

To extend these results to electron scattering, we only need to look at the additional terms present in Eqs. (4.22) and (4.23), an example of which is given in Fig. 4.4. The mixed-nuclear-electronic term has limits of

$$\begin{aligned} \lim_{q\to 0}\left[-2\sum_\alpha \int_0^\infty Z_\alpha \Pi_\alpha(R_{i\alpha}) \operatorname{sinc}(qR_{i\alpha})\,\mathrm{d}R_{i\alpha}\right] &= -2N_\mathrm{e}\sum_\alpha Z_\alpha \overset{\text{neu}}{=} -2N_\mathrm{e}^2 \\ \lim_{q\to\infty}\left[-2\sum_\alpha \int_0^\infty Z_\alpha \Pi_\alpha(R_{i\alpha}) \operatorname{sinc}(qR_{i\alpha})\,\mathrm{d}R_{i\alpha}\right] &= 0, \end{aligned} \tag{4.26}$$

where we use the symbol $\overset{\text{neu}}{=}$ to indicate equality for a neutral atom/molecule. Secondly, the purely nuclear term gives limits of

$$\begin{aligned} \lim_{q\to 0} \sum_{\alpha\beta} Z_\alpha Z_\beta \operatorname{sinc}\left(qR_{\alpha\beta}\right) &= \left(\sum_\alpha Z_\alpha\right)^2 \\ \lim_{q\to\infty} \sum_{\alpha\beta} Z_\alpha Z_\beta \operatorname{sinc}\left(qR_{\alpha\beta}\right) &= \sum_\alpha Z_\alpha^2. \end{aligned} \tag{4.27}$$

Combining these with the x-ray results shown earlier, we get limits for the elastic, inelastic and total terms at small momentum transfer of

$$\begin{aligned} \lim_{q\to 0} |\xi_{mn}(q)|^2 &= 0 \text{ for } m \neq n \\ \lim_{q\to 0} |\xi_{mm}(q)|^2 &= N_\mathrm{e}^2 + \left(\sum_\alpha Z_\alpha\right)^2 - 2N_e\sum_\alpha Z_\alpha \overset{\text{neu}}{=} 0 \\ \lim_{q\to 0} \Xi_{mn} &= N_\mathrm{e}^2 + \left(\sum_\alpha Z_\alpha\right)^2 - 2N_e\sum_\alpha Z_\alpha \overset{\text{neu}}{=} 0. \end{aligned} \tag{4.28}$$

These are shown in Fig. 4.4. The limits for elastic and total scattering are equal, as in x-ray scattering, since there is no inelastic scattering at zero momentum transfer.

For large momentum transfer, the limits are given as

$$\begin{aligned} \lim_{q\to\infty} \sum_{n\neq m} |\xi_{mn}(q)|^2 &= N_\mathrm{e} \\ \lim_{q\to\infty} |\xi_{mm}(q)|^2 &= \sum_\alpha Z_\alpha^2 \\ \lim_{q\to\infty} \Xi_{mn} &= N_\mathrm{e} + \sum_\alpha Z_\alpha^2. \end{aligned} \tag{4.29}$$

This time, the additional term of $\sum_\alpha Z_\alpha^2$ is present in both the elastic and inelastic scattering due to the constant same-nucleus scattering background. Finally, we mention that we have not included the proportionality of the Rutherford cross-section here, which does have a q^{-4} dependence, changing the scaling of the signals.

4.3 — Photo-electron Spectroscopy

In photo-electron spectroscopy, we measure the kinetic energy of a laser-ionised electron to deduce information about the electron binding energies in the molecule.[165–167] In this work, we concentrate on *valence* photo-electron spectroscopy,[166,167] where the laser only has enough energy to ionise the higher-energy valence electrons in the system.

The two quantities of interest in photo-electron spectroscopy are the ionisation potential and the photo-electron cross-section. We first concentrate on the latter, which can be calculated using the observable operator[iv] of

$$\hat{O}^{\text{pes}}_{mm} = \langle\psi_m|\hat{\mu}^\dagger|\psi_f\rangle|\chi_f\rangle\langle\chi_f|\langle\psi_f|\hat{\mu}|\psi_m\rangle = \mu^*_{mf}|\chi_f\rangle\langle\chi_f|\mu_{fm}, \tag{4.30}$$

where $\hat{\mu}$ is the dipole moment operator. In photo-electron spectroscopy, $|\psi_f\rangle$ is an ionised state. As before, we will ignore the off-diagonal elements, which give effects related to electronic coherence, as they are irrelevant here.

Ionisation is a complicated process, so we will limit ourselves to a simple set of approximations. Firstly, that we can write the ionised electronic wavefunction as a product of an ionic ($N_\text{e} - 1$) state ($|\varphi_f\rangle$) and a free-electron state ($|\vartheta_f\rangle$), as $|\psi_f\rangle = |\varphi_f\rangle|\vartheta_f\rangle$.[168,169] This is valid when there is little overlap of the ionised and free-electron wavefunctions, which often makes it a better approximation when the free electron is high-energy.[56,170]

Applying this to Eq. (4.30), we can write[168]

$$\mu_{fm} = \langle\vartheta_f|\langle\varphi_f|\hat{\mu}|\psi_m\rangle. \tag{4.31}$$

There are methods that allow us to calculate these matrix elements from ab initio wavefunctions, generally using a further series of approximations made about the interaction of the free electron with the ionic state (e.g. making the approximation that the ionic state can be well modelled by a point charge). We have not used these methods in this thesis, so we shall only cover them briefly at the end of the discussion.

Instead, we will make a series of approximations that entirely disregard the free-electron wavefunctions, allowing for the calculation of approximate *relative* cross-sections for different transitions.[171] Here, writing the integrals explicitly rather than in bracket form is useful. Eq. (4.31) is written as

$$\begin{aligned}\mu_{fm} &= \sqrt{N_\text{e}}\int_{-\infty}^{\infty}\vartheta^*_f(\boldsymbol{r}_1)\hat{\mu}(\boldsymbol{r}_1)\int\cdots\int_{-\infty}^{\infty}\varphi^*_f(\boldsymbol{r}_2,\ldots,\boldsymbol{r}_n)\psi_m(\boldsymbol{r}_1,\boldsymbol{r}_2,\ldots,\boldsymbol{r}_n)\mathrm{d}\boldsymbol{r}_1\mathrm{d}\boldsymbol{r}_2\ldots\mathrm{d}\boldsymbol{r}_n \\ &= \int_{-\infty}^{\infty}\vartheta^*_f(\boldsymbol{r}_1)\hat{\mu}(\boldsymbol{r}_1)\varrho_{mf}(\boldsymbol{r}_1)\mathrm{d}\boldsymbol{r}_1\end{aligned} \tag{4.32}$$

Here, we have introduced the concept of the Dyson orbital

$$\varrho_{mf}(\boldsymbol{r}_1) = \sqrt{N_\text{e}}\int\cdots\int_{-\infty}^{\infty}\varphi^*_f(\boldsymbol{r}_2,\ldots,\boldsymbol{r}_n)\psi_m(\boldsymbol{r}_1,\boldsymbol{r}_2,\ldots,\boldsymbol{r}_n)\mathrm{d}\boldsymbol{r}_2\ldots\mathrm{d}\boldsymbol{r}_n,$$

which is the overlap of the N_e and $(N_\text{e} - 1)$ electron wavefunctions[v]. Physically, we can interpret this as the 'effective orbital from which the electron was ionised'.

[iv] We have ignored the dipole operator's interaction with the field as $E\boldsymbol{\epsilon}\cdot\hat{\mu}$, where E and $\boldsymbol{\epsilon}$ are the electric field strength and polarisation vector, respectively. These effects are unimportant for the discussions we are having here.

[v] The $\sqrt{N_\text{e}}$ term comes from the fact that any of the N_e indistinguishable electrons could be ionised.

We can approximate the magnitude of $\hat{\mu}_{fm}$ by claiming that the interaction with the $\vartheta(\boldsymbol{r}_1)\hat{\mu}(\boldsymbol{r}_1)$ term is constant for all different ionisation channels. From this, the relative ionisation cross-sections for different channels are equal to the square of the norm of the Dyson orbital,

$$\sigma_{\text{rel}}^{\text{PES}} \approx |\langle \varrho_{mf} | \varrho_{mf} \rangle|^2. \tag{4.33}$$

This is a real number between zero and one, with higher numbers indicating stronger transitions. The Dyson norm measures the overlap between the neutral and ionic wavefunctions. When this value is large, it indicates that the ionic state can be reached by simply removing one electron from the neutral wavefunction. When it is small, it indicates that one would have to both ionise *and* excite the molecule. The latter process requires two separate interactions with a photon and thus is not possible with only one photon. As a shorthand, we shall call the transitions *Koopmans' forbidden* when $\sigma_{\text{rel}}^{\text{PES}} \approx 0$, whereas they are called *Koopmans' allowed* for $\sigma_{\text{rel}}^{\text{PES}} \approx 1$.

Of course, this approximation is relatively poor — it contains no information about the dipole operator or free electron — but it allows a relatively cheap calculation and is available whenever one can calculate both the ion and the neutral wavefunctions. Higher-level methods explicitly consider the free-electron in Eq. (4.31), requiring more computational power. These methods range from the simple ezDyson[168,172] method to the more precise R-Matrix approach,[173,174] but both are beyond the scope of this work.

Until now, we have not mentioned the additional nuclear wavepacket terms in Eq. (4.30). In this thesis, we use two distinct cases, the first being trajectory simulations. Here, $\chi_m(\boldsymbol{R}, t) = \delta(\boldsymbol{R} - \boldsymbol{R}_u(t))$, and we simply use the point of the trajectory to calculate the cross-section. Chapter 9, on the other hand, discusses vibrationally resolved photo-electron spectra, where we use the eigenstates of the harmonic oscillator to model the vibrational wavefunctions.[175,176] For succinctness, we shall not discuss these models here.

Ionisation Potentials

As we have just discussed the photo-ionisation cross-sections, we are left to describe the photo-ionisation energy. Total energy has to be conserved, giving

$$\hbar\omega = E_{\text{IP}} + E_{\text{KE}}, \tag{4.34}$$

where ω is the angular frequency of the ionising photon, E_{IP} is ionisation potential, the potential energy difference between the initial and final states of the molecule,[vi] and E_{KE} is the kinetic energy of the system. As the kinetic energy is of the free electron and ionised molecule (i.e. a continuum), this condition can be satisfied for any value of $\hbar\omega > E_{\text{IP}}$. However, we can make some general statements about where the two contributions to the energy are from.

While the final state is the combined state of the $N_{\text{e}} - 1$ electron core and the free electron, the potential energy difference is entirely located on the core molecule and is a property of the given molecule/ion system. The kinetic energy, on the other hand, is almost entirely located on the electron, as it is far less massive than the ionised core (i.e. $M_{\text{ion}} > 1800\, m_{\text{e}}$). Due to the conservation of momentum,

$$|\dot{r}_1| = M_{\text{ion}} |\dot{R}_{\text{ion}}| \tag{4.35}$$

where $\dot{r}_1$ and $\dot{R}_{\text{ion}}$ are the translational velocity of the electron and ion, respectively. In the centre-of-mass frame, the velocity of the electron is far higher than the ion. As kinetic energy depends quadratically on the velocity, the electron dominates it even further.

[vi] We will switch between ionisation potential and *binding energy*, which (for our purposes) are synonymous.

As such, any photon above the ionisation threshold can ionise the molecule, with the excess energy being taken by the electron. Experimentally, one cannot simply measure the absorbance of photons, as in a photo-absorption experiment: multiple photon energies ionise the same electronic transition. We, therefore, shift to measuring the kinetic energy of the electron. From this, in addition to knowing the energy of the ionising photon, we can reverse Eq. (4.34) to find E_{IP}.

Computationally, E_{IP} can be calculated using electronic structure theory. For some wavefunction-based methods, one can directly calculate the ionisation potential from the neutral wavefunction, which is generally denoted by prepending 'IP' to the method name [177–181] (e.g. IP-LR-CC3, which calculates the ionisation potential from a CC3 calculation). The method we shall primarily use is the so-called 'delta' (Δ) method, where we calculate the ionisation potential using the formula

$$E_{\mathrm{IP}}^{i\to f} = E_f^{N_\mathrm{e}-1} - E_i^{N_\mathrm{e}} \tag{4.36}$$

where $E_f^{N_\mathrm{e}-1}$ and $E_i^{N_\mathrm{e}}$ are the energies of the ionic state f and neutral state i, respectively. To perform this, we calculate the ion and neutral molecule at the same nuclear geometry, with the energy difference being the ionisation potential. To denote this, we shall use a Δ, e.g. ΔCASSCF.

— II —

Norbornadiene & Quadricyclane: Valence States

— 5 —

Electronic Structure of the Valence States

In this chapter, we describe the electronic structure of the valence states of norbornadiene and quadricyclane. These states are critical in understanding this system's photoswitch nature. This work is taken with only minor alterations from J. C. Cooper, A. Kirrander, *Electronic structure of norbornadiene and quadricyclane*, *submitted*.

The electronic structure of the excited states in the QC/NBD system is challenging. Even when not considering Rydberg states, the system exhibits strong multi-configurational electronic structure with dramatic changes as the molecule distorts between the QC and the NBD isomers during the dynamics. Consequently, different electronic structure methods can yield quite different results, and many suffer significant stability issues. Benchmarking predictions against experimental data is non-trivial. Standard spectroscopy only reveals information about the bright states of the two isomers, and then only in the Franck-Condon regions (see Chapter 9), and the dynamics is so fast that it has been difficult until recently to perform experiments on the time-scale. Therefore, the electronic structure must be assessed via secondary properties such as quantum yields and, as here, by carefully comparing different electronic structure methods.

This chapter aims to undertake a series of theoretical explorations of the QC/NBD system and to provide systematic benchmarks for this important system, concentrating on the electronic structure of the unsubstituted molecule. The insights provided by systematically evaluating

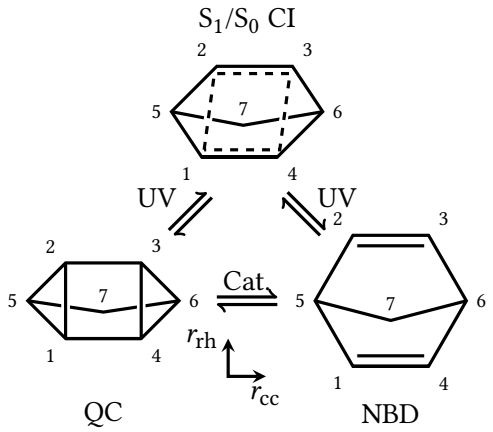

Figure 5.1: Reaction schematic. QC transforms to NBD (and vice versa) with UV light via a rhombic conical intersection (CI) with partial bonding. The ground state reaction requires catalysis. The two 'wings' of the molecule (carbons 1 & 2, and 3 & 4) have double bonds in NBD, which break to form the single bonds holding the four-carbon ring in QC. The coordinates defined in Eqs. (5.1) and (5.2) are used as approximate x and y coordinates, respectively.

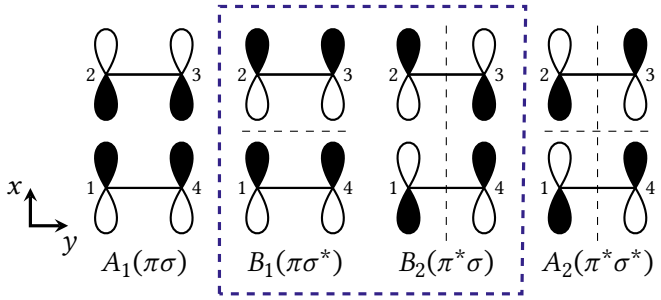

Figure 5.2: Schematic of the four principal orbitals, with only carbons 1-4 and their p_x orbitals shown (cf. Fig. 5.1). In NBD, the B_1 and B_2 orbitals are the HOMO and LUMO, respectively, and vice versa in QC. Inter-nuclear nodes are drawn as dashed lines. All four orbitals constitute the (4,4) active space, while the dashed box denotes the (2,2) active space. Orbitals from electronic structure calculations are shown in the Figs. B.1 and B.2.

different electronic structure methods allow us to make observations regarding static vs. dynamic correlation, the role of doubly-excited character, the validity of the results away from the Franck-Condon region, and to discuss the different electronic structure methods considered. In doing so, we report extensive benchmarks using multi-configurational active space methods (CASSCF, XMS-CASPT2, and MRCI), as well as coupled cluster methods (LR-CC3 and LR-CCSD). These systematic comparisons allow us to evaluate the electronic structure methods and identify those suitable for dynamics.

More generally, we aim to find a series of feasible-for-dynamics electronic structure methods. A necessary prerequisite for dynamics simulations is accurate, computationally feasible, and globally valid electronic structure models. Several recent publications highlight the impact of potential energy surfaces and their couplings on non-adiabatic simulations,[182–185] and the electronic structure models presented here can be exploited to investigate how comparatively subtle changes in the potential energy surfaces affect the photochemical dynamics.

One of the first studies to consider the role of the excited electronic states in the dynamics was carried out by Antol, who used an augmented CASSCF(4,4)+3s approach to predict how an excited 3s state may decay through a doubly and then a singly excited state to a conical intersection with the ground electronic state.[186] Coppola et al. used CASSCF(4,7) and CASPT2 to highlight the role of the doubly-excited state in non-adiabatic transfer,[187] in close accord with Antol.

We also mention two *primarily* dynamics studies, which are discussed more in the next chapter. Hernandez et al. performed surface-hopping dynamics simulations (including on a substituted derivative).[53] Finally, Valentini et al. used CASSCF(4,8)-level theory to model coherent control experiments in the QC/NBD system.[188] For completeness, we mention the work of Chapter 10, where we simulated the dynamics in photoexcited QC using RMS-CASPT2(2,6) electronic structure and compared the results to time-resolved photoelectron spectroscopy experiments.[1] All the previous treatments listed above include Rydberg states, differing primarily in how and which additional Rydberg orbitals are included, and most employ active spaces closely related to the (4,4)-active space. Some previous studies consider also more systematically the role of substitutions on the QC/NBD system.[18,39]

5.1 — Qualitative Photochemistry

In this section, we discuss the general trends in the electronic structure of QC/NBD. These qualitative aspects manifest in all the electronic structure methods investigated here and

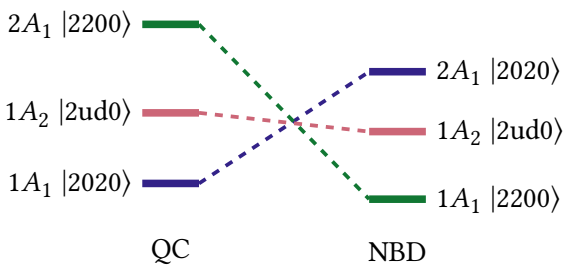

Figure 5.3: State correlation diagram for the QC/NBD system, with energy increasing up the diagram. Figure drawn to scale for SA(3)-CASSCF(2,2)/p-cc-(p)VDZ energies.

provide general insights into the overall photochemical behaviour of this system. Notably, they constitute an essential background for analysing the efficacy of the various approaches to the electronic structure.

Consider first the two isomers shown schematically in Fig. 5.1. NBD (right) has two double-bonded 'wings' formed by atoms C_1=C_4 and C_2=C_3, respectively. In QC (left), the wings move closer together as the molecule undergoes retro-[2+2]-cyclo-addition, whereby the double bonds break and cyclise to form the four-membered ring of QC. Given the central role played by the four carbons C_1-C_4, it is reasonable to start with a simple Hückel-like picture. The four symmetrised combinations of C(p_x)-orbitals are shown in Fig. 5.2, with the x-axis aligned with the C_1−C_2 and C_3−C_4 bonds in QC and the y-axis with the C_1=C_4 and C_2=C_3 bonds in NBD. The former bonds have predominantly σ-character, while the latter are π-character.

Each orbital has a symmetry label, which we refer to throughout the text, sometimes combined with a pithy label that indicates the π-bonding character for the wings (along y) and the σ-bonding character between the wings (along x). For example, in the $B_1(\pi\sigma^*)$ orbital the label in parenthesis signifies that the orbital has bonding character along the C_1−C_4 and C_2−C_3 π-bonds, *but* anti-bonding character for the C_1−C_2 and C_3−C_4 σ-bonds. As each carbon contributes one electron, we have four electrons in these orbitals. The corresponding configuration state functions (CSFs) in this subsystem are labelled as $|\eta_{A_1}\eta_{B_1}\eta_{B_2}\eta_{A_2}\rangle$, where η denotes the occupation for each orbital, either 0, 1 (u for up and d for down spin), or 2.

We consider three states: the ground S_0 ($1A_1$) state, the first excited S_1 ($1A_2$) valence state, and the second, doubly excited S_2 ($2A_1$) valence state. The S_1 ($1A_2$) state is the simplest, with |2ud0⟩ the leading configuration at both QC and NBD geometries. The two A_1 states, S_0 and S_2, are more complicated. In NBD, S_0 has |2200⟩ character while S_2 has |2020⟩. In QC, this is reversed, with the ground state having |2020⟩ character and S_2 |2200⟩. This can be rationalised using the orbital characters in Fig. 5.2, and it is clear exciting either the S_1 or S_2 state from the NBD minimum will cause motion towards the QC minimum, or vice versa.

The correlation between states is shown pictorially in Fig. 5.3. Thus, the origin of the MOST and photoswitch nature of this system is apparent: the ground state isomerisation involves a change in the character of the wavefunction, resulting in a large barrier, while the excited states couple to the other isomer's ground state, leading to efficient excited-state isomerisation.

For non-radiative decay, the S_1/S_0 conical intersection (CI) plays a crucial role, as depicted in Fig. 5.1. We show the representative minimum energy conical intersection (MECI) geometry in Fig. 5.4. The S_1 state has A_2 symmetry and thus the MECI distorts to C_2 symmetry, with a distinctive rhombic arrangement of atom C_1-C_4. This distortion resembles other [2+2] systems, such as the well-studied ethylene dimerisation,[44,45,189,190] with the frame of the molecule (specifically C_{5-7}) holding the system in a '2_s+2_s' arrangement. The A_2 displacement indicates that the intersection has both left- and right-handed variants — we shall not distinguish them. At the S_1/S_0 conical intersection, the wavefunction is exceptionally multi-configurational,

with all three of the $|2020\rangle$, $|2ud0\rangle$ and $|2200\rangle$ configurations strongly occupied in the S_0 and S_1 states.

During dynamics, the molecule will break the C_{2v} symmetry, and so we shall drop the state symmetry labels and use only the adiabatic S_n labelling scheme, punctuated with a leading character label to keep track of the state character. Finally, we stress that the model introduced here does not include the Rydberg or other valence states that appear between the singly- and doubly-excited valence states in the gas phase. The current adiabatic labels S_n are thus only valid in the context of this model. A complete analysis of the spectra of these molecules in the gas phase is given Chapter 9,[2] and more details on why this approximation is valid are given in Appendix B.1.

5.2 — Computational details

Electronic structure calculations

Electronic structure calculations are performed using OpenMolcas v23.02[191] (CASSCF, XMS-CASPT2), COLUMBUS 7.6[192] (CASSCF, MRCI) and e^T 1.9[193] (LR-CC). For CASSCF calculations, the results from OpenMolcas and COLUMBUS are effectively identical. The XMS-CASPT2 calculations are performed with a level-shift of $0.2i$, the minimum value required to remove all intruder states. The MRCI calculations are performed using COLUMBUS with the uncontracted formalism, and the XMS-CASPT2 use the single-state single-reference formulation in OpenMolcas. Cholesky decomposition[191,193] (CD) is used when possible, and the inclusion of this does not significantly change the results. All correlated methods (MRCI, CASPT2, LR-CC) use frozen carbon 1s orbitals. Compute times are reported for a single-threaded OpenMolcas calculation running on an Intel® Xeon® Silver 4314 CPU with a clock-speed of 2.40GHz.

The electronic structure calculations are not overly sensitive to the basis, provided the basis set is sufficiently diffuse. In view of future non-adiabatic dynamics simulations, which require many electronic structure evaluations, we have developed a custom basis that is both efficient and accurate for this specific system. The basis is an altered version of cc-pVDZ.[194], denoted p-cc-(p)VDZ. We remove the polarisation functions from the hydrogens, giving a [4s|2s] contraction equivalent in size to def2-SV(P) or 6-31G*, and add only the additional p diffuse functions from the aug-cc-pVDZ basis[195] to the carbons, resulting in a [9s5p1d|3s3p1d] contraction. All calculations presented in this work, except when explicitly denoted otherwise, use the p-cc-(p)VDZ basis. The full contraction is given in Table B.1.

Interpolations of internal coordinates

To compare the different electronic structure methods, we calculate the electronic structure along linear interpolations in internal coordinates (LIICs), which provide effective one-dimensional 'reaction coordinates'. We use two different sets of LIICs. The first, which is similar to that used in Chapter 10, connects the QC ground state equilibrium geometry to the S_1/S_0 MECI and proceeds to the NBD ground state equilibrium. We note that the combined LIIC involves a change in direction at the S_1/S_0 MECI. The second LIIC proceeds from the NBD ground state to the S_1 minimum, and then to the S_1/S_0 MECI. This approximates the path for dynamics that proceeds via the S_1 minimum. This second LIIC does not include the final path from the MECI towards QC since this is already included in the first LIIC.

The first LIIC (QC→S_1/S_0→NBD), used in Figs. 5.6 to 5.8, is defined based on molecular geometries optimised using CASSCF(2,2)/p-cc-(p)VDZ for CASSCF calculations, while the LIIC is based on MRCI(2,2)/p-cc-(p)VDZ optimised geometries when comparing all other electronic structure methods. The second LIIC (S_1/S_0→S_1 min→NBD), used in Fig. 5.10, exists

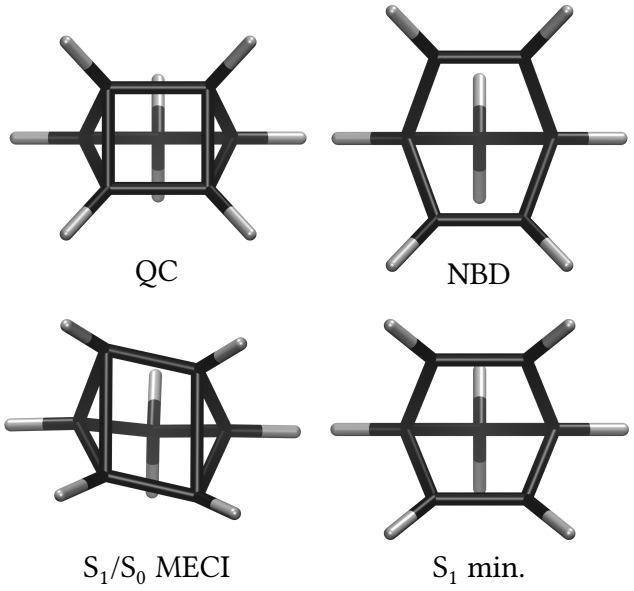

Figure 5.4: Representative molecular geometries. The QC ground state (top left) has the characteristic four-membered ring, whereas the NBD (top right) has two separate double-bonded 'wings'. The S_1/S_0 MECI (bottom left) has a distinct rhombic arrangement of the four-carbon moiety, while the S_1 minimum (bottom right), which appears in some of the calculations, is quite similar to the NBD ground state, with slightly closer wings. The optimised geometries shown are obtained using SA(3)-CASSCF(2,2)/p-cc-(p)VDZ.

in one version only, obtained using CASSCF(2,2)/p-cc-(p)VDZ geometries. For reference, the CASSCF(2,2)/p-cc-(p)VDZ optimised geometries are shown in Fig. 5.4.

Finally, we show two-dimensional potential energy surfaces in Figs. 5.9 and 5.11. These are calculated by using linear interpolations in Cartesian coordinates. Figure 5.9 shows potential energy in the plane that contains the NBD and QC minima and the S_1/S_0 MECI, and Fig. 5.11 in the plane containing the NBD and S_1 minima and the S_1/S_0 MECI.

5.3 — Results

Static correlation

The multi-configurational and doubly-excited character of the NBD/QC system means that single-reference methods, such as ADC(2) and TDDFT, often give poor results, especially around the critical S_1/S_0 CI. The exception to this are high-order coupled cluster calculations, which are discussed later, but these are too expensive for dynamics in a system of this size. As such, we focus mainly on multi-configurational methods.

From the qualitative discussion in Section 5.1, it is clear that a global representation of the electronic states requires that the active space includes the $|2200\rangle$, $|2020\rangle$, and $|2ud0\rangle$ configurations, which make leading contributions to the three states. A standard approach would be to utilise the complete set of the four orbitals and electrons as detailed in Fig. 5.2, i.e. a CASSCF(4,4) approach. Almost all previous work on the excited states of these molecules used methods based on this active space, generally including Rydberg states.[53,186,188] We show how the addition of Rydberg states affects these potentials in Appendix B.1.

Alternatively, one could remove the A_1 and A_2 orbitals; these orbitals are fully occupied or unoccupied in the important configurations. This leads to a CASSCF(2,2) approach, which has

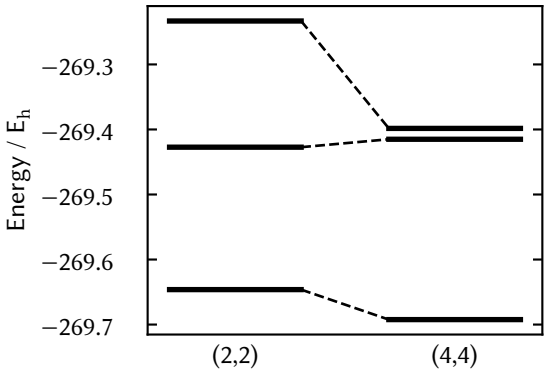

Figure 5.5: Absolute energies for the three states S_0, S_1, and S_2 at NBD equilibrium geometry for the (2,2) (left) and (4,4) (right) active spaces, calculated at the SA(3)-CASSCF/p-cc-(p)VDZ level. Note that although the state-averaged energy is lower for the (4,4) calculation, the S_1 state energy is *higher* for the (4,4) active space compared to the (2,2).

particular computational advantage as state-averaging over three states leads to both orbitals always having a state-averaged occupation number of 1, leading to very stable convergence.

This additional stability is evident in practice. The (4,4) active space has trouble converging to the same active space in QC-like geometries due to the formation of the σ-bond; the A_1 orbital, with σ-bonding character, drops significantly in energy, while the A_2 orbital, with σ^*-anti-bonding character, rises significantly, leading to those orbitals being replaced in the optimisation. A third choice is a (4,3) active space, which gives similar results to the (2,2) active space but exhibits similar instabilities as the (4,4) active space.

We find that the (2,2) active space provides a better qualitative description of the potential energy surfaces, with the (4,4) active space biased against the S_1 $|2ud0\rangle$ state. This is seen in Fig. 5.5, which shows the absolute energies for the (2,2) and (4,4) active spaces at the NBD geometry. The critical S_1 $|2ud0\rangle$ state has a *higher* absolute energy in the larger (4,4) active space than the (2,2), While this may seem counter-intuitive, as the (4,4) state has more parameters and hence should give a lower variational energy, this only applies to the optimised *state-averaged* energy rather than the energy of individual states.

The poor description of S_1 in CASSCF(4,4) can be rationalised using orbital occupations. The two A_1 states contain four orbitals with occupations significantly different from 2 or 0, indicating that all four orbitals contribute to the correlation. The A_2 state, on the other hand, only has the central two orbitals $B_1(\pi\sigma^*)$ and $B_2(\pi^*\sigma)$ with occupations not close to 2 or 0, and is not highly correlated. CASSCF(4,4), therefore, describes the two A_1 states better than the A_2 state, leading to qualitatively incorrect energy gaps, while CASSCF(2,2) gives a more balanced description of the individual states. This pattern is seen in other molecules with two π-bonds, such as cyclopentadiene[196] and 1,3-cyclohexadiene[197], where the doubly-excited state is *lower* in energy than the singly-excited state in CASSCF. Only by including more correlation, in those cases via XMS-CASPT2, does one retrieve the correct state ordering.

Here, we note that the CASSCF(2,2) does not describe the S_2 state well in either NBD or QC. Specifically in the region around the NBD ground state equilibrium, the CASSCF(2,2) method does not include the $|uudd\rangle$, $|2002\rangle$, and $|0220\rangle$ configurations, which all contribute $\approx 10\%$ to the doubly excited state. This leads to a significant increase in energy of the S_2 state for CASSCF(2,2), as seen in Table 5.1. Fortunately, both the S_1 and S_0 states are well described, even in regions with significant doubly-excited character. Additionally, we do not expect S_2 to be populated to any notable degree during photoexcited dynamics (see the discussion below, Chapters 6 and 8, and Appendix B.1), so the poor description should not affect simulations.

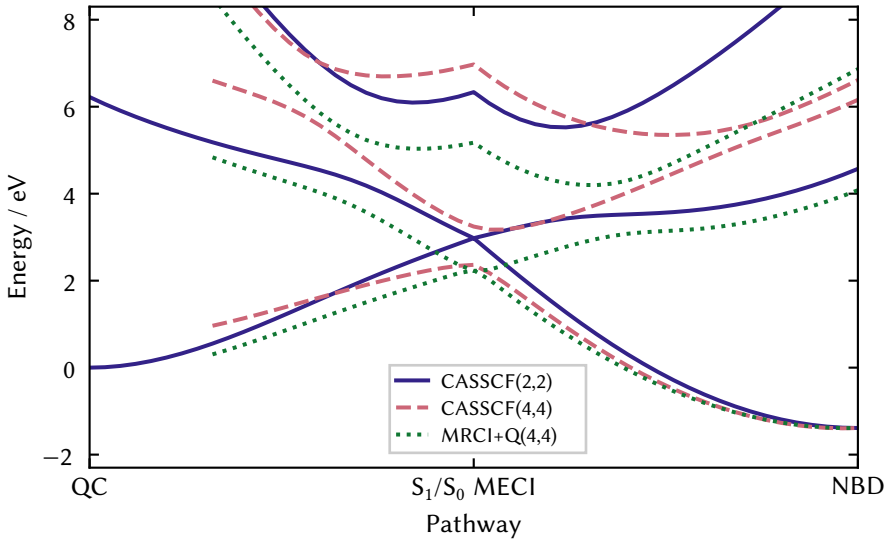

Figure 5.6: Energies for S_0, S_1, and S_2 calculated using SA(3)-CASSCF(2,2) (solid indigo lines), SA(3)-CASSCF(4,4) (dashed rose), and MRCI+Q(4,4) (dotted green) with the p-cc-(p)VDZ basis set. The (4,4) active space fails to converge around QC and is thus not shown in that region. CASSCF(2,2) and MRCI+Q(4,4) agree on the shape of the potential but not on the excitation energy at the NBD ground state equilibrium. Details of the LIIC pathway are given in Section 5.2

The analysis so far only concerns the NBD geometry. A better overview is gained by making the comparison using potential energy cuts (PECs) along the LIICs introduced earlier (see Section 5.2 for details), with the results shown in Fig. 5.6. The indigo solid lines are the relative energies for the three states in the SA(3)-CASSCF(2,2) calculation. We start on the right of the diagram, corresponding to NBD. The ground state, which has primary $|2200\rangle$ character, begins to rise as we move towards the centre of the plot, the S_1/S_0 MECI. Correspondingly, the S_1 state, with primary $|2ud0\rangle$ character, comes down in energy to meet the ground state at the MECI. In the CI region, in the middle of the plot, these two states are of mixed character, containing strong contributions from the $|2200\rangle$, $|2ud0\rangle$ and $|2020\rangle$ configurations. The S_2 state starts at much higher energy but then descends, mixing with the other two states. We note that in CASSCF(2,2), the doubly excited state is not well described, as mentioned earlier, but the two dynamically important states — S_0 and S_1 — are well described across the LIIC. Finally, as we continue left in the plot, towards QC, the lowest two states separate again. The ground state, now with primary $|2020\rangle$ character, comes down to a value approximately 1 eV above the NBD ground state minimum. This difference between QC and NBD ground state energies is the difference exploited for energy storage in MOST systems.[18,20] Correspondingly, the S_1 state again acquires primary $|2ud0\rangle$ character, and the S_2 state rises very high in energy, where it is of primary $|2200\rangle$ character.

The rose dashed lines in the same plot show the relative energies for SA(3)-CASSCF(4,4). At the NBD equilibrium geometry, the S_0 obtained by (4,4) is quite similar to (2,2), but as observed above, the S_1 $|2ud0\rangle$ state appears at around 7.5 eV, far higher than the experimental value of 5.25 eV.[2,49,50,198–203] In terms of dynamics, this would have a severe impact, both due to the energy shift and changes in gradients. Additionally, this pushes it closer to the S_2 $|2020\rangle$ state, leading to their interaction region appearing closer to the NBD geometry. Moving towards the MECI, the two states do not quite meet, an artefact of using the CASSCF(2,2) geometries for the LIIC. When the states separate as we move to QC, we can see a notably steeper S_1 state,

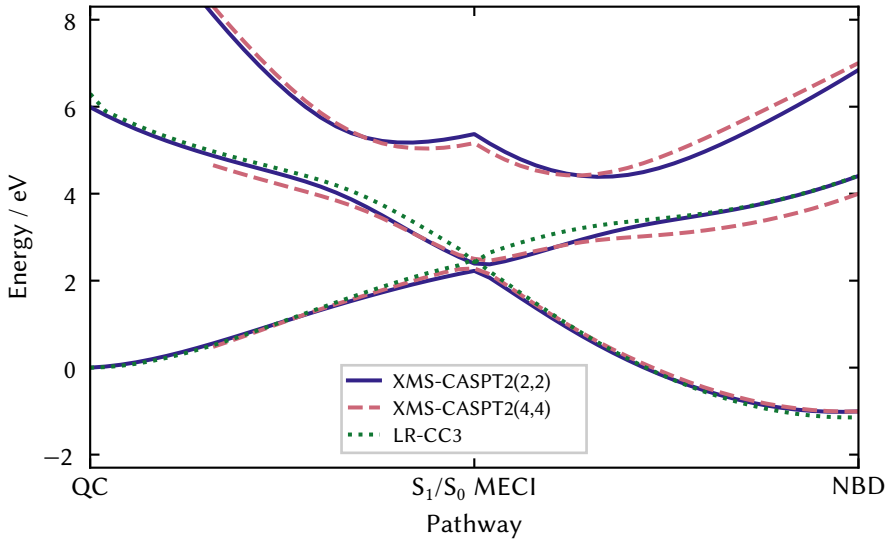

Figure 5.7: Energies for S_0, S_1, and S_2 calculated using XMS-CASPT2(2,2) (solid, indigo), XMS-CASPT2(4,4) (rose, dashed), and LR-CC3 (green, dotted) with the p-cc-(p)VDZ basis set. All three methods agree well and also with MRCI+Q(4,4) shown in Fig. 5.6. XMS-CASPT2(4,4) shows a notably lower and different shape potential around the NBD geometry. Details of the LIIC pathway are given in Section 5.2.

again reflecting the poor description of the $|2ud0\rangle$ state. As mentioned earlier, the active space is unstable in QC, so we do not show the energies.

In summary, the CASSCF(2,2) calculations, while exceptionally simple, give a balanced description of the potential energy surfaces. On the other hand, the CASSCF(4,4) calculations specifically bias *against* the S_1 $|2ud0\rangle$ state, increasing its energy. This is further confirmed in the next section, where we add dynamic correlation.

Dynamic correlation

Methods beyond CASSCF are required to recover the dynamical correlation. To evaluate the methods, we use a very similar LIIC, except calculated with a correlated method (MRCI(2,2)/p-cc-(p)VDZ, see Section 5.2). We now discuss MRCI, XMS-CASPT2, and, finally, methods that do not define an active space, such as linear response theories.

MRCI

We first focus on MRCI, which considers excitations from reference configurations taken from CASSCF. This method gives high-quality energies and wavefunctions but lacks size-extensivity and is computationally expensive compared to perturbative and density-functional-based methods. The calculations shown here are MRCI+Q, which uses only single and double excitations[vi] and adds a size-consistency correction (here the renormalised Davidson correction, Eq. (3.12)).

For the (2,2) active space, the MRCI reference weights for all three roots are approximately the same, indicating that the quality of all three states in the original CASSCF calculation is similar. Indeed, the CASSCF(2,2) calculations show nice overall agreement with the MRCI+Q(2,2) calculations, as shown in Fig. B.6. The highest S_2 state comes down in energy in the MRCI

[vi]The use of MRCI(m,n) denotes MRCISD performed on a CASSCF(m,n) reference.

compared to CASSCF(2,2), but in dynamics at reasonably low energies, say < 8 eV, this state is not expected to be populated.

For the (4,4) active space, it is crucial to include the Davidson correction (see Fig. B.6). Interestingly, MRCI+Q(4,4) gives a similar potential energy surface to CASSCF(2,2), as shown in Fig. 5.6 (green dotted lines). Notably, the two states are relatively parallel on the right-hand side of the pathway, only beginning to diverge around the conical intersection. The lack of agreement between the CASSCF(4,4) and MRCI+Q(4,4) calculations reflects the comments about the S_1 $|2ud0\rangle$ state above; the reference weight of this state is much lower than the other two states, confirming its poor description in the CASSCF picture.

Overall, the MRCI+Q calculations give excellent quality potential energy surfaces, but the computational expense means they are unsuitable for *on-the-fly* dynamics. This is especially true since the Davidson correction only corrects the energy and not the underlying wavefunction, meaning that it is not possible to calculate analytical gradients and couplings.

XMS-CASPT2

An alternative to MRCI is CASPT2, with XMS-CASPT2[123] the most popular dynamically-correlated multi-reference electronic structure method for dynamics. This is a variant of the MS-CASPT2 method[122] that gives exceptionally high-quality, smooth wavefunctions and potential energy surfaces,[204,205] yet is computationally less expensive than its variational cousin MRCI.[122] Crucially, analytical gradients and non-adiabatic coupling vectors have been implemented in multiple software packages.[123,129,191,206] Other forms of multi-reference perturbation theory, such as QD-NEVPT2, MS-CASPT2 and XMC-QDPT2, give similar results, as expected.

At first glance, the XMS-CASPT2 calculations with the (2,2) active space, shown as the solid indigo lines in Fig. 5.7, agree well with the MRCI+Q(4,4) calculations (Fig. 5.6) across all states. Furthermore, XMS-CASPT2(4,4) calculations, also included in Fig. 5.7, agree well with *both* these methods, with only minor differences in the excitation energy of S_1. So far, the conclusion is that MRCI+Q(4,4) produces credible reference potential energy surfaces but is unsuitable for *on-the-fly* dynamics. The three methods that *are* feasible for dynamics, namely CASSCF(2,2), XMS-CASPT2(2,2) and (4,4), all agree on the overall topography of the potential energy surfaces. In the next section, we turn to non-active space methods as a final arbiter.

Non-active space methods

As a final check, we perform LR-CC3,[207] which generates excitation energies from a high-quality coupled-cluster ground state wavefunction. Although this method is unstable around ground state conical intersections, it provides highly accurate energies elsewhere.[207,208] Most importantly, LR-CC3 calculations are relatively free of human bias, as they have no active space. In Fig. 5.7, we show the calculations for LR-CC3 for the ground and first excited $|2ud0\rangle$ state, compared to XMS-CASPT2. The LR-CC3 agrees closely with the XMS-CASPT2 and MRCI+Q calculations for both active spaces, indicating that both methods do not show significant human bias. It agrees particularly well with XMS-CASPT2(4,4), with the two states being parallel across the majority of the potential energy surfaces. Additionally, this indicates a nice qualitative agreement with the CASSCF(2,2) calculations. Unfortunately, LR-CC3 is exceptionally expensive, which, combined with its instability, makes it unsuitable for dynamics simulations. Other coupled cluster methods, such as LR-CC2 and LR-CCSD, do not describe doubly-excited states well and so are not well-suited for this particular system.

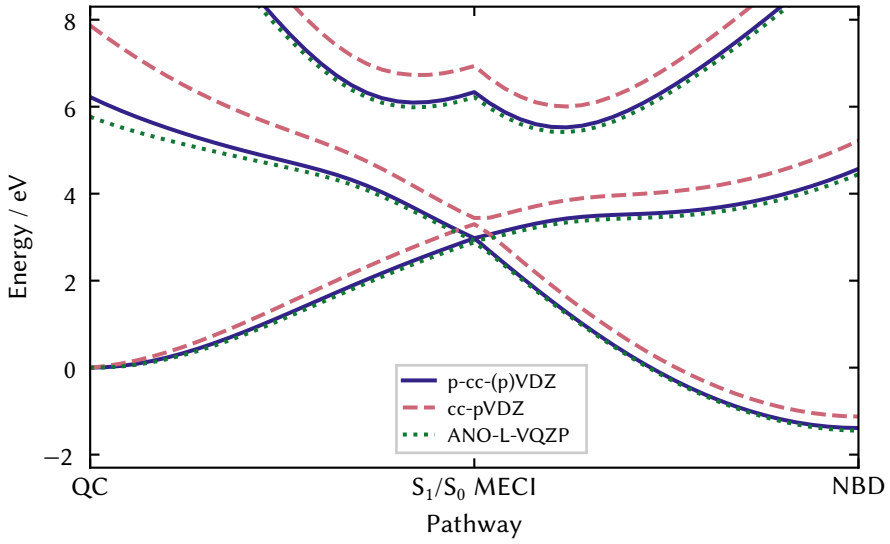

Figure 5.8: Basis set comparison of p-cc-(p)VDZ (solid indigo), cc-pVDZ (dashed rose), and ANO-L-VTQZ (dotted green), using the SA(3)-CASSCF(2,2) method. The S_0, S_1, and S_2 energies agree very well for p-cc-(p)VDZ and ANO-L-VTQZ, which both have sufficiently diffuse character, while cc-pVDZ shows a significant increase in energy for the S_1 and S_2 excited states. Details of the LIIC pathway are given in Section 5.2.

Basis sets

As mentioned earlier, the electronic structure calculations in QC/NBD are relatively insensitive to the choice of basis. However, accurate energies require that the basis is sufficiently diffuse. This is particularly notable for the S_1 $|2ud0\rangle$ state, which has a marked diffuse character due to strong mixing with the $3p_x$ Rydberg state near the QC equilibrium geometry.[1,2] To demonstrate, we compare SA(3)-CASSCF(2,2) energies using the p-cc-(p)VDZ and cc-pVDZ basis sets in Fig. 5.8. The p-cc-(p)VDZ basis, which lacks hydrogen polarisation functions but adds diffuse p functions, shows a significantly lower excitation energy for the valence state than cc-pVDZ, especially near the QC ground state equilibrium geometry. The large ANO-L-VTQZ basis agrees well with the p-cc-(p)VDZ, justifying the new contraction.

The p-cc-(p)VDZ basis uses only 135 spherical functions, reducing compute time for a single-point SA(3)-CASSCF(2,2) by two orders of magnitude compared to the ANO-L-VQZP basis. This computational efficiency is crucial for non-adiabatic dynamics simulations, which can involve a vast number of evaluations of the electronic structure. Finally, we note that if the Rydberg states are to be accounted for in the calculations, even more specifically-adapted diffuse basis sets are required.[1]

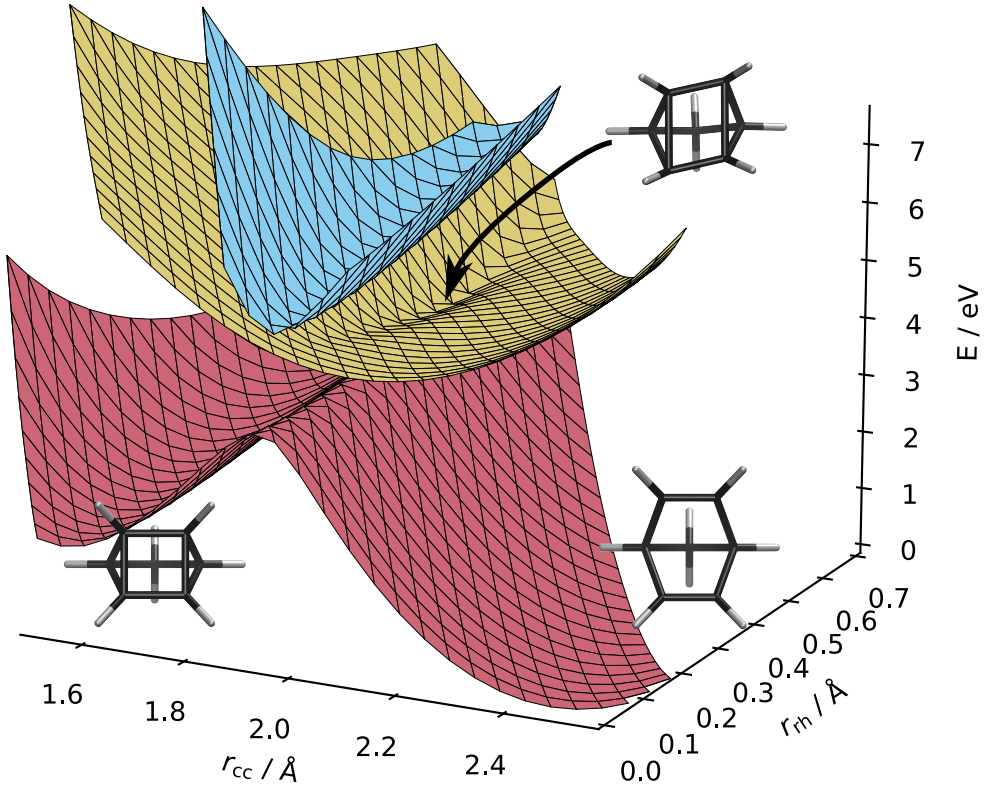

Figure 5.9: Potential energy surfaces in the plane defined by the NBD and QC minima and the S_1/S_0 MECI, calculated at the CASSCF(2,2)/p-cc-(p)VDZ level. The surfaces are plotted as a function of r_{cc} and r_{rh} (see Eqs. (5.1) and (5.2)). The S_0 surface (rose) has two clear minima corresponding to the equilibrium geometries of QC ($(r_{cc}, r_{rh}) \approx (1.5, 0)$ Å) and NBD ($(r_{cc}, r_{rh}) \approx (2.5, 0)$ Å), separated by a large barrier. The S_1 surface (yellow) connects with the S_0 surface at the rhombic conical intersection on top of this barrier, indicated by the arrow. The S_2 surface (light blue) interacts most strongly at $r_{cc} \approx 2.0$ Å, halfway between the two minima. Molecular structures from Fig. 5.4 are included for reference.

Table 5.1: Selected carbon-carbon distances (see Eqs. (5.1) to (5.3)) and vertical excitation energies calculated for CASSCF(2,2) /p-cc-(p)VDZ optimised geometries (with XMS-CASPT2(2,2)/ANO-L-VQZP excitation energies in brackets) for the QC and NBD ground state equilibrium geometries, the S_1/S_0 MECI, and the S_1 minimum. Leading configurations are given in occupation number representation for each of the three states S_0-S_2 in the format $|\eta_{A_1}\eta_{B_1}\eta_{B_2}\eta_{A_2}\rangle$ (orbitals as in Fig. 5.2), with *Mix* indicating that the states contain strong contributions from all of the $|2200\rangle$, $|2ud0\rangle$, and $|2020\rangle$ configurations.

Geometry	r_{cc} / Å	r_{rh} / Å	r_{db} / Å	S_1 / eV	S_2 / eV	S_0	S_1	S_2
QC	1.55	0	1.53	6.22 (5.75)	14.02 (11.59)	$\|2020\rangle$	$\|2ud0\rangle$	$\|2200\rangle$
NBD	2.47	0	1.33	5.96 (5.34)	11.24 (7.85)	$\|2200\rangle$	$\|2ud0\rangle$	$\|2020\rangle$
S_1/S_0 MECI	1.94	±0.50	1.44	0 (0.20)	3.36 (3.11)	Mix	Mix	Mix
S_1 min.	2.12	0	1.41	2.85 (2.85)	4.56 (3.29)	$\|2200\rangle$	$\|2ud0\rangle$	$\|2020\rangle$

5.4 — Discussion

Critical points on the potential energy surface

For the sake of visualisation, we define three coordinates involving carbon atoms C_1-C_4, as

$$r_{\mathrm{cc}} = \frac{1}{2}\left(r_{12} + r_{34}\right) \tag{5.1}$$

$$r_{\mathrm{rh}} = r_{13} - r_{24} \tag{5.2}$$

$$r_{\mathrm{db}} = \frac{1}{2}\left(r_{14} + r_{23}\right), \tag{5.3}$$

where $r_{ij} = |\mathbf{R}_j - \mathbf{R}_i|$ indicates the distance between carbons i and j (see Fig. 5.1 for the numbering of the atoms). r_{cc} is a measure of the *wing-separation* and is the mean distance between the two ethylenic moieties, with a large value in NBD and a small in QC. r_{rh} represents the *rhombicity* and is the difference between the two diagonal distances across the four-carbon ring C_1-C_4. This is zero at the NBD and QC ground states and increases as the four-carbon ring distorts to rhombic or parallelogram-like geometries (as seen at the S_1/S_0 MECI in Fig. 5.4). Finally, r_{db} corresponds to the mean length of the carbon bonds that acquire double bond character (and hence shorten) in NBD. We show LIIC pathways in the $(r_{\mathrm{cc}}, r_{\mathrm{rh}})$-plane in Fig. B.3.

Figure 5.9 shows the potential energy surfaces for the three important states in the plane defined by the QC and NBD minima and the S_1/S_0 MECI. The barrier between the two ground state minima is immediately obvious, with two distinct wells on the ground state surface corresponding to QC and NBD. The conical intersection linking to the ground state appears on top of this barrier, which explains the photoswitch nature of the system — depending on the path through the intersection, a wavepacket can end up in either potential well. Finally, the S_2 state sits well above the S_1 state at the geometries shown in Fig. 5.9, with a trough mirroring the potential barrier on the ground state. The change of character in the ground state wavefunction is evident, with strong coupling between the $|2020\rangle$ and $|2200\rangle$ configurations.

The NBD, QC, and S_1/S_0 MECI geometries remain relatively consistent across the different electronic structure methods (see Table 5.2 later). However, in some methods, an additional S_1 minimum with C_{2v} symmetry and 1^1A_2 $|2ud0\rangle$ character is found. This local minimum appears at higher energies than the S_1/S_0 MECI, with the molecular geometry approximately halfway between QC and NBD ground-state geometries ($r_{\mathrm{cc}} \approx 2.1$ Å, $r_{\mathrm{db}} \approx 1.4$ Å). Notably, the plane shown in Fig. 5.9 *does not* contain the S_1 local minimum. In the electronic structure methods where this minimum does not appear, a first-order symmetric saddle-point separates the left- and right-handed variants of the S_1/S_0 CI.

Since the S_1 minimum appears relatively close to the Franck-Condon region of NBD, see Fig. 5.4, we anticipate it may significantly affect the dynamics. A deep minimum imprints a valley on the potentials, attracting the initially excited wave packet before allowing it to proceed to the CI. Without this minimum, there is a ridge, and the wavepacket will evolve directly towards the CI. Interestingly, at the geometry of the local minimum, the S_0 and S_1 states have different symmetry (A_1 and A_2, respectively), and thus do not interact. When displacing towards the S_1/S_0 CI (an A_2 distortion), both states change to the A irreducible representation, leading to coupling and mixed $|2ud0\rangle$ and $|2020\rangle$ character in both states.

The vertical excitation energies and the leading configurations at these four molecular geometries are given in Table 5.1. As discussed earlier, the ground state wavefunctions for NBD and QC have different leading configurations, whereas the S_1 state always maintains the $|2ud0\rangle$ configuration. At the MECI geometry, the S_0 and S_1 states are degenerate, and the second excited state is much lower in energy than near the NBD and QC minima. The electronic states are thus strongly multi-configurational, with all three states having significant contributions of the $|2200\rangle$, $|2020\rangle$ and $|2ud0\rangle$ configurations.

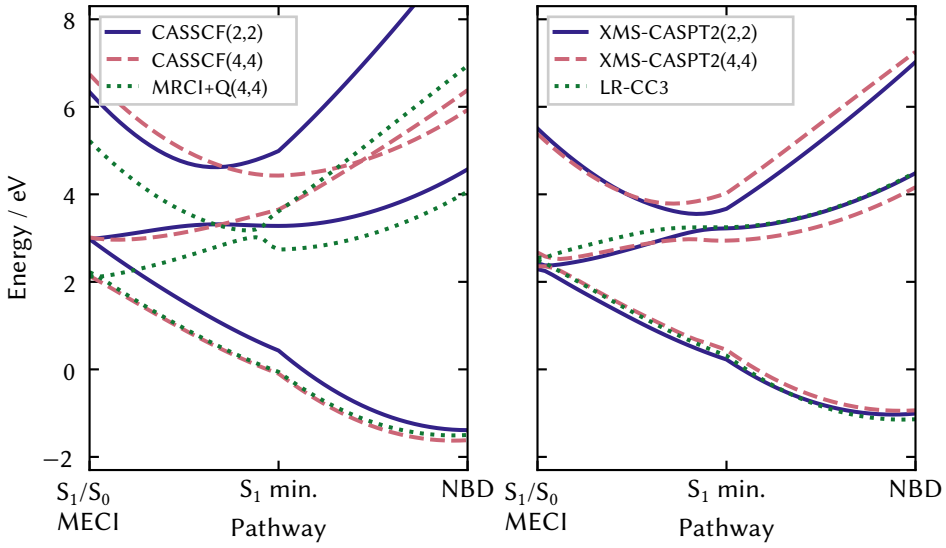

Figure 5.10: Energies for S_0, S_1, and S_2 calculated along the LIIC pathway from the S_1/S_0 MECI to the S_1 minimum, and finally to the NBD equilibrium geometry (see Section 5.2 for details). All calculations employ the p-cc-(p)VDZ basis. Left: CASSCF(2,2) (indigo solid), CASSCF(4,4) (rose dashed), and MRCI+Q(4,4) (green dotted). The CASSCF(4,4) is again qualitatively incorrect, whereas CASSCF(2,2) shows a qualitatively correct shape, including a barrier between the S_1 minimum and the S_1/S_0 MECI. The MRCI+Q(4,4) shows a small artefact around the S_1 minimum due to the Davidson correction and the two excited states mixing. Right: XMS-CASPT2 [(2,2) solid indigo, (4,4) rose dashed] and LR-CC3 (dashed green). All three methods look very similar, but the XMS-CASPT2(2,2) shows no barrier between the S_1 minimum and S_1/S_0 MECI, while the other two only have a very small one.

Further, a S_2/S_1 CI appears when dynamical correlation is included. This CI epitomises the aforementioned mixing of the $|2020\rangle$ character into the S_1 state, but, as it is a peaked CI being approached from the lower S_1 surface, we do not expect the S_2 state to significantly affect the dynamics.[85] Further discussion is presented in Appendix B.1.

Nature of the potential energy surfaces

In the following, we specifically discuss two key points on the potential energy surfaces. The first is the S_1 minimum, which only appears when using a subset of the electronic structure methods, and the second is the S_1/S_0 conical intersection, which governs decay onto the ground electronic state. While all electronic structure methods evaluated provide reasonably similar descriptions of the conical intersection, even subtle differences in the topography of the potential energy surfaces near a conical intersection could have consequences for the photoexcited dynamics. For simulations, it is thus crucial to describe this region as accurately as possible.

The S_1 minimum

As previously mentioned, the local symmetric S_1 $|2ud0\rangle$ minimum geometry is not present in all methods; namely, XMS-CASPT2(2,2), CASSCF(4,4) and MRCI(4,4) do not show it.[vii] This is

[vii] We have not optimised the minimum using MRCI+Q or LR-CC3, since those methods do not have analytical gradients available, but we believe that the methods show minima, as discussed later.

due to the increase in energy of the $|2ud0\rangle$ state (vide supra). This leads to the S_1 state being of primary $|2020\rangle$ character, leading to a strong slope to the S_1/S_0 MECI, eliminating the possibility of a local minimum. In CASSCF(4,4) and MRCI(4,4), this simply means that a local minimum would exist on the S_2 surface, still with primary $|2ud0\rangle$ character. For XMS-CASPT2(2,2), the crossing of the states occurs very close to the would-be minimum, distorting the potentials and leading to no observed minimum. Further discussion of the S_2/S_1 crossing is included in Appendix B.1.

To explore this region of configuration space, we construct a different LIIC pathway, first going from the NBD ground state geometry to this local S_1 minimum and then onwards to the S_1/S_0 MECI geometry.

The potential energy cuts for the previously shown methods are shown on this pathway in Fig. 5.10. The key feature in this pathway is a barrier between the S_1 minimum and S_1/S_0 MECI, which must be present for there to be an excited state minimum. Clearly, CASSCF(2,2), XMS-CASPT2(4,4) and LR-CC3 all show a small barrier, while CASSCF(4,4) and XMS-CASPT2(2,2) do not. The apparent barrier in MRCI+Q(4,4) is most likely to be an artefact of the optimisation procedure. CASSCF(4,4) stands out as clearly divergent, with a crossing of S_2 and S_1, showing that it lacks even the correct qualitative description. CASSCF(2,2), on the other hand, is at least qualitatively correct, although the conical intersection is higher than the other methods. LR-CC3 and XMS-CASPT2(4,4) agree closely on the shape of the potentials, with only a small energy offset — we would expect almost identical dynamics from these methods. Finally, we note that the aforementioned XMS-CASPT2(2,2) S_2/S_1 CI occurs just off the pathway shown here, but we can see that the S_2 state is notably closer in energy at the S_1 minimum than in other methods, indicating much stronger influence.

To highlight these effects, in Fig. 5.11 we show the S_1 potential energy surface in the plane defined by the NBD and S_1 minima and the S_1/S_0 MECI. For CASSCF(2,2) (top left), XMS-CASPT2(4,4) (bottom left) and LR-CC3 (bottom right), the overall shape of the potential energy is consistent, with a notable slope towards the S_1 minimum (at $(r_{cc}, r_{rh}) \approx (2.1, 0)$ Å). We can clearly see the S_1 minimum, with a characteristic 'pinching' of the contour lines around a saddle-point between the minimum and the conical intersection. XMS-CASPT2(2,2) (Fig. 5.11, top right) shows an entirely different shape, with a gradient pushing away from the would-be minimum and no obvious saddle-point. This is due to the crossing of the $|2ud0\rangle$ and $|2020\rangle$ states, leading to the S_2/S_1 conical intersection (see further discussion in Appendix B.1).

In summary, with both XMS-CASPT2(4,4) and LR-CC3 all showing an S_1 minimum, we believe the evidence leans towards the presence of a bound local minimum on the excited state, as predicted by CASSCF(2,2).

The S_1/S_0 conical intersection

The central S_1/S_0 conical intersection plays a central role in the non-radiative decay to the ground state. As mentioned previously, all three $|2200\rangle$, $|2020\rangle$, and $|2ud0\rangle$ configurations are important in this region. To analyse the performance of the different electronic structure methods in this region, we use the 'local linear approximation' of Fdez. Galván et al.,[78] covered in Section 2.2. The orthonormalised branching plane vectors X and Y are shown in Fig. 5.12. X is a wing-separation coordinate related to both r_{cc} and r_{db}; extension along positive X moves towards the NBD ground state, while negative X tends towards QC. Y is a rhombic distortion clearly related to r_{rh}, with positive displacement increasing the rhombicity and negative displacement increasing the squareness of the four-carbon ring. Unsurprisingly, these vectors are reminiscent of the branching-plane vectors in ethylene dimerisation.[44,189,190] The energy gap is smallest along the Y coordinate, and thus motion along X is most likely to induce

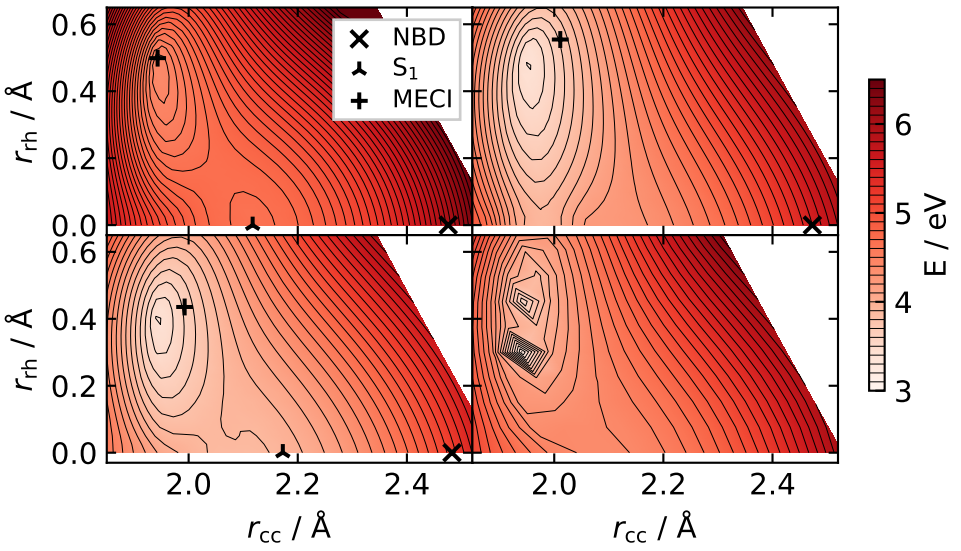

Figure 5.11: S_1 potential energies in the Cartesian plane defined by the NBD and S_1 minima and the S_1/S_0 MECI geometries, calculated at CASSCF(2,2)/p-cc-(p)VDZ level. Energies calculated with CASSCF(2,2) (top left), XMS-CASPT2(2,2) (top right), XMS-CASPT2(4,4) (bottom left), and LR-CC3 (bottom right). Locations of optimised geometries (if they exist) are shown for the active space methods — we note that, for XMS-CASPT2, these are not the minimum geometries in this plane, as it is calculated using the structures at CASSCF(2,2) level. All but the XMS-CASPT2(2,2) have a similar overall shape, with a notable gradient towards the S_1 minimum. LR-CC3 shows instability around the conical intersection but is smooth elsewhere.

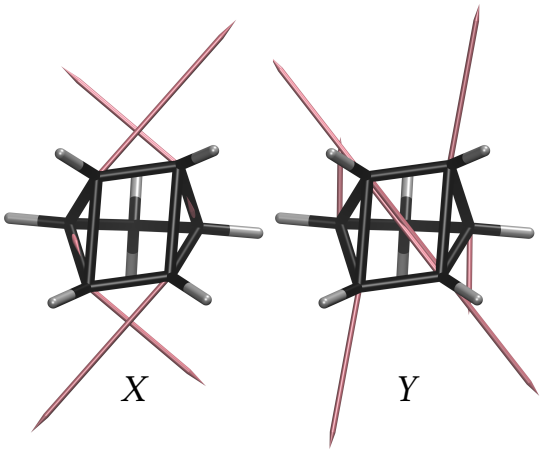

Figure 5.12: Branching plane X and Y vectors from S_1/S_0 MECI, optimised at CASSCF(2,2)/p-cc-(p)VDZ level.[78] Displacements here lie approximately in the plane of the four-carbon ring. The X vector shortens the C_1C_4 bond and lengthens the C_1C_2 bond, forming NBD in the positive direction and QC in the negative. The Y coordinate controls the rhombicity, with negative Y displacement forming the square four-carbon ring of NBD and QC. Hydrogen displacements are small and thus not shown.

Table 5.2: Conical intersection parameters. P and B parameters and carbon-carbon distances (in Ångstroms) for the S_1/S_0 MECI optimised with the (2,2) and (4,4) active spaces for SA(3)-CASSCF, XMS-CASPT2, and MRCI, all with the p-cc-(p)VDZ basis. The conical intersections all have a C_2 optimised geometry.

Method	(m,n)	P	B	r_{cc}	r_{db}	r_{rh}
CASSCF	(2,2)	0.79	0.86	1.94	1.44	±0.50
	(4,4)	0.82	1.82	2.03	1.51	±0.75
MRCI	(2,2)	0.58	0.83	1.96	1.45	±0.49
	(4,4)	0.78	1.11	1.99	1.48	±0.62
XMS-CASPT2	(2,2)	0.56	1.17	2.01	1.49	±0.56
	(4,4)	0.30	0.83	1.99	1.49	±0.44

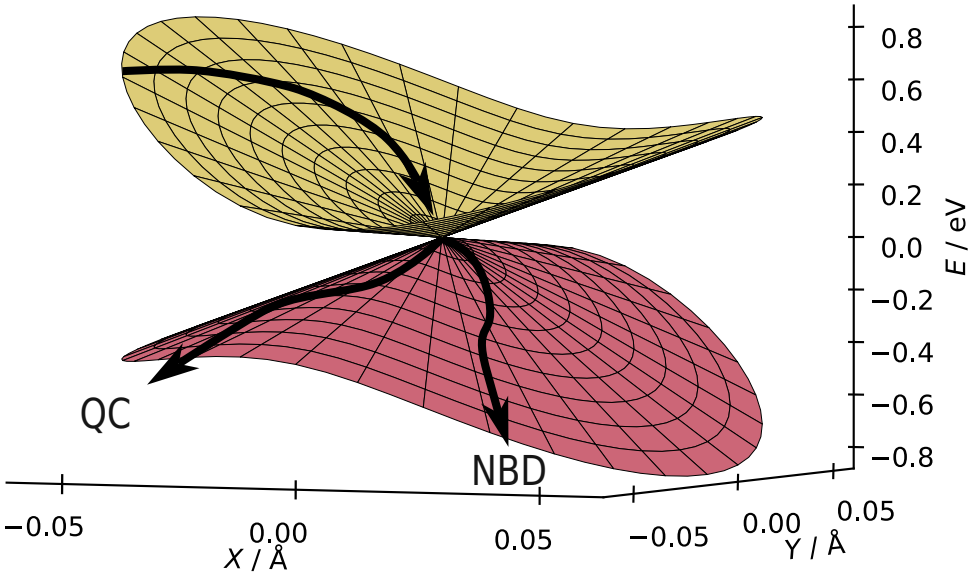

Figure 5.13: Local linear approximation of energies in the branching plane of the S_1/S_0 MECI, optimised at CASSCF(2,2)/p-cc-(p)VDZ level. This is a peaked bifurcating conical intersection, and the branching plane vectors are shown in Fig. 5.12. Approximately, NBD is located towards positive X and negative Y, and QC towards negative X and Y. Two plausible reaction paths are shown, one pointing towards QC and the other towards NBD.

non-adiabatic effects.[78] We can also mention that this analysis has previously been applied to this system,[18,187] albeit in the context of different electronic structure theories.

Table 5.2 gives the P and B values (see Section 2.2) for the MECI geometries for the multi-configurational methods tested here (standard MRCI is shown due to the lack of analytical gradients/couplings in MRCI+Q). All methods agree that this is a peaked conical intersection ($P < 1$), which agrees well with previous studies and is concordant with the rapid dynamics seen in experimental work. The different methods, however, do not agree on the number of minima, with methods alternating between predicting bifurcating and single-path intersections. With the exception of the CASSCF(4,4), with a value of $B = 1.823$, all methods converge on values around $B = 1 \pm 0.2$, indicating that if there are two minima, one is shallow.

In Fig. 5.13, we show the energies in the branching plane for CASSCF(2,2), with the other methods in this study giving very similar surfaces. Here, we can see the ground state potential

barrier, in line with the potential energy surface shown in Fig. 5.9. The (quasi)bifurcating nature reflects this system's utility as a photoswitch — there are two minima, corresponding to the QC and NBD products, which both can be accessed from this intersection. In the present case, NBD has the deeper ground state minimum, while the minimum in the QC direction is shallower and more sensitive to the method used for the calculation. The borderline values of B hint at the unsubstituted system's low quantum yield; no significant potential energy well promotes the conversion of excited NBD into QC. In the context of applications, we suspect that substituted systems with both a lower B value *and* the deeper minimum towards QC would lead to a more efficient route for the formation of QC and, thus, a higher quantum yield.

These numbers provide a valuable distillation of the potential energy surfaces and help assess the similarity of the different electronic structure methods. However, we must remember that while the nature of the conical intersection is important to the outcome of the dynamics, the dynamics preceding the CI are likely to play an even more critical role.

Interestingly, we notice that the earlier results by Hernandez et al.,[53], which indicate significant formation of ground state NBD at relatively short time-scales, are based on electronic structure calculations similar to the CASSCF(4,4) we show. This aligns nicely with the pronounced single-path nature of the conical intersection observed in this particular method.

5.5 — Conclusions

A multi-configurational analysis of the electronic structure of the valence states of quadricyclane and norbornadiene is presented. The previously used CASSCF(4,4) is shown to disagree with higher-level methods, including XMS-CASPT2, MRCI and LR-CC3, while the compact CASSCF(2,2) model is found to yield qualitatively correct results. Additionally, we present a small basis which provides excellent results compared to larger basis sets, limiting the computational time and, thus, the computational cost of dynamics simulations.

The system displays a complex set of potential energy surfaces. As they contain different orbital occupations, the two ground-state minima are separated by a significant barrier. Connecting the two is a singly excited state that spans the two minima, providing a key relaxation channel through a rhombic conical intersection well-known from other [2+2]-cyclo-additions.[44,190] In the region surrounding this CI, the wavefunction gains significant doubly-excited character, and the dynamics through this intersection is posited to be able to form either isomer on the ground state.

The effects of different electronic structure methods on the potential energy surfaces are demonstrated, specifically concerning the presence of an S_1 minimum and the shape of the S_1/S_0 conical intersection. The S_1 minimum, present in the highest-level methods, is absent in the XMS-CASPT2(2,2) calculations. On the other hand, the conical intersection is fairly consistent between low- and high-level multi-configurational methods, with only comparatively minor differences in the topography related to the number of available pathways on the ground state surface.

From this work, three electronic structure methods suitable for dynamics are identified: CASSCF(2,2), XMS-CASPT2(2,2) and XMS-CASPT2(4,4). Clearly, further work performing the actual dynamics simulations is essential to better understand the interplay between dynamics and electronic structure, both in this system specifically and more generally. Furthermore, the erroneous CASSCF(4,4) model can be used as a control case, making it possible to assess how much the dynamics are affected by qualitatively incorrect surfaces. The effect of the conical intersection topography on the outcome of the dynamics is quite interesting, particularly regarding how dynamics prior to and at the conical intersection may affect the (short-time) quantum yields of products.

This work constitutes the foundations of our work on the valence states. This is built upon further in the following three chapters, which explore the dynamics of NBD, the observables observed from those dynamics, and finally, the dynamics of QC.

— 6 —

Dynamics of Norbornadiene

As the norbornadiene/quadricyclane isomerisation reaction is a [2+2]-cyclo-addition/reversion, the reaction on the ground state is formally Woodward-Hoffman forbidden, while the excited state reaction occurs readily.[16,44] The photoexcited dynamics, starting from NBD, can excite into a singly-excited valence state, with absorption centred at around 5.25 eV.[2] The molecule decays to the ground electronic state via a rhombic conical intersection (CI, shown in Figs. 5.1 and 5.4), which sits on top of the ground state reaction barrier from where it can access the potential energy minima of both isomers.

In the previous chapter, we introduced a set of simplified three-state valence-only models of the electronic structure: CASSCF(2,2), XMS-CASPT2(2,2), and XMS-CASPT2(4,4). All three approaches provide reasonable approximations to higher-level electronic structure methods that are too expensive computationally to be feasible for simulations, yet there are subtle differences between the three methods' potential energy surfaces. The most notable difference is the absence of a symmetric local minimum geometry on the S_1 state when using XMS-CASPT2(2,2), which is present in the other two methods. Additionally, the previously used CASSCF(4,4) model[53,188] was shown to perform poorly compared to higher-level methods.

Previous simulations in this system include quantum dynamics using a reduced dimensionality model by Valentini et al.,[188] primarily in the context of coherent control. Hernandez et al.[53] performed surface-hopping dynamics, including on some substituted isomers, and achieved qualitative agreement with product formation ratios. These previous works used extensions of the CASSCF(4,4) method to deal with Rydberg states, which are important at higher energies than what we study here.

In the context of dynamics, the QC/NBD system presents an archetypal example of efficient internal conversion via a conical intersection, with the dynamics dominated by a comparatively small number of nuclear degrees of freedom. This chapter shows that three parameters (interatomic distances) are sufficient to characterise the dynamics. The molecular wavepacket exhibits highly coherent vibrational dynamics, likely the cause of its utility as a photoswitch, and a very fast decay. These properties make it an excellent model system for benchmarking nuclear dynamics methods, with the speed of the dynamics ensuring affordable simulations even for comparatively computationally demanding methods.

In the following, we evaluate dynamics simulated using the same initial conditions, with the electronic structure evaluated using both CASSCF and XMS-CASPT2, with both the (2,2) and (4,4) active spaces. Our comparative study demonstrates how the dynamics is affected by the subtle differences in the potential energy surfaces, allowing us to suggest how the efficiency of the photoisomerisation process in QC/NBD might be improved.

This work is part of a submitted article, J. C. Cooper, C. Brown, J. Kára, A. Kirrander, *submitted*. The author of this thesis completed all computational work and analysis.

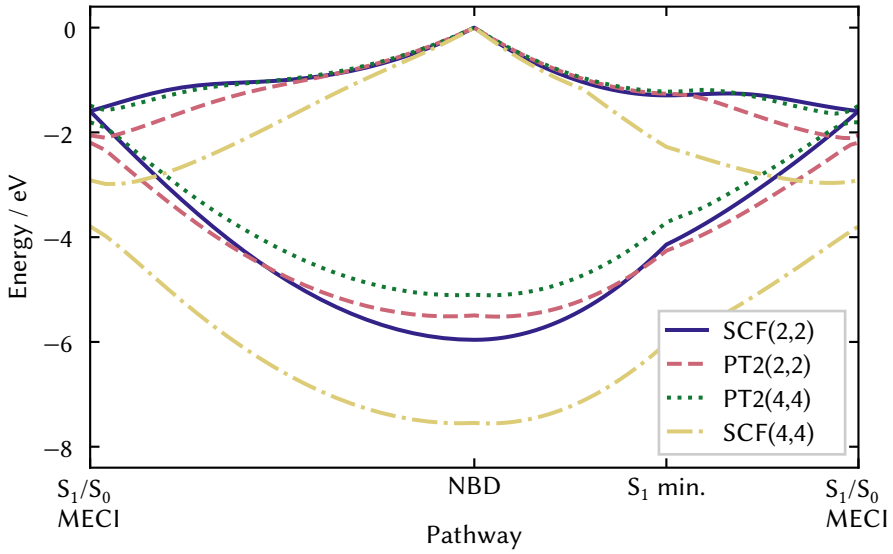

Figure 6.1: Potential energy surfaces for the S_0 and S_1 state along two idealised pathways from the NBD minimum to the S_1/S_0 conical intersection. The first, going from the centre to the left of the plot, goes directly between the NBD and the S_1/S_0 CI. The second, on the right of the plot, passes through the local S_1 minimum. While the CASSCF(2,2) (indigo solid lines, 'CAS' removed for brevity), XMS-CASPT2(2,2) (rose dashed, 'XMS-CAS' removed) and XMS-CASPT2(4,4) (green dotted) methods are fairly similar, CASSCF(4,4) (yellow dash-dot) completely disagrees. Within the concordant methods, XMS-CASPT2(2,2) shows steeper gradients around the conical intersection and is not energetically bound at the S_1 minimum. The pathways are calculated using linear interpolation in internal coordinates (LIICs), all geometries are calculated using CASSCF(2,2)/p-cc-(p)VDZ, and the energy zero has been set at the vertical excitation point to highlight the different dynamics after similar excitation. These pathways represent the idealised reaction coordinates detailed in Fig. 6.2.

6.1 — Theory

Electronic Structure theory

In Chapter 5, we arrived at four electronic structure methods suitable for the dynamics. These are all multi-configurational methods, comprising SA(3)-CASSCF(2,2), XMS(3)-CASPT2(2,2), XMS(3)-CASPT2(4,4), and SA(3)-CASSCF(4,4).[127,209] The first three agree qualitatively with each other on the topography of the potential energy surfaces, while the fourth does not, and is only included to contextualise previous work.[53,188] For clarity, we will drop the state-averaging from the acronyms. All four methods use the same basis set, p-cc-(p)VDZ (see Chapter 5 and Table B.1), which is a pruned version of aug-cc-pVDZ.

The key results of Chapter 5 are shown in Fig. 6.1. The centre geometry of the plot corresponds to the S_0 minimum of NBD, the starting point of the simulations. From there, the dynamics can either proceed straight to the S_1/S_0 conical intersection, as shown on the left-hand side of the plot, or can first visit the S_1 minimum geometry, shown on the right-hand side (shown schematically in Fig. 6.2, see Fig. 6.3 for geometries). We propose these as two plausible pathways for the excited-state dynamics, after which the dynamics will transfer to the ground state and move to the QC and NBD minima. Our primary three methods, CASSCF(2,2), XMS-CASPT2(2,2) and XMS-CASPT2(4,4) all show qualitatively similar potentials, while CASSCF(4,4) clearly does not. Inside the primary methods, we see that the key

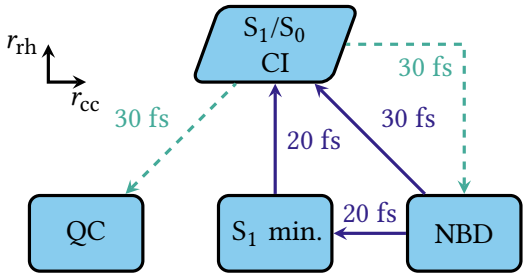

Figure 6.2: Schematic of the photochemical pathways. Each box represents an idealised geometry, positioned approximately as in Fig. 6.3. The symmetry-related partner to the S_1/S_0 CI, located below the $r_{rh} = 0$ line, is not shown. indigo solid lines indicate excited state dynamics, starting from NBD and proceeding to the S_1/S_0 CI with or without going through the S_1 minimum. Green dashed lines indicate ground state processes, with both QC and NBD formed after passage through the intersection. Approximate time-scales of each process are shown. The relative probability of these processes is determined principally by the electronic structure method used in the dynamics.

point of disagreement is at the S_1 minimum, where XMS-CASPT2(2,2) does not show a barrier while the other methods do.

Internal Coordinates Used for Analysis

The surface-hopping simulations are performed in Cartesian coordinates and thus include all nuclear degrees of freedom. As in Chapter 5, we use a set of three coordinates to analyse the nuclear geometries. These all involve carbon atoms C_1-C_4 and are defined in Eqs. (5.1) to (5.3). We will also make use of the velocities along these directions, calculated by finite differences in the trajectories and denoted by e.g. $\dot{r}_{cc} = \mathrm{d}r_{cc}/\mathrm{d}t$.

Fig. 6.3 shows critical geometries for the studied methods in the (r_{cc}, r_{rh})-plane, which we will refer to extensively in our analysis of the dynamics. The ground state minimum of NBD (also referred to as the Franck-Condon region) is where our excited state dynamics starts. This is situated at $r_{cc} \approx 2.5$ Å and $r_{rh} = 0$, conforming to the symmetric C_{2v} geometry of NBD shown schematically in Fig. 5.1. Moving left along the $r_{rh} = 0$ line, we first note the S_1 minimum, only present in a subset of the electronic structure methods, and then the QC ground state minimum at $r_{cc} \approx 1.5$ Å. Above and below the $r_{rh} = 0$ line, we see the two symmetry-related S_1/S_0 minimum energy conical intersections (MECIs). The two MECI geometries have C_2 symmetry, as discussed in Chapter 5.

We note two points: first, these three coordinates span the entire set of displacements of the irreducible representation A of the planar C_2 four-carbon ring. Secondly, r_{rh} is not orthogonal to either r_{cc} or r_{db} except at symmetric C_{2v} geometries. While we show these coordinates as a plane (e.g. in Fig. 6.3), these are projections from the curved manifold of all 39 dimensions. Further discussions of the coordinate system are given in Appendix B.2.

Valentini et al., in their reduced-dimensionality model, used a set of internal coordinates closely related to these three distances. Unlike our choices, their coordinates included both angles and displacements of hydrogen atoms but were entirely centred on the lower four-carbon ring, as in our study. These choices were necessitated by their use of a fully quantum propagation method, which requires a limited number of nuclear degrees of freedom to be computationally feasible. In contrast, we choose our carbon-carbon distances for their conceptual simplicity but have made no approximation concerning the internal degrees of freedom in the simulations. Additionally, we find that the branching plane vectors of the

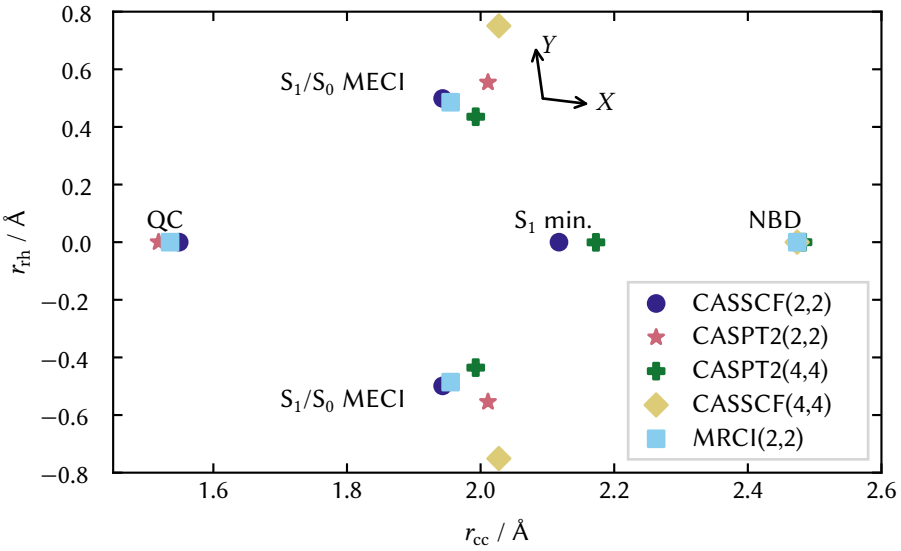

Figure 6.3: Optimised geometries for various methods shown on (r_{cc}, r_{rh}) plane. All methods agree on the location of the NBD ground state. The QC ground state cannot be calculated using (4,4) methods, and the S_1 minimum is only present in some methods. The S_1/S_0 MECI is described consistently by all methods but CASSCF(4,4), which seems to overestimate the rhombicity. The branching plane vectors X, Y of the CASSCF(2,2) MECI are shown, with other methods giving similar values.

S_1/S_0 conical intersections (shown in Fig. 5.12 and as vectors in Fig. 6.3) are almost entirely contained within these three distances, which further supports that these variables allow for a detailed study of the motion in the branching plane.

6.2 — Computational Details

The surface-hopping simulations were performed using our in-house code. The dynamics was propagated with a velocity-Verlet algorithm[210] for the nuclei and a matrix-exponential propagator method for the electronic equation of motion. The time-step (Δt) was fixed at 5 a.u. ($\approx$ 0.12 fs) for the nuclei and 0.25 a.u. ($\approx$ 0.006 fs) for the electronic component, and all dynamics was initiated on the S_1 state. Tully's original version of the hopping probability was used[62], along with the energy-based decoherence correction[88] (as in Eq. (2.44)) with the standard value of $C = 0.1$ E_h, on the coefficients, not the populations, as per the original formulation[88]. Analytical non-adiabatic coupling (NACME, $\boldsymbol{d}_{mn}$) vectors were used to propagate the wavefunction coefficients and were linearly interpolated across the nuclear time-step. NACME vectors were phase corrected by ensuring that $\boldsymbol{d}_{mn}(\boldsymbol{R}_u(t)) \cdot \boldsymbol{d}_{mn}(\boldsymbol{R}_u(t + \Delta t)) > 0$ for $m \neq n$, with $\boldsymbol{R}_u(t)$ the position of the trajectory at time t. For XMS-CASPT2(2,2), the 'CSF' contribution to the coupling was neglected[78,129,211]. To reduce computational time for the XMS-CASPT2(4,4) calculations, the NACMEs are not calculated between states separated by more than 0.1 E_h ($\approx$ 2.71 eV) or when both states have quantum populations below the value 0.01. These approximations did not change the simulation outcomes in testing. After hopping, the momentum was re-scaled along the non-adiabatic coupling vector, and frustrated hops were not reflected. The classical populations were analysed using bootstrapping (with 10000 samples). In total, 639 trajectories were calculated for each electronic structure method and were propagated for 3300 a.u. ($\approx$ 80 fs). The (2,2) active space trajectories conserved total

energy on the excited state to within 0.01 eV, while the (4,4) active space generally conserved to within 0.1 eV (more detailed analysis provided in Appendix B.2). On the ground state, larger energy fluctuations were observed, but these did not affect the rate of population transfer nor the assignment of reaction channels. Additional computational details for the CASSCF(4,4) dynamics are provided in Appendix B.2. An example individual trajectory is provided in Fig. B.15.

Electronic structure calculations were performed using Molpro 2022[212] for CASSCF, OpenMolcas v23.3[191] for XMS-CASPT2(2,2) and BAGEL[206] for XMS-CASPT2(4,4). Different programs for XMS-CASPT2 were used due to NACME instabilities for OpenMolcas in the (4,4) active space. All calculations were state-averaged over three singlet states (S_0, S_1, and S_2) and used density fitting (Molpro/BAGEL, using aug-cc-pVDZ-JKFIT as the density fitting basis) or Cholesky decomposition (OpenMolcas, using the `RICD` keyword). The XMS-CASPT2 calculations used an imaginary shift of 0.2 E_h and no IPEA shift. The XMS-CASPT2(4,4) used the single-state single-reference (SS-SR) approximation[205]. Oscillator strengths were calculated using the CAS-SI method, using the PM-CASSCF functions for XMS-CASPT2(2,2), except for XMS-CASPT2(4,4), which used a full calculation of the transition dipole moment. These are only used illustratively; no further calculation depends on this approximation. The basis set was p-cc-(p)VDZ throughout, as described in Chapter 5.

Ab initio multiple spawning (AIMS) calculations were performed using the Molpro 2022.2 program with the FMS90 interface[212,213] with the independent first generation and zeroth-order saddle point approximations.[214] All AIMS calculations used CASSCF(2,2)/p-cc-(p)VDZ for the electronic structure with all three singlet states. The threshold to enter spawning mode was $|\boldsymbol{d}_{mn}(\boldsymbol{R}_u(t))| > 3$ a.u.. The dynamics was propagated on a 10 a.u. ($\approx$ 0.24 fs) time-step, dropping down to 2 a.u ($\approx$ 0.048 fs) in coupling regions. During periods of non-energy convergence, a minimum time-step of 0.1 a.u. ($\approx$ 0.002 fs) was used. Trajectories were not allowed to spawn if they had a population less than 0.005 and used an `OMax` value of 0.1. Testing of these parameters showed no strong dependence on the specific parameter values. Trajectories were propagated until $t = 2500$ a.u. ($\approx$ 60 fs) with the default Gaussian width parameters of 22.7 a.u. (carbons) and 4.7 a.u. (hydrogens). The trajectories used the same initial conditions as the surface hopping dynamics.

6.3 — Results

Initial Conditions

To keep the comparisons between the individual methods as consistent as possible, we use the same initial conditions for all four electronic structure methods. For simplicity, we select the initial conditions from a Wigner-sampled ground state harmonic oscillator[100], using the optimised geometries and frequencies from CASSCF(2,2). All four methods yield close equilibrium molecular geometries in the NBD ground state, with only minor variations in the vibrational frequencies, especially in the key 'wing-flapping' modes. However, Wigner-sampling of the different ground state minima gave similar distributions overall.

The excited state (the A_2 symmetry S_1) is formally dipole-forbidden at symmetric C_{2v} geometries, necessitating a post-Condon treatment. The Wigner-sampling method is a variant of the nuclear ensemble approach and accounts for Herzberg-Teller effects via Monte Carlo integration of the transition dipole moment over the ground state harmonic oscillator wavefunction. No specific coordinate was identified where Herzberg-Teller effects were particularly prominent, presumably reflecting that 27 non-totally-symmetric modes can increase the oscillator strength. The spectrum calculated at the CASSCF(2,2) level of theory is shown as a solid

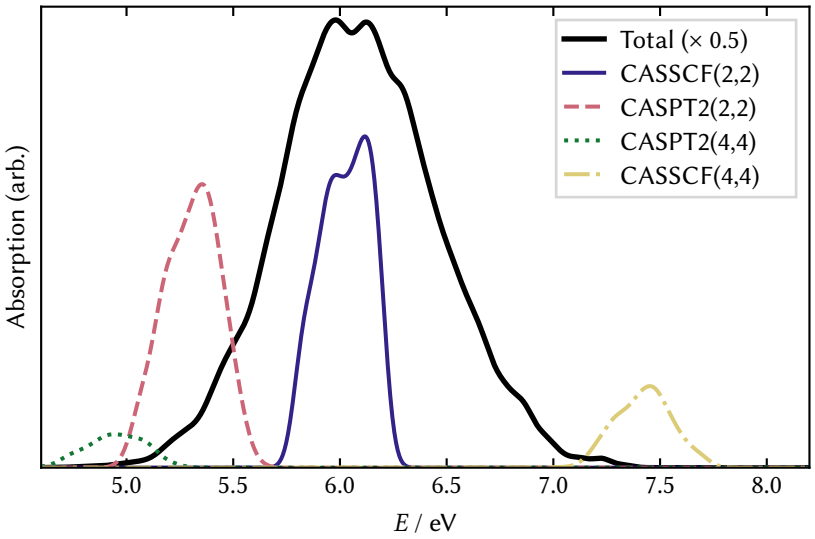

Figure 6.4: Wigner-sampled absorption spectrum obtained from 10000 points. All individual transitions are broadened by a Gaussian with full-width at half-maximum (FWHM) of 0.1 eV. The black solid line indicates the Wigner-sampled S_1 absorption for CASSCF(2,2) (scaled as ×0.5), while the other lines correspond to the spectrum contributions from the initial conditions used in the actual dynamics only (i.e. a subset of 639 of the Wigner points). The initial geometries yield lower initial energies for XMS-CASPT2(2,2) (light blue dashed) and XMS-CASPT2(4,4) (green dotted) methods than CASSCF(2,2) (indigo solid), while the CASSCF(4,4) (yellow dashdot) is much higher. Both (4,4) methods have a lower net cross-section.

black line in Fig. 6.4, and presents as a broad peak centred at ≈ 6 eV, the vertical excitation energy.

We chose initial conditions for the dynamics using a stochastic algorithm[215] inside a [5.8, 6.2] eV window, a relatively large range reflecting the anticipated bandwidth when using a very short pump pulse with an FWHM pulse duration under 10 fs (assuming Gaussian pulses). All excitations were into the S_1 state[i]. In Fig. 6.4, we also show the spectra resulting from the selected initial conditions but with the various electronic structure methods used in the present study. CASSCF(2,2) predicts higher initial energies than either of the XMS-CASPT2 methods, which both predict an excitation centred around 5 eV, in better agreement with experiments. The CASSCF(4,4) method, following Chapter 5, shows much higher excitation energies. Notably, the (4,4) active space yields a lower oscillator strength in both CASSCF and XMS-CASPT2. As the initial momenta are the same but the potential energies are not, each electronic structure method will result in a different total energy. This will certainly affect long-term dynamics on the ground state. However, we only consider the short-time non-adiabatic decay, which is dominated by the dynamics on the initially excited electronic state and its potential energy surface between the Franck-Condon region and the conical intersection (cf. Fig. 6.1).

[i] In CASSCF(2,2) and XMS-CASPT2, this had $|2ud0\rangle$ character. In CASSCF(4,4), 81 of the 639 trajectories had $|2020\rangle$ character. Running the dynamics starting on S_2 (with $|2ud0\rangle$ character) for these trajectories made no appreciable difference to the S_0 population.

Table 6.1: Fitting parameters for the sum of error functions fit (Eq. (6.1)) for each electronic structure method tested. For CASPT2(2,2), a satisfactory fit is achieved with only two error functions. The CASSCF(2,2) shows little (8 %) population transfer for the fast (≈ 30 fs) direct pathway, while the other two show significant transfer. The final error function shows the increase in time for the CASSCF(2,2) and CASPT2(4,4) and corresponds to the portion of the wavepacket moving via the S_1 minimum pathway.

	Function 1			Function 2			Function 3		
Method	t_1 / fs	a_1	c_1 / fs^{-1}	t_2 / fs	a_2	c_2 / fs^{-1}	t_3 / fs	a_3	c_3 / fs^{-1}
CASSCF(2,2)	27	0.06	0.45	38	0.41	0.38	44	0.38	0.11
CASPT2(2,2)	29	0.45	0.28	37	0.48	0.09			
CASPT2(4,4)	33	0.31	0.22	44	0.33	0.42	54	0.24	0.14

Dynamics

With four viable electronic structure methods, we now analyse the differences in dynamics starting on the S_1 state. All other parameters are kept identical for maximum consistency, including the initial conditions, as discussed previously. We first consider the population transfer. In doing this, we find that the CASSCF(4,4), which gave some suspect results even in static analysis, gives qualitatively different results, and we only discuss it further in Appendix B.2. After that, we discuss the quantum yields for the remaining three methods, define three separate reaction channels (decay pathways), and disentangle the population transfer. We then discuss the molecular geometries visited by each set of trajectories, again examining the differences between both methods and reaction channels, before finally discussing the role of the velocity at the crossing geometry.

Populations

Three of the four evaluated electronic structure methods yield very similar results for the population transfer, as shown in Fig. 6.5. The CASSCF(2,2) and the two XMS-CASPT2 calculations exhibit the same ultrafast S_1 to S_0 decay, with $> 80\%$ of the S_1 population having decayed by $t = 60$ fs. In contrast, CASSCF(4,4) exhibits a markedly slower and less efficient decay. This immediately resonates with the previous analysis of the topography of the electronic states shown in Chapter 5. In the interest of being concise, we shall leave the CASSCF(4,4) dynamics to a brief discussion in Appendix B.2, focusing on CASSCF(2,2) and the two XMS-CASPT2 methods hereon.

The CASSCF(2,2) and XMS-CASPT2 simulations find little population transfer to the S_2 state, despite some non-adiabatic coupling in the vicinity of the S_2/S_1 CI (Appendix B.1) encountered well before the trajectories experience coupling to the S_0 state. This lends further credence to the analysis that the S_2/S_1 intersection does not lead to significant population transfer (due to its peaked character) and that the S_1 state has a mix of $|2ud0\rangle$ and $|2020\rangle$ character around the S_1/S_0 conical intersection.

Some minor differences between the three similar population decays are present. The CASSCF(2,2) and XMS-CASPT2(4,4) dynamics decay more slowly, with the largest population transfer occurring at $t \approx 40$ fs. The XMS-CASPT2(2,2) decays quicker, with the main portion of the transfer happening 10 fs earlier. Notably, XMS-CASPT2(2,2) gives a smooth rise, while CASSCF(2,2) and XMS-CASPT2(4,4) have a distinct kink, albeit at different times and population

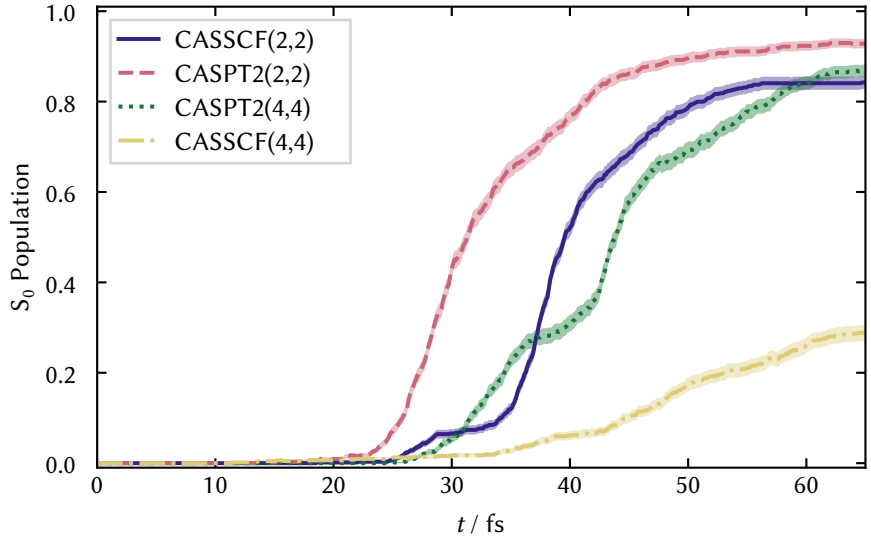

Figure 6.5: The populations on the electronic ground state S_0 as a function of time calculated using surface hopping and different electronic structure theories. The lines in the centre of each shaded field indicate the bootstrapped mean population, and the shaded area indicates one standard deviation. The XMS-CASPT2(2,2) (rose dashed line) rises quickly at $\approx$ 25 fs, while the CASSCF(2,2) (indigo solid) and XMS-CASPT2(4,4) (green dashed) start rising later with a distinct kink, albeit at different times. The rise of these three methods slows at $\approx$ 50 fs, reaching $\approx$ 80% % at $t = 60$ fs. The CASSCF(4,4) (yellow dashdot) results are strikingly dissimilar.

values. For a more quantitative analysis, we fit the rises to a sum of error functions,

$$P_{\text{fit}}(t) = \sum_{i}^{N} \frac{a_i}{2} \left(\text{erf}(c_i(t - t_i)) + 1\right), \tag{6.1}$$

where $P_{\text{fit}}(t)$ is the fitted population as a function of time, $\text{erf}(t)$ is the error function, and a_i, c_i, and t_i are fitting parameters. For each error function, a_i ($0 \leq a_i \leq 1$) corresponds to the amount of population transfer, t_i (≥ 0) the centre of population transfer, and c_i ($-2 \leq c_i \leq 2$) is the rate of population transfer. The results are shown in Table 6.1. The choice of error functions as a fitting basis is somewhat phenomenological, considering the Gaussian wavepacket approximation; given a localised coupling region (like a conical intersection), the fraction of the wavepacket which has experienced the coupling (and hence hopped, in our model) is given by an error function centred at the time when the centre of the Gaussian hits the coupling region. We mention that this model is clearly only appropriate in the short-term coherent limit, and more statistical processes should dominate at longer times.

For CASSCF(2,2), the bulk of the population transfer occurs in the latter two error functions, which make up 79% of the total 85% transfer. The small initial decay captured by the first error function only makes up 6% of the transfer. In XMS-CASPT2(2,2), most of the transfer is in the first rise, coinciding with CASSCF(2,2), with a slower decay occurring later. Only two error functions give a satisfactory fit here, reflecting a lack of complexity compared to the other two methods. XMS-CASPT2(4,4) shows a similar decay structure to CASSCF(2,2), albeit slightly delayed, but has a much more substantial first decay, with over 30% of the trajectories transferring. Notably, the final transfers have longer c values, indicating that the excited state wavepacket becomes more spread later in the simulation.

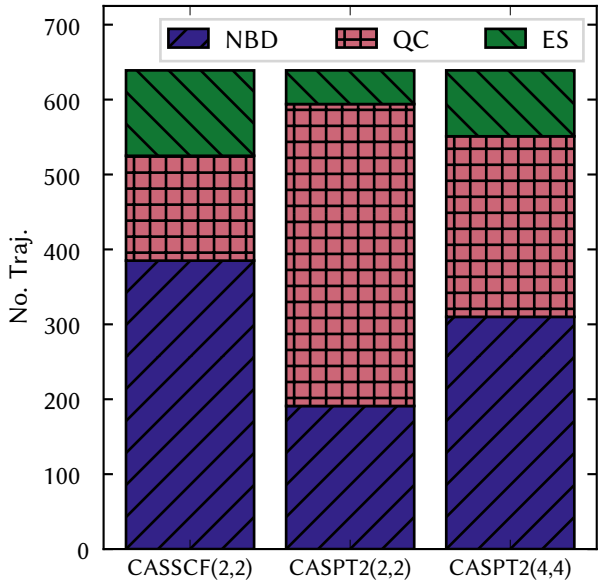

Figure 6.6: Numbers of trajectories in different pathways. The trajectories are sorted according to simulation (electronic structure method) and their final destination (NBD, QC, and ES; see text). The CASSCF(2,2) dynamics has the greatest number of trajectories ending up as NBD (indigo, /-hatching), while CASPT2(2,2) has the most QC-ending trajectories (rose, +-hatching). The CASPT2(4,4) yields intermediate numbers. All three simulations have under 20% of ES trajectories at the end of the simulation (green, \-hatching)

Quantum Yields

It is helpful to identify three different reaction channels in the dynamics according to the character of the trajectories at times close to the end of the simulation. Firstly, we determine if the trajectories are still on the excited state at t_{split} (with $t_{\text{split}} = 2200$ a.u. (≈ 53 fs) for CASSCF(2,2) and $t_{\text{split}} = 2600$ a.u. (≈ 63 fs) for the two XMS-CASPT2 methods). This time is defined as the first point that the initial decay stops (see Fig. 6.5). If the trajectory is still on the excited state, it is labelled as an 'excited-state' (ES) trajectory. The variation in t_{split} reflects the subtly different dynamics, with XMS-CASPT2 trajectories having lower velocities on the excited state, leading to slightly slower decay dynamics.

Of the trajectories which have decayed down to S_0 by t_{split}, we split these into two channels. The first channel leads to NBD-like molecular geometries on the ground electronic state (labelled NBD). This is a non-reactive channel, where the excited molecule returns to the ground state via the S_1/S_0 conical intersection and reforms norbornadiene. According to spectroscopic evidence, this seems to be the predominant pathway in long-time measurements.[20] The second channel yields QC-like geometries (labelled QC), quickly decaying to form quadricyclane. This channel is the 'reactive pathway' to be optimised for photoswitch and MOST applications. We split these two channels using the value of r_{cc} at the end-point of the dynamics (≈ 80 fs), with values above 2 Å recognised as NBD-forming and values below as QC-forming trajectories. This split is particularly evident at 80 fs, as this corresponds roughly to the time taken to decay to the ground state and then make half of an oscillation in the ground-state potential energy well. Since the conical intersections are located at roughly the midpoint between the two isomers, this means that at this point, the two sets of trajectories achieve maximum separation.

The trajectories that remain on the excited state at the end of the simulations are more likely to follow a statistical pattern than the two short-lived channels, which are distinctly

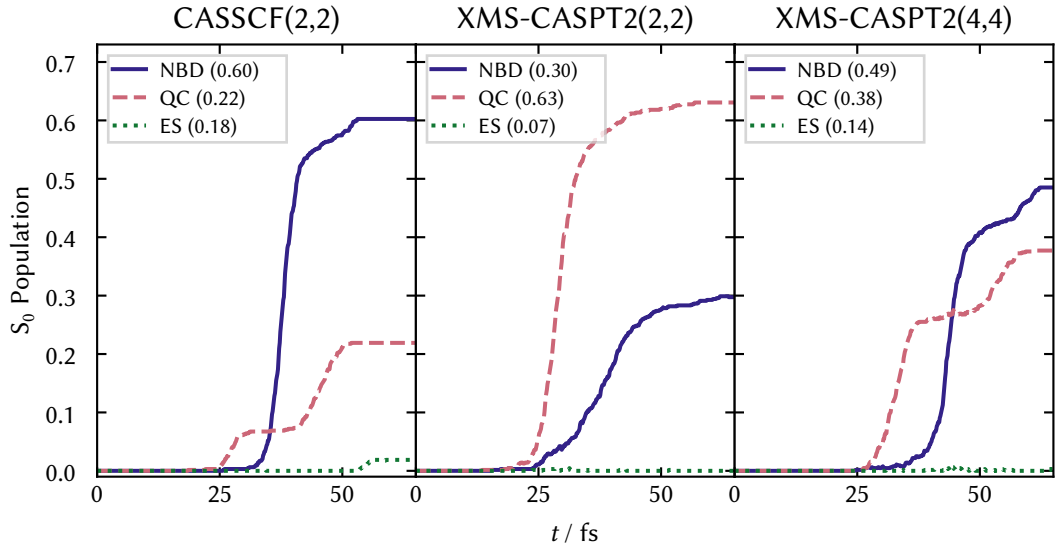

Figure 6.7: The populations on the electronic ground state S_0 (as shown in Fig. 6.5) separated according to trajectory outcome. The fraction of trajectories in each category is given in brackets in the legend of each panel. The left panel shows the results for CASSCF(2,2), the middle CASPT2(2,2), and the right CASPT2(4,4). All methods show an initial increase in S_0 population of QC-trajectories (rose dashed lines) at $\approx$ 30 fs and NBD-trajectories (indigo solid) at $\approx$ 40 fs. Intriguingly, a second rise for the QC-trajectory populations is observed for CASSCF(2,2) and XMS-CASPT2(4,4). The ES trajectories (green dotted) S_0 population is shown as a dotted green line. This is mainly due to trajectories that have yet to decay onto the ground state, but there is a small contribution from trajectories that hop back to the excited state from the ground state.

non-ergodic. Notably, since the same conical intersections are accessed when exciting from either isomer, only the rapid, non-ergodic channels are useful for controlling a photoswitch. For ergodic processes, the outcome of the excited state dynamics is decided by the nature of the conical intersection, which, since it is identical in both cases, leads to the same products. We note that ergodic processes are sufficient for MOST applications, but it is crucial that the conical intersections preferentially lead to the higher-energy isomer.

The distinctions drawn here are not the same as experimentally measured long-time quantum yields; those will be affected significantly by dynamical and thermal processes on the ground state. The electronic structure methods used in this study have not been extensively tested to determine ground state properties (e.g. barrier heights and transition states), so we constrain our dynamics to the excited state decay and the processes immediately after. On these short time-scales, splitting the trajectories into those that immediately form QC or NBD allows for a detailed analysis of the dynamics at the conical intersection. Finally, we also do not distinguish between trajectories which decay through the 'right-handed' (positive r_{rh}) and 'left-handed' (negative r_{rh}) conical intersections, as they are symmetrically equivalent geometries with identical dynamics.

Fig. 6.6 shows the relative numbers of these three pathways for each electronic structure method. The CASSCF(2,2) simulations show the least propensity for reaction, with most of the trajectories returning to their NBD origins. On the other hand, the XMS-CASPT2(2,2) simulations are the most reactive, with just over 60% of the trajectories immediately forming the QC product. The XMS-CASPT2(4,4) results fall between the two, with 50% of the trajectories

returning to the NBD reactant and 40% forming the QC product. All three methods have a similar < 20 % ES channel, indicating that this system has a very coherent, fast decay.

To examine the decay characteristics of each channel, we turn to Fig. 6.7, which shows the S_0 populations for each method, split by reaction channel. Considering first the top panel of Fig. 6.7, which shows the results for CASSCF(2,2), we see clearly that the NBD-ending trajectories appear with a single rise at approximately 40 fs. The population for the QC-ending trajectories exhibits more structure; a sharp initial rise at approximately 30 fs is followed by a second rise at around 45 fs. The initial rise corresponds to a small group of trajectories that immediately decay to QC, constituting around one-third of the QC-ending trajectories. The later rise is somewhat slower than the NBD-ending ensemble. As expected, the ES trajectories show little activity except for a slight increase around the 40-60 fs mark from 'back-hopping' trajectories, which hop to the ground state and immediately return to the excited state.

The results for XMS-CASPT2(2,2) are quite different, as shown in the middle panel of Fig. 6.7. Here, the dominant QC-ending channel exhibits only one feature, which corresponds to a coherent decay at early times — intriguingly on a similar time-scale to the early CASSCF(2,2) QC-forming trajectories. The NBD-ending trajectories decay more slowly than in CASSCF(2,2), with a notable tail. This confirms the results of the earlier fitting, finding that two error functions adequately fit the populations. Finally, XMS-CASPT2(4,4) again exhibits an intermediate version of the dynamics. The QC-ending trajectories have a similar double rise to CASSCF(2,2), but the height of the two rises is flipped, while the NBD-ending trajectories are somewhat coherently formed at later times, with the same tail seen as in XMS-CASPT2(2,2).

A closer analysis of the channel-separated population rises also shows the QC and NBD channels often rise at the same time, reflecting that these processes are not entirely efficient; the passage of a wavepacket through the intersection does not lead to all of the constituent parts behaving identically. This feature is also seen later when analysing the velocities at the crossing point.

As we used the same set of initial conditions for each electronic structure method, we can investigate the dependence of the outcome on the initial condition. No statistically significant correlation was found between the initial conditions and outcomes for different electronic structure methods. This leads us to conclude that the primary factor in deciding the nature of each reaction channel is the potential energy surface between the Franck-Condon region and the conical intersection regions, and not a feature of the initial condition (as it is in Chapter 10).

Molecular Geometries

The dynamics of each trajectory, projected onto the (r_{cc}, r_{rh}) plane, is shown in Fig. 6.8 (see also Fig. 6.3 for specific stationary points in this plane). For clarity, we only show each trajectory while it remains on the excited states. Immediately, we notice a distinct difference in the shape of the overall dynamics for the three electronic structure methods considered. Starting with CASSCF(2,2), the trajectories, which are excited in the region of $r_{cc} \approx 2.5$ Å and $r_{rh} \approx 0$ Å, first reduce r_{cc}, proceeding along the $r_{rh} \approx 0$ Å line. At $r_{cc} \approx 2.0$ Å , the trajectories split into two sets, one with positive and one negative r_{rh}. Each set circles back, forming a 'fishhook' structure. The NBD-ending and QC-ending trajectories disappear soon after (indicating passage through the intersection to the ground state), while trajectories in the ES channel oscillate with less discernible structure after the initial fishhook motion.

The XMS-CASPT2(2,2) trajectories, on the other hand, look significantly different. Both QC- and NBD-ending trajectories seem to start more diagonally, almost immediately breaking the symmetry around $r_{rh} = 0$. The QC-ending and NBD-ending trajectories disappear soon after at $r_{cc} \approx 2.0$ Å and $r_{rh} \approx 0.5$ Å, again via the S_1/S_0 conical intersection. The coherence of these trajectories is clear, even in this reduced dimensionality representation, and agrees

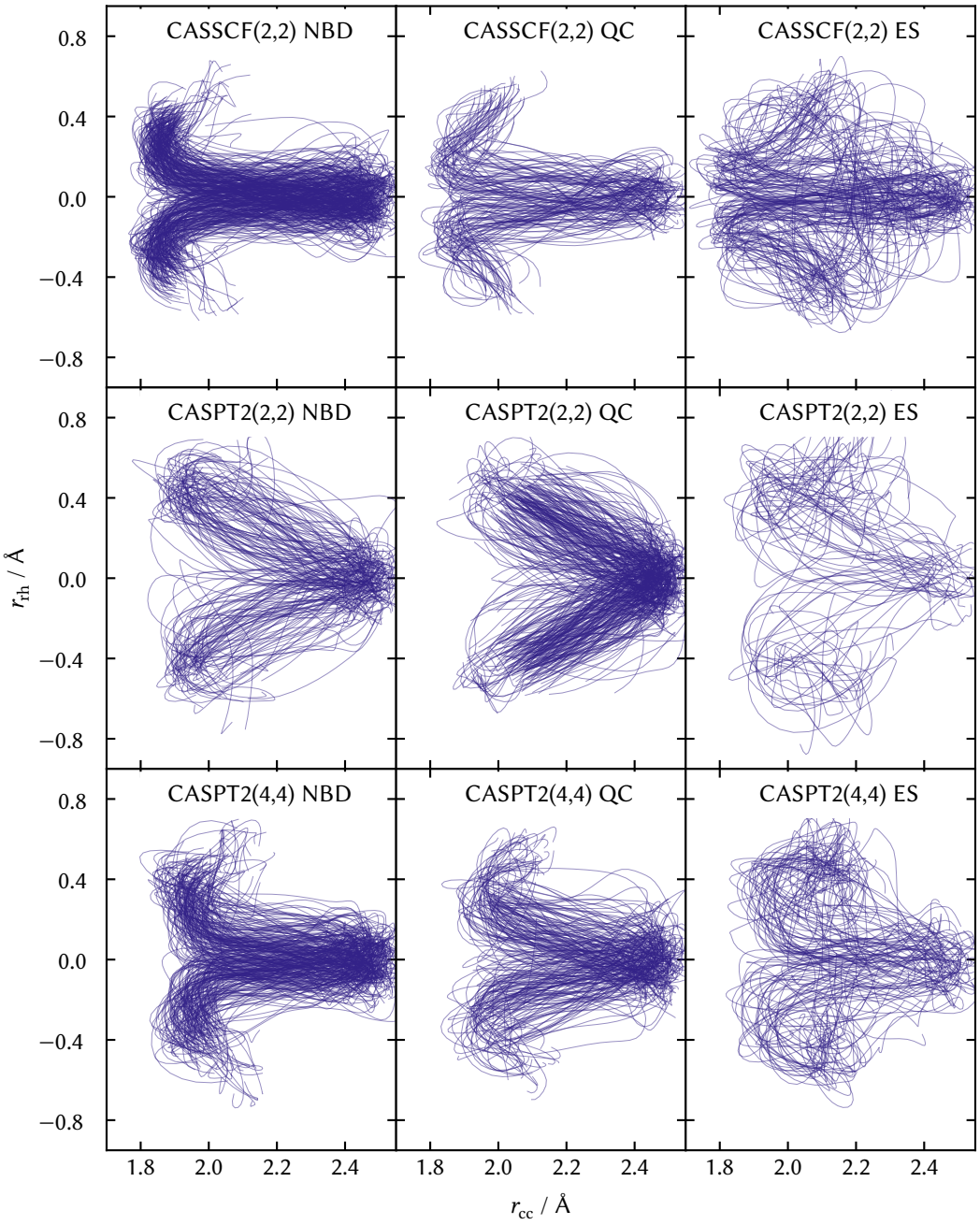

Figure 6.8: Trajectories plotted in the (r_{cc}, r_{rh})-plane, with time as the parametric variable. The key geometries are shown in Fig. 6.3. Each row shows a different electronic structure method, and each column corresponds to a set of trajectories with the same destination (NBD/QC/ES, see text). In all cases, the trajectories are only shown while they remain on the excited state. Trajectories start from the cluster centred at $r_{cc} \approx 2.5$ Å and $r_{rh} \approx 0$ Å (i.e. the NBD Franck-Condon region), and decay to the ground state at the S_1/S_0 conical intersection ($r_{cc} \approx 2$ Å and $r_{rh} \approx \pm 0.5$ Å). The CASSCF(2,2) and XMS-CASPT2(4,4) agree broadly on the initial shape, while the XMS-CASPT2(2,2) shows qualitatively different dynamics.

nicely with the population decays discussed earlier. The ES trajectories are more spread out, exhibiting less obvious coherence. Finally, XMS-CASPT2(4,4) (bottom panel) shows the same 'fishhook' structure as CASSCF(2,2), albeit a bit more spread out.

The two extreme cases, CASSCF(2,2) and XMS-CASPT2(2,2), correspond to either the rhombic character increasing later or immediately, are shown schematically in Fig. 6.2, and can be understood by reference to an analysis of the topography of the excited state potential energy surfaces as shown in Fig. 5.11 and Chapter 5. The local C_{2v} symmetry S_1 minimum at $r_{cc} \approx 2.1$ Å and $r_{rh} = 0$ Å, which is present in both CASSCF(2,2) and XMS-CASPT2(4,4), helps to confine the wavepacket in the region between the conical intersection and the FC region in the excited state. The wavepacket is thus tightly bunched with only little rhombic distortion. In XMS-CASPT2(2,2), which does not have this minimum, the potential energy surface is ridged along $r_{rh} \approx 0$. This cleaves the wavepacket much earlier in the dynamics, giving a more direct mechanism.

The two dynamical pathways are seen in the left- and right-hand sides of Fig. 6.1. The XMS-CASPT2(2,2) potential is notably steeper on the S_1 state around the conical intersection and also drops just after the S_1 minimum. This clearly agrees with the previous point, with the dynamics able to break the symmetry much earlier. The other two methods, CASSCF(2,2) and XMS-CASPT2(4,4), show much more proclivity to stay in symmetrical geometries due to a subtle barrier, which can be seen between the S_1 minimum and the conical intersection in Fig. 6.1. This argument is also lent credence by the slightly less deep minimum in XMS-CASPT2(4,4) (cf. Fig. 6.1), explaining the intermediate nature of these dynamics — the minimum does not confine the dynamics quite as strongly as in CASSCF(2,2), but does not spread as strongly as in XMS-CASPT2(4,4). After passage through the intersection, the dynamics is relatively simple; the trajectories are funnelled towards the ground state minima.

Geometries and Velocities at Crossing

To link the individual nature of each trajectory on the excited state to its final destination, we examine the molecular geometry and the velocity vectors at the instant of hopping to the electronic ground state ($S_1 \rightarrow S_0$). For the ES trajectories, we examine the point of closest energy separation to the ground state during the first 50 fs to decipher the specific causes that may prevent these trajectories from reacting. Figure 6.9 shows the crossing geometries split according to method and destination.

The CASSCF(2,2) hopping geometries are tightly grouped, with two lobes centred at $r_{cc} \approx 1.9$ Å and $r_{cc} \approx \pm 0.4$ Å (cf. the S_1/S_0 MECI in Fig. 6.3). The NBD-ending trajectories are particularly compact, while the QC-ending trajectories are spread towards larger r_{cc} values. Manual analysis of the QC-ending trajectories indicates that many of them pass to the ground state at the second crossing, with the crossing very soon after the first (non-hopping) crossing. This keeps them on the excited state slightly longer and prejudices towards QC formation. For the ES trajectories, the points of closest separation are distributed randomly across the entire r_{rh} axis, reflecting that those particular trajectories simply miss the conical intersection without any further unifying feature.

The XMS-CASPT2(2,2) shows a much larger spread in r_{cc} and seems also to exhibit a definite increase in r_{cc} for the QC-ending trajectories. This may appear counter-intuitive, as one would expect that QC-ending trajectories would pass onto the ground state closer to the QC ground-state minimum at lower values of r_{cc}, but we later see that the velocity plays a larger role. The XMS-CASPT2(4,4) crossing geometries look more similar to the CASSCF(2,2), with two tight groups and small tail to longer r_{cc}. In both XMS-CASPT2 methods, trajectories cross at slightly larger values of r_{cc}, as per the MECI optimisations shown in Fig. 6.3.

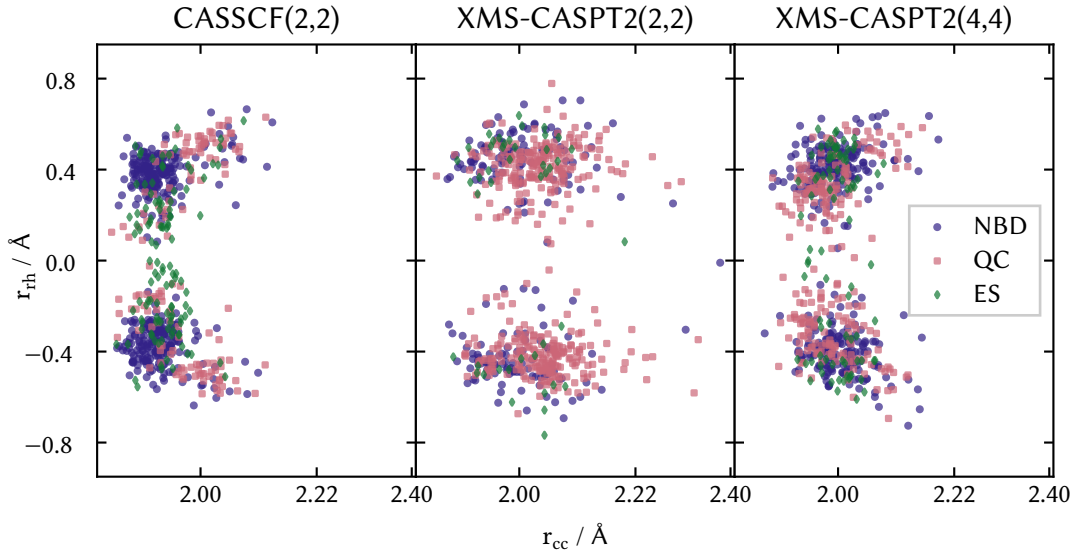

Figure 6.9: The values of r_{cc} and r_{rh} at each crossing geometry (for trajectories leading to NBD (indigo circles) or QC (rose squares)), or point of minimum energy separation between S_1 and S_0 for ES trajectories (green diamonds). Left: CASSCF(2,2). The crossing geometries are closely grouped around $r_{cc} = 1.9$ Å and $r_{rh} \pm 0.4$ Å (cf Fig. 6.3). The ES trajectories have minimum energy separation points distributed across r_{rh}. Middle: XMS-CASPT2(2,2). The crossing geometries are more spread in r_{cc} and have slightly larger r_{rh}. QC-ending trajectories have larger r_{cc}. Right: XMS-CASPT2(4,4). The geometries are grouped similarly to CASSCF(2,2) but with a slightly larger r_{cc}. QC-ending trajectories have slightly lower r_{rh}.

In Fig. 6.10, we show the crossing (or point of nearest separation for ES trajectories) velocities, depicted as vectors in the (r_{cc}, r_{db}) plane. The vectors are centred at the crossing time, shown on the x-axis, and crossing double-bond length along the y-axis, and are plotted separately for each set of trajectories. We reiterate that NBD has a high value of r_{cc} and a low value of r_{db}, while QC has the opposite, and, thus, we have included arrows in Fig. 6.10 indicating the approximate velocity needed to create QC and NBD from the conical intersection. Further analysis of the rest of the dynamics in the r_{db} coordinate is shown in Appendix B.2.

Examining the results for XMS-CASPT2(2,2), the initial early dynamics splits the wavepacket and sends the trajectories directly to the conical intersections. We see this clearly with the group of trajectories at $t \approx 30$ fs all pointing towards QC, with decreasing r_{cc} and increasing r_{db}. The direction, which is well aligned with the X vector in the branching plane, causes a highly efficient transfer to the ground state as per the prediction of Fdez. Galván et al. that non-adiabatic transitions should be particularly strong along X.[78] This rationalises the earlier observation that the QC-ending trajectories hop at relatively large, more NBD-like r_{cc} values (see Fig. 6.9); they maintain their momentum on the ground state, overcoming the potential energy barrier separating QC and NBD, and continue to the QC ground state.

The CASSCF(2,2) trajectories, on the other hand, predominantly turn around before hitting the conical intersection, as shown in Fig. 6.8. Their velocity, now directed towards positive r_{cc} and negative r_{db}, pushes the trajectories towards the NBD ground state, increasing the formation of NBD. This is seen in the top panel of Fig. 6.10, where a group of indigo arrows can be seen at $t \approx 40$ fs, all pointing down and right, aligning with the NBD forming vector. This delineation in this analysis is clear, and one can even see that the slower QC-forming

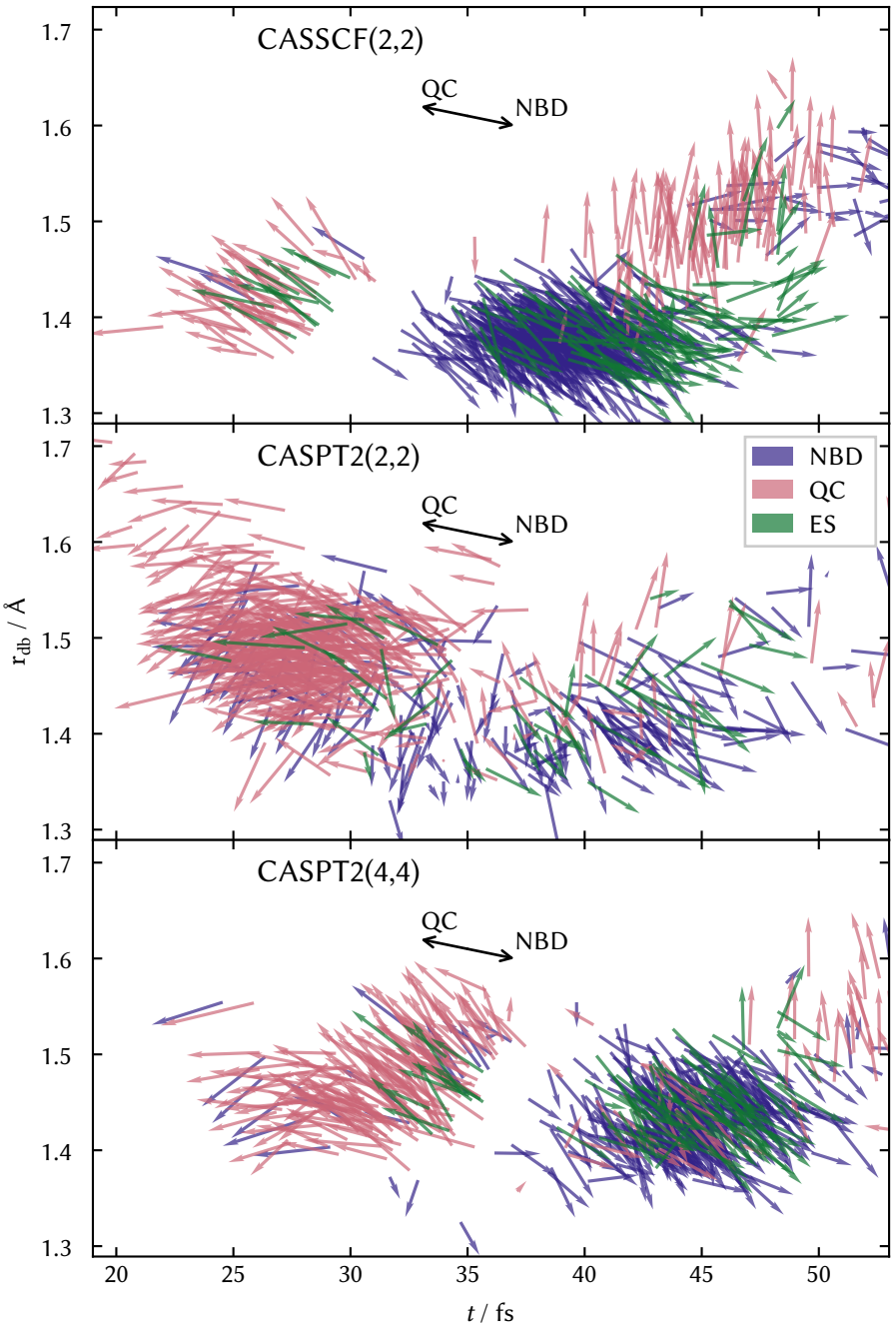

Figure 6.10: Velocity vectors. The base of each vector represents the S_1/S_0 crossing times (x-axis) and r_{db} values (y-axis) split into methods (rows) and result (colour: NBD indigo, QC rose, and ES green). The direction of the vector represents the velocity, with $\dot{r}_{cc}$ along the x-axis and $\dot{r}_{db}$ along the y-axis. For clarity, the approximate velocity needed to form QC and NBD from the S_1/S_0 CI is indicated as the black vector — alignment with these vectors indicates motion towards the respective isomer at the point of crossing. ES trajectories are shown at the point of minimum energy separation from the ground state. Top: CASSCF(2,2). The NBD-forming trajectories coherently form at 40 fs, with crossings having $\dot{r}_{cc} > 0$ and $\dot{r}_{db} < 0$. The QC-forming trajectories have either negative or zero $\dot{r}_{cc}$, but positive $\dot{r}_{db}$. Middle: CASPT2(2,2). The QC-forming trajectories form early, all having $\dot{r}_{cc} < 0$, while the NBD-ending trajectories are later. Bottom: CASPT2(4,4). This panel shows features of both previous panels. This figure is also shown more clearly separated in Fig. B.17.

trajectories in CASSCF(2,2) (at ≈ 45 fs) show an increasing r_{db}, clearly separating them from the NBD-forming trajectories.

Finally, the XMS-CASPT2(4,4) trajectories show a mixture of the behaviour of the other two methods, aligning nicely with all other observations of this being the intermediate case. These results, combined with the insights from the analysis of the populations and excited state geometries, explain the difference in quantum yield between the simulations. Trajectories that have been 'reflected' before the intersection have velocity pushing them towards the NBD ground state, and so *do not* react. In contrast, trajectories that continue directly to the intersection carry velocity towards QC, and so *do* react.

These results are opposed to what might be expected from a purely static (or topographical) analysis of the conical intersections (cf. Table 5.2). The XMS-CASPT2(2,2) surface indicates a purely 'single-path' intersection, with only one local minimum in the direction of the NBD ground state minimum and a (small) barrier in the direction of the QC ground state minimum. The prediction from this would be the formation of only ground-state NBD, without any QC. However, as the XMS-CASPT2(2,2) trajectories approach directly from the Franck-Condon region (i.e. the NBD ground state), the momentum is directed away from NBD. This leads to them passing through the intersection with enough kinetic energy to pass over the barrier, directly forming QC as a photoproduct. CASSCF(2,2) and XMS-CASPT2(4,4), on the other hand, predict a 'bifurcating' conical intersection, with a minimum both in the direction of the QC and NBD ground state minima, suggesting the formation of *both* products. However, the pre-conical intersection dynamics aligns the trajectories back towards the NBD ground state, preferentially forming NBD.

For the slower trajectories, when the energy has had more time to disperse among all of the vibrational coordinates, the intersection's topography should have a more significant role. In this case, the velocity inside the branching plane will be decreased, and the dynamics inside the branching plane will be more affected by the gradient of the conical intersection. We do see some evidence of this in the lack of a second decay in the XMS-CASPT2(2,2) QC-ending trajectories (see Fig. 6.7). The slower trajectories are more liable to follow the 'single-path' conical intersection to form NBD. This effect is not present in either the CASSCF(2,2) or XMS-CASPT2(4,4) trajectories with bifurcating intersections, where slower trajectories do form QC.

Ab Initio Multiple Spawning

As the CASSCF(2,2) method is very efficient, frozen Gaussian methods are computationally tractable. Here, we use ab initio multiple spawning (AIMS), as described in Chapter 2. As the dynamics occurs on identical surfaces, the pre-hopping dynamics is identical for surface hopping and AIMS.

In Fig. 6.11, we show the S_0 population for the AIMS dynamics compared with the surface hopping (labelled dTSH) performed with identical initial conditions and electronic structures. It is immediately apparent that the surface hopping dynamics decays approximately 10% more than the AIMS dynamics, showing a very similar overall shape. This difference is quite a significant deviation, indicating that even this relatively simple decay, with only one crossing region, can cause disagreements between dynamics methods. The difference in decay was not caused by an increased population on the S_2 state, with both methods agreeing that it remains very marginally populated.

Unfortunately, AIMS is a somewhat opaque algorithm with many user-set parameters, making it hard to be sure one has converged. We used values for the various thresholds that are identical to, or better than, those suggested by Lassmann and Curchod,[216] and tested extensively to try to identify any specific threshold we would have set 'incorrectly'. Variation

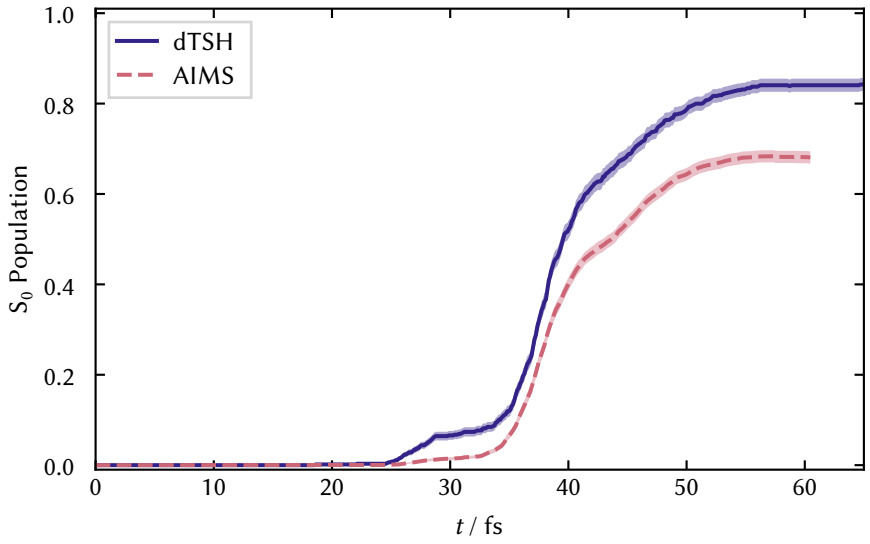

Figure 6.11: S_0 population for EDC surface hopping (dTSH, indigo solid line) and AIMS (rose dashed line), both calculated with CASSCF(2,2)/p-cc-(p)VDZ and identical initial conditions. The AIMS population decay is notably lesser than in surface hopping, reaching an asymptotic value of ≈ 0.7 at its final time of 60 fs. Other than that, the overall shapes of the decay are similar. Populations are estimated by bootstrapping, with the central line indicating the mean and the coloured region one standard deviation.

of the different parameters and thresholds leads to an (at most) 1% increase in the S_0 decay rate, slightly, but not significantly, improving the agreement with surface hopping. As surface hopping is effectively a parameter-free algorithm (with only C in the EDC (Eq. (2.44)) being variable), we are confident that the results have converged to their theoretical limit.

Aside from the populations, we can also examine the quantum yields and geometries of AIMS. As the amount of decay is decreased, the amount of NBD-ending and QC-ending decreases, with quantum yields of NBD = 0.50, QC = 0.18 and ES = 0.32. To compare the quantum yields, we therefore use the ratio of NBD:QC, finding that the AIMS calculations return a ratio of NBD:QC = 2.88, compared to a ratio of NBD:QC = 2.75 for the surface hopping calculations, indicating close agreement. Thus, we infer that the disagreement between surface hopping and AIMS is just that initial coherent decay is less strong, but the underlying dynamics of the different channels remains quite similar. This is understandable when considering that AIMS and surface hopping propagate on the same surfaces, and the continuous vs. discrete nature of the population transfer in the two methods. A more detailed analysis of the other properties is possible (e.g. bond lengths), but this leads to almost identical results to the surface hopping, with the differences only relating to the difference in the decay amplitude, rather than any qualitative changes in the dynamics.

6.4 — Conclusions

To summarise, the mixed-quantum-classical dynamics of photoexcited norbornadiene (NBD) has been simulated using four different levels of electronic structure theory. The destination of individual trajectories is first and foremost affected by their evolution on the excited state, before passing through the conical intersection. QC-forming trajectories generally have a decreasing wing-separation at the hopping geometry, while NBD-forming trajectories exhibit

an increasing wing-separation. This observation is consistent across all electronic structure methods considered, although the individual branching ratios change due to the prior dynamics. In slower trajectories, there was some evidence that subtle differences in the topography at the intersection had some effect on the outcome.[82] This dovetails with previous studies, which show effects on the decay outcomes either from different initial conditions (either positions or momenta)[45,217,218], light interaction,[219–221], or substitution.[68,222] Here, we show this by changing the potential energy surfaces but keeping all else constant. Aside from anything else, this stresses the need to perform a full dynamics simulation to predict quantum yields, and that static analysis of the potential energy surfaces alone cannot reliably predict the dynamics.

Of the four electronic structure methods, CASSCF(4,4), which has been used previously,[53,188] was excluded from more careful analysis due to it having quite different results in the dynamics. In the remaining three methods, the CASSCF(2,2) and XMS-CASPT2(4,4) dynamics broadly agree regarding both populations and molecular geometries. The initially excited state population, which decays within 60 fs, proceeds via a rhombic S_1/S_0 conical intersection to the ground state, forming more NBD than QC. The initial dynamics occurs primarily along the $r_{\mathrm{rh}} = 0$ dividing line, before the trajectories are reflected and break the symmetry to approach the conical intersection (CI). Upon passage through the CI, the trajectories appear in the QC or NBD ground state minimum within 80 fs of the initial excitation.

The XMS-CASPT2(2,2) simulations give similar population decays but strikingly different dynamics, despite using the same active space as CASSCF(2,2). The dynamics immediately breaks the symmetry and proceeds directly to the conical intersection. On the ground state, the trajectories decay to the two separate minima as in the other methods, but QC is preferentially formed. Due to the results of Chapter 5, in particular the comparison with MRCI+Q and LR-CC3, we believe that a S_1 minimum *does* exist, and therefore the real-life dynamics are likely to be more similar to the CASSCF(2,2) and XMS-CASPT2(4,4) dynamics. However, the XMS-CASPT2(2,2) dynamics provide an exciting example of just how significant a difference can be found from only marginally different potentials.

The close comparison of the dynamics leads to insights into possible routes for the engineering of substituted molecules suitable for various applications. Even though we suspect it to be incorrect, we can see that that dynamics akin to XMS-CASPT2(2,2), along a more 'ridged' potential energy surface (with a maximum along the $r_{\mathrm{rh}} = 0$ line), directs the wavepacket directly to the CI and causes the efficient, coherent formation of QC. We could utilise this principle in 'designing' molecules, engineering the potential energy surfaces to favour this pathway. Indeed, the current *state-of-the-art* molecular systems have asymmetric substitution,[20], and this mechanism could already play a part in their effectiveness.

Finally, we compared the calculations of CASSCF(2,2) to AIMS dynamics, finding that the surface hopping dynamics predicted a significantly more rapid decay to the ground state. Otherwise, the predictions of the methods are in close agreement, with similar quantum yields and geometries observed. It is currently unclear whether the AIMS calculations have converged to the parameter limit, but if they have, this discrepancy encourages the completion of more tests on how the addition of nuclear quantum effects changes this reaction, for example, using ab initio multi-configurational Ehrenfest dynamics[87] or variational multi-configurational Gaussian dynamics[96]. Finally, greater knowledge of the dynamics after photoexcitation of QC would allow for a better understanding of how dynamics before passage through the conical intersections affects the end products, and is explored in Chapter 8.

The work in this chapter used the same initial conditions for all methods, primarily to isolate the differences between the excited state potential energy surfaces from the description of the ground state minimum. Limited initial testing shows that the dynamics of XMS-CASPT2(2,2) are affected by using Wigner sampling at the XMS-CASPT2(2,2) level, with a marginally slower

population decay and slightly lower proportion of QC formation. It does not, however, change the geometry dynamics seen in Fig. 6.8, nor does it change the qualitative picture seen in the dynamics. This indicates that the CASSCF(2,2) Wigner-sampling is suitable to understand the dynamics of these methods, as well as allowing for a much closer comparison of the dynamics. We mention that we expect these issues to be largest in the XMS-CASPT2 dynamics, and are therefore not the reason that the CASSCF(4,4) dynamics is so divergent.

In summary, we have presented a series of simulations of the non-adiabatic dynamics of photoexcited norbornadiene. We anticipate that our analysis and predictions of the photoexcited dynamics will be challenged and complemented by future measurements using ultrafast time-resolved spectroscopic [1,223,224] and scattering [149,225,226] experimental techniques. Therefore, in the next chapter, we use these dynamics to predict these variables and comment on what can, or cannot, be observed in these experiments.

— 7 —

Ultrafast Experiments on Norbornadiene

Comparison with experimental measurements is a cornerstone of validation of theoretical models. Converging non-adiabatic dynamics simulations is challenging at best, and at worse impossible. On the other hand, ultrafast experiments provide true results, in the sense that the underlying dynamics is the actual dynamics of the molecule. However, ultrafast experiments project complex multi-dimensional dynamics onto lower-dimensional observables, and a significant amount of information is invariably lost in this process. Further, experimental measurements are inherently limited in terms of their resolution, not to mention the innate technical challenges of performing practical work. Therefore, attempting to deduce the underlying dynamics of a molecule purely experimentally is incredibly challenging.[227] Instead, most experiments rely on extensive comparisons to theoretical simulations.

It is therefore common to publish ultrafast experimental results alongside theoretical calculations, often including full non-adiabatic simulations of the dynamics.[1,131,135,140,143,228–230] Published papers almost always demonstrate close agreement between the theoretical predictions and the experimental data, with little consideration of confirmation bias. Therefore, our guiding question is: does this agreement actually imply that the theoretical dynamics are correct?

For this comparison, we use the four sets of simulations of Chapter 6 to predict time-dependent observables. We then attempt to determine for each observable the key features it is sensitive to. In a sense, we are using the dynamics as a set of four plausible experimental results, trying to see what can be understood about the dynamics purely from the experimental observables. Given that we know exactly what happens in these dynamics, we can then evaluate our predictions. The differences between the four sets of simulations range from rather subtle, e.g. comparing CASSCF(2,2) and XMS-CASPT2(4,4), all the way to qualitatively different. e.g. CASSCF(2,2) vs. CASSCF(4,4).

To understand exactly how the results differ, we can separate the experimental predictions into their component channels. For example, we can analyse how the NBD-forming channel differs from the QC-forming channel, and whether those differences are consistent between electronic structure theories. In particular, we highlight how each experimental technique provides information about a different facet of the system. Here, we show x-ray scattering[i] and photo-electron spectroscopy, two very popular methods for ultrafast dynamics.

Ultimately, this chapter not only aims to increase our understanding of the relationship between theory and ultrafast experiments, but also to advocate for a more critical perspective on the conclusions derived from combined theory-experiment studies. We also recommend multi-modal approaches in ultrafast experimental studies, recognising that only the combined

[i]We do not show results for electron scattering as the independent atom model, which is the primary model used here, shows primarily quantitative differences in electron and x-ray scattering (see Appendix A and Ref. 231)

information gained from complementary techniques allows us to understand these complex phenomena.

7.1 — Computational Details

All calculations of observables used the dynamics detailed in Chapter 6 for the underlying geometries and electronic wavefunctions (see computational details therein). The x-ray scattering cross-sections used the independent atom model (IAM) with form factors taken from the *International Tables of Crystallography.*[232] These calculations were performed for every time-step using a grid of $0 \leq q$ / a.u. ≤ 10, with a spacing of 0.05 a.u (1 a.u. ≈ 1.89 Å^{-1}), for the momentum transfer. For the fixed initial reference (see Eq. (7.8)), we used the ground state Wigner sampled ensemble (10000 points, see Chapter 6), calculated at the CASSCF(2,2)/p-cc-(p)VDZ level. Ab initio scattering calculations were performed using our in-house code. The calculations used Cartesian basis functions, which gave energies and wavefunctions similar to spherical basis functions. The ab initio scattering calculations are far more computationally demanding than IAM, and were thus performed every 100 a.u. ($\approx$ 2.4 fs) on a momentum-transfer q grid half as dense as for the IAM calculations. Similarly, the ab initio scattering calculations were only performed for a representative 50% of the CASSCF(2,2) dynamics ensemble, using the CASSCF(2,2) electronic structure for the wavefunction.

Photo-ionisation energies were calculated by a 'Δ' method, made by calculating the (doublet) ionic states and taking the absolute energy differences with respect to the singlet states (see Section 4.3). We used the corresponding ionic electronic structure for each set of dynamics, found by removing one active space electron. This gives SA(2)-CASSCF(1,2) for CASSCF(2,2), XMS(2)-CASPT2(1,2) for XMS-CASPT2(2,2), XMS(4)-CASPT2(4,4) for XMS-CASPT2(4,4) and SA(4)-CASSCF(3,4) for CASSCF(4,4). The state-averaging was chosen to ensure all available channels were seen. The p-cc-(p)VDZ basis, with density-fitting or Cholesky decomposition, was used for all electronic structure calculations. The CASSCF calculations used Molpro 2022.2[212], the XMS-CASPT2(1,2) calculations OpenMolcas v23.02[191], and the XMS-CASPT2(3,4) calculations Bagel[206] (commit `800fbe2`). Further details on the electronic structure theory can be found in Chapters 5 and 6).

Photo-electron cross-sections were calculated using the Dyson norm method, using the norm of the Dyson orbital between the neutral and ionic states as a relative cross-section (see Section 4.3). For XMS-CASPT2, these were performed using the PM-CASSCF states described in Section 3.4.[233] The author knows of no implementation of Dyson orbitals for full XMS-CASPT2 wavefunctions currently available, so no definitive benchmarking can be performed, but other properties show acceptable agreement when using the PM-CASSCF wavefunctions.[234] Calculations were performed every 20 a.u. ($\approx$ 0.5 fs) concurrently with the trajectory propagation, ensuring the correct wavefunction was used. The neutral wavefunction was used as the initial guess for the ionic wavefunction.

7.2 — Experimental Resolution

For Gaussian pulses, the time-bandwidth product P^{tb} is given by

$$P^{\text{tb}} = \Delta E \Delta t \geq 4\hbar \ln 2 \tag{7.1}$$

where ΔE and Δt are the full-widths-at-half-maximum (FWHMs) in energy and time respectively. This relation, which is equivalent to the energy-time uncertainty principle, limits the resolution of the overall measurement.

In the previous section, we used a top-hat excitation window between 5.8 and 6.2 eV. To make the following calculations easier, we will use a Gaussian of equivalent variance to this function, which gives a Gaussian FWHM of

$$\Delta E = \sqrt{\frac{2}{3}\ln(2)} \cdot \mathscr{W} \tag{7.2}$$

where $\mathscr{W}$ is the full width of the top-hat function, here 0.4 eV, giving $\Delta E \approx 0.2719$ eV.

Henceforth, we shall assume that all pulses are Gaussian, and all pulses are Fourier-limited (i.e. they satisfy the equality in Eq. (7.1)). For the excitation pulse studied, this gives a FWHM in time of $\Delta t_{\mathrm{pu}} \approx 6.7118$ fs, where the 'pu' indicates this is the pump pulse. As we cannot change the dynamics ex post facto, we must use this (or worse) time resolution in our predictions. On the other hand, the probe pulse (labelled as 'pr') can be changed after performing the dynamics, as the dynamics does not depend on its value. The overall time uncertainty of the experimental setup is the cross-correlation of the pump and probe pulses, which gives a Gaussian with

$$\Delta t = \sqrt{(\Delta t_{\mathrm{pu}})^2 + (\Delta t_{\mathrm{pr}})^2}. \tag{7.3}$$

This value is the minimal uncertainty in time of the entire measurement process, and in experimental comparisons, we will broaden the signal by this width. In contrast to time, the energy uncertainty of the pump pulse has already been accounted for in the selection process for the dynamics and, hence, need not be considered further. Therefore, the energy uncertainty we use to broaden the measurement process is simply given by the probe pulse, i.e. $\Delta E = \Delta E_{\mathrm{pr}}$.

For total x-ray scattering, the uncertainty in momentum transfer Δq is given by

$$\Delta q \approx \frac{q \Delta E}{E_0}, \tag{7.4}$$

where E_0 is the mean energy of the x-ray pulse. Most modern x-ray scattering experiments occur in the ten keV range, and so even with a very narrow time-uncertainty (e.g. $\Delta t_{\mathrm{pr}} = 1$ fs, giving $\Delta E_{\mathrm{pr}} = 1.82$ eV and the total time-resolution $\Delta t \approx \Delta t_{\mathrm{pu}}$), the overall uncertainty in the measurement is very low, at approximately $\Delta q/q \approx 10^{-4}$.[ii] In the calculations, we use a grid size larger than this value, so the effect of energy uncertainty on total scattering experiments can be neglected. Further, pulses in the $\Delta t_{\mathrm{pr}} = 1$ fs range are available currently at XFELs,[236–238] at least in the soft x-ray range.

In time-resolved photo-electron spectroscopy, the picture is simpler. From Eq. (4.34), the error in the measured binding energy E_{IP} is given by

$$\Delta E_{\mathrm{IP}} = \sqrt{(\Delta E_{\mathrm{pr}})^2 + (\Delta E_{\mathrm{KE}})^2} \tag{7.5}$$

where E_{KE} is the electron kinetic energy. If there is minimal uncertainty in the measurement of electron kinetic energy (i.e. $\Delta E_{\mathrm{KE}} \approx 0$), then the uncertainty in the binding energy is simply the uncertainty in the probe pulse.

To perform the broadening in time, we use a convolution, defined as

$$\sigma^{\mathrm{c}}(t) = \int_{-\infty}^{\infty} \sigma(\tau) g(t - \tau, \Delta t) \mathrm{d}\tau, \tag{7.6}$$

where $\sigma(t)$ and $\sigma^{\mathrm{c}}(t)$ are the original and convolved observables (here differential scattering cross-section or photo-ionisation cross-section), and $g(t, \Delta t)$ is a normalised Gaussian of FWHM Δt. This is performed for each value of q or E, depending on the observable.

[ii] The LCLS facility currently advertises $\Delta E/E \approx 10^{-3}$.[235]

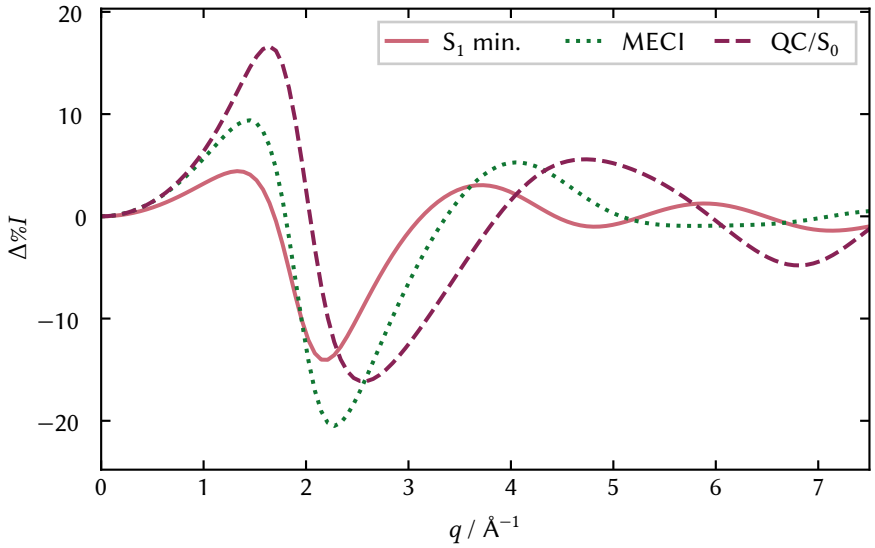

Figure 7.1: Percent-difference total x-ray scattering for the S_1 local minimum (rose solid lines), the S_1/S_0 MECI (green dotted lines) and the QC ground state minimum (purple dashed). All three geometries are quite reminiscent, reflecting that all involve distortion in the r_{cc} direction (see Fig. 6.3). All patterns use the IAM for the scattering and geometries calculated using CASSCF(2,2).

As described, the scattering pattern is calculated without broadening, using Eq. (4.2). The photo-electron spectrum is broadened according to the formula

$$\sigma(t, E) = \sum_{u}^{N_{\text{traj}}} \sum_{f}^{N_{\text{ion}}} |\varrho_{if}(\boldsymbol{R}_u(t))|^2 g(E, \Delta E_{\text{pr}}), \tag{7.7}$$

where N_{traj} is the number of trajectories, N_{ion} the number of ion states, $\varrho_{if}(\boldsymbol{R}_u(t))$ is the Dyson orbital between neutral active state i and ionic state f at nuclear geometry $\boldsymbol{R}_u$, which is a function of time t for each trajectory u. Again, $g(E, \Delta E_{\text{pr}})$ represents a Gaussian, but this time in energy, with FWHM ΔE_{pr} determined by the theoretical pump pulse.

7.3 — X-ray Scattering

Scattering calculations are ubiquitously shown as a *percent-difference*, $\Delta\%I(t, q)$, which is given by

$$\Delta\%I(t, q) = 100\% \cdot \frac{I(t, q) - I(t \ll 0, q)}{I(t \ll 0, q)} \tag{7.8}$$

where $I(t)$ is the scattering signal at pump-probe delay time t. This is the difference in scattering between a given time and the initial state (before the interaction with the pump pulse), modulated by the strength of the signal and expressed as a percentage.

For reference, in Fig. 7.1 we show the x-ray total percent-difference scattering signal at the S_1 minimum, the QC minimum and the S_1/S_0 MECI, relative to the NBD minimum. The signals all start at $\Delta\%I = 0$ at $q = 0$, as all samples show the same value of scattering (i.e. $I(t, q = 0) = N_e^2 = 2500$). After that, the individual geometries show similar patterns, with the two primary features being the peak at $q = 1.5$ Å^{-1} and the trough at $q = 2.5$ Å^{-1}, which we will take to be the signatures of the motion away from the NBD minimum. The differences get

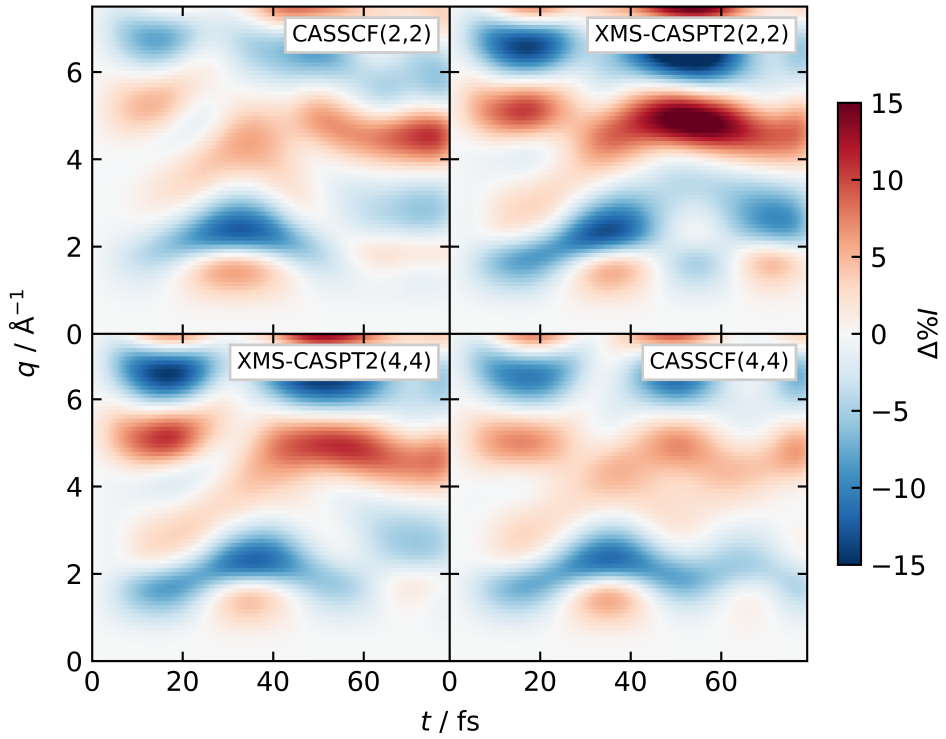

Figure 7.2: Percent-difference scattering patterns for the four ensembles. Top left: CASSCF(2,2). Top right: XMS-CASPT2(2,2). Bottom left: XMS-CASPT2(4,4). Bottom right: CASSCF(4,4). All patterns show a strong feature at ≈ 40 fs corresponding to passage through the conical intersection, but differ at long times due to different quantum yields.

less pronounced at higher values of momentum transfer, as the scattering patterns all converge to their large momentum transfer limit (i.e. $I(t, q = \infty) = N_e = 50$).

We show the scattering patterns for the individual dynamics ensembles in Fig. 7.2. At very early times, the patterns all have $\Delta\%I \approx 0$, indicating their proximity to the reference pattern, the Wigner-sampled NBD ground state minimum. At around $t = 30$ fs, all sets exhibit a strong negative feature at around $q = 2$ Å^{-1}, with a smaller positive feature appearing at $q = 1.5$ Å^{-1}. This is due to the motion of the wavepacket away from the Franck-Condon region towards the S_1/S_0 MECI and S_1 minimum geometries, as discussed in earlier chapters (see Fig. 7.1). We note that it is difficult to differentiate between the signals from CASSCF(2,2) and XMS-CASPT2(2,2), despite the notably different dynamics of the two ensembles (see Chapter 6).

At $t \approx 30$ fs, the wavepacket begins to decay to the ground state and split into the respective final products. The CASSCF(2,2) and XMS-CASPT2(4,4) ensembles show an apparent downward tilt of the strong negative feature, clearly splitting into two features. XMS-CASPT2(2,2) shows this feature splitting *but* staying at higher momentum transfer values. This matches well with the results in Chapter 6, with the XMS-CASPT2(2,2) ensemble showing significant differences at this point to the CASSCF(2,2) and XMS-CASPT2(4,4). Finally, the CASSCF(4,4) ensemble shows an almost oscillatory feature, reflecting the much longer excited state dynamics (see Appendix B.2).

Towards the end of the simulations, the CASSCF(2,2) shows both lower signal strength and a negative feature at $q = 0.5$ Å^{-1}, a strong indication that the system has returned to where it started in NBD. In contrast, XMS-CASPT2(2,2) shows a much stronger overall signal and a positive feature at low momentum transfer, indicating the formation of QC, as clearly shown

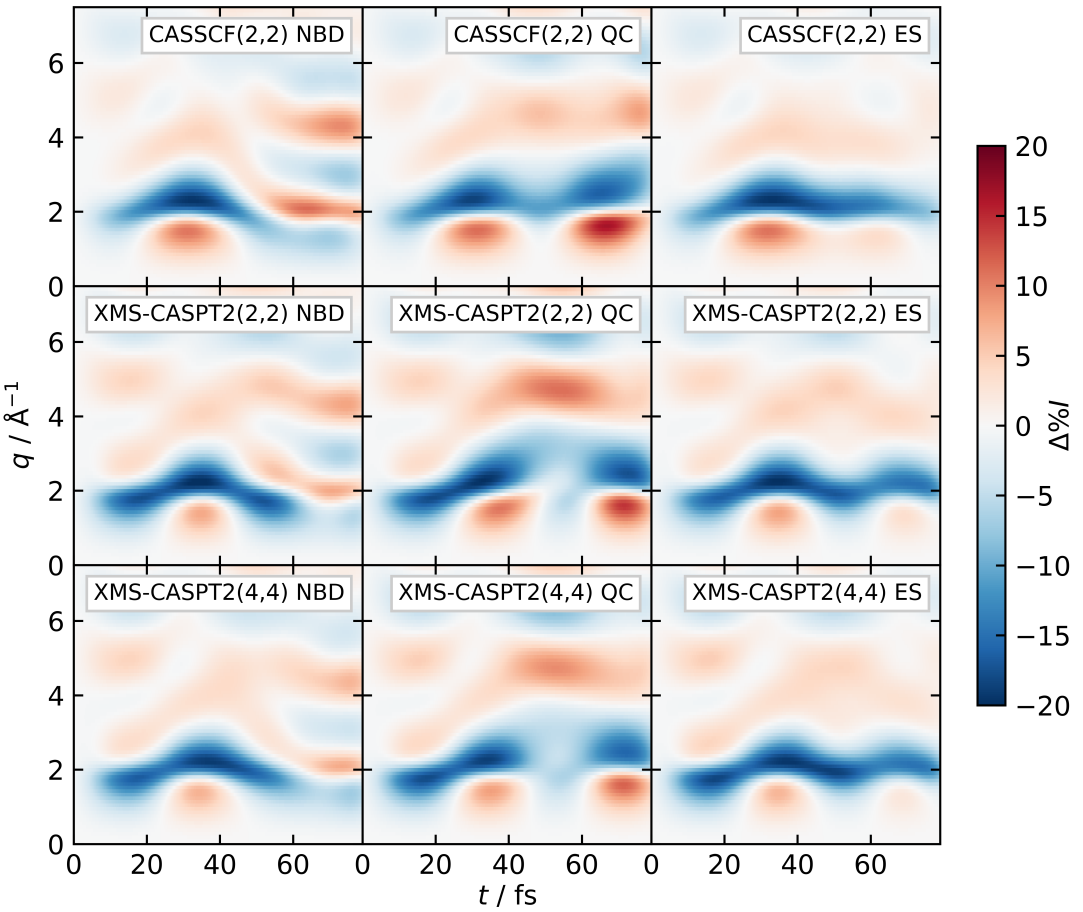

Figure 7.3: X-ray total scattering, separated into electronic structure method (rows: CASSCF(2,2) top, XMS-CASPT2(2,2) middle, and XMS-CASPT2(4,4) bottom) and reaction channel (columns: NBD-ending left, QC-ending middle, and ES right). The differences between the reaction channels are clear throughout for the different dynamics ensembles, but the differences between electronic structure theories within each reaction channel are more subtle.

in the static patterns of Fig. 7.1. Pleasingly, the XMS-CASPT2(4,4) shows a signal somewhere in between, perhaps slightly favouring the more similar dynamics of the CASSCF(2,2).

To understand how the individual features arise, we plot the scattering patterns separated into different reaction channels in Fig. 7.3 (details given in Chapter 6). Here, we do not plot the CASSCF(4,4) ensemble, as it does not neatly fall into the same set of reaction channels. The first column shows the NBD-ending trajectories for each of the different electronic structure methods, showing that the overall structure of these patterns is exceptionally similar, with similar behaviour seen across the entire range of time and momentum transfer.

The QC-ending trajectories (middle column, Fig. 7.3) show some separation, with the CASSCF(2,2) and XMS-CASPT2(2,2) trajectories showing a notably different shape at $t \approx 55$ fs. This reflects the differing nature of the two sets of QC-ending trajectories in the two methods, with CASSCF(2,2) showing a less direct pathway than XMS-CASPT2(2,2). XMS-CASPT2(4,4), which showed both paths in the dynamics, again shows a pattern with features of both others. The ES trajectories all show a similar oscillation, again indicating the motion around the central part of the potential energy surfaces, not yet forming either ground state isomer.

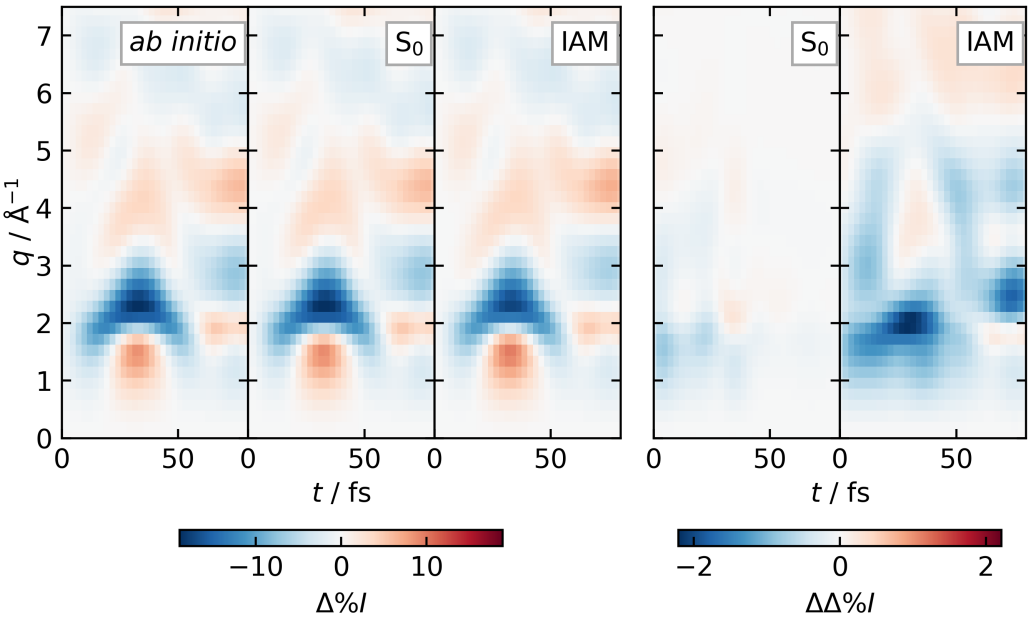

Figure 7.4: Ab initio scattering. The total x-ray scattering for CASSCF(2,2) dynamics. Left: full ab initio percent-difference signal. Centre left: ground state ab initio percent difference signal (labelled S_0). Centre: IAM percent difference signal. All three plots look reassuringly similar. Centre right: ground state vs full ab initio double difference signal. The overall magnitude of this signal is minimal, indicating few electronic effects present. Right: IAM vs full ab initio double difference signal. The discrepancies are much larger but still under ±2% difference, approximately 10% of the total percent difference signal.

One of the benefits of scattering experiments is the uniform cross-section — all parts of the wavepacket scatter with probability equal to their density, and there is no bias towards specific geometries. Along with the clear separation of the different reaction channels in Fig. 7.3, this could potentially allow ultrafast x-ray scattering experiments to disentangle the quantum yields of the process, even if it could not directly show the details of the excited state pathway.

However, it is difficult to imagine that a scattering experiment could pick out the nuanced differences shown in the early-time dynamics of the CASSCF(2,2), XMS-CASPT2(2,2) and XMS-CASPT2(4,4) ensembles. The early-time patterns of each ensemble are very similar, indicating a general lack of sensitivity of ultrafast x-ray scattering to very subtle changes in structure.

Electronic Effects in X-ray Scattering

As discussed in Section 4.2, the x-ray total scattering cross-section is the Fourier transform of the two-electron pair-distribution function. Despite this, much of the signal is related to the nuclear positions, as the electron-electron distances are often closely related to the interatomic distances (e.g. for core electrons). Here, we ask whether there are features in the scattering that are related to electronic effects in the signal. These range from *state-specific* effects, which we define as being due to the different densities between electronic states, to more general effects arising from changes in chemical bonding and correlation at different geometries.

In Fig. 7.4, we show the x-ray scattering pattern calculated in three different ways: The leftmost plot shows the full *ab initio* scattering signal (see Appendix A), calculated using

$c_m^u(t) = \delta_{mi_u}$ in Eq. (4.2), i.e. the signal from the active state. This represents our 'best prediction'. Second from left is the 'S_0' scattering signal, found by performing the ab initio scattering but using the ground state density, i.e. $c_m^u(t) = 1$ if $m = 0$ in Eq. (4.2). This becomes identical to the full ab initio signal as the wavefunction decays to the ground state, as the calculations use the same density. Clearly, any differences between these two signals arise purely from the difference in electron density between the two electronic states. Finally, third from the left are the IAM results. These differ as the electrons are directly tied to 'their' nucleus and cannot distort due to bonding or correlation effects. Additionally, the IAM signal does not change with different electronic states. The difference between this and the previous signals is, therefore, both a state-specific effect and a reflection of the inadequacy of the IAM.

The three patterns are very similar to the naked eye, with only minor differences. Therefore, on the right of the figure, we show the *double-difference* scattering, defined as

$$\Delta\Delta\%I(t,q) = \Delta\%I(t,q) - \Delta\%I^{\text{ref}}(t,q), \tag{7.9}$$

the difference between a percent-difference pattern and a reference (here, the full ab initio scattering pattern).

Second from the right (Fig. 7.4) is the double-difference for the ground state signal, with the differences exclusively down to differences in the electronic contributions from the excited electronic states as compared to the ground state. This signal is small, indicating that electronic effects in the scattering signal are subtle, showing well under 1% in the double-difference pattern (i.e. 5% of the total variation in the percent-difference signal), and primarily present at early times when the electronic wavefunction is most diffuse. The fading of the difference at longer times occurs when the wavefunction of the dynamics returns to the ground state, at which point the 'ab initio' and the 'S_0' signals become identical.

On the far right of Fig. 7.4 is the double-difference for the IAM. As expected, the IAM shows much more significant deviation than the ground state signal, peaking at over 2% in the double difference (i.e. $> 10\%$ of the total variation in the percent-difference signal). It is also interesting to note that the IAM shows its most significant deviation at ≈ 40 fs, when the trajectories reach the conical intersection. This is perhaps unsurprising, since the complex nature of the wavefunctions around the conical intersection cannot possibly be well described by the simple independent atom model.

Overall, there are electronic effects in x-ray scattering, but they are small compared to the absolute magnitude of the signal. This both confirms the utility of the IAM and the fact that the x-ray scattering signal gives mostly nuclear information, at least in a standard molecular pump-probe experiment, but also that subtle electronic effects are present and noticeable in the signal. With current experimental resolution,[239,240] it is difficult to imagine that the state-specific effects will be clear, but 'post-IAM' effects in the scattering signal can and have been identified.[157]

7.4 — Photo-electron Spectroscopy

For photo-electron spectroscopy, to be consistent with experiment[1,139,241] we shall show the difference signal

$$\Delta\sigma_{\text{PES}}(t, E_{\text{BE}}) = \sigma_{\text{PES}}(t, E_{\text{BE}}) - \sigma_{\text{PES}}(t \ll 0, E_{\text{BE}}), \tag{7.10}$$

where $\sigma_{\text{PES}}(t, E_{\text{BE}})$ is the photo-electron spectrum for a given time t and binding energy E_{BE}. This removes the signal from the non-excited portion of the initial ground state wavefunction, which is static in the limit of only one-photon excitation processes. Therefore, the spectra will show two sets of features with opposite signs: the excited state signal, which gives a positive signal, and the ground state bleach signal, which gives a negative. Later, we shall show the

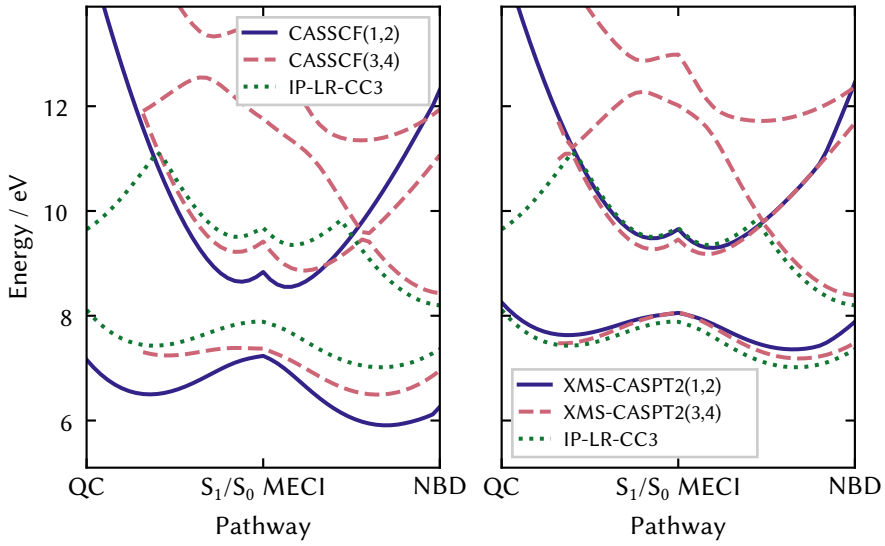

Figure 7.5: Ionic potential energy surfaces on the QC→S_1/S_0 MECI→NBD LIIC (see Section 5.2). For each, the energy zero has been set at the QC minimum. Left: CASSCF(1,2) (solid indigo lines) shows two states, the lower relatively flat at 7 eV and the higher changing much more rapidly, which corresponds to D_2 in Table 7.1. CASSCF(3,4) (rose dashed) shows two more states, corresponding to the D_1 and D_2 in Table 7.1. IP-LR-CC3 (green dotted, both panels) shows a similar lower state but requires more roots to find the additional states. Right: The XMS-CASPT2 [(1,2) indigo solid, (3,4) rose dashed] and IP-LR-CC3 calculations all agree strongly when they find the same states, but there are additional channels in XMS-CASPT2(3,4) not seen in the other methods. As in Chapter 5. we do not show the results for the (4,4) active space in QC.

signal split into both individual reaction and ionisation channels, using the plain $\sigma_{\mathrm{PES}}(t, E_{\mathrm{BE}})$ for simplicity.

Nature of the Ionic Potential Energy Surfaces

To calculate the theoretical time-resolved photo-electron spectra, we first need a way of describing the ionic states. Here, we use a simple method — we use the same electronic

Table 7.1: Ionic states, calculated at the NBD geometry using ΔXMS-CASPT2(3,4)/p-cc-(p)VDZ, using XMS-CASPT2(4,4) for the neutral states. Ionisation potentials (E_{IP}) and Dyson norm cross-sections are shown for ionisation from S_0 and S_1. The wavefunction character is shown in occupation number representation (orbitals in Fig. 5.2), with weights over 20% shown. States that can be described in the (2,2)/(1,2) active space are denoted in the final column.

	E_{IP} / eV			Cross-section		
State	S_0	S_1	Character	S_0	S_1	In (1,2)?
D_0	8.42	3.42	$\|2u00\rangle$	0.93	0.47	Yes
D_1	9.33	4.32	$\|u200\rangle$	0.94	0.03	No
D_2	12.61	7.61	$0.66\|20u0\rangle + 0.21\|02u0\rangle$	0.03	0.30	Yes
D_3	13.31	8.30	$0.47\|200u\rangle + 0.37\|uud0\rangle$	0.05	0.32	No

Table 7.2: Probe energy bandwidths ΔE_{pr} and total experimental time-resolutions Δt for a given probe pulse resolution Δt_{pr}, relative to an excitation pulse resolution of $\Delta t_{\mathrm{pu}} = 6.7118$ fs. All quantities are full-widths-at-half-maximum (FWHMs).

Δt_{pr} / fs	ΔE_{pr} / eV	Δt / fs
1	1.8250	6.7859
6.7118	0.2719	9.4919
20	0.0912	21.0962
40	0.0456	40.5592

structure theory with a single electron removed from the active space, e.g. CASSCF(2,2) gives CASSCF(1,2). Details of all of these are provided in the Computational details above.

In Fig. 7.5, we show the potential energy cuts for these methods, using the high-level IP-LR-CC3 as a reference. We can first notice the two states in CASSCF(1,2) (left panel, solid indigo lines), with a relatively flat state at ≈ 7 eV and a very steep state which transitions between 14 and 9 eV across the plot. These states represent the two states made from the $|2u00\rangle$ and $|20u0\rangle$ configurations, with the former making up D_0 on the right of the pathway and D_1 on the left.[2,242,243] These two states are *Koopmans' allowed* from the S_1 state (of $|2ud0\rangle$ character). To understand the other doublet states, we need to move to a method with more flexibility — XMS-CASPT2(3,4).

These potentials of XMS-CASPT2(3,4) (dashed rose lines, right panel of Fig. 7.5) clearly also show the two states of $|2u00\rangle$ and $|20u0\rangle$ character but add a low lying D_1 state in NBD, which rises in energy across the potential. We include the binding energies, cross-sections, and configurations for the four states in Table 7.1. Here, we can see that D_1, with $|u200\rangle$ character, cannot be described in the CASSCF(1,2) calculations. Thankfully, this state is *Koopmans' forbidden* from the S_1 state, and so should not significantly affect the predicted signal from the excited state dynamics.

We finally note that these are not complete descriptions of all ionic states. This is analogous to the earlier case in Chapter 5, where we ignored the Rydberg and other valence states to concentrate on our model space. While this does imply we do not describe certain ionisation channels, the important (high cross-section) channels are described, and the non-important channels all occur higher in energy, above the ground state ionisation potential of ≈ 8.5 eV. This is important as transitions larger than the ground state IP are more challenging to observe in an experiment, as the spectrum is congested with the ground state bleach signal.

Time/Energy Resolution

Before we delve into the actual appearance of the signals and the differences in the dynamics, we first examine the experimental resolution. As discussed earlier, shorter pulses give poorer energy resolution, and thus, our goal is to find the pump pulse which would maximise the detail in the spectra. We test four different pulses, detailed in Table 7.2, showing the results for the CASSCF(2,2) dynamics in Fig. 7.6

Immediately, it is clear that the shortest probe pulse duration ($\Delta t_{\mathrm{pr}} = 1$ fs, (upper left panel, Fig. 7.6) is unusable, due to two reasons: the energy resolution of the pulse ($\Delta E_{\mathrm{pr}} = 1.82$ eV) is too large, and there is still an overall ≈ 7 fs time-resolution in the signal due the pump pulse. At the other end of the scale, the longer durations of 20 and 40 fs (Fig. 7.6, bottom left and right panels respectively) show little detail as the motion occurs more quickly than the time-resolution. Even though we have very high energy resolution, the energetic spread of

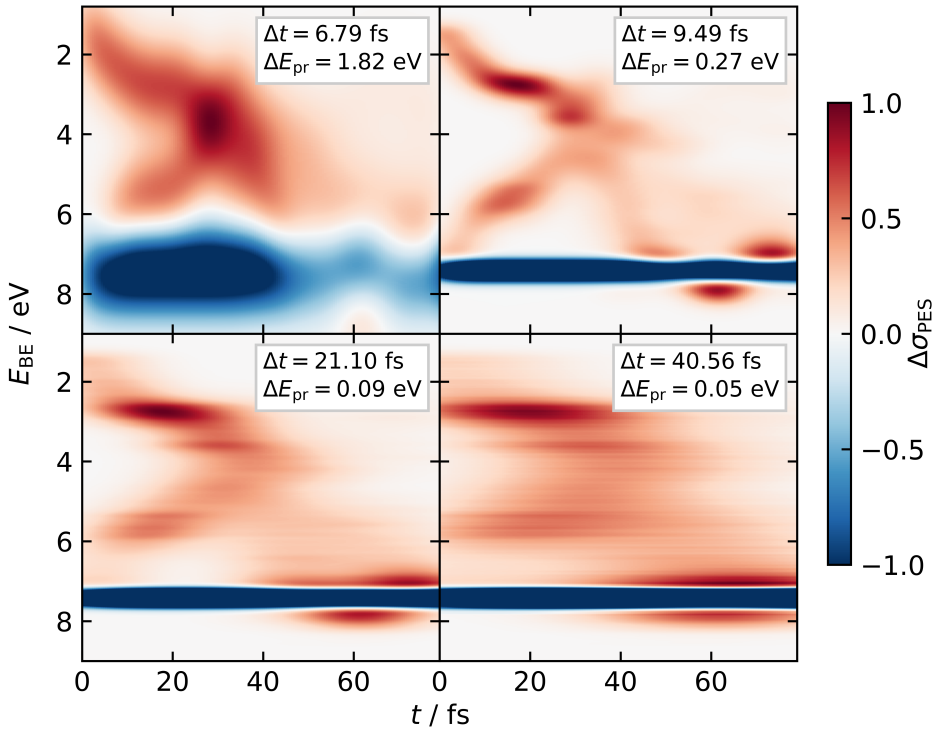

Figure 7.6: TRPES calculations for various experimental pulse shapes, as listed in Table 7.2. All calculations are for CASSCF(2,2) dynamics and use the Dyson norm approximation. The shortest probe pulse (upper left panel, $\Delta t = 6.79$ fs, $\Delta t_{\mathrm{pr}} = 1$ fs) and longer probe pulses (bottom left panel, $\Delta t = 21.10$ fs, $\Delta t_{\mathrm{pr}} = 20$ fs and bottom right panel, $\Delta t = 40.56$ fs, $\Delta t_{\mathrm{pr}} = 40$ fs) show little structure. The upper right panel shows the $\Delta t = 9.49$ fs, $\Delta t_{\mathrm{pr}} = 6.71$ fs probe pulse, which matches the resolution of the pump pulse, shows detail in both energy and time. The individual spectra have been normalised to aid comparison.

the excitation process (and hence the trajectories) is wider, meaning we do not gain much energy resolution either.

The middle ground of $\Delta t_{\mathrm{pr}} = \Delta t_{\mathrm{pu}}$ (top right panel, Fig. 7.6) shows the most structure, with enough resolution to pick out features in both energy and time.[iii] Although these results only show the CASSCF(2,2) dynamics, the other sets of dynamics give very similar results, and we use the $\Delta t_{\mathrm{pr}} \approx 6.71$ fs probe pulse for all TRPES data.

Here, we briefly note that we believe that this approximate level of experimental resolution ($\Delta E \approx 0.3$ eV, $\Delta t \approx 10$ fs) to be a 'Goldilocks zone' for this kind of ultrafast decay process. 0.3 eV is enough energy resolution to notice the significant changes as the molecule breaks bonds, and 10 fs is fast enough to capture the dynamics of all but hydrogenic motion. Moving to much shorter or longer pulses either compromises the timescale or the energy, either way obscuring the dynamics.

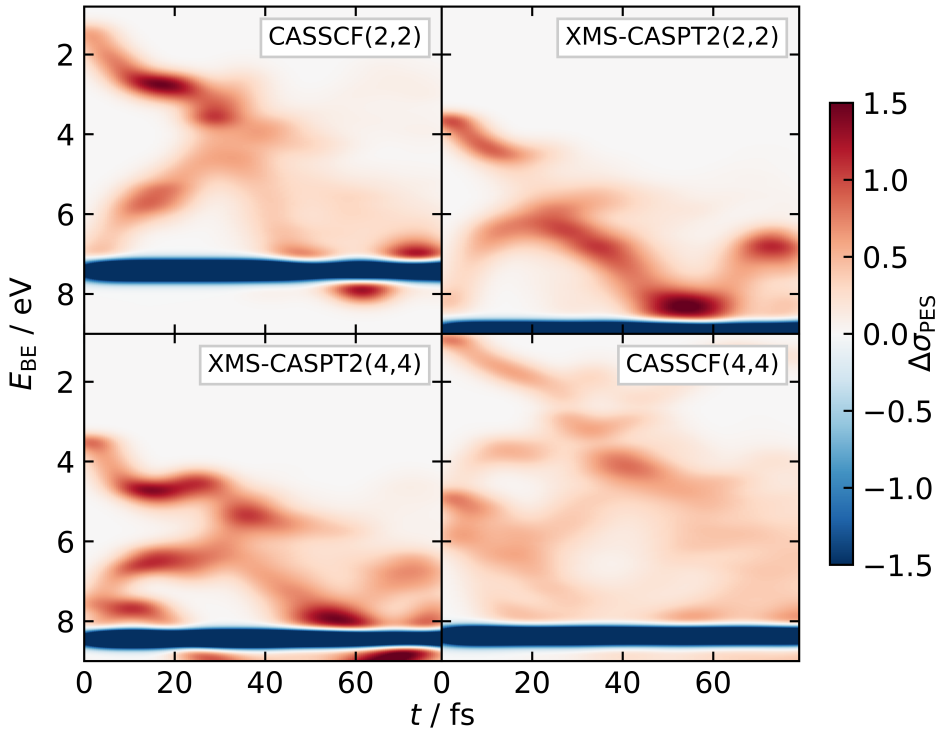

Figure 7.7: Time-resolved photo-electron spectra for different sets of dynamics. The two (2,2) active space methods (upper panels) show similar structure, albeit with a notable binding energy shift. The XMS-CASPT2(4,4) (lower left) shows a few additional features while still resembling the (2,2) methods, with CASSCF(4,4) (lower right) adding even more. All spectra show a similar double feature at early times, with a low-binding energy and a high-binding energy feature moving together and crossing, signalling passage through the conical intersection.

Electronic Structure Methods

The simulated time-resolved photo-electron spectra are shown in Fig. 7.7, separated into the different electronic structure methods. We first notice the similarity between the CASSCF(2,2) and the two XMS-CASPT2 signals. There are two principle features, one decreasing and one increasing in binding energy as we move away from $t = 0$. At the conical intersection (≈ 40 fs), these two features meet, and then the majority of the signal proceeds to around $E_{IP} = 8$ eV, indicative of the formation of both ground state NBD and QC (see Table 7.1). We also notice that the ground state bleach (the strong negative feature) is higher in the CASSCF(2,2) calculations, reflecting the energy of D_0 being too low, as seen in Fig. 7.5.

The time-scale for the dynamics is immediately apparent. For example, the XMS-CASPT2(2,2) dynamics give a crossing of the two early features at around 25 fs, earlier than in CASSCF(2,2) and XMS-CASPT2(4,4) (cf. Fig. 6.5). In addition, we can use the lack of low-binding-energy features at later times to infer that the wavepacket has moved down the potential to the ground state. The CASSCF(4,4) dynamics, on the other hand, shows a significant signal at lower binding energies and later times, reflecting the longer excited state lifetime. We also note

[iii] $\Delta t_{pr} = \Delta t_{pu}$ always gives the highest combined resolution, as the overall time-bandwidth product is

$$P^{tb} = \Delta E \Delta T = 4\hbar\ln(2)\sqrt{(\Delta t_{pu})^2 + (\Delta t_{pr})^2}\sqrt{(\Delta t_{pu})^{-2} + (\Delta t_{pr})^{-2}},$$

using the equality in Eq. (7.1) and Eq. (7.3). This function is minimal ($P^{tb} = 8\hbar\ln(2)$) at $\Delta t_{pr} = \Delta t_{pu}$.

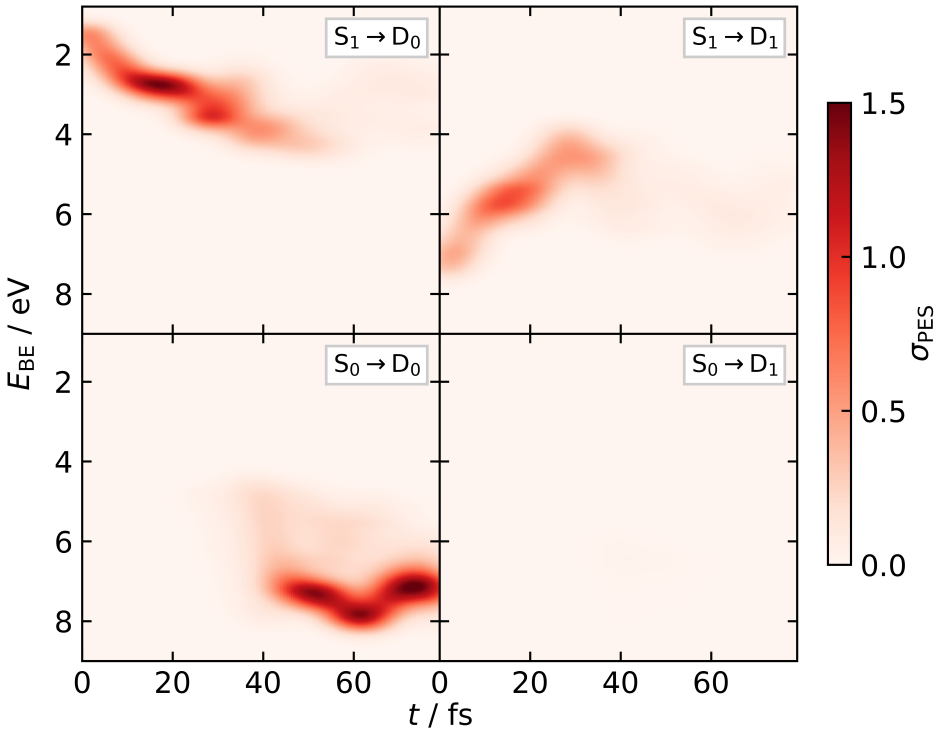

Figure 7.8: Ionisation channels for CASSCF(2,2) dynamics. Ionic states were calculated using CASSCF(1,2), with cross-sections calculated with Dyson norm approximation. The $S_1 \rightarrow D_0$ descends from $E_{BE} \approx 2$ eV to $E_{BE} \approx 4$ eV, meeting with the rising $S_1 \rightarrow D_1$ channel at 40 fs. After that, most of the signal is from the $S_0 \rightarrow D_0$ ground state channel, which oscillates around the ground state minima, and no $S_0 \rightarrow D_1$ signal is seen.

that even the qualitatively incorrect CASSCF(4,4) shows a somewhat similar signal, but the presence of extra channels due to the mixture of S_1 and S_2 dynamics (cf. Appendix B.2) is immediately visible.

Here, it is worth discussing what can be understood about the dynamics *only* from these observables. As just discussed, the electronic decay time-scale is evident from all sets of dynamics, especially the extended excited state lifetime of CASSCF(4,4). Further, we could predict the reformation of NBD in CASSCF(2,2) and XMS-CASPT2(4,4) due to the longer-time signal occurring at the same binding energy as the ground state bleach signal. Contrastingly, we could predict the formation of a new isomer in XMS-CASPT2(2,2) by the signal's strong presence above the bleach. That being said, we likely could not easily distinguish product ratios, as the signals of the two isomers both overlap in energy and give different cross-sections.

In the following few sections, we cover how each of the features in the signals arises, covering both photo-ionisation and reaction channels.

Photo-ionisation Channels

In this section, we break down the spectra into separate ionisation channels, defined by an initial (neutral) and final (ionic) state (e.g. $S_1 \rightarrow D_0$ indicates the channel from the first excited neutral singlet state to the ground ionic doublet state). In principle, these different signals are

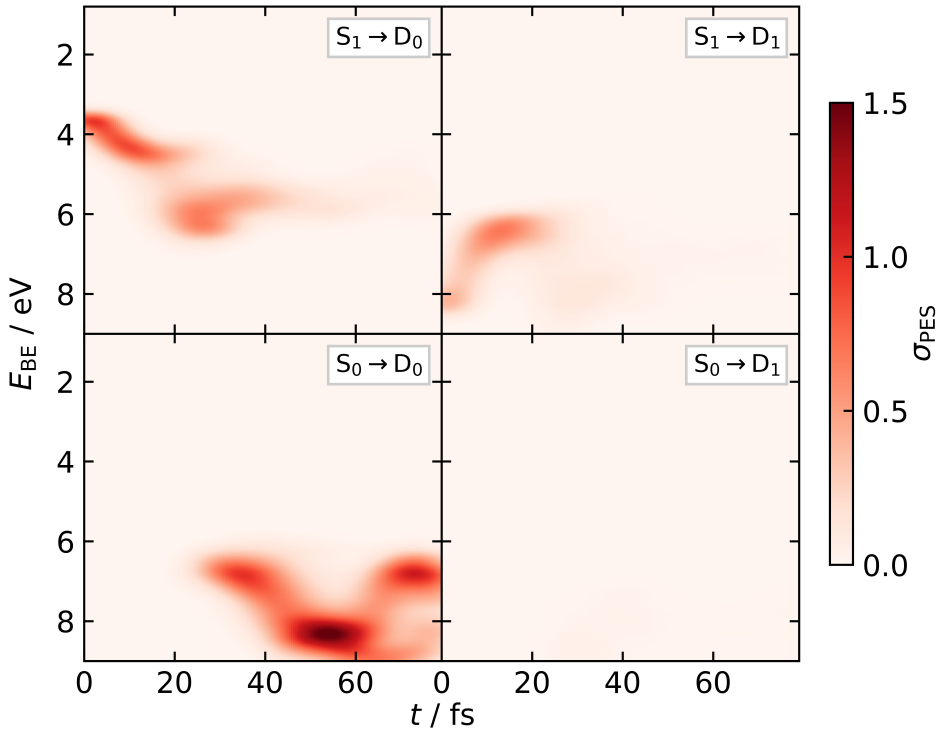

Figure 7.9: Ionisation channels for XMS-CASPT2(2,2) dynamics. Ionic states were calculated using XMS-CASPT2(1,2), with cross-sections calculated with Dyson norm approximation. This displays very similar behaviour to the CASSCF(2,2) spectra (Fig. 7.8), except notably quicker and at higher binding energies.

all observed simultaneously on the detector.[iv] In a theoretical calculation, we can separate these channels to interpret the makeup of the total spectrum. For clarity, we will only show strongly contributing channels and again drop the analysis of CASSCF(4,4).

In Fig. 7.8, we show this separation for the CASSCF(2,2) dynamics. The low- and high-binding-energy features in the total spectra arise from the $S_1 \rightarrow D_0$ feature (top left panel in Fig. 7.8) and $S_1 \rightarrow D_1$ feature (top right panel in Fig. 7.8). Their meeting, at $t = 40$ fs, foretells population decay onto S_0 eV, as states are closest at the conical intersection geometry (see Fig. 7.5), where the orbital energies are close to degenerate. We notice that the initial binding energy for $S_1 \rightarrow D_0$ is predicted at 2 eV, higher than the correct value of ≈ 3.5 eV. This comes from two separate issues in CASSCF(2,2) — firstly, the first excitation energy is at ≈ 6 eV, higher than the correct value of ≈ 5.25 eV. Secondly, the first ionisation energy is approximately 1 eV too low, as seen in Fig. 7.5.

On the ground state, the only significant contribution is from the $S_0 \rightarrow D_0$ channel, as the $S_0 \rightarrow D_1$ channel is Koopmans-forbidden (and high energy). The $S_0 \rightarrow D_0$ channel shows a quick decay before the emergence of a strong feature at $t = 45$ fs, containing *mainly* NBD features from highly vibrationally excited ground state dynamics (see Chapter 6).

The spectra of XMS-CASPT2(2,2), shown in Fig. 7.9, show the same features as CASSCF(2,2) despite the different dynamics. The meeting of the two excited state channels is earlier,

[iv] Unless one measures photo-electron angular distributions, which give information of the angular momentum of the departing free electrons, relative polarisation axis of the probe pulse. In that case, it might be possible to separate the individual channels.

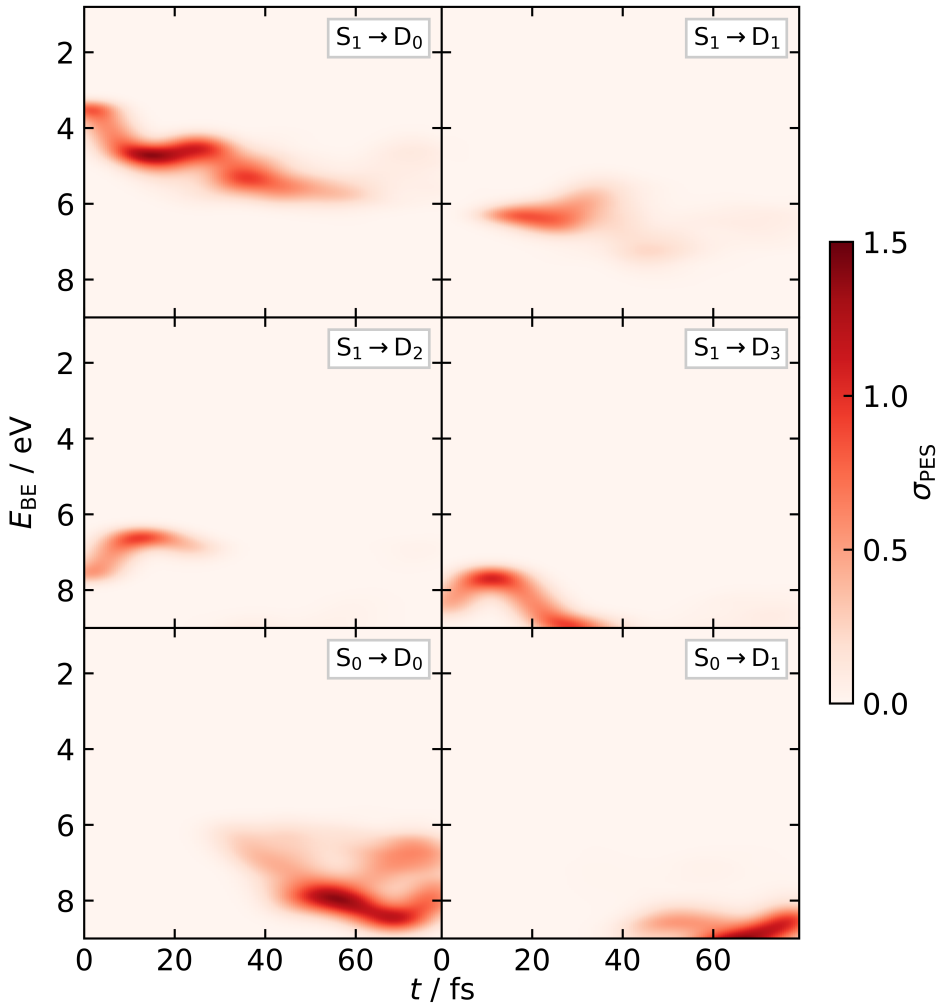

Figure 7.10: Ionisation channels for XMS-CASPT2(4,4) dynamics. Ionic states were calculated using XMS-CASPT2(3,4), with cross-sections calculated with Dyson norm approximation.

reflecting the faster decay (cf. Fig. 6.5), and the $S_0 \rightarrow D_0$ channel shows a strong signal from mainly vibrationally excited QC ground state dynamics.

For the XMS-CASPT2(4,4) dynamics, shown in Fig. 7.10, the $S_1 \rightarrow D_0$ channel is strongly reminiscent of the two (2,2) methods. The $S_1 \rightarrow D_1$ and $S_1 \rightarrow D_2$ channels together make up the $S_1 \rightarrow D_1$ channel in the (2,2) methods, understood by comparing the potential energy cuts of XMS-CASPT2(2,2) and XMS-CASPT2(4,4) (in Fig. 7.5, right panel). The additional state (of $|u200\rangle$ character) in the XMS-CASPT2(3,4) calculations (D_1 in the Franck-Condon region, see Table 7.1), quickly rises in energy above the $|20u0\rangle$ state. The difference is thus just an artefact of the adiabatic labelling, and the signal comes from the transition of $|20u0\rangle$ character. Finally, the $S_1 \rightarrow D_3$ channel, which cannot be calculated in the (2,2) methods, shows a feature at very high binding energy very early in the dynamics — the ground-state bleach signal would likely obscure this.

When the dynamics passes on to the ground state at around 40 fs, the $S_0 \rightarrow D_0$ channel shows similar results to the (2,2) active space methods, but we can see the presence of two signals — clear evidence of *both* NBD and QC formation. On the other hand, the $S_0 \rightarrow D_1$ channel does

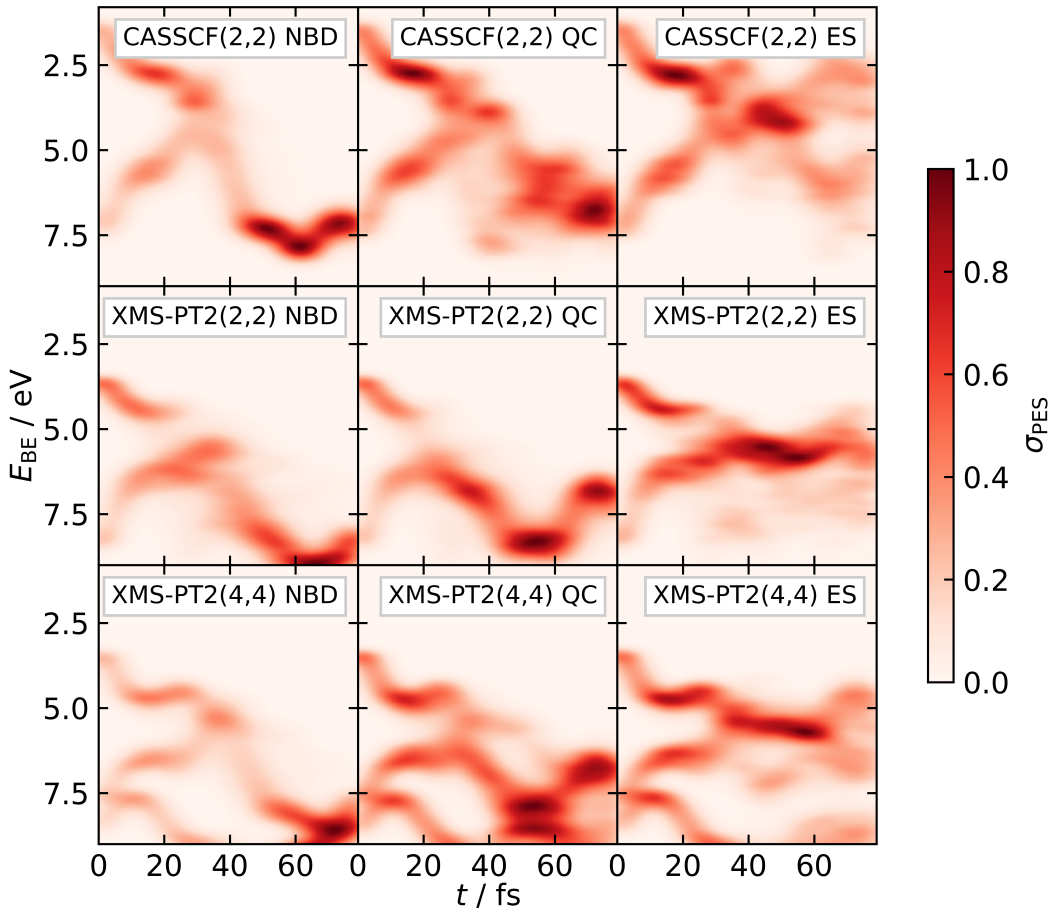

Figure 7.11: Time-resolved photo-electron spectra for each method and reaction channel. Top row: CASSCF(2,2). Middle row: XMS-CASPT2(2,2) (denoted XMS-PT2(2,2)). Bottom row: XMS-CASPT2(4,4) (denoted XMS-PT2(4,4)). Left column: NBD-forming trajectories. Middle column: QC-forming trajectories. Right column: ES trajectories. As opposed to Fig. 7.3, the differences between the different reaction channels are relatively minor compared to those between the different electronic structure methods. The cross-section has been normalised so all panels' maximum signal is unity.

show some signal, again reflecting that D_1 has a different character around the Franck-Condon region and that it is *Koopmans' allowed* from the ground state.

Reaction Channels

Figure 7.11 shows the photo-electron spectra split into individual reaction channels. Again, we do not show the CASSCF(4,4) dynamics, as it does not neatly fit into the same schema we used for the other methods. Immediately, we can see that the separation between the methods (i.e. down the columns) is larger than the separation between the pathways (i.e. along the rows). This contrasts strongly with the x-ray scattering data.

The first column shows the TRPES predictions for the NBD-forming channel of the dynamics. The NBD-forming channel is coherent for all ensembles, with one path leading to a strong oscillation in ground state NBD (at $\approx$ 8 eV, $\approx$ 60 fs). The final oscillation is somewhat obscured

in the difference signal in Fig. 7.7, as it occurs at the ground state bleach energy — hardly surprising, as both signals arise from ground state NBD.

The QC-forming pathway (centre column, Fig. 7.11) shows a bit more structure. For the XMS-CASPT2(2,2), there is only one coherent channel, which forms ground state QC very rapidly upon photo-excitation (see Chapter 2). This gives a single, relatively clean channel with little spread. For the other two methods, there are two separate decays (as shown in Fig. 6.7), and we see some evidence of multiple features after passage through the intersection ($\approx$ 40 fs). We also notice that the binding energy on the ground state is marginally lower that the NBD-ending trajectories, in line with the lower ionisation potential in QC. This signal appears above the ground state bleach as visible in the combined XMS-CASPT2(2,2) data (e.g. the top right panel of Fig. 7.7). Therefore, a useful marker for QC formation *from* NBD dynamics would be a notable signal above the ground state bleach.

Finally, the ES trajectories (right column, Fig. 7.11) show most of their signal at 6 eV or lower binding energies, notably higher than the corresponding QC and NBD channels. While some trajectories have larger binding energies, these are likely either exploring a particularly odd part of the potential, or have a particularly strong $S_1 \rightarrow D_1$ absorption.

7.5 — Conclusions

Predictions of experimental x-ray scattering and time-resolved photo-electron spectroscopy signals are presented using the four sets of dynamics shown in Chapter 6. The results are analysed extensively, splitting the predicted signals into their contributing components, and features in the signals are related to the underlying dynamics.

The x-ray scattering clearly contains structural information, can delineate between the individual reaction channels, and could even be used to experimentally measure quantum yields. However, it is difficult to distinguish between the different sets of dynamics, indicating a lack of sensitivity to subtly different reaction channels. The x-ray scattering is also not particularly sensitive to the time-scale of the reaction, with all methods predicting relatively similar initial signals despite the high time-resolution used ($\Delta t \approx 7$ fs). These conclusions will almost certainly be system-dependent, and this system, with relatively subtle geometry change compared to others,[132,244,245] does not show particularly large changes in the signal.

We have investigated the presence of purely electronic signals by comparing ab initio scattering patterns for the CASSCF(2,2) trajectories. This shows small deviations compared to the independent atom model ($\approx$ 2%, $\approx$ 10% of the signal variation), again confirming the utility of the IAM approximation. Further, the purely electronic component of the scattering signal, found by subtrhcting the signal for the active state from the ground state, was shown to be small ($\approx$ 0.5%, $\approx$ 3% of the signal variation) and mostly present at early times. Therefore, determining which electronic state is populated is difficult in x-ray scattering, and likely only possible through secondary attributes like significant changes in the dynamics. While these results are clear, they are far from absolute, and certainly an area for further exploration.

It is difficult to extract any vibrational information for time-resolved photo-electron spectra. As we only have one variable that significantly changes (binding energy) through the dynamics, the signals from different nuclear geometries overlap, making their discrimination difficult. TRPES may be able to provide some guidance into the ground-state product ratios, but that is only true when the products have substantially different ionisation potentials and the signal is present above the ground-state bleach. We also comment here that, despite the ability to potentially measure quantum yields, the true ratios are also hidden behind the photo-ionisation cross-sections, the determination of which can be complex.

That being said, time-resolved photo-electron spectra are very sensitive to electronic information. The lowering in energy of the wavepacket is apparent from all plotted spectra, which leads to easy parsing of the time-scale of the decay. One can even estimate the passage through the intersection by the crossing of the $S_1 \rightarrow D_0$ and $S_1 \rightarrow D_1$ features.

This chapter mainly constitutes a qualitative study, attempting to find critical features which distinguish different scattering patterns and spectra. Further work using higher-quality calculations for the observables, in particular for the photoelectron spectra, could provide a more quantitative analysis. For scattering, the path forward is simple, with the use of ab initio scattering giving essentially perfect results and allowing extension to electron scattering. Time-resolved photo-electron spectroscopy, however, requires treatment of the departing electron, which is non-trivial. While a range of different methods are available, the calculation using R-matrix theory,[173,174] would certainly lead to an acceptable benchmark. This work also did not touch on photo-electron angular distributions, which could plausibly be used to distinguish the individual ionisation channels, further validating the models shown.

This work implies that ultrafast photo-electron spectroscopy constitutes a promising avenue to challenge the predictions in this thesis experimentally. The overall time-resolution should ideally be close to $\approx$ 10 fs, with a pump exciting at $\approx$ 5.25 eV. Using a probe with comparatively low energy, $\approx$ 6 eV, we could likely monitor the nonradiative decay process through the crossing of the $S_0 \rightarrow D_0$ and $S_0 \rightarrow D_1$ features. but a higher-energy probe, $>$ 8 eV, would allow direct measurement of ground state dynamics, potentially confirming the formation of QC. Such experiments would be challenging, but rapid advances in new light-generation technologies, such as hollow-core fibres, bring hope that they are achievable.[137,246]

A different avenue for the experimental exploration of this system would be x-ray scattering. In this case, the absolute time-resolution is not as important, as the scattering patterns did not show great sensitivity to the decay lifetime. However, the notably different signals of the NBD and QC decay pathways might be able to definitively state the branching ratio, indirectly lending credence to a specific channel in the dynamics. These last two suggestions neatly summarise the clear conclusion of this chapter. On its own, each experiment is insufficient. Only in their combination, with a healthy dose of theoretical guidance, can we begin to understand the dynamics.

— 8 —

Dynamics of Quadricyclane

In Chapter 6, we calculated and compared the dynamics of NBD with four electronic structure theories. This explored the differences in dynamics arising from subtle changes in the potential energy surfaces while keeping the initial conditions constant. In this chapter, we do the opposite — we hold the potential energy surface constant while changing the starting point of the dynamics. This gives an alternative view, allowing us to understand which features are inherent to the potentials and which are dependent on the initial conditions.

For this, we use the other isomer as a starting point, simulating the photo-excited dynamics of QC. For clarity, we shall denote these as the QC-initiated dynamics, with the work of Chapter 6 denoted as the NBD-initiated dynamics. We use our simplest model of the potentials, the CASSCF(2,2) method. We limit the study to this electronic structure model as it exhibits reasonable dynamics, as discussed in Chapter 6, and as there is a lack of suitable alternatives; XMS-CASPT2(2,2), as shown in Chapter 6, does not show qualitatively correct dynamics and XMS-CASPT2(4,4) does not converge around the QC isomer, rendering the dynamics unusable.

For QC, this electronic structure model is less closely matched to experiments than in NBD. Excitation into the valence state of QC happens much closer to the Rydberg manifold — see the two following chapters – and thus, dynamics would consist of significant coupling to these states. This is discussed more in Appendix B.1 and Chapter 10.

In addition to investigating the photochemistry of QC, this chapter aims to use the different dynamics in QC to help understand and contextualise the observations in NBD. In particular, the system's dynamics around and before the conical intersection, and how the physical observables (e.g. quantum yields) change around this critical juncture. Aside from being of purely theoretical interest, understanding what affects the quantum yields of this system has potential uses in the engineering of this system for increased efficiency in applications.

To do this, we effectively retrace our steps, selecting a suitable set of initial conditions and performing surface hopping simulations, keeping all parameters identical. As the two molecules (and their dynamics) are very similar, we can reuse almost all the machinery used in the previous analyses. For the comparisons to be as vivid as possible, we will use equivalent figures as those used in Chapter 6 (and refer to the corresponding figure in the caption).

8.1 — Computational Details

All electronic structure calculations were performed using the Molpro 2022.2 package[212], using SA(3)-CASSCF(2,2) with the p-cc-(p)VDZ basis (described in Chapter 5). Density fitting was used with the aug-cc-pVDZ-JKFIT basis. The electronic structure was state-averaged over three singlet states. Further details are shown in Chapter 5.

Dynamics calculations were performed with an in-house code, performing Tully's fewest switches surface hopping.[62] The calculations were performed using all three states optimised in the electronic structure. The energy-based decoherence correction[88] was applied (using

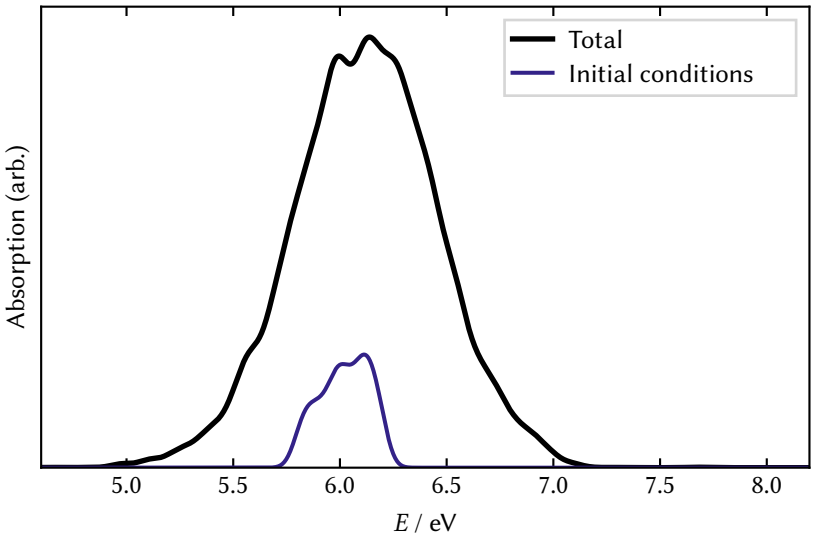

Figure 8.1: Wigner-sampled absorption spectrum for valence-only model of QC. The total spectrum (thick black line) is calculated from 10000 Wigner points broadened by a 0.1 eV Gaussian, with the contribution to the spectrum from the initial conditions of the dynamics shown in indigo. Equivalent to Fig. 6.4 for NBD.

$C = 0.1$ E_h), scaling the coefficients (not the populations). The electronic propagation was performed with a matrix-exponential propagator with a time-step of 0.25 a.u. ($\approx$ 0.006 fs), using the non-adiabatic coupling vector to calculate the time-derivative couplings. The nuclear propagation was performed with a velocity-Verlet integrator, with a time-step of 5 a.u ($\approx$ 0.12 fs). The propagation was performed until 8000 a.u ($\approx$ 193 fs). Energy re-scaling was performed along the non-adiabatic coupling vector, with no reflection for frustrated hops. For brevity, we have not discussed all of the parameters as they exactly match the CASSCF(2,2) dynamics performed in Chapter 6, with the propagation performed with identical versions of the surface hopping and electronic structure codes. In total, 453 trajectories were propagated, all initiated on the S_1 surface. 90% of trajectories conserved total energy to within 0.01 eV on the excited state, increasing to 97% at 0.1 eV., as shown in Fig. B.12. This was worse than the NBD dynamics (cf. Chapter 6), likely due to the longer propagation and slightly different dynamics. An example trajectory is shown in Fig. B.16.

8.2 — Results

Initial Conditions

Matching the method used in the NBD-initiated dynamics, we utilise a Wigner-sampling method to select initial conditions, as described in Section 2.4, showing the simulated spectrum in Fig. 8.1 alongside the contribution to the full spectrum from the initial conditions used in the dynamics. The overall shape of the spectrum is relatively simple, with a single broad peak centred at $\approx$ 6.2 eV, the vertical excitation energy. In concord with the NBD-initiated dynamics, we use a $[5.8, 6.2]$ eV (top-hat) excitation window, giving the same estimated time-uncertainty of $\Delta t_{\text{pu}} \approx 6.71$ fs, and all conditions selected are on S_1. It is worth mentioning that the QC ground state is approximately 1 eV higher than the NBD ground state, leading to the trajectories having a higher total energy.

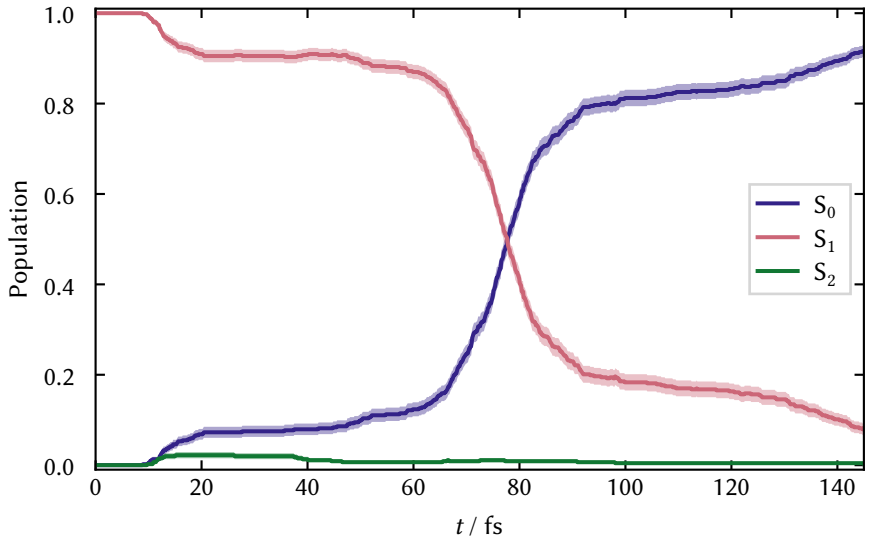

Figure 8.2: Adiabatic state populations for the QC-initiated surface-hopping dynamics. The dynamics occurs primarily on the ground and first excited states, with the second excited state showing minimal population. The dynamics shows an early decay, at ≈ 10 fs, but the largest decay happens at ≈ 80 fs, with 80% of the population having transferred by 100 fs. Equivalent to Fig. 6.5 for NBD.

Secondly, the excitation window is slightly below the vertical excitation energy of 6.22 eV, contrasting with NBD, where we centred the excitation around the vertical excitation energy (at 5.96 eV, see Table 5.1). This preferentially chooses initial conditions further down the well, perhaps marginally speeding up the dynamics. Out of the 10000 initial Wigner-sampled points, 453 were selected as initial conditions for the dynamics.

Population and Reaction Channels

In Fig. 8.2, we show the bootstrapped population and errors for each of the three states of QC. Immediately, we can notice that QC has a much longer excited-state lifetime than NBD (cf. Fig. 6.5), with the majority of the decay onto the ground state happening at 80 fs, much later than the 40 fs decay of NBD. Apart from that, there are some similarities, with a small initial rise of ground state population, followed by a notably coherent principal decay and a very low S_2 population. Unlike in NBD, there is a significant delay between the first and second rises.

In the NBD-initiated dynamics, we defined three separate reaction channels: NBD-ending, QC-ending, and excited-state. We can reuse these definitions with only minor tweaks for the QC-initiated dynamics.

Firstly, we define the *excited-state* (ES) trajectories. These were defined in the NBD-initiated case as trajectories that have not decayed to the ground state after the bulk of the decay. Here, we only need to change the time used to separate the trajectories — we use 4150 a.u. (≈ 100 fs). The other two channels, NBD-ending and QC-ending, are defined almost identically as in the NBD-initiated case, with those with end geometries with $r_{cc} > 2$ Å being classified as NBD-ending and those with $r_{cc} < 2$ Å as QC-ending. Unlike previously, the definition of the 'reactive' channel in the QC-initiated dynamics changes to the NBD-ending channel, as this channel involves a change in isomer.

The one difference we find is the presence of some trajectories that do not visit the rhombic S_1/S_0 CI, instead breaking one or more of the C_1C_5 (or the equivalent C_2C_5, C_3C_6, or C_4C_6)

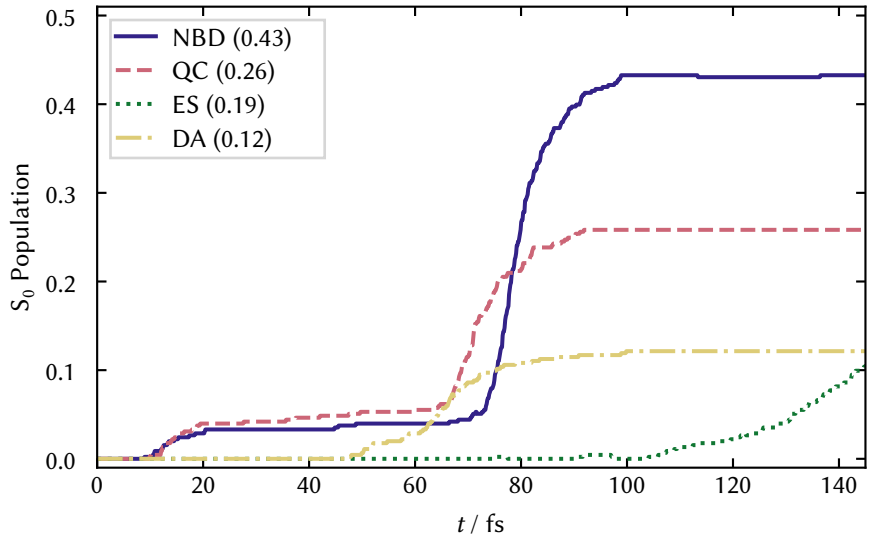

Figure 8.3: S_0 population for each of the three reaction channels for dynamics of QC-initiated dynamics. The very early dynamics ($\approx$ 10 fs) is split between the QC-ending (rose dashed lines) and NBD-ending channels (indigo solid), but most of their decay occurs later, at $\approx$ 80 fs. Later, DA trajectories (yellow dash-dot) show a notable rise just before the main rise of the other channels, while the ES trajectories (green dashed) show little decay to S_0. Equivalent to Fig. 6.7 for NBD-initiated dynamics.

bonds before reaching the ground state. The final stage of this reaction would be the full retro-Diels–Alder reaction,[247] shown in Fig. 8.4, removing one of the ethylenic wings to form 1,3-cyclopentadiene and acetylene. We will understand why these reactions occur in the next section, but the active space has not been tested in describing this process, so we do not trust the dynamics to be unbiased. As such, we remove them from our analysis when we compare the QC trajectories to the NBD trajectories, as this pathway is absent. These trajectories, which we call the 'DA' (Diels–Alder) pathway, form about 12% of the total number of trajectories and are identified by having a $S_1 \rightarrow S_0$ crossing geometry with $r_{cc} > 2.3$ Å, confirming this value with a manual analysis.

In Fig. 8.3, we show the channel-separated populations. Immediately, we notice the very fast ($\approx$ 10 fs) initial decay contains both NBD- and QC-ending trajectories. When we reach the principal coupling region, the QC-ending trajectories show a smooth rise to their asymptotic value of 0.26, the quantum yield for this pathway. In contrast, the NBD-ending trajectories

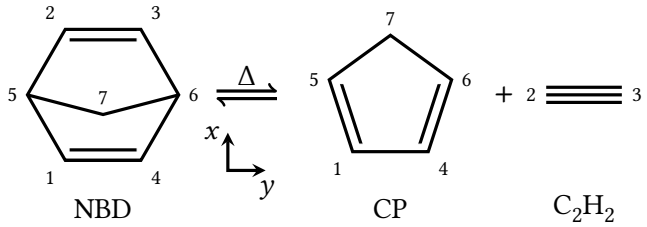

Figure 8.4: Formation of 1,3-cyclopentadiene (CP) and acetylene (C_2H_2) from NBD, via a [4+2] cyclo-addition. This reaction, which occurs after the excitation of QC, is denoted the 'Diels–Alder' channel. It proceeds either with C_2C_5- and C_3C_6-cleavage (as here) or C_1C_5- and C_5C_6-cleavage.

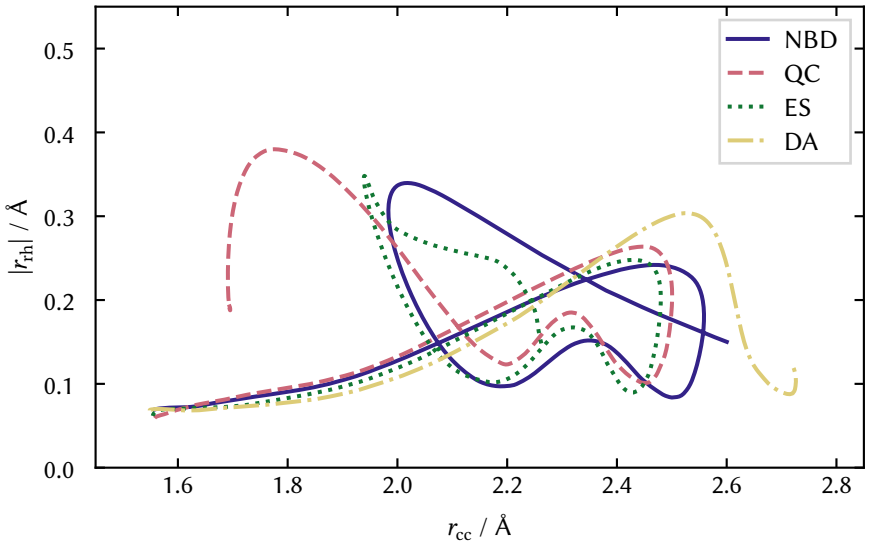

Figure 8.5: Average trajectories in the $(r_{cc}, |r_{rh}|)$-plane for QC-initiated dynamics, separated by reaction channels. We stress these averages should only be used as qualitative reaction paths. The trajectories all initially form excited NBD (at $(r_{cc}, |r_{rh}|) \approx (2.5, 0.1)$ Å), then returning through the S_1/S_0 conical intersection, where they diverge. Notably, the pathways all oscillate around the centre of the potential ($r_{rh} \approx 0.1$ Å). We show the DA channel (yellow dash-dot lines) until r_{cc} and r_{rh} are no longer good coordinates to represent these trajectories. Loosely equivalent to Fig. 6.8.

have a slower but more significant decay, with a final quantum yield of 0.43. By definition, the ES trajectories are much slower, with the decay not being complete by the end of the figure at 150 fs. Finally, the Diels–Alder trajectories decay quite early, which we shall show to be due to significant differences in the dynamics (vide infra).

It is notable here that the ratio of NBD- and QC-ending trajectories is quite different to those found in the NBD-initiated dynamics, with a branching ratio of NBD:QC = 1.65, compared to the value of NBD:QC = 2.73 in the NBD-initiated dynamics. Even if one ignores the initial very fast (≈ 10 fs) decay, the ratio is around NBD:QC ≈ 2, well below the value of the NBD-initiated dynamics.

Geometry Analysis

In the QC-initiated dynamics, 'spaghetti plots', akin to Fig. 6.8, are difficult to read, as the dynamics visits the same points in the (r_{cc}, r_{rh})-plane multiple times. As such, we show idealised 'average trajectories', calculated as

$$\bar{r}(t) = \frac{1}{N_{tr}} \sum_{u}^{N_{tr}} r_u(t), \tag{8.1}$$

where r_u indicates the value for trajectory u of the coordinate we are using, here r_{cc} or $|r_{rh}|$, using the absolute value of r_{rh} to avoid the cancellation of the positive and negative branches. This does cause the trajectories to be artefactually displaced from the $r_{rh} = 0$ line, the average when no absolute value is used. We note that averaged trajectories are only meaningful within a coherent pathway; thankfully, that is the case here.

In Fig. 8.5, showing the average trajectories in the $(r_{cc}, |r_{rh}|)$-plane for the QC-initiated dynamics, we see that the initial section of the dynamics is the same for all reaction channels,

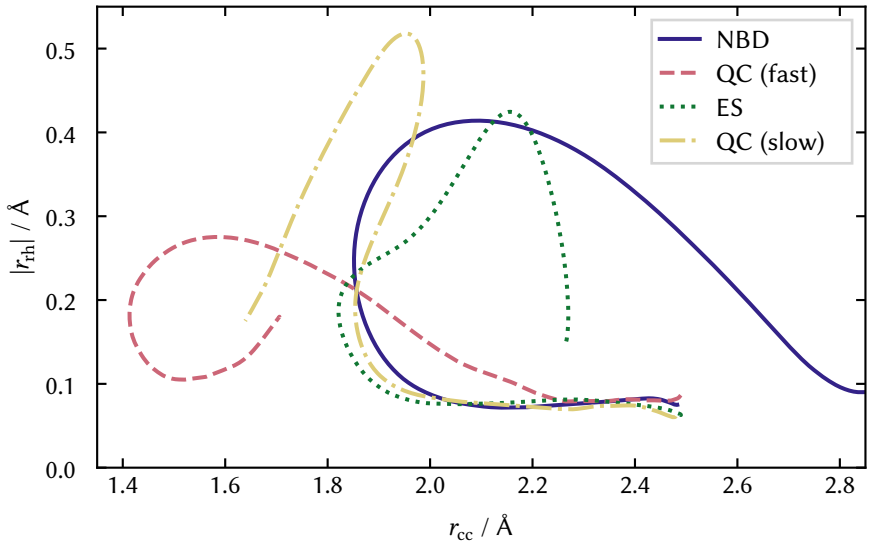

Figure 8.6: Average trajectories in the $(r_{cc}, |r_{rh}|)$-plane for NBD-initiated dynamics, split into separate reaction channels. Dynamics calculated with CASSCF(2,2) (see Chapter 6). Here, we have further split the QC-ending trajectories into a fast (rose dashed lines) and slow (yellow dash-dot) set, corresponding to the two rises in Fig. 6.7, upper panel. All channels, except the QC (fast) channel, first move symmetrically along the $r_{rh} \approx 0.1$ Å line, turning around before hitting the conical intersection and splitting. The NBD-ending trajectories (indigo solid) head back to the initial geometry, the NBD ground state minimum, while the NBD-ending (slow) trajectories move to the QC minimum. The ES trajectories (green dotted) oscillate around the centre of the potentials. Data taken by averaging over Fig. 6.8.

with the average trajectory smoothly moving away from the initial point at $(r_{cc}, |r_{rh}|) \approx (1.5, 0.1)$ Å, quickly reaching $(r_{cc}, |r_{rh}|) \approx (2.5, 0.25)$ Å and transiently forming NBD (albeit rhombically distorted) on the excited state *after* exciting QC.

After, the Diels–Alder trajectories overshoot the NBD structure, with the momentum in the wing separation coordinate sufficient to break one of the bonds connecting the wings (any of the C_1C_5 equivalent bonds). At this point, the efficacy of the electronic structure method has not been tested, so we do not show the rest of the pathway *and* remove them from the rest of the dynamics. Because of this, we can no longer be confident in our predictions for the ensemble as a whole, but we can still be confident in the other trajectories and the relative ratios between them.

The three other groups of trajectories (NBD, QC, and ES) all turn back, moving to lower $|r_{rh}|$ and then quickly oscillating.[i] This again shows the importance of the local minima on the S_1 excited state, located at $(r_{cc}, r_{rh}) \approx (2.1, 0)$ Å, which pulls the trajectories back towards $r_{cc} = 0$, keeping them close to the centre of the potentials.

The three average trajectories then move towards the S_1/S_0 conical intersection (at $(r_{cc}, r_{rh}) \approx (1.9, 0.4)$ Å). Here, the QC-ending trajectories hop to the ground state, maintaining their velocity towards negative r_{cc}, quickly turning to head to the minimum whence they came. The NBD-ending trajectories, on the other hand, turn and head to the NBD ground state minimum (at $(r_{cc}, |r_{rh}|) \approx (2.5, 0)$ Å). The ES trajectories fall somewhere in the middle, oscillating around the middle of the potential energy surfaces on the excited state.

[i] The dynamics cross the $r_{cc} = 0$ line in the data without the absolute value.

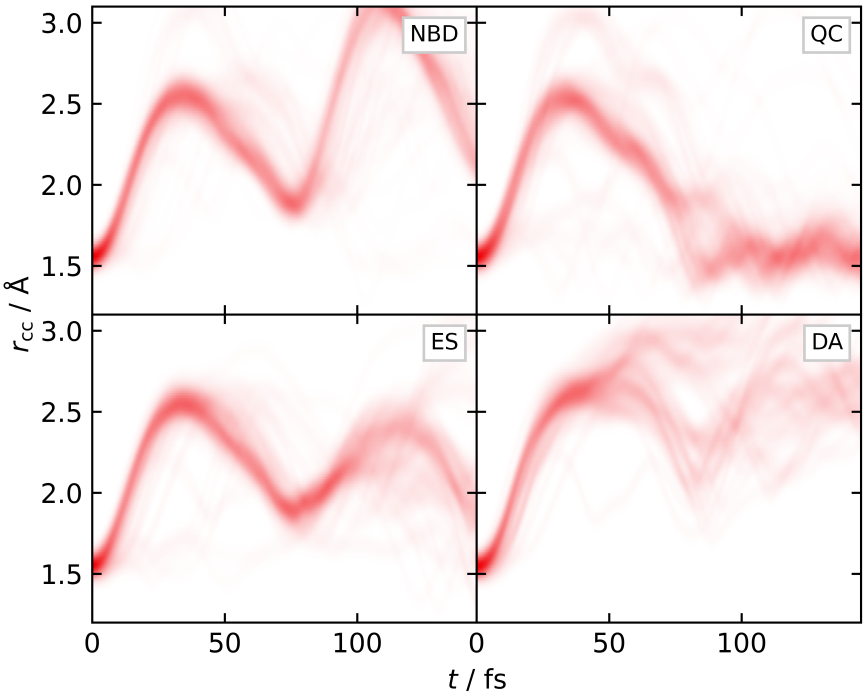

Figure 8.7: r_{cc} heat-map for the QC-initiated dynamics, separated into the reaction channels. All start similarly, extending r_{cc} to 2.5 Å. After this, the NBD-ending (top left), QC-ending (top right), and ES (bottom left) trajectories decrease r_{cc}, reaching the conical intersection at $\approx$ 80 fs and diverging. The Diels–Alder trajectories (bottom right) split at the maximum of r_{cc}, indicating vastly different dynamics.

For contrast, we also show the average trajectories for the CASSCF(2,2) NBD-initiated dynamics in Fig. 8.6, again split into the three different trajectory pathways. We have further split the QC trajectories into a 'fast' and 'slow' branch, according to whether they were part of the first or second decays in Fig. 6.5. We can see that the trajectories have much less excitation in the r_{rh} coordinate before reaching the conical intersection, allowing them to approach the intersection (at $(r_{cc}, r_{rh}) \approx (1.9, 0.4)$ Å) with increasing r_{cc}. After this, the NBD-ending and the QC-ending (slow) trajectories soon return to their respective ground state minima, while the ES trajectories oscillate around the excited state. Finally, we can see the QC (fast) trajectories, which do not turn around at all, quickly crossing over and heading straight to the ground state.

To get a complete picture of all of the dynamics, in Figs. 8.7 and 8.8, we show 'heat maps', which plot the density of the trajectories in one coordinate as a function of time. For r_{cc} (Fig. 8.7), the dynamics is initially somewhat reminiscent of the dynamics of NBD, with a fast, coherent motion in the r_{cc} coordinate. Unlike in NBD, the QC trajectories start by lengthening this coordinate, eventually reaching a maximum value of $r_{cc} = 2.5$ Å. As before, the Diels–Alder trajectories (bottom right) overshoot NBD, and we do not consider them further. For the three other channels (NBD, QC, and ES), the dynamics hereon is very similar to the NBD dynamics; the trajectories swiftly move from $r_{cc} = 2.5$ Å to the conical intersection at $t \approx 80$ fs and $r_{cc} \approx 2$ Å, where they separate into three distinct groups: the NBD-ending trajectories transition to the ground state and turn sharply upwards, reacting to form ground state NBD. The QC-ending trajectories decay to the ground state and continue their momentum through the intersection,

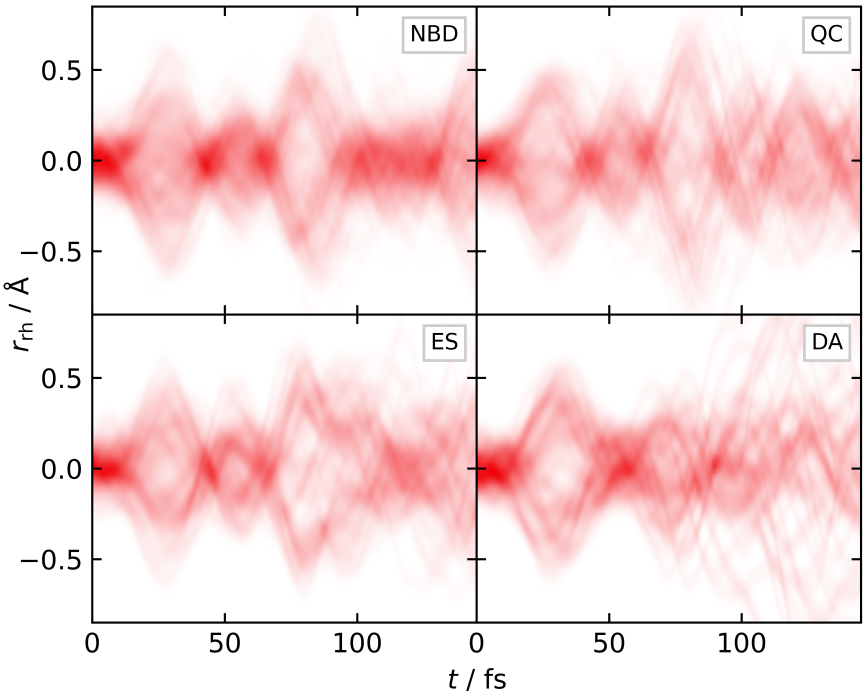

Figure 8.8: r_{rh} heat-map for the QC-initiated dynamics. Again, all trajectories start similarly, with r_{rh} increasing in magnitude at ≈ 40 fs. After that, the trajectories re-converge, crossing the $r_{rh} = 0$ line twice before reaching the conical intersection at ≈ 80 fs. The Diels–Alder trajectories (bottom right) do not return to the $r_{rh} = 0$ ground state minima.

returning to their starting point of QC, and the ES trajectories continue oscillating around the centre of the coordinate.

Moving on to the r_{rh} coordinate, we can see a similar picture, with the NBD, QC and ES trajectories all showing very similar dynamics until the crossing point of 80 fs. Here, we see three distinct wobbles as the trajectories separate along the r_{rh} axis, aligning nicely with our understanding from the average trajectories, before hitting the conical intersection. Overall, this paints a very similar picture to the dynamics starting in NBD, except for the initial dynamics moving from QC to NBD (or rather, a rhombically distorted excited state version of NBD).

At this point, we can see that the Diels–Alder trajectories are substantively different from the others in the ensemble (and the NBD-initiated dynamics). As we both do not trust the dynamics after this point (due to not designing the electronic structure to deal with these processes) and the fact that the investigation of the QC dynamics is to contextualise the NBD dynamics, we will no longer include the Diels–Alder pathway in our analyses.

Velocity at Points of Crossing

In Fig. 8.9, we show the velocities in the (r_{cc}, r_{db})-plane, mirroring . The velocities are depicted as a vector (with the x-axis as $\dot{r}_{cc}$ and the y-axis as $\dot{r}_{db}$) centred at the time and the value of r_{db} at the $S_1 \rightarrow S_0$ crossing. As before, we include the velocities required to form NBD and QC from the S_1/S_0 CI in black. We first notice a strong group of trajectories at very early times, corresponding to the initial decay seen in Fig. 8.2. All trajectories show some degree of non-adiabatic coupling in this region, as seen in the example trajectory in Fig. B.16. As

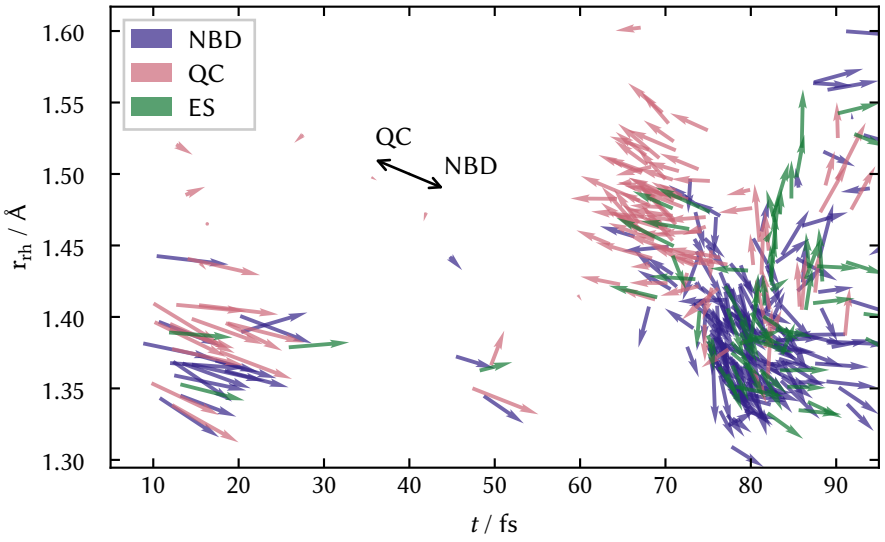

Figure 8.9: Velocities at crossing points for QC-initiated dynamics. The vectors represent the velocities in the (r_{cc}, r_{db})-plane (i.e. the x-component equals $\dot{r}_{cc}$ and the y-component $\dot{r}_{db}$), with the base the time and value of r_{db} at crossing. Points of closest separation (within the first 100 fs) are shown for the ES trajectories. For clarity, the displacement from the S_1/S_0 CI to NBD and QC is shown as the black arrow. An initial grouping of trajectories shows an exceptionally fast decay, but most trajectories decay at $\approx$ 80 fs, with northwest-pointing vectors leading to QC formation and southeast-pointing vectors to NBD formation. Equivalent to Fig. 6.10 for NBD.

the wavefunction moves from QC to NBD on the S_1 surface, the character of the ground state changes from $|2020\rangle$ to $|2200\rangle$ (cf. Table 5.1), swapping with the S_2 state. As such, these two states both move close in energy to the S_1 state (e.g. in Fig. B.16). Coupling can therefore occur between S_1 and either of these states, and is strongest when the system is far from the symmetrical C_{2v} geometries. The trajectories favour hopping to S_0, both as the upwards population transfer is small and the few hops seen are often frustrated.[ii]

In the main bulk of the decay (at around 80 fs), we notice a similar pattern to that seen in the NBD dynamics, with the QC-ending trajectories (rose arrows) all showing $\dot{r}_{cc} < 0$ and $\dot{r}_{db} > 0$ (i.e. velocity towards QC) and all NBD-ending trajectories showing $\dot{r}_{cc} > 0$ and $\dot{r}_{db} < 0$ (i.e. velocity towards NBD). This, in addition to the results in the mean trajectories, lets us begin to understand why the observed branching ratio of NBD:QC is lower in the QC-initiated dynamics than in the NBD-initiated dynamics. The pre-conical intersection dynamics in the QC-initiated dynamics aligns the trajectories with negative $\dot{r}_{cc}$ (i.e. moving towards QC). In the NBD-initiated dynamics, the motion is quite different, with the trajectories aligned to have positive $\dot{r}_{cc}$ (i.e. moving towards NBD). This observation confirms the result of the NBD-initiated dynamics, showing that the dynamics before the conical intersection (and thus velocity near it) is the crucial variable for the outcome of the dynamics of this molecule.

As for what causes the separation between the QC-ending and NBD-ending trajectories, we can see in Fig. 8.9 that the NBD-ending trajectories both have much stronger negative $\dot{r}_{db}$ and decay slightly later. We postulate that the somewhat later crossing time affords one more

[ii] This can be understood by considering the S_2/S_1 CI branching plane vectors, shown in Fig. B.8. The initial velocity is toward NBD, i.e. approximately along negative Y, the gradient difference, and has little component along X, the non-adiabatic coupling. Therefore, the projection of the velocity along the coupling is low, giving little transfer *and* frustrated hops (cf. Fig. 2.5).

half-oscillation in the r_{db} coordinate, as well as more time to be reflected off the large potential wall on the excited state (see e.g. Fig. 5.11, where the low-r_{cc} side of the conical intersection is steeply repulsive). Both factors align the velocity towards NBD.

Finally, we return to the trajectories that decay very early ($\approx$ 10 fs). These trajectories all decay to the ground state with very strong positive velocity in the $\dot{r}_{cc}$ direction (i.e. towards NBD) but are split roughly equally between QC-ending and NBD-ending. Manual analysis shows that all of these trajectories visit the NBD isomer on the ground state, confirming our statement that the velocity at hopping is the critical factor in which ground state isomer is formed. However, roughly half of the trajectories rebound off the ground state potential well with enough momentum to crest the barrier, reforming ground state QC. Therefore, all of the trajectories in the early dynamics do form NBD, as predicted by the positive $\dot{r}_{cc}$, but it is the ground state dynamics which reforms QC.

8.3 — Conclusions

Dynamics simulations of photo-excited QC were performed using parameters identical to the simulations of NBD. The two ensembles showed clear similarities, with the QC-initiated dynamics even transiently forming NBD before reaching the intersection. Apart from approximately a tenth of the trajectories, which undergo a separate retro-Diels–Alder reaction, similar pathways to those in the NBD-initiated dynamics are seen, with two coherent decay channels forming NBD and QC and one slower channel which remains on the excited state. The dynamics proceeds through the same S_1/S_0 conical intersection, which has a notably rhombic geometry, but the overall decay to the ground state is slower than in the NBD-initiated dynamics, with an excited state lifetime of around 80 fs. Again, very little S_2 population was seen.

The relative ratio of NBD to QC formation is lower than that seen in the NBD-initiated dynamics, explained by the dynamics before reaching the conical intersection. In the NBD-initiated dynamics, the trajectories approach the intersection with increasing r_{cc}, leading to a far higher proportion of NBD formation (NBD:QC = 2.73). Conversely, the QC-initiated dynamics have much more excitation in the r_{rh} coordinate, leading to an approach to the intersection with decreasing r_{cc} and a lower proportion of NBD (NBD:QC $\approx$ 2, removing the very fast trajectories). As the two dynamics were performed on identical surfaces, it is clear that the nature of the approach is the defining feature of dynamics in this system, rather than the local topography of the intersection, confirming the results of Chapter 6.

A few trajectories revealed an alternative decay channel involving very rapid coupling ($\approx$ 10 fs) and a highly coherent decay directly to ground-state NBD. Enhancing this pathway, likely by forcing the molecule to break the symmetry earlier, could have practical applications for photoswitch systems, providing a potentially efficient and coherent conversion pathway. However, one would also need to suppress the vibrational NBD→QC ground state conversion, affecting roughly half of the trajectories, to make this approach viable.

Overall, this dynamics provides an intriguing contrast to the dynamics presented in Chapter 6, highlighting the sensitivity of dynamics to their initial conditions, especially in this coherent, non-ergodic limit. Unfortunately, this particular dynamics is challenging to isolate experimentally, as we have deliberately not included Rydberg states, which would affect the absorption process. We showcase a combined experimental/theoretical study of this system in Chapter 10.

— III —

Norbornadiene & Quadricyclane: Experiments

— 9 —

Absorption Spectra

This chapter covers the vibrationally resolved absorption and photo-electron spectra of NBD and QC. A set of high-resolution absorption spectra were taken at the SOLEIL synchrotron using Fourier transform spectroscopy. We concentrate on the low-energy, dynamically important, spectroscopically bright states of NBD and QC. This leaves out the notable exception of the low-lying valence state of NBD, which was the topic of the previous sections, as it has low oscillator strength and does not show any vibrational structure. For brevity, we have not covered the theory used in this work in this thesis, namely Franck–Condon calculations[175,176,248] and the MP2[127,249] and ADC(2)[180,250] methods, but they are well covered elsewhere.

This work was taken with only minor changes from J. C. Cooper, D. M. P. Holland et al., *J. Chem. Phys*, **160**, 064305 (2024)[2], with the permission of AIP publishing. The work represented here is shortened to the most pertinent results, generally of the low-energy regions of the absorption and photo-electron spectra. More depth can be found in Cooper et al..[2]

The calculations were all performed by the author of this work, whereas the joint interpretation of experimental data with theoretical calculations was conducted in collaboration with David Holland and Mike Ashfold. As I did not contribute to the experimental data collection, I shall include a brief description here.

The data were captured at the DESIRS beamline[251] at the SOLEIL synchrotron (Paris, France), using the Fourier-transform spectrometer[252]. This calculates the absorption spectrum by forming an interferogram between two optical paths of different lengths. The interferogram is then Fourier-transformed to retrieve the absorption spectrum, which we shall refer to as an FTS. Prior to being measured, the photon beam passes through a low-pressure vapour cell containing gaseous QC or NBD. The NBD data was taken without significant contamination, while the QC data had a small contamination of NBD from the synthesis. The NBD absorption is significantly larger than QC, and so this contamination had a relatively large effect on the raw data. To rectify this, the NBD data (multiplied by a small constant) was subtracted from the QC data until there was no presence of peaks attributable to NBD.

9.1 — Computational Details

Calculations were undertaken with the algebraic diagrammatic construction (second order) (ADC(2)) and the Møller-Plesset perturbation theory (second order) (MP2) methods. These related methods afford a consistent description of the ground and excited electronic states and a balanced description of valence and Rydberg excited states in a single-reference manner. The ADC(2), MP2 and CC2 calculations were performed using the `ricc2`[250] program in the TURBOMOLE 7.5 package,[253] using the resolution-of-the-identity (RI) technique, to obtain vertical transition energies and oscillator strengths. All ion calculations were performed using unrestricted Hartree-Fock as a reference. All optimisations/frequency (wavenumber) calculations used the aug-cc-pVQZ basis,[195] which was found to agree well with the larger d-

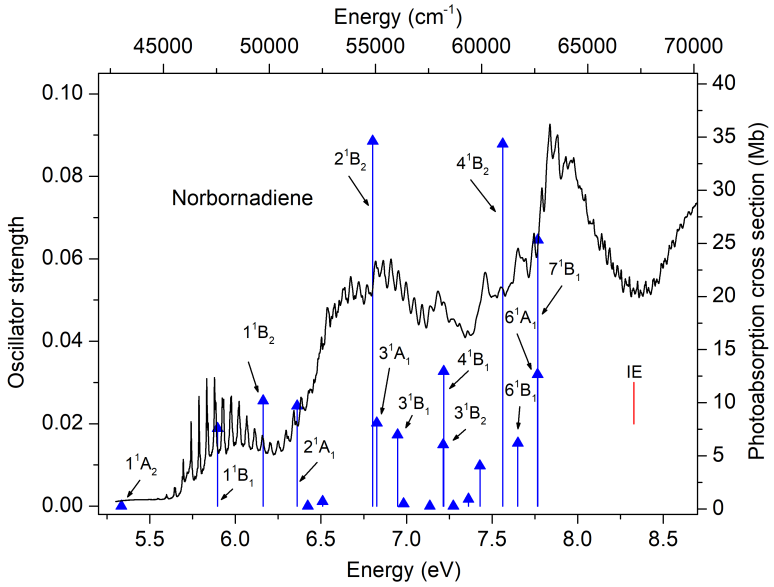

Figure 9.1: NBD vertical excitations. The experimental spectrum is shown as the black line for the measured region, with vibronic structure seen across the entirety of the spectrum. Vertical transitions (ADC(2)/aug-cc-pVQZ, Table 9.1) are shown as blue arrows, with the height defined by the oscillator strength (arrow tip not included). The first ionisation continuum is marked with the red line. Reproduced from Cooper et al., *J. Chem. Phys*, **160**, 064305 (2024), with the permission of AIP Publishing.

aug-cc-pV5Z basis and basis set extrapolated values. Benchmark calculations were performed with MS-CASPT2 and LR-CCSD, both of which gave similar results to those reported here.[2] All optimised geometries gave predominantly single-configurational ground states, generating good Hartree-Fock references for the response theory calculations. The present calculations were performed without explicit symmetry, except for the 1^1B_2 valence state of NBD, which has a C_{2v} 1st-order saddle-point geometry very close to the NBD ground state minimum. We conjecture that this saddle-point has a sufficiently long lifetime to support a few vibrational oscillations in the photoexcited molecule, giving some lifetime-broadened vibrational structure (as reported by Robin and Kuebler[254]). The imaginary frequency of this saddle-point breaks either the C_5C_7 or the C_6C_7 bond and leads to formation of a toluene-like intermediate with significant planarisation of the six-membered ring, significantly separated from the ground state NBD minimum. In order to run Franck-Condon calculations on this state, the mode was forced to be real and positive (i.e. the saddle point was assumed to be a minimum in all modes).

The excitation characters of the various vertical transitions were determined using natural transition orbitals (NTOs)[255–258] calculated using the TheoDORE package.[259] NTOs represent separable particle and hole orbital pairs, with their relative weights showing the contribution each particle/hole pair makes to any given transition. Typically, therefore, transitions with mixed character will be carried by several NTO pairs, whereas pure transitions tend towards one pair with unit weight. We will denote the orbitals using a symmetry label. For clarity, we shall use lower-case symmetry labels for valence orbitals (shown in Fig. B.1), descriptive names for Rydberg orbitals (e.g. $3p_x$), and upper-case symmetry labels for electronic states. In this work, we do not show images of the Rydberg orbitals as they are typical examples, but full details, including NTO plots, can be found in Cooper et al..[2]

Table 9.1: Calculated first ten excitations and oscillator strengths from the NBD ground state. Calculations performed with ADC(2)/aug-cc-pVQZ. Vertical excitation energies (VEEs) are given in eV. With each electronic state, the weights of individual excitations, calculated using natural transition orbitals (NTOs), are shown, along with the character of the electronic transition. NBD shows primarily Rydberg states, intermixed with some valence transitions (notably 1^1A_2 S_1 and 1^1B_2 S_3.

State				Excitation 1			Excitation 2		
Sym.	Adia.	ΔE_{vert}	Osc. Str	Hole	Particle	Cont.	Hole	Particle	Cont.
1^1A_2	S_1	5.334	0.0000	$5b_1$	$5b_2$ V	91.4			
1^1B_1	S_2	5.896	0.0189	$5b_1$	$8a_1$ 3s	90.1			
1^1B_2	S_3	6.162	0.0255	$7a_1$	$5b_2$ V	77.9	$5b_1$	$3a_2$ V	12.8
2^1A_1	S_4	6.361	0.0243	$5b_1$	$6b_1$ $3p_x$	75.1	$7a_1$	$8a_1$ 3s	17.4
2^1A_2	S_5	6.423	0.0000	$5b_1$	$6b_2$ $3p_y$	90.8			
2^1B_1	S_6	6.510	0.0012	$5b_1$	$9a_1$ $3p_z$	90.7			
2^1B_2	S_7	6.802	0.0886	$5b_1$	$4a_2$ $3d_{xy}$	80.5	$7a_1$	$5b_2$ V	10.8
3^1A_1	S_8	6.826	0.0202	$7a_1$	$8a_1$ 3s	75.3	$5b_1$	$6b_1$ $3p_x$	15.8
3^1B_1	S_9	6.947	0.0173	$5b_1$	$10a_1$ $3d_{y^2}$	85.3	$7a_1$	$6b_1$ $3p_x$	6.6
4^1A_1	S_{10}	6.983	0.0006	$5b_1$	$7b_1$ $3d_{xz}$	82.5	$7a_1$	$9a_1$ $3p_z$	9.5

Vibrational calculations were performed using the FCClasses 3.0 package,[248] using an adiabatic Hessian sum-over-states method to allow resolution of individual vibronic transitions.[260] For the QC and NBD ground states and each excited state considered, a minimum was optimised, and subsequent frequency calculations were performed, thereby creating vibrational harmonic oscillator wavefunctions. The overlap of the vibrational wavefunctions of the initial and final states was calculated and squared to give the Franck-Condon factor (FCF). Anharmonicity was not considered as it was not particularly apparent in the experimental spectra. Time-independent calculations[248] were checked against the time-dependent method to ensure that the effects of the truncation of the sum-over-states were minimal. Transition dipole moment gradients were calculated by numerically differentiating the transition dipole moment at the ground state minimum, and subsequently used in the calculation of Herzberg-Teller contributions to the 1^1B_1 – 1^1A_1 (3s←$5b_1$) transition in NBD. Theoretical 'stick' spectra, generated from the calculated vibrational transition intensities and excitation energies, were convolved with a Gaussian function to facilitate comparison between simulated band profiles and the corresponding experimental spectra. The width of the Gaussian function was chosen to optimise the comparison.

Calculations of the ground (1^2B_1) state of the NBD cation using the MP2/aug-cc-pVQZ method returned normal mode wavenumbers that (in some cases) were significantly lower than the experimental values, and thus a discrepancy in the Franck-Condon envelope. Using the related CC2/aug-cc-pVQZ method gave vibrational envelopes for the ground state ion in much better agreement with the experimental data.

9.2 — Vertical Transitions, Geometries, and Vibrations

As before, the geometries of QC and NBD are shown in Fig. 1.2, along with the definition of the coordinate system. Calculated vertical energies and oscillator strengths for transitions from the ground state to the first ten singlet excited states of NBD and QC, are listed in Tables 9.1 and 9.2, respectively. For each excited state, the principal particle/hole orbital pairs for the corresponding vertical transition are also given. As these data show, the excited states of QC

Table 9.2: Calculated first ten electronic excitations and oscillator strengths for the QC ground state minimum. Calculations performed with ADC(2)/aug-cc-pVQZ. Vertical excitation energies are shown in eV. NTO weights shown when above 20%, with orbital character also denoted. All states shown are dominated by pure Rydberg transition.

State				Excitation 1		
Sym.	Adia.	ΔE_{vert}	Osc. Str	Hole	Particle	Cont.
1^1B_2	S_1	5.477	0.0002	$5b_2$	$8a_1$ 3s	91.1
1^1A_2	S_2	5.814	0.0000	$5b_2$	$6b_1$ $3p_x$	91.2
2^1A_1	S_3	5.925	0.0007	$5b_2$	$6b_2$ $3p_y$	90.7
2^1B_2	S_4	6.019	0.0017	$5b_2$	$9a_1$ $3p_z$	91.0
3^1B_2	S_5	6.480	0.0001	$5b_2$	$10a_1$ $3d_{y^2}$	90.9
3^1A_1	S_6	6.534	0.0133	$5b_2$	$7b_2$ $3d_{yz}$	90.7
1^1B_1	S_7	6.565	0.0147	$5b_2$	$4a_2$ $3d_{xy}$	90.7
2^1A_2	S_8	6.660	0.0000	$5b_2$	$7b_1$ $3d_{xz}$	91.0
4^1B_2	S_9	6.832	0.0114	$5b_2$	$11a_1$ $3d_{x^2-z^2}$	91.1
3^1A_2	S_{10}	6.863	0.0000	$2a_2$	$8a_1$ 3s	88.4

in the vertical region all have dominant Rydberg character; the first predominantly valence state lies much higher in energy. In contrast, the π and π^* orbitals in NBD ensure that several predominantly valence excited states (labelled V in Table 9.1) are interspersed between, and mixed with, the Rydberg states of NBD at energies within the range investigated in the present work. Note, the various Rydberg state potentials typically support two local minima — one QC-like, the other NBD-like — corresponding to the respective minima of the QC and NBD cations.[1,186]

Normal mode vibrational wavenumbers for the ground states, the excited electronic states formed by 3s←HOMO electron promotion, and the ground state cations, of both NBD and QC, at the respective minimum energy geometries, are given in Table 9.4. Also included in Table 9.4 are the normal mode vibrational wavenumbers for the 1^1B_2 valence state in NBD. Note, in both molecules, the calculated normal mode wavenumbers for the 3s, 3p and 3d Rydberg states are very similar (reflecting the similar topographies of the respective potential energy surfaces), so only the values for the respective 3s states are listed. The vibrational modes are numbered using the Herzberg convention.[175] The normal mode wavenumbers for the ground (1^1A_1) state neutral molecules and the associated nuclear displacements accord well with those reported previously for NBD[261] and QC.[262]

Comparisons between the simulated vibronic bands and the experimental spectra involved the following sequence of actions. The FC predicted intensity distribution was placed on a total energy scale by summing the theoretical adiabatic excitation energy (the separation between the minima of the ground and excited state potentials) with the vibrational energy contribution. In all cases the simulations employed the calculated harmonic wavenumbers (Table 9.4), except those of the absorption band due to the transition into the 3s 1^1B_1 Rydberg state of NBD (Figs. 9.3 and 9.4) where a scaling factor of 0.94 was used. The resulting vibronic simulations matched the experiment well, apart from a (generally small) energy offset. Comparisons shown in this work are post-application of an appropriate energy shift to the simulated data, the magnitude of which is reported in the relevant figure caption. This energy offset is a consequence of the incorrect excitation energies in the theoretical data.

Comparisons between the vibrational simulations and the experimental spectra revealed additional transitions beyond the simple cold (0 K) Franck-Condon picture. In the case of the

3s 1^1B_1 state of NBD, Herzberg-Teller effects were considered up to first order. Additionally, the wavenumbers of several normal modes of NBD are sufficiently low (see Table 9.4) that hot-band excitations (i.e. excitations from levels with $v' > 0$) are readily identifiable in the room temperature spectrum.

Finally, we note that the $3p_x\ 1^1A_2$ state in QC couples strongly with the $5b_2(\pi)5b_1(\pi^*)$ valence state upon opening of the angle between the two four-member rings (i.e. distorting towards the NBD geometry). This can be expected to preclude the observation of any associated vibrational structure (due to lifetime broadening), and to provide a route for non-adiabatic coupling back to the ground state on short time-scales[1]. This work is covered in Chapter 10.

Table 9.3 provides a summary of the geometric structures of NBD and QC used in this chapter in two coordinates: r_{cc} and r_{db} as defined in Eqs. (5.1) and (5.3). For all of the geometries here, $r_{rh} = 0$, and they have C_{2v} symmetry. The two carbon-carbon 'wings' are well separated in the NBD ground state equilibrium geometry, as evidenced by the large r_{cc} (2.46 Å). r_{db} is short (1.34 Å), reflecting the double bond in the respective C=C moieties. This contrasts with the ground state of QC, with formal C_1C_2 and C_3C_4 single bonds; the r_{cc} and r_{db} values therefore mirror typical CC single bond values (≈ 1.5 Å). We note that the present values of r_{cc} and r_{db} in the 1^1A_1 state of QC are very similar to the results obtained by Palmer et al.[242] using the MP4(SDQ) approach. In both molecules, the equilibrium geometry of the 3s Rydberg state closely mirrors that of the ground state cation. In both cases, these geometries are displaced from those of the corresponding ground state neutral species with the deformation towards the other isomer.

9.3 — Norbornadiene

Overview of Spectrum

The low energy end of the low resolution (2.13 meV FWHM), absolute photoabsorption cross section of NBD is plotted in Fig. 9.1, together with the theoretically predicted electronically excited states using the transition energies and oscillator strengths given in Table 9.1. The overall appearance of the spectrum is similar to those reported previously,[50,198,199,254,263] and the present theoretical predictions are consistent with the earlier results of Roos et al..[198]

The results from earlier electron impact experiments have also been used. In regard to valence transitions of NBD, Doering and McDiarmid identified two dipole forbidden transitions

Table 9.3: Optimised geometries for various states in the two molecules, with distances defined in Eqs. (5.1) and (5.3). All geometries are C_{2v}. The ground state agrees closely with the results of previous chapters. The Rydberg states (NBD $1^1B_1\ S_2$ and QC $1^1B_1\ S_2$) show intermediate values between the two extremes of the ground states, closely mirroring their respective ions. Finally, the NBD valence excited state ($1^1B_2\ S_3$) is positioned fairly close to the NBD ground state.

Molecule	State	r_{cc} / Å	r_{db} / Å
NBD	$1^1A_1\ S_0$	2.46	1.34
	$1^1B_1\ S_2$ 3s	2.22	1.37
	$1^1B_2\ S_3$ V	2.46	1.40
	1^2B_1 Ion	2.24	1.38
QC	$1^1A_1\ S_0$	1.51	1.54
	$1^1B_1\ S_2\ 3p_y$	1.66	1.47
	1^2B_2 Ion	1.67	1.47

Table 9.4: Vibrational wavenumbers (in cm^{-1}) for NBD and QC electronic states. For NBD, the ground (1^1A_1) and ionic (1^2B_1) state calculations were performed with MP2/aug-cc-pVQZ, and the Rydberg (3s 1^1B_1) and valence (V 1^1B_2) excited state with ADC(2)/aug-cc-pVQZ. The negative wavenumber for ν_{39} in the 1^1B_2 state is the imaginary frequency of the transition state. For QC, the ground (1^1A_1) state calculations were performed with MP2/aug-cc-pVQZ, the ionic (1^1B_2) state calculations with CC2/aug-cc-pVQZ, and the Rydberg (3s 1^1B_2) excited state with ADC(2)/aug-cc-pVQZ.

		Norbornadiene				Quadricyclane		
Sym.	Mode	1^1A_1	3s 1^1B_1	V 1^1B_2	1^2B_1	1^1A_1	3s 1^1B_2	1^2B_2
A_1	ν_1	3265.5	3212.5	3259.8	3254.2	3262.6	3201.0	3277.0
	ν_2	3168.3	3161.1	3173.5	3212.8	3230.8	3181.7	3249.8
	ν_3	3089.4	3071.9	3115.5	3089.5	3081.1	3094.7	3118.6
	ν_4	1608.2	1547.2	1447.8	1519.3	1493.3	1492.2	1494.4
	ν_5	1491.4	1474.6	1400.5	1480.4	1372.5	1451.4	1386.9
	ν_6	1256.4	1279.6	1124.6	1278.9	1282.2	1367.4	1348.7
	ν_7	1124.0	1117.4	1089.0	1124.0	1104.5	1171.6	1079.3
	ν_8	960.4	1004.9	963.9	1005.2	1017.7	1055.1	1061.2
	ν_9	903.6	917.1	738.8	914.9	964.7	1022.9	939.0
	ν_{10}	784.7	829.8	602.9	839.1	924.9	935.6	881.7
	ν_{11}	747.2	772.0	496.2	772.8	819.2	772.8	752.6
	ν_{12}	427.5	394.9	245.3	383.0	732.3	729.1	668.8
A_2	ν_{13}	3239.4	3208.2	3239.7	3236.2	3242.4	3198.2	3259.5
	ν_{14}	1297.0	1287.4	1258.4	1285.6	1209.2	1251.1	1253.5
	ν_{15}	1267.6	1240.7	1187.0	1244.1	1193.2	1177.5	1187.3
	ν_{16}	1138.1	1130.7	1034.9	1141.6	1047.2	1048.4	1076.9
	ν_{17}	938.0	970.4	954.2	965.1	1016.2	990.5	1004.7
	ν_{18}	914.1	881.7	692.7	896.2	852.6	812.4	825.2
	ν_{19}	721.7	703.1	516.0	707.2	710.9	625.3	632.3
	ν_{20}	453.9	370.4	286.9	376.6	532.7	382.4	389.9
B_1	ν_{21}	3263.7	3211.9	3258.3	3252.6	3252.3	3199.9	3267.5
	ν_{22}	3166.1	3160.8	3238.2	3166.9	3141.0	3175.2	3189.6
	ν_{23}	1568.9	1421.6	1768.0	1509.7	1267.8	1563.0	1330.6
	ν_{24}	1229.9	1168.9	1248.1	1174.4	1064.9	1101.4	1076.9
	ν_{25}	1077.2	1079.1	1056.3	1086.8	1011.9	1047.4	1003.5
	ν_{26}	1032.9	1001.8	978.1	1005.9	931.2	979.9	983.4
	ν_{27}	929.6	862.5	954.1	865.8	857.7	927.3	846.2
	ν_{28}	677.6	717.6	566.8	720.3	794.5	728.7	702.0
	ν_{29}	505.9	449.5	454.9	449.7	391.1	414.9	412.2
B_2	ν_{30}	3240.1	3205.9	3238.2	3237.7	3254.6	3198.4	3267.8
	ν_{31}	3165.8	3174.8	3172.7	3211.5	3227.8	3190.4	3247.7
	ν_{32}	1341.4	1360.3	1307.2	1360.2	1387.8	1386.1	1413.0
	ν_{33}	1272.4	1281.4	1127.1	1284.9	1281.9	1272.5	1286.2
	ν_{34}	1166.5	1207.7	963.1	1206.4	1245.0	1262.6	1265.9
	ν_{35}	975.2	1017.4	888.9	1039.9	1056.6	1006.9	1067.4
	ν_{36}	930.7	950.6	866.8	984.4	975.9	950.8	960.4
	ν_{37}	899.3	912.0	671.7	916.1	921.6	809.9	905.2
	ν_{38}	819.4	802.0	443.1	849.1	710.3	767.6	768.2
	ν_{39}	550.7	372.3	-325.8	577.4	664.0	502.6	641.4

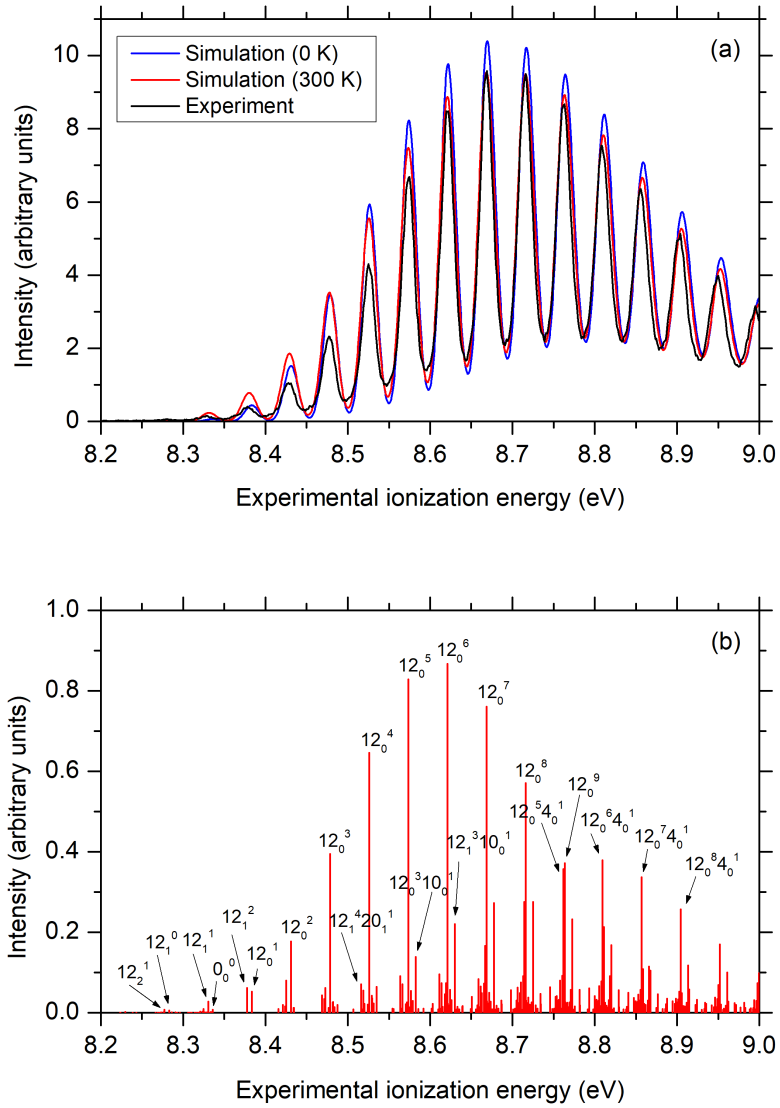

Figure 9.2: (a) A comparison between the experimental 1^2B_1 state photo-electron band of NBD[242] and our hot (300 K) and cold (0 K) vibrational simulations. The simulations have been obtained from the theoretical stick spectra after convolving with a Gaussian function of 20 meV (FWHM) to facilitate the comparison with the experimental spectrum. (b) The 300 K stick spectrum, employing the calculated adiabatic ionisation energy and ground and excited state vibrational wavenumbers (Table 9.4). All calculated spectra in this Figure have been shifted to higher energy by 0.299 eV so that the 12_0^8 transition aligns with the experimental peak at 8.716 eV. Reproduced from Cooper et al., *J. Chem. Phys*, **160**, 064305 (2024), with the permission of AIP Publishing.

at ≈ 5.25 (the state of interest in the Chapters 5 to 8) and ≈ 7.50 eV, and two dipole allowed transitions at ≈ 5.95 and ≈ 6.65 eV.[49]

Since the geometry of a Rydberg state molecule is generally similar to that of the ionic state onto which the series converges, the FC factors connecting the ground and Rydberg states are expected to be similar to those connecting the ground and corresponding ionic state. This is particularly useful for Rydberg states belonging to series converging onto the 1^2B_1 state of the NBD cation as the photo-electron band exhibits extensive vibrational structure.[242] Moreover, as the 1^2B_1 state photo-electron band is the only band containing vibrational structure, it is a reasonable starting assumption that any Rydberg absorption band exhibiting vibrational structure is likely to correspond to a member of a series converging onto the 1^2B_1 state ionisation limit.

Fig. 9.2(a) compares the experimental 1^2B_1 state photo-electron band recorded using a room temperature sample of NBD[242] with our hot (300 K) and cold (0 K) vibrational simulations of the corresponding structure. The simulations have been obtained from the theoretical stick spectra (only the 300 K stick spectrum is shown in Fig. 9.2(b)) after convolving with a Gaussian function of 20 meV (FWHM) to facilitate the comparison with the experimental spectrum. The simulated spectra, employing the calculated adiabatic ionisation energy and ionic ground state vibrational wavenumbers (Table 9.4), have been shifted in energy so that the 12_0^8 transition aligns with the experimental peak at 8.716 eV. As reported previously, the spectrum is dominated by progressions in the lowest wavenumber totally symmetric (A_1) normal mode 12 (the 'wing-flapping' or 'butterfly'-like C-C-C bending motion) – alone or in combination with other modes. The hot (300 K) and cold (0 K) vibrational simulations show that, contrary to a recent analysis,[242] the peak in the experimental spectrum at 8.328 eV incorporates the adiabatic transition and the peak at 8.279 eV arises solely through hot-band transitions.

In accord with previous studies[49,50,198–203,254,263] the present calculations predict that the first excited singlet state of neutral NBD is a valence state (sometimes termed the V1 state), arising via the optically forbidden 1^1A_2 – 1^1A_1 ($5b_2$←$5b_1$) transition and with a vertical excitation energy of 5.33 eV (Table 9.1). This conclusion is consistent with our previous work (Chapter 5) and evidence from electron impact investigations,[49,200,201] indicating that a peak observed at ≈ 5.25 eV should be ascribed to a singlet←singlet, optically forbidden transition, and with the optical activity study reported by Lightner et al.[203] Palmer et al.[199] considered the effect of Herzberg-Teller coupling in the 1^1A_2 state and suggested that such contributions might be observable close to threshold in the absorption spectrum.

It has long been accepted that excitations into two states (one valence and the other Rydberg) occur in the energy range ≈ 5.6 – 6.3 eV,[49,50,198–201,254,263] with the structured progression (with an average peak separation of ≈ 45 meV, that is again attributable to FC activity in ν_{12}) associated with transitions to the 3s 1^1B_1 Rydberg state and the underlying continuum with excitation into the 1^1B_2 valence state, sometimes termed the V2 state (Fig. 9.1). This co-existence was first established by Robin and Kuebler[254,263] (using high-pressure measurements) and later confirmed by Xing et al.[50] (using 2+1 REMPI measurements).

The 1^1B_2 valence state involves major contributions from two one-electron excitations, $5b_2$←$7a_1$ and $3a_2$←$5b_1$, and the present calculations predict a vertical transition energy of 6.16 eV (Table 9.1). The electron impact studies[200] associated a peak occurring at 5.95 eV with this optically allowed π^*←π transition. A comparison between the simulated vibrational structure associated with the transition into the 1^1B_2 state (employing the calculated 1^1B_2 state vibrational wavenumbers (Table 9.4)) and the spectrum recorded by Robin and Kuebler[254,263] is shown in Fig. C.1. The poorly resolved structure in the simulated spectrum, after convolving the calculated stick spectrum (not shown) with a 40 meV FWHM Gaussian function and

shifting in energy so that the features peaking at 5.73 eV align, is in good qualitative accord with the experimental data. The diffuseness of this absorption band is a clear indicator of the short-lived nature of this 1^1B_2 valence state. A non-lifetime broadened simulation of this same band (similarly shifted in energy), calculated with a resolution ($\approx$ 2 meV FWHM) matching that employed in the present experimental study, shows much richer structure (Fig. C.1). The vibrational excitations associated with the major peaks in the spectrum plotted in Fig. C.1 have been labelled.

The vibrational progressions appearing between 5.5 and 6.3 eV have been observed previously in single photon[50,198,199,254,263] and 2+1 REMPI[50,198] studies, and associated with transitions to a single Rydberg state (the 3s 1^1B_1 state). This work, including reassignments of the band origin, is shown in the next section. As a consequence of these revisions, and the anticipated envelope of the absorption band due to transitions into the 1^1B_2 valence state, all the sharp structure appearing in the experimental spectrum between $\approx$ 5.5 and 6.0 eV is assigned to vibrational progressions associated with transitions into the 3s 1^1B_1 Rydberg state. No evidence is found for resolved peaks associated with transitions into the 1^1B_2 valence state.

The present calculations predict vertical transition energies of 6.36 and 6.51 eV for the $2^1A_1 - 1^1A_1$ ($3p_x \leftarrow 5b_1$) and $2^1B_1 - 1^1A_1$ ($3p_z \leftarrow 5b_1$) Rydberg excitations, respectively, with the former transition having the higher oscillator strength (Table 9.1). The vibrational structure associated with the 1^2B_1 state photo-electron band spans a width of $\approx$ 0.8 eV.[242] This is a similar width to that of the absorption band observed between 5.5 and 6.3 eV (Fig. 9.1). Also relevant to the interpretation of these absorption bands are the findings from the REMPI studies,[198] which suggested that the symmetry of the excited state associated with the sharp structure observed in the range 5.636 – 5.975 eV was B_1 or B_2, whilst the structure between 6.048 and 6.794 eV was associated with one or more states of A_1 symmetry.

To investigate whether the experimental evidence might be affected by the data being recorded using different techniques (one-photon absorption in the present work; two-photon absorption in Roos et al.[198]), one- and two-photon excitation cross sections were calculated for excitation to some of the lower energy excited states of NBD, under various photon polarisation conditions. When calculating two-photon excitation cross sections, the photon energy was set to half the transition energy (i.e. the process was treated as a one-colour, two-photon excitation). The results from these calculations (Table C.1) show that the two-photon excitation cross section for the $3p_x$ 2^1A_1 Rydberg state is much higher than that for the 3s 1^1B_1 Rydberg state. Thus, the two overlapping transitions have significantly different relative transition probabilities under one- vs. two-photon excitation. Note, however, that REMPI detection probabilities depend on more than just the initial multi-photon transition strengths. The ionisation probability is also a sensitive function of the stability of the resonance-enhancing state; shorter-lived excited states typically have a much lower ionisation (and thus detection) efficiency.[264]

From hereon we focus on the one-photon absorption data. The peaks in the range $\approx$ 5.5 – 6.4 eV (Fig. 9.1), generally associated with the $1^1B_1 - 1^1A_1$ ($3s \leftarrow 5b_1$) transition, become noticeably broader and the vibrational envelope more complex as the excitation energy increases. This trend is consistent with an excited state lifetime that decreases with increasing energy, as a result of pre-dissociation and/or anharmonic coupling to the increasing density of background vibrational levels, as suggested by Xing et al.[50] In that study, the observed reduction in the lifetime of the higher vibrational levels in the Rydberg state was attributed to a rapid depletion through coupling between the 3s 1^1B_1 Rydberg and 1^1B_2 valence states.

The present calculations give an oscillator strength for the $2^1A_1 - 1^1A_1$ ($3p_x \leftarrow 5b_1$) transition that is $\approx$ 30% greater than that for the $1^1B_1 - 1^1A_1$ ($3s \leftarrow 5b_1$) transition (Table 9.1). The measured spectrum displays several short, somewhat irregular, vibrational progressions with $\approx$ 45 meV

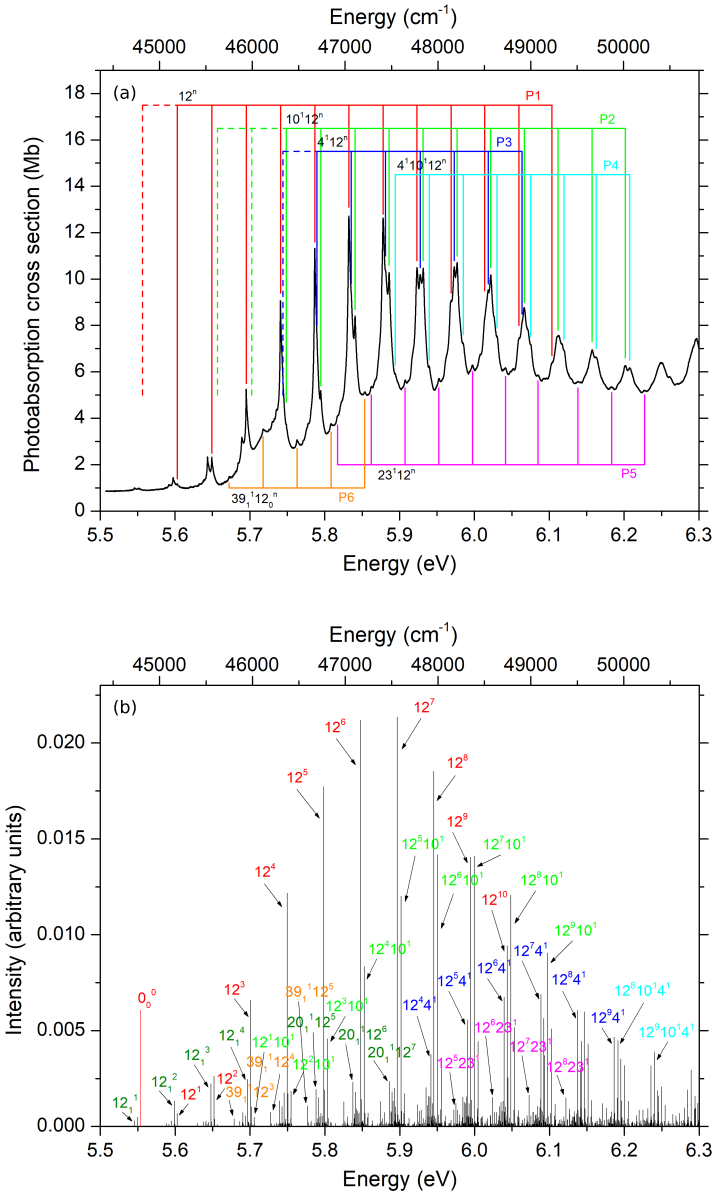

Figure 9.3: (a) The absolute photoabsorption cross section of NBD in the energy range encompassing vibrational structure due to the $1^1B_1 - 1^1A_1$ (3s←5b_1) transition. The estimated positions for the origins of progressions P1, P2 and P3 are marked with dashed lines. (b) Simulation of the vibrational structure associated with the $1^1B_1 - 1^1A_1$ transition in NBD in the form of a stick spectrum. Only the stronger vibrational excitations have been labelled, and only transitions stronger than the 0-0 transition have been plotted. The calculated excitation energies have been shifted to higher energy by 0.1349 eV so that the energy for the 12_0^1 excitation coincides with the experimental value of 5.6029 eV. The spectrum employs the calculated vibrational wavenumbers (Table 9.4). For display purposes, the intensity of the stick representing the 0-0 (origin) excitation has been multiplied by a factor of 50 and plotted in red. Reproduced from Cooper et al., *J. Chem. Phys*, **160**, 064305 (2024), with the permission of AIP Publishing.

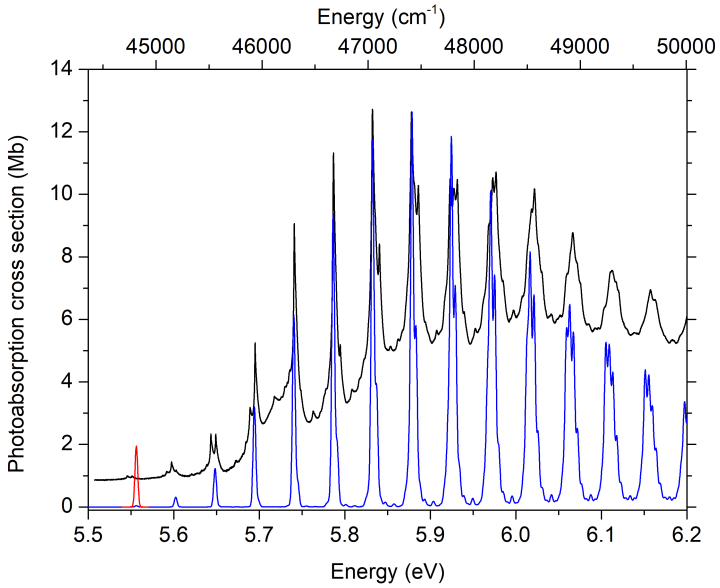

Figure 9.4: Comparison between the experimental (black trace) and simulated vibrational structure associated with the transition to the 3s 1^1B_1 Rydberg state of NBD. The main simulation (blue) is for a 0 K sample (i.e. all molecules initially in the $v = 0$ level), while the localised red trace shows the origin band re-plotted on a ×50 expanded vertical scale. The vibrational wavenumbers employed in the simulation are the calculated values (Table 9.4, multiplied by a scaling factor of 0.94, and the simulated spectrum has been shifted to higher energy by 0.126 eV so that the peak due principally to the 12_0^6 excitation aligns with the experimental peak at 5.8323 eV. Reproduced from Cooper et al., *J. Chem. Phys*, **160**, 064305 (2024), with the permission of AIP Publishing.

peak spacings in the energy range between ≈ 6.0 and 6.5 eV. These short progressions are not included in the extended progressions discussed in detail in the discussion of the structure of the 3s state, shown next, since it is reasonable to propose that they could be attributable to transitions to the $3p_x$ 2^1A_1 state – in accord with the present theoretical predictions and the REMPI polarisation results. Bearing in mind the likely vibrational envelopes of the overlapping transitions into the 3s 1^1B_1 and $3p_x$ 2^1A_1 states (i.e. wherein the bands associated with absorption to the lowest v''_{12} levels are weak), it remains uncertain whether some of the absorption contributing to the broader peaks at energies above ≈ 6 eV should be attributed to the $3p_x$ 1^1A_1 state rather than to the 3s 1^1B_1 state. Excitations into the $3p_z$ 2^1B_1 state (with a predicted transition energy of 6.51 eV) might also contribute to the spectrum at the high energy end of this region, but the calculated oscillator strength for this transition (0.001) is low (Table 9.1).

As we move to higher energies, the spectrum becomes more congested and, accordingly, the assignments become more tentative. Further, at high energies the density of states increases significantly, shortening the lifetime and, hence, broadening the features of the spectrum. As such, we do not include it here, and reference the reader to our more complete work.[2]

Vibronic Progressions in the 3s State

Our high resolution (0.27 meV FWHM) photoabsorption spectrum of NBD, covering the energy range 5.5 – 6.3 eV, is plotted in Fig. 9.3(a). Six progressions, all associated with the 1^1B_1 – 1^1A_1 (3s←$5b_1$) transition, are labelled (P1 – P6) and colour-coded. The predicted vibrational

structure associated with the 1^1B_1 – 1^1A_1 transition, in the form of a stick spectrum, is plotted in Fig. 9.3(b), where only the stronger vibrational excitations are labelled. The simulation includes Herzberg-Teller coupling. The very good agreement between the simulated and observed structure allows the bands in the experimental spectrum to be assigned.

As discussed in previous studies,[50,198,199,254,263] the progressions associated with the 1^1B_1 – 1^1A_1 (3s←5b_1) transition involve excitation of ν_{12}, the wing-flapping mode, either alone or in combination with other modes. The first step in unravelling the vibrational assignments comes from comparing (Fig. 9.4) the present experimental spectrum and a simulation for the 1^1B_1 – 1^1A_1 transition at 0 K (i.e. with all ground state molecules in their $\nu' = 0$ level). The origin (0-0) band is extremely weak (Fig. 9.4); its calculated FCF is almost 500-times smaller than that of the strongest (n = 7) member of the 12_0^n progression. Unsurprisingly, therefore, when the simulated and experimental spectra are aligned (using the 12_0^6 band as the reference), the theoretically predicted origin band is too weak to be discerned in the room temperature absorption spectrum. The peak observed at 5.6029 eV actually corresponds to the 12_0^1 member of progression P1. Thus, our experimentally determined energy for the (unobserved) origin band is 5.5567 eV, assuming that the energetic spacing between the 0-0 and 12_0^1 transitions is the same as that between the 12_0^1 and 12_0^2 transitions.

Similar comparisons between the experimental spectrum and the vibrational simulations have enabled estimation of the origins for the P2 and P3 transitions, and the estimated origins for the P1, P2 and P3 progressions are marked in Fig. 9.3 using dashed lines.

Our vibrational simulations indicate that progressions P2 (green) and P3 (blue) involve excitation of the ν_{12} mode in combination with the excitation of a single quantum of the ν_{10} (another wing-flapping mode) or the ν_4 (C=C stretch) mode, respectively, both of which have a_1 symmetry. The experimental spectrum yields separations of 100.0 meV (806.6 cm^{-1}) and 187.6 meV (1513.1 cm^{-1}) for one quantum in the ν_{10} and ν_4 modes, respectively, in the 3s 1^1B_1 Rydberg state. In comparison, our calculated (harmonic) energies for the ν_{10} and ν_4 modes are 102.9 and 191.8 meV (829.8 cm^{-1} and 1547.2 cm^{-1}), respectively (Table 9.4).

It now becomes evident, in accord with our vibrational simulation, that progression P4 (cyan) corresponds to excitation of ν_{12} in combination with a single quantum in both the ν_4 and the ν_{10} modes. Note, in contrast to the earlier studies,[50,199] these intervals obtained in the present analysis all match well with predicted totally symmetric excited state vibrational modes. FC activity in these modes can be understood by reference to the calculated changes in equilibrium geometry upon excitation from the ground state to the 3s 1^1B_1 Rydberg state (see Table 9.3). ν_{12} and ν_{10} both involve wing-flapping motions and are thus sensitive to r_{cc}, which decreases upon excitation to the Rydberg state. The observed FC activity in the symmetric C=C stretch mode, ν_4, is similarly understandable given the predicted increase in r_{db} upon excitation to the Rydberg state.

The inclusion of Herzberg-Teller coupling, allowing the excitation of an odd number of quanta in non-totally symmetric vibrational modes, explains the appearance of progression P5 (magenta) which involves the excitation of ν_{12} in combination with a single quantum of the ν_{23} (b_1) mode (involving stretching of the C_1C_5, C_5C_2, C_3C_6 and C_6C_4 single bonds). The sticks corresponding to this progression are labelled in Fig. 9.3. Using the excitation energies of 5.9524 eV for the $23_0^1 12_0^5$ transition and 5.7868 eV for the 12_0^5 transition leads to an energy of 165.6 meV (1335.7 cm^{-1}) for one quantum of excitation in the ν_{23} mode in the 3s 1^1B_1 Rydberg state. The calculated energy for this mode is 176.3 meV (1421.6 cm^{-1}, Table 9.4). Given the $^1B_1$ state symmetry, activity in this b_1 mode presumably reflects vibronic interaction with a near-resonant, optically allowed electronic state of $^1A_1$ symmetry – plausibly the 2^1A_1 state.

Next, we consider hot-band transitions. Vibrational simulations were calculated for ground state NBD molecules, and are most likely to include excitation in the low energy ν_{12} (a_1), ν_{20} (a_2,

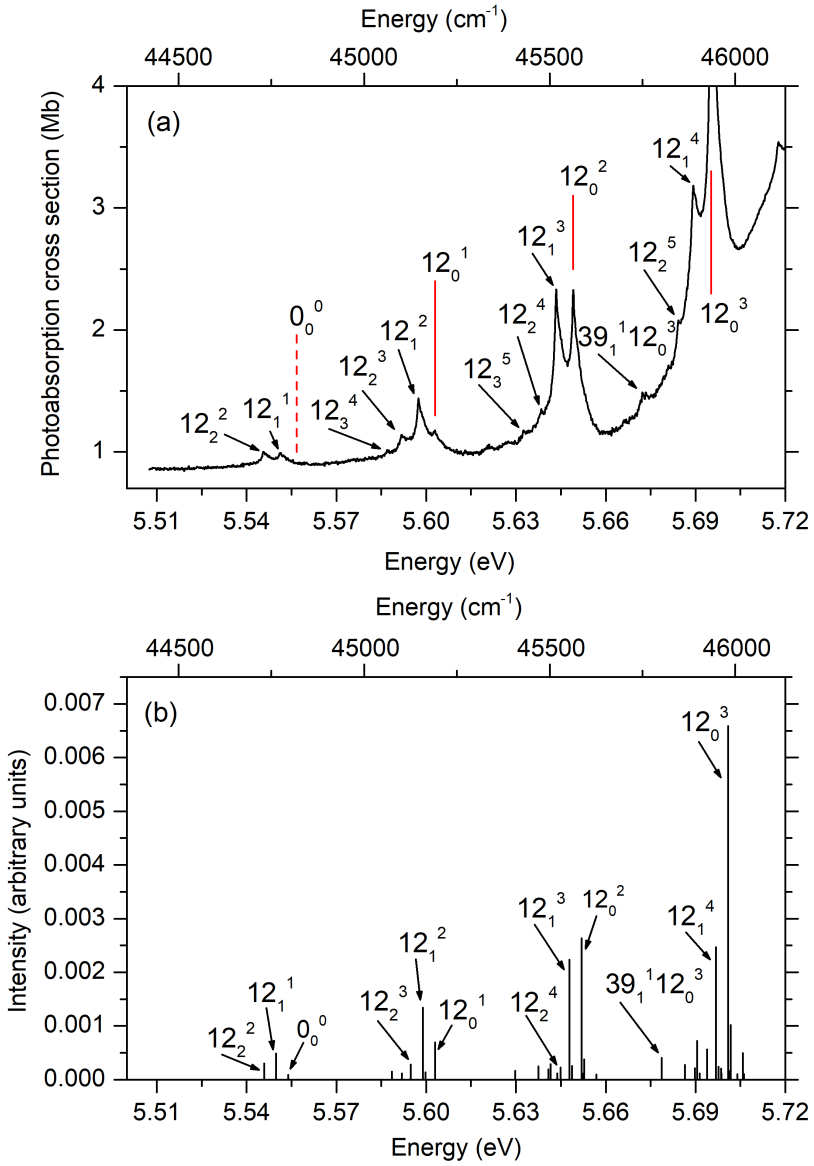

Figure 9.5: (a) The absolute photoabsorption cross section of NBD in the energy region close to threshold. Peaks due to hot-band transitions are labelled, as well as those associated with progression P1. A peak associated with progression P6 (the hot-band progression built on ν''_{39} = 1) is also labelled. The estimated position of the origin (0-0) band is marked with a dashed line. (b) A simulation of the vibrational structure associated with the $1^1B_1 - 1^1A_1$ transition. The calculated excitation energies have been shifted to higher energy by 0.1349 eV so that the energy for the 12_0^1 excitation coincides with the experimental value of 5.6029 eV. Reproduced from Cooper et al., *J. Chem. Phys*, **160**, 064305 (2024), with the permission of AIP Publishing.

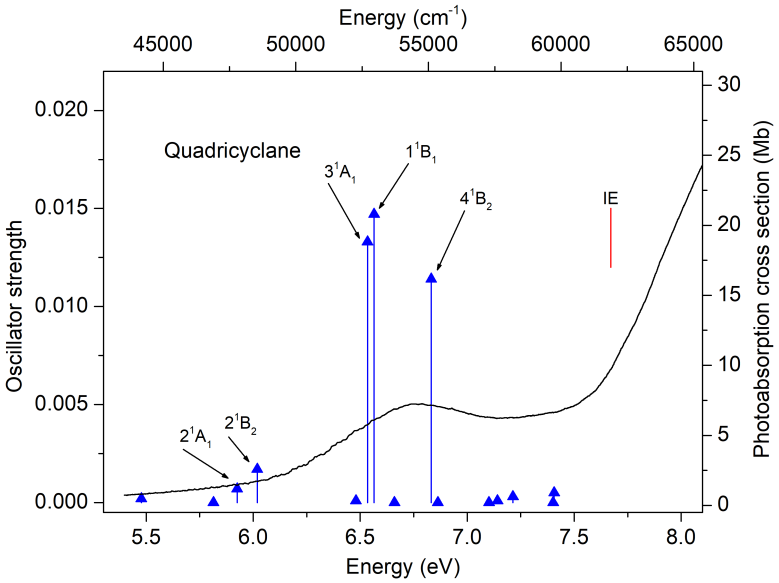

Figure 9.6: QC vertical excitations. Unlike in NBD, there is very little vibronic structure seen in the experimental spectrum (black line). Vertical transitions (ADC(2)/aug-cc-pVQZ, Table 9.2) are shown as blue arrows, again with the height defined by the oscillator strength. The ionisation continuum is very low, showing the amount of strain in the system. Reproduced from Cooper et al., *J. Chem. Phys*, **160**, 064305 (2024), with the permission of AIP Publishing.

ring twist), ν_{29} (b_1, CH_2 wag) or ν_{39} (b_2, ring pinching/twisting) modes. We show the threshold region of the NBD in Fig. 9.5. The simulated hot-band spectrum for the ν_{12} mode allows all the observed structure to be assigned. Note the absence of a peak corresponding to the origin. The excellent match between the experimental and simulated spectra after inclusion of the hot-band structure — for example, the relative intensities of the triplet feature at excitation energies of ≈ 5.60 eV, the doublet of comparably intense features ≈ 5.65 eV, and the features with up to three quanta in ground state modes — is key to confirming the proposed numbering of the 12_0^n progression and thus the true energy of the (unobserved) band origin. The present analysis shows that the feature hitherto attributed to the $1^1B_1 - 1^1A_1$ origin by Xing et al.[50] and, later, by Palmer et al.[199] is actually the 12_0^1 transition.

As already mentioned by Robin and Kuebler,[254] the relative intensities of progressions P1 – P4 vary as a function of the number of quanta in ν_{12}, with P1 being the strongest progression for low values of ν_{12}, whereas P2 and P4 become more prominent for the higher vibrational levels (particularly evident above 6.1 eV). Our simulations indicate that a progression due to $10^2 12^n$ excitations becomes significant at energies above 6.0 eV and will contribute to the apparent broadening of the peaks associated with the higher vibrational levels.

9.4 — Quadricyclane

In QC, we start by exploring the vibrational structure in the 1^2B_2 state photo-electron band of QC, as these theoretical predictions help guide our interpretation of the bands in the QC photoabsorption spectrum. The simulation, shown as a stick spectrum in Fig. 9.7(a), has been shifted in energy so that the stick representing the $10_0^1 12_0^1$ excitation aligns with the feature at 7.858 eV in the experimental spectrum. The simulation employs the calculated vibrational wavenumbers for the 1^2B_2 ionic state given in Table 9.4. The present simulation is in very

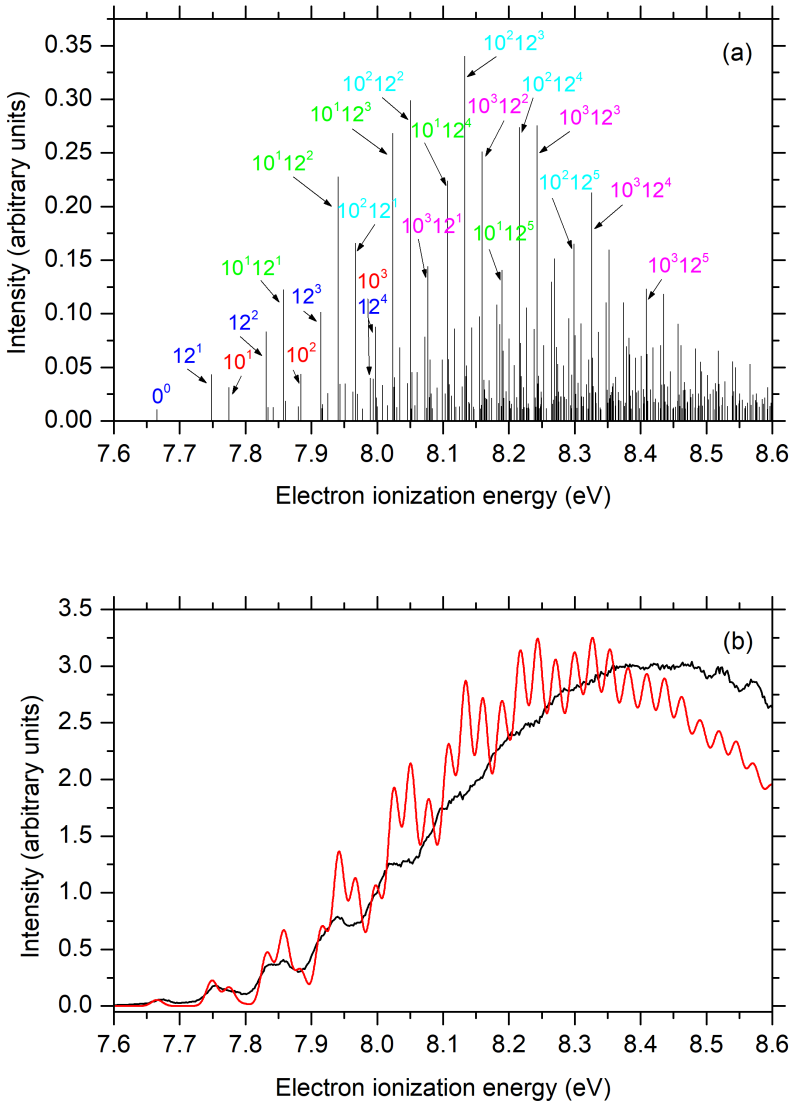

Figure 9.7: (a) A stick spectrum showing the simulated vibrational structure associated with the first (1^2B_2) photoelectron band of a 300 K sample of QC. Only the stronger vibrational excitations are labelled and, since all originate from the $v' = 0$ level, the subscript zero has been omitted from each label. The simulation has been shifted to lower energy by 0.057 eV so that the stick representing the $10_0^1 12_0^1$ excitation aligns with the feature at 7.858 eV in the experimental spectrum.[242] The simulation employs the calculated vibrational wavenumbers for the 1^2B_2 ionic state given in Table 9.4 (b) Comparison between the experimental 1^2B_2 state photoelectron band of QC[242] (black trace) and the 300 K vibrational simulation obtained by convoluting the stick spectrum shown in (a) with a 20 meV FWHM Gaussian function (red trace). Reproduced from Cooper et al., *J. Chem. Phys*, **160**, 064305 (2024), with the permission of AIP Publishing.

good accord with that reported previously by Palmer et al.,[242] and displays rich vibrational structure attributable to excitation of several a_1 symmetry normal modes. At the low energy end of the band, the structure arises primarily through excitation of two modes (ν_{10} and ν_{12}), either alone or in combination with each other. Ascending in energy, these two modes are predicted to be excited in combination with other modes, principally ν_{11}, ν_8, ν_6 and ν_5. All these modes involve (symmetric) deformation of the heavy atom skeletal modes, primarily C–C stretch and CCH bending motions.[262]

A comparison between the experimental 1^2B_2 state photo-electron band of QC, measured at a photon energy of 30 eV,[242] and a convolved (20 meV FWHM) version of this vibrational structure is shown in Fig. 9.7(b). The convolved simulation has been shifted in energy as already described for the stick spectrum. The total width of the measured photo-electron band is almost 2 eV, with a vertical ionisation energy of ≈ 8.4 eV, but vestigial vibrational structure is only evident on the low energy side (spanning the first ≈ 0.5 eV). The adiabatic ionisation energy is 7.671 eV.[242] The peaks at the high energy side of the experimental photo-electron band (first appearing at ≈ 8.45 eV) are due to NBD contaminant in the QC sample and can be disregarded. As previously,[242] the convolved FC simulation reproduces the broad structures on the low energy side of the experimental photo-electron spectrum well, thereby providing confidence in the use of our current simulations to guide our interpretation of the QC photoabsorption spectrum. Only the 1^2B_2 state photo-electron band of QC exhibits any vibrational structure.[242] Hence, any features showing similar structure in the pure QC absorption spectrum are likely to be associated with Rydberg states formed through excitation from the $5b_2$ orbital.

The low energy part of the pure QC absolute photoabsorption spectrum is plotted in Fig. 9.6, together with the theoretically predicted excited electronic states using the transition energies and oscillator strengths given in Table 9.2. The present calculations confirm the conclusions reached previously[187,265] that transitions to Rydberg states dominate the low energy region of the absorption spectrum of QC. As noted earlier the saturated nature of the bonding in QC ensures that vertical excitation to states with dominant $\pi\pi^*$ valence character occur at substantially higher energies.

The present calculations give a vertical excitation energy of 5.48 eV for the lowest energy spin-allowed transition in QC, the 1^1B_2 – 1^1A_1 (3s←$5b_2$) excitation, and a low oscillator strength. The experimental spectrum does not exhibit a distinct threshold; the absorption cross section is seen to increase gradually from the low energy limit of the current measurements (5.4 eV). Time-resolved photo-electron spectroscopy studies[48] returned a term value (with respect to the vertical ionisation limit) of 2.88 eV for the 3s 1^1B_2 Rydberg state in QC. This corresponds to a vertical transition energy of ≈ 5.5 eV, in good agreement with the current theoretical prediction. As can be seen in Fig. 9.6, the overall vibronic signal seen in the spectrum is minimal, especially in contrast with NBD (Fig. 9.1). This is primarily due to spectral congestion, as well as strong non-adiabatic coupling to reactive valence states, as discussed in Chapter 10. The vibrational features that can be determined are discussed in more length in Cooper et al..[2]

9.5 — Conclusions

High-resolution absorption spectra of both NBD and QC were analysed and assigned. The absorption spectrum of NBD exhibits some sharp structure due to transitions into Rydberg states, superimposed on several broad bands attributable to valence excitations. Some resolved, but much weaker, structure also appears in the photoabsorption spectrum of QC. Assignments have been proposed for some of the absorption bands using calculated vertical excitation

energies and oscillator strengths obtained with the ADC(2) method. The character of the excited state has been investigated using NTOs, and several of the transitions in NBD have been shown to possess a mixed Rydberg/valence character.

Simulations of the excited state vibrational structure were generated from calculated transition intensities and excitation energies. These calculations include excitations allowed within the FC approximation, and also those appearing through Herzberg-Teller coupling. Hot-band excitations have also been studied. Simulations of the vibrational structure associated with ionisation into the 1^2B_1 state in NBD and the 1^2B_2 state in QC are consistent with the measured photo-electron spectra and proved helpful in identifying absorption bands due to transitions into Rydberg states associated with series converging onto these limits.

A comparison between the predicted vibrational structure for the $1^1B_1 - 1^1A_1$ (3s←$5b_1$) transition in NBD and the experimental absorption spectrum in the energy range $\approx 5.5 - 6.3$ eV allowed the excitation energy of the origin band to be established and the active vibrational modes to be identified. Six vibrational progressions have been assigned in the $1^1B_1 - 1^1A_1$ absorption band. Four of these progressions involve excitation to Franck-Condon active modes of a_1 symmetry. Another involves excitation of the ν_{23} (b_1) mode, enabled by Herzberg-Teller coupling, while the sixth is assigned as a hot-band progression involving the ν_{39} (b_2) mode. The present vibronic analysis reveals the need for some reassignments relative to those proposed previously.[50,199]

For dynamics, the most notable feature of this work is the multitude of long-lived, sharply resolved Rydberg states in NBD. Experimentally, it is known that these states decay on a sub-picosecond time-scale[266], but it is clear that there is at least some dynamics beforehand. As future time-resolved spectroscopic works on this molecule will likely investigate this part of the potential energy surfaces, it is clear that a full non-adiabatic simulation of the Rydberg/valence coupled dynamics of NBD is necessary, and will likely have relatively long-lived Rydberg states.

— 10 —

Rydberg & Valence Dynamics in Quadricyclane

In this chapter, we explore the dynamics of quadricyclane, including Rydberg states in the calculations. This work was motivated by a time-resolved photo-electron spectroscopy (TRPES) experiment performed at the FERMI free electron laser in Trieste, where an excitation laser of 6.2 eV was used, exciting Rydberg and valence states, and the dynamics was probed by a $\approx$ 19 eV ionising laser. In the experiment, two distinct features were seen: one attributable to long-lived Rydberg dynamics, while the other seemed to imply much more rapid dynamics, which will be attributed to direct valence excitation.

First, we will briefly cover the experimental results, before discussing the electronic structure of the NBD/QC system when one considers both Rydberg and valence states. This is a much more challenging task that is undertaken in Chapter 5, as the electronic structure method must give an equally good description to both the Rydberg and valence states. As such, compromises are made, and while we find an efficient and relatively accurate method, more recent work showed the dynamics of the valence state to be only qualitatively correct.

After choosing the electronic structure method, we find that that the experiment directly excites two pure valence states and one mixed-Rydberg/valence state. The results of the simulations are almost entirely dependent on the nature of the initially excited state, with the Rydberg states predicting slow, meandering dynamics, while the mixed-Rydberg/valence state, which is the state in question in Chapters 5 and 8, gives a rapid decay straight to the ground state.

This work was reproduced with only minor additions from K. Borne, J. C. Cooper et al., *Nat. Chem.*, **16**, 2024, 499-505, with permission from Springer Nature. The author of this thesis completed all theoretical work and contributed both to the writing and interpretation of experimental data, but completed no experimental work. For reference, we include a small discussion of the specifics of the experiment here.

The experiment was performed at the FERMI free-electron laser[267] at the Low Density Matter beamline.[268,269] XUV probe pulses at 18.97 eV using an initial seed laser at 261.4 nm. The UV pump pulse were generated using the fourth-harmonic of a Ti:sapphire laser at 6.18±0.02 eV. The delay of the XUV probe pulse to the UV pump pulse was varied between -500 and 1000 fs, with an overall instrument response function of 186 ± 28 fs (FWHM). The data was collected with a magnetic bottle electron spectrometer[135], using a retardation voltage of 9.7 eV, and overall gave an energy resolution of $\approx$ *±0.5 eV.*

10.1 — Computational Details

Electronic structure calculations for the neutral species were performed using RMS-CASPT2 [124,125] based on SA(9)-CASSCF(2,6) with the 6-31G(d) basis augmented by additional diffuse functions (8s8p contracted to 1s1p) centred on the bridging CH_2 fragment (contraction shown in Table C.2). The active space contained two valence orbitals (as the CASSCF(2,2) in Chapter 5),

as well as one 3s Rydberg and three 3p Rydberg orbitals (images shown in Fig. C.2). No 3d orbitals were included in this study, as their presence was not seen in the experimental data. The lowest six (S_0–S_5) states were deemed sufficient to describe the dynamics observed, though state-averaging over the first nine roots returned by the calculations was required for convergence. All nine states were active in the simulations, however, only a very small fraction of population ever appeared on the states S_6 and above during the dynamics. We note that this approach fails to capture the second valence excited state of NBD[263] but this omission is judged to have little impact on the dynamics initiated by photo-exciting QC. Electronic structure calculations for the molecular ion were performed with the same method and basis, although with one electron removed, i.e., RMS-CASPT2/SA(6)-CASSCF(1,6), using the neutral orbitals as an initial guess. This accounts for all ionisations from the active electron, including the D_0 and D_1 ionic states of interest (see Fig. C.3 for further details). The absence of Rydberg states in the ion wavefunction leads to lower relative energies in the ion than the neutral, leading to a small bias towards lower E_{IP} values. All calculations included an imaginary shift of 0.5 E_h to remove intruder states and were performed in a development branch of OpenMolcas[191] implementing gradients for RMS-CASPT2.[129]

The potential energy curves in Fig. 3 are calculated along linear interpolation in internal coordinates (LIIC) that connects the ground state equilibrium geometry of QC to the S_1/S_0 MECI, and then along a LIIC from this MECI geometry to the ground state equilibrium geometry of NBD. This is very similar to the first LIIC shown in Chapter 5, but is calculated using different geometries. The C_4-ring geometry at the MECI is rhombic[186,188] and does not lie directly between the equilibrium geometries of the two isomers, as shown in Fig. 6.3. Since this is an essentially barrier-less process, there is no obvious conceptual advantage in considering a minimum energy pathway over the LIICs.

Non-adiabatic trajectories were run using the surface-hopping method with a locally modified version of SHARC 2.1.[270] Couplings were calculated using the local-diabatic approach. Limited numerical issues with the stability of the gradients were mitigated by a variable time-step for the integration, which halved upon non-conservation of energy. The initial conditions were selected from a Wigner-sampled ground state QC geometry using the delta-pulse method[100] inside a 5.75 ± 0.07 eV window, chosen to overlap well with the calculated partial absorptions to the 3p Rydberg states of QC (Fig. 10.3). Trajectories were categorised into those excited into S_2 (121 trajectories, 45%) and those excited into S_3 and S_4 (146 trajectories, 55%). Strictly, one-photon excitation $S_0 \rightarrow S_2$ is forbidden at the equilibrium geometry and the excitation is therefore attributable to the Herzberg-Teller effect with the transition gaining strength from the mixing of valence character into the S_2 state. Inspection showed that within the envelope of the Wigner sampling, the character of the states remained separated, with the S_2 state corresponding to the $3p_x$/V configuration, whereas the S_3 and S_4 states each involved a mixture of excitations to the $3p_y$ and $3p_z$ orbitals. This separation is confirmed by the distinctly different, excitation-character-dependent, dynamics displayed by the respective sets of trajectories. A very small sample (5 trajectories) was excited to the S_1 (3s) state at this energy. These are not considered further in the current analysis. For the analysis, the trajectories were sorted according to initial state, allowing resolution of the dynamics into state-specific components. A small portion (7% of the total) of trajectories undergo a retro-Diels-Alder reaction from NBD-like geometries (as shown in Fig. 8.4) after passing through the MECI geometry, yielding C_5H_6 and C_2H_2 fragments, but these were excluded from the analysis as the selected active space cannot describe the fragmentation pathway accurately. Molecular geometries were analysed using the same set of coordinates as used earlier, defined in Eqs. (5.1) and (5.2).

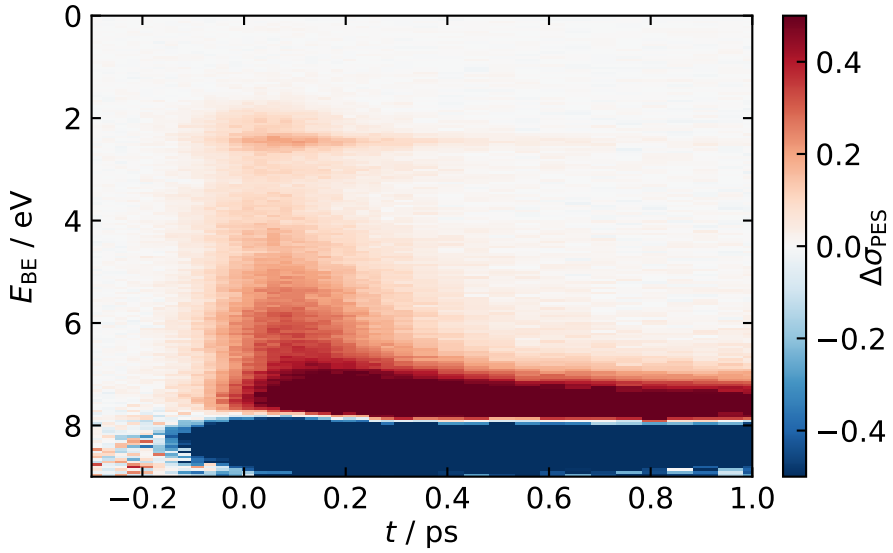

Figure 10.1: Time-resolved experimental photo-electron spectra for quadricyclane. Photoelectron spectra as a function of binding energy (E_{BE}, with respect to the first ionisation potential, D_0) and pump–probe time delay (t) between pump (UV) and probe (XUV) pulses, plotted as the electron yield difference between spectra taken with and without the UV-excitation pulse ($\Delta\sigma_{PES}$). Values of $\Delta\sigma_{PES}$ are arbitrary. Negative delays correspond to the probe pulse preceding the pump pulse. Data taken from and further details shown in Borne et al..[1]

Photo-ionisation cross-sections and energies were calculated by selecting a random time point in each 5-fs period within each trajectory. The squared Dyson norm (see Section 4.3) was calculated between the active state in the surface hopping and all ionic states, and used as an approximation to the photo-ionisation cross-section. The method yields qualitatively lower cross-sections for valence states than for Rydberg states when compared to experiment so, for display purposes, the intensities in Fig. 10.7 with E_{BE} >3 eV have been multiplied by a factor of 3. The ionisation potential difference between QC and NBD is roughly 0.3 eV with E_{IP}^{QC} = 7.67/8.4 eV and E_{IP}^{NBD} = 8.02/8.7 eV (first value from present vertical calculations in Table 1, second value approximate vertical values from Figs. 9.2 and 9.7, respectively).

10.2 — Experimental Results

Figure 10.1 shows the time-resolved photo-electron spectra (TRPES) taken at FERMI, initiated from gas-phase QC by a UV excitation pump pulse at 200.6 nm (6.18 eV), followed by an XUV ionisation probe pulse at 18.97 eV (65.35 nm).

Several prominent features are apparent. A narrow and long-lived feature at ≈ 2.3 eV binding energy (E_{BE}), visible as a faint horizontal line in Fig. 10.1, is assigned to two of the three 3p Rydberg states of QC in accordance with the literature.[48] The 3s Rydberg state can be seen at a E_{BE} of ≈ 2.9 eV in Fig. 10.1 but has a weaker signature than in earlier studies,[48] suggesting less excitation to the 3s state at 200.6 nm compared to 208 nm. Figure 10.1 also shows a spectrally broad and short-lived vertical feature in the E_{BE} range of ≈ 1.5–7 eV between $t = 0 - 0.2$ ps, which merges into a long-lived horizontal band at ≈ 7–8 eV E_{BE}, both of which were not observed in the earlier work that did not have a sufficient photon energy to ionise this E_{BE} region. These observations suggest the existence of a rapid (<100 fs) de-excitation pathway leading to the formation of vibrationally hot photo-products, while the longer timescale of

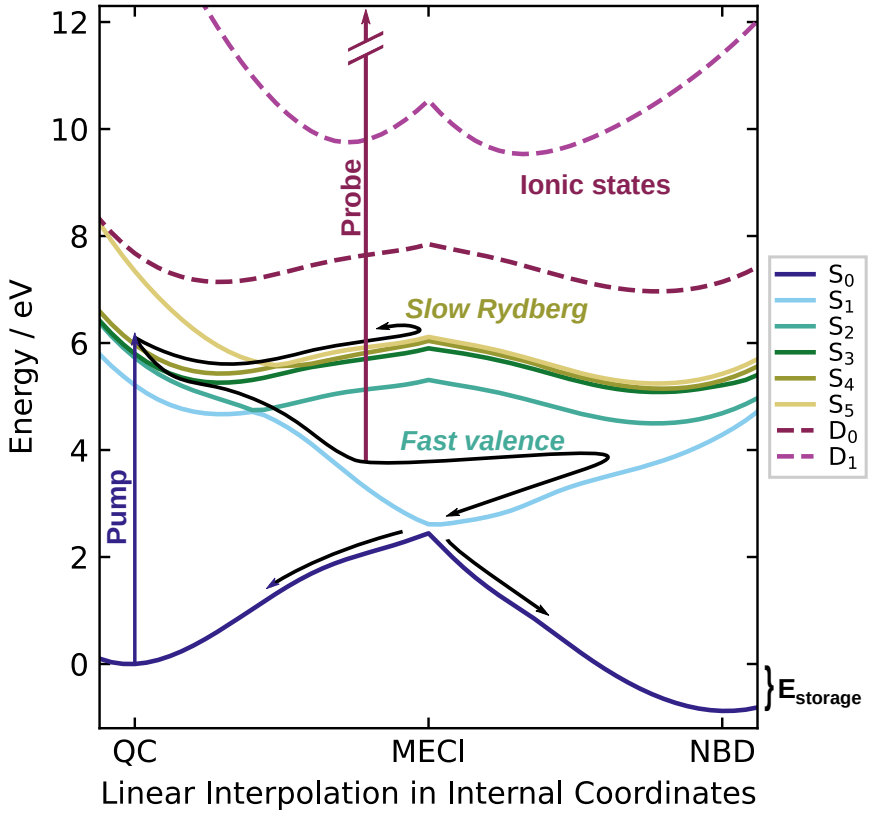

Figure 10.2: Potential energy curves for the ground state S_0 and excited states S_1–S_5, as well as the cation ground state D_0 and first excited state D_1 (dashed lines), calculated along the LIICs, first from QC to the S_1/S_0 MECI and then from the MECI to NBD, using RMS-CASPT2(2,6)/6-31G(d)+ (Section 10.1). The two proposed reaction pathways are indicated schematically by black arrows, with the slow Rydberg pathway supporting vibrational motions on the Rydberg states before relaxing via the S_1 state, while the fast valence pathway descends on S_1, bypassing the MECI on the initial descent, before crossing onto the S_0 ground state to form both products. The molecular geometry at the MECI has a distinct rhombic distortion. $E_{storage}$ indicates the energy stored in QC relative to NBD (≈ 1 eV). Corresponding vertical excitation energies are listed in Table 1,

the Rydberg-associated features indicates the existence of a second, slower decay mechanism, which corresponds to the pathway identified in earlier work.[48] Finally, there is a pronounced negative signal in the difference spectrum in the E_{BE} range 8–9 eV, assigned to the depletion of the QC ground state, followed by a partial recovery.

10.3 — Electronic Structure Theory

Unlike in the previous sections concentrating on the valence states, in this chapter we also consider Rydberg states. Mixed-Rydberg-valence dynamics has a particular set of requirements above and beyond plain valence dynamics. In particular, calculations with Rydberg states must contain extremely diffuse basis sets to describe the large separation of the Rydberg electron from the central core. Secondly, the methods must be dynamically correlated. If they are not, one characteristically underestimates the excitation energy, as Rydberg states are, by their very nature, less correlated than valence states.

Table 10.1: Excitation energies and ionisation potentials for the first five singlet states and lowest doublet ionic state. Calculated at RMS-CASPT2(2,6)/6-31G(d)+, with all values given in eV and the character of the state inlcuded in brackets.

State	QC (character)	MECI (character)	NBD (character)
S_1	5.29 (3s)	0.00 (V)	5.25 (V)
S_2	5.82 ($3p_x$/V)	2.74 (3s)	5.61 (3s)
S_3	5.88 ($3p_y$)	3.31 ($3p_x$)	6.11 ($3p_y$)
S_4	6.05 ($3p_z$)	3.47 ($3p_y$)	6.28 ($3p_x$)
S_5	7.53 ($3p_x$/V)	3.53 ($3p_z$)	6.34 ($3p_z$)
IP ($S_0 \rightarrow D_0$)	7.67	5.26	8.02

In Fig. 10.2, we show the potential energy curves, calculated using RMS-CASPT2/6-31+G(d) (see methods), for the QC↔S_1/S_0↔NBD LIIC. This method is ideally suited to this study, as the state-specific Fock operator allows for a good description of both the Rydberg and valence states, whereas a state-averaged Fock operator (as in XMS-CASPT2) would lead to a mixed description, not correctly describing either manifold. Further details on this LIIC can be found in the computational details and Chapter 5. Starting from the QC ground state minimum geometry on the left-hand side, we can see a large array of states centred at $\approx$ 6 eV. This manifold contains the three 3p Rydberg states, with the upper two being of pure Rydberg character (S_3 $3p_y$ and S_4 $3p_z$) and the lower mixed Rydberg/valence S_2 $3p_x$/V[i]. Below, there exists the 3s state, and above, the partner of the Rydberg/valence state, the S_5 V/$3p_x$ state. The valence and $3p_x$ Rydberg state mix as they are both A_2 symmetry, while the other Rydberg states are not A_2, and so do not mix.

Moving to the right, we approach the S_1/S_0 MECI geometry. While the Rydberg states stay relatively flat at $\approx$ 6 eV, the Rydberg/valence state descends to meet the ground state, forming the intersection. As this occurs, the Rydberg character of the state is lost, leaving a pure valence state. Accordingly, the partner state, S_5, descends into the Rydberg manifold, becoming of pure $3p_x$ character, and these characters remain as we move to NBD. Excitation energies and characters are tabulated in Table 10.1 Looking back at the work in Chapter 5, we can clearly identify the valence state as being consistently described between these two works, except around the QC minimum, where the state interacts with the Rydberg manifold.

The potential energy curves in Fig. 10.2 suggest the possible mechanisms that underpin the features observed in the TRPES data, with the two pathways indicated schematically by black arrows. From the QC ground state, the bandwidth of the pump pulse (±0.02 eV) allows excitation to a manifold of closely spaced states with 3p Rydberg character. Population in the $3p_y/3p_z$ Rydberg states (S_3 and S_4 in the FC region) then evolves via a (comparatively) slow Rydberg pathway on the rather flat Rydberg manifold at excitation energies of $\approx$ 6 eV; we anticipate that this would correspond to the pathway observed previously.[48]

Due to the similar topographies of the Rydberg and ground-state ion (D_0) adiabatic potential energy surfaces, the E_{BE} values for the slow Rydberg pathway can be expected to be relatively constant—as observed experimentally. Conversely, in the fast valence pathway, the population in the strongly mixed Rydberg–valence $3p_x$/V state (S_2 in the FC region) is subject to efficient non-adiabatic coupling to S_1, funnelling down towards a conical intersection with the S_0 state. In the proposed model, the E_{BE} values for the fast valence pathway would increase rapidly,

[i] V indicates the $|2ud0\rangle$ configuration in the language of Chapter 5. This state, denoted as a mixed Rydberg/valence state, is the same state excited in Chapter 8. There, we use a diffuse basis, allowing the active space to become more diffuse to describe the state, whereas here we see contributions from both valence and Rydberg orbitals.

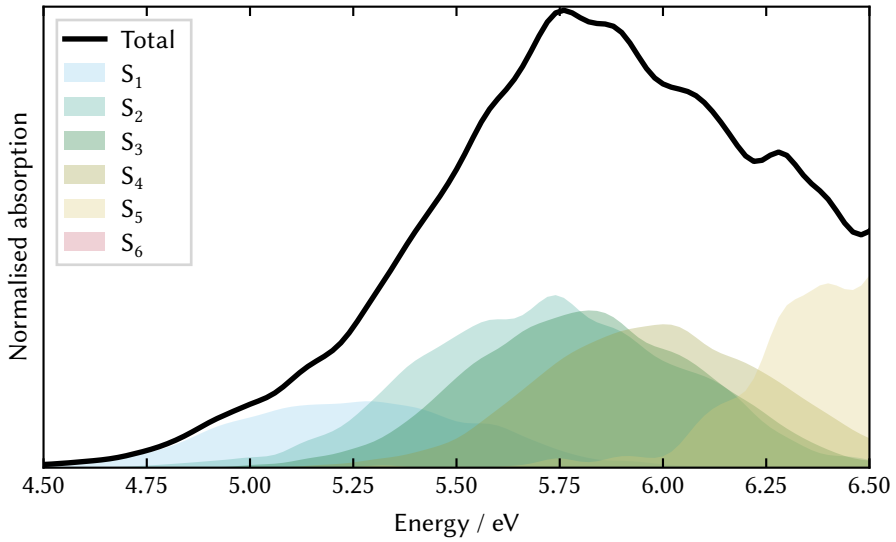

Figure 10.3: Wigner-sampled absorption spectrum of QC using 10000 initial conditions broadened with a Gaussian (FWHM=0.1 eV). Calculated using geometries and energies at the RMS(9)-CASPT2(2,6)/6-31G(d)+ level. The black line indicates the total spectrum, found by adding all the individual state contributions, shown as the shaded regions. The excitation peaks at ≈ 5.8 eV, where the excitation occurs.

consistent with the short-lived structure observed for experimental E_{BE} values in the range of ≈ 1.5–7 eV.

10.4 — Dynamics

We confirm these hypothesised mechanisms using non-adiabatic mixed quantum–classical trajectory simulations (Section 10.1). The simulations divulge that the photo-dynamics of excited QC are strongly dependent on the initial excited state. Figure 10.3 shows the absorption spectrum of the molecule, split into the contributions from the separate states. Immediately, it is clear that multiple states will be excited.

In Figs. 10.4, 10.6 and 10.7 we show the results of the simulations, separated into two sets. Dynamics initiated on the S_2 ($3p_x$/V) state are labelled *fast valence* (always shown on the top row), while dynamics initiated on the S_3 and S_4 ($3p_y$ and $3p_z$) states are labelled *slow Rydberg* (always shown on the bottom row). The plots in Figs. 10.4 and 10.5 show heat-maps of the nuclear dynamics along the r_{cc} and r_{rh} coordinates, respectively, as defined in Eqs. (5.1) and (5.2), which together define the motion between QC, NBD and the S_1/S_0 CI. The left and right sides show the trajectories on the excited states and ground state, respectively. Figure 10.6 shows the time-dependent electronic-state populations and the fraction of population best defined as NBD-like, while the false-colour maps in Fig. 10.7 finally show the contributions to the simulated TRPES spectrum to aid comparison with the experimental data in Fig. 10.1.

We first examine the simulation results for the fast valence mechanism, corresponding to trajectories initiated on the S_2 ($3p_x$/V) state. One-photon excitation to the $3p_x$/V state from the S_0 state is symmetry forbidden at the exact equilibrium geometry, but the transition gains strength from the Herzberg–Teller effect (45% excitation fraction; Methods). The nuclear dynamics in the electronic excited states (Fig. 10.4, left side) breaks the C_1C_2 and C_3C_4 bonds, allowing the molecule to deform towards NBD-like geometries (r_{cc} > 2.0 Å). The wave packet

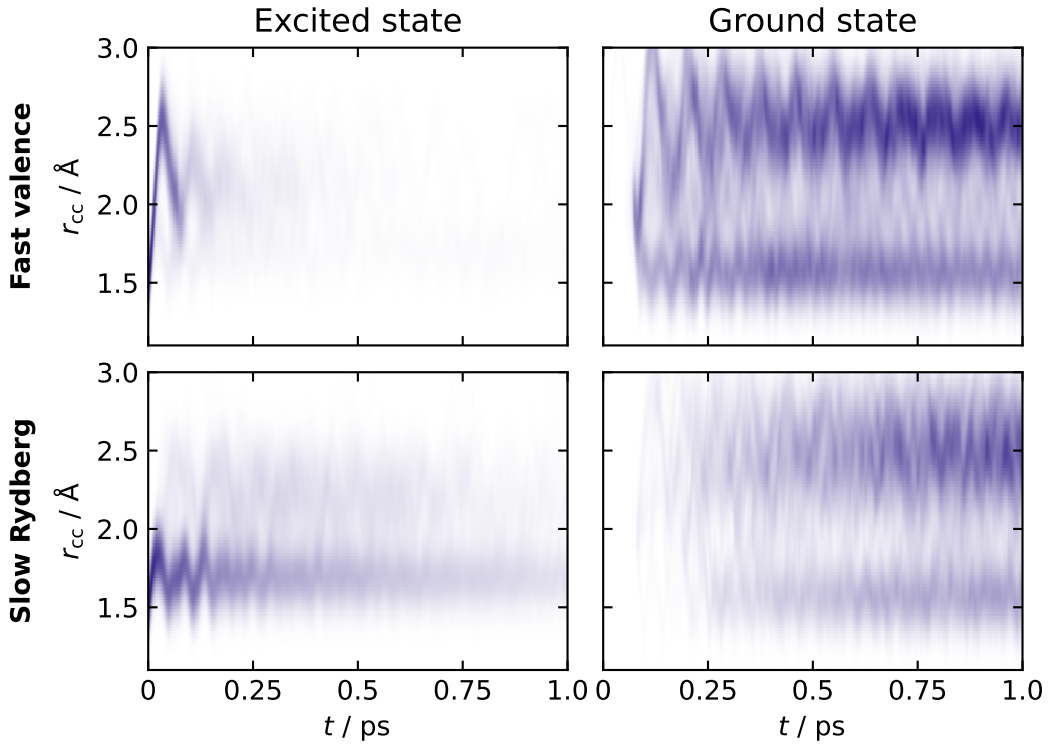

Figure 10.4: r_{cc} heat-maps, with excited state density in the left and ground state density in the right. The valence channel (top row) shows an extremely fast single oscillation on the excited state, before moving to the ground state, where it oscillates. The slow Rydberg pathway (bottom row) has much less motion, with the trajectories merely oscillating around the QC Rydberg minimum at 1.75 Å, where they slowly decay via the same mechanism as the valence channel.

then returns towards QC-like geometries (smaller r_{cc}) and crosses to the S_0 ground state via a conical intersection, appearing on the right side. It immediately partitions into QC-like and NBD-like geometries. The recurrences in the upper map reflect the persistence of the 'butterfly'-like vibrational motion of the NBD products when they first reach the S_0 state (with wave number $\nu = 428$ cm^{-1}, see Table 9.4). The corresponding motion in QC has a higher wave number ($\nu = 721$ cm^{-1}, see Table 9.4) but can also be discerned in the lower maps. In the r_{rh} coordinate (Fig. 10.5, top row), we see an immediate breaking of the symmetry on the excited state, and a large distortion to rhombic geometries. The wavepacket then rebounds once, crossing the $r_{rh} = 0$ line before moving the ground state, where it incoherently vibrates.

This picture is confirmed in the populations (upper plot, Fig. 10.6), which shows almost immediate population transfer from S_2 to S_1 via internal conversion, followed by another rapid internal conversion to S_0, with only a small fraction (<10%) of the population remaining in the Rydberg manifold after 1 ps. The time-dependent fraction of molecules with NBD-like geometries (that is, with $r_{cc} > 2.0$ Å) in the same graph shows a rapid early increase and then decline (mirroring the S_1 state population), finally converging to a branching ratio of ≈ 3:2 for NBD-like to QC-like geometries in the S_0 state. This ratio is set by the decay dynamics rather than energetics, as the timescales are far too short for thermalisation on the ground state.

The theoretically predicted TRPES signal in Fig. 10.7 (top panel) shows a curved band of intensity evolving from the E_{BE} values of the Rydberg state (≈ 2.1 eV) down to that of the S_0 state (≈ 7 eV), in good accord with the 'hockey-stick'-shaped feature in the experimental

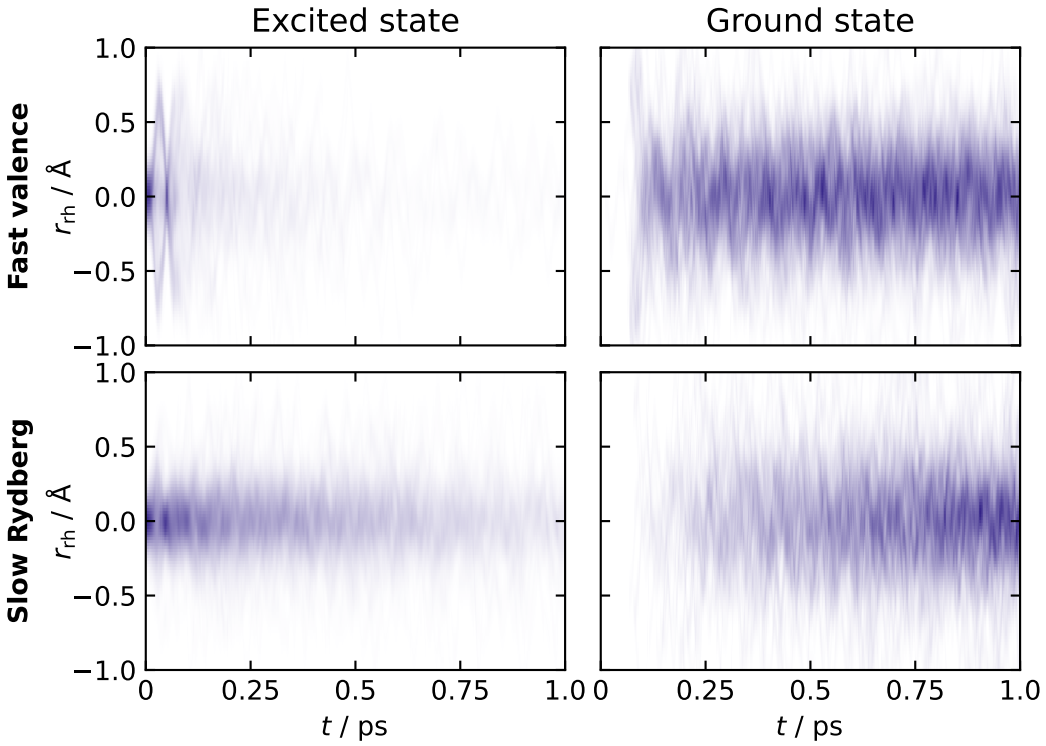

Figure 10.5: r_{rh} heat-maps, with excited state density in the left and ground state density in the right. The fast valence channel (top row) gives a single, large amplitude oscillation before moving to the ground state, then oscillating incoherently. The slow Rydberg pathway (bottom row) overall stays much less rhombically distorted, although shows some small deviations due to the coupling to the valence decay channel.

data (Fig. 10.1). In part, this broad feature reflects the very fast motion of the wave packet down the $3p_x$/V surface, with a corresponding rapid increase in the E_{BE} with respect to D_0. In addition, there is a smaller contribution from the D_1 ionisation channel when the wave packet approaches the MECI. Figure 10.4 (upper left panel) shows that the bond breaks and reforms in under 100 fs, faster than the instrument response function of the experiment, making these features appear almost simultaneously at time $t = 0$.

Next, we consider the slow Rydberg pathway with trajectories initiated on the S_3/S_4 ($3p_y/3p_z$) states, shown in the bottom row of the figures. Already on the left side of Fig. 10.4, it is apparent that the excited-state dynamics persist for substantially longer than in the fast valence mechanism, and that the dynamics are more centred at QC-like molecular geometries (r_{cc} < 2.0 Å), with only a small fraction of the trajectories exploring NBD-like geometries in the 3p excited states, discernible as a faint signal at r_{cc} > 2.0 Å. The r_{rh} coordinate (Fig. 10.5, bottom row), shows similarly slow, long-lived dynamics, without significant rhombic distortion. Examining the populations in Fig. 10.6, we see a comparatively slow but steady deactivation of the Rydberg manifold states (S_2 and higher) with a matching increase in S_0 population. The decay proceeds via the same $3p_x$/V state as the fast valence mechanism, evidenced by the build-up of population in the S_1 intermediate state, which acts as a funnel towards the S_0 state via the conical intersection. It appears that this dynamical decay process is similar between the fast valence and slow Rydberg channels, as the fraction of NBD (Fig. 4b, bottom) approaches the same value at long times.

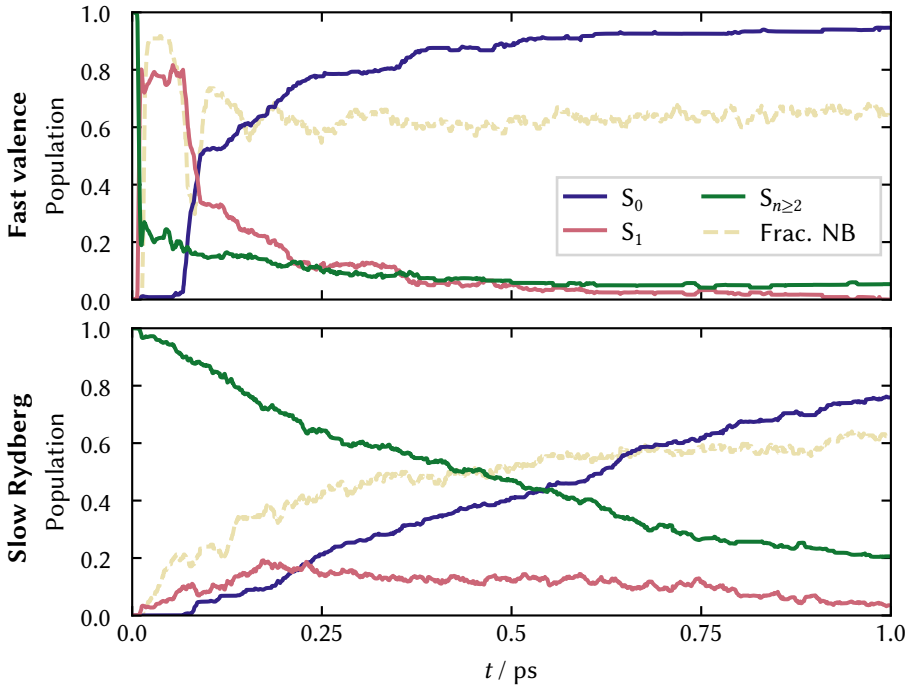

Figure 10.6: Populations and fraction of trajectories in NBD-like geometry ($r_{cc} > 2.0$ Å). The population on states higher that S_1 has been summed. The fast valence pathway (top) quickly decays to the ground state, with the majority of the decay happening before 500 fs. The population decay happens via the S_1 state, which has a large transient population. The slow Rydberg pathway (bottom) decays much more slowly, but comes to agree on the fraction of population in NBD.

The simulated TRPES signal in Fig. 10.7 shows a long-lived feature with $E_{BE} \approx 2.1$ eV, corresponding to the 3p Rydberg states (with potentials along the LIIC of interest that closely track that of the D_0 ionic state), in good accord with the experimental data, which show the corresponding feature attributable to ionisation from these Rydberg states at $E_{BE} \approx 2.3$ eV (Fig. 10.1). At long times, the TRPES signal seen in the slow Rydberg and fast valence dynamics are essentially identical. Both pathways involve similar ultimate decays to the S_0 state, yielding similar branching ratios of hot QC and NBD products. Note that the vertical ionisation potentials of QC and NBD are similar, differing by ≈ 0.3 eV (Methods). Thus, the TRPES signals of hot ground-state QC and NBD species overlap, and the experimentally observed bleach recovery in Fig. 10.1 includes components from both isomers.

Notwithstanding the very good agreement between experiment and theory, some discrepancies are evident. The simulations return longer Rydberg state lifetimes than observed experimentally, which could reflect shortcomings in the electronic structure theory, for example, regarding the strength and location of the couplings with the $3p_x$/V state, additional decay paths not accounted for by the active space used or the accuracy of the predicted ionisation cross-sections.

In summary, TRPES studies using XUV photons from a seeded FEL have provided new and detailed insights into the relaxation pathways of electronically excited QC molecules formed by photoexcitation at 200.6 nm, from Rydberg states through to vibrationally excited hot ground-state QC and NBD molecules. We present observations of the dominant relaxation

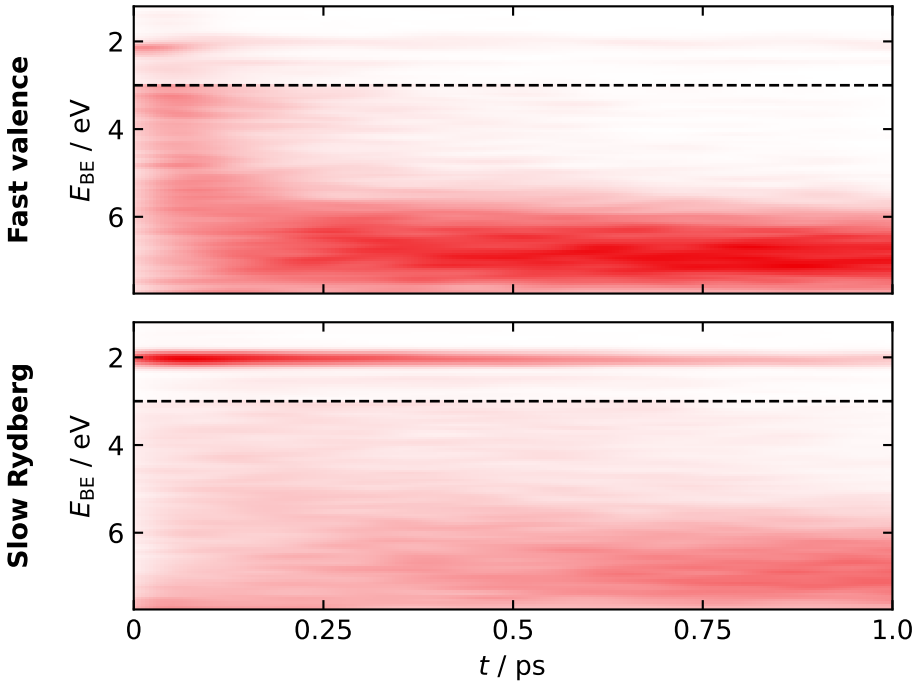

Figure 10.7: Predicted time-resolved photo-electron spectra. The fast valence pathway (top) shows a 'hockey-stick' feature, with the binding energy quickly decreasing from 3 eV to a broad signal at 7 eV. The slow Rydberg channel (bottom) shows the characteristic constant binding-energy feature of Rydberg states, which slowly decays. The decay happens by a similar channel to the valence pathway, but without the coherent start. Features above 3 eV binding energy have been multiplied by three to better match experimental spectra. Convolved with a bi-variate Gaussian of 94 fs and 0.1 eV.

pathway in QC, involving strong Rydberg–valence coupling, alongside the previously observed Rydberg-state-mediated isomerisation.[48] The present combined experimental and theoretical study shows that all three 3p Rydberg states of QC are excited by the 200.6 nm pump pulse. The lowest-energy ($3p_x$) state is strongly coupled to a valence state, giving rise to the fast valence pathway characterised by ultrafast electronic decay and nuclear motion. The other two support initial nuclear dynamics in the Rydberg manifold, prior to comparatively slower decay to the ground state (identified here as the slow Rydberg pathway). The simulations suggest that ≈ 40% of the vibrationally excited ground-state products sampled at pump–probe delays of ≈ 1 ps correspond to QC-like structures, irrespective of the decay pathway followed, and that this early-time partitioning is determined by the molecular dynamics rather than thermodynamics.

The insights provided by the present study point to key features that affect the photodynamics: the partial absorption cross-sections, the strength of the non-adiabatic couplings to the valence excited state and the relative stabilities and geometries of the regions of maximal interstate coupling, that is, the conical intersection between the S_1 and S_0 states. For potential applications, these properties could be manipulated using substituent groups, using spatial confinement and/or by the choice of excitation wavelength.[18,52,53,271] For instance, the detailed nature of valence/Rydberg mixing in the valence state controls its energy and accessibility, which could be used to affect the system's function as a molecular photoswitch. The manner

in which the wave packet approaches the S_1/S_0 conical intersection region is also important, and this could be manipulated either in the preparation of the wave packet or by altering the position and shape of the conical intersection.

From a broader photochemical perspective, one might conjecture that the bipartite dynamics found here will be a common feature whenever a manifold of Rydberg states intersects valence states in the FC region.[272–274] The excitation energies to Rydberg states typically fall within ≈ 3 eV of the associated ionisation limit, and, in most small to medium-sized molecules, will overlap with those of one or more excited valence states. Rydberg excitations will manifest as a longer-lived trapping component, whereas excitations to valence states (or, as here, to a mixed Rydberg–valence state) will lead to more-rapid relaxation that gives rise to broad features in the photoelectron spectrum. Broadband excitation can excite both types of states, leading to both types of mechanism. Bifurcation of wave packets has been reported previously, for example, in the photo-isomerisation of stilbene[275] and in photoexcited inverse dithienylethene derivatives,[276] but in most such cases studied hitherto, the bifurcation arises as a result of sampling a 'transition-state'-like region of a common excited state (for example, a $\pi\pi^*$ state), the potential energy surface of which supports multiple minima.

The current results demonstrate the utility of TRPES with XUV probes for characterising complex photochemical mechanisms. Comparison with previous experiments[48] indicates that a systematic examination of the effect of excitation wavelength would be useful. Ideally, this should be coupled to complementary experimental work more sensitive to molecular geometry. For instance, ultrafast electron diffraction and ultrafast x-ray scattering experiments[131,134,228,244] might offer further insights into the dominant conical intersection and, at longer times, reveal fragmentation products from the hot ground-state molecules. We anticipate that future experiments should provide an even deeper understanding of the intriguing ultrafast ring re-configurations in this photoswitch molecule.

— 11 —

Conclusions

Over the last six chapters, we have presented a detailed analysis of a model photoswitch system's electronic structure, dynamics and experimental observables.

We first explored the nature of the valence states, starting with the electronic structure in Chapter 5. Here, we investigated the system's qualitative photochemistry, finding the topographically important features of the potential energy surfaces. This work provided a general framework for simulating these systems, accurately describing the regions that drive photochemical behaviour. This was highlighted by a detailed, multi-method description of the single S_1/S_0 conical intersection. All methods agreed that the intersection was peaked, but predicted different numbers of pathways on the ground state surface. In addition, an excited state minimum was identified and confirmed using high-level electronic structure methods. This minimum was posited to play a role in the dynamics, with the methods that lacked the feature potentially providing qualitatively different results.

An important outcome of Chapter 5 was four dynamically-feasible electronic structure models. These models were benchmarked against each other and high-level MRCI+Q and LR-CC3 methods, finding that the CASSCF(4,4) method, previously used on the system, produces qualitatively dubious results. The other three methods all agreed on the approximate shape of the potentials, with only minor differences. This consensus lends more credibility to the ensuing dynamics simulations, but also provides an intriguing testbed of subtly different potential energy surfaces on which to evaluate different non-adiabatic dynamics methods. Finally, we introduced a custom basis set, p-cc-(p)VDZ, which achieves results almost identical to larger basis sets for a fraction of the cost.

In Chapter 6, we simulated the non-adiabatic dynamics of the system using the four electronic structure methods, using otherwise identical parameters in the simulations. Building on the qualitative, static analysis of the potential energy surfaces presented in Chapter 5, we found that the CASSCF(4,4) electronic structure yields qualitatively incorrect results, while the other electronic structure models gave approximately similar results. Looking more closely, we found that the presence of the S_1 local minimum significantly affected the results, with the one model not predicting the minimum, XMS-CASPT2(2,2), resulting in notably different molecular dynamics. Most interestingly, the branching ratios depended primarily on the velocity of the trajectories before they reached the conical intersection region rather than on the hopping region or the local topography of the intersection,[68,85,217,221,277] which changed through the electronic structure methods. These results, which contrast the purely static analysis, underscore the importance of performing simulations when predicting photochemical reaction outcomes.

With the dynamics established, Chapter 7 focused on experimental observables, calculating time-resolved x-ray scattering patterns and photo-electron spectra. These two experimental techniques offer plausible routes for establishing the validity of our predicted dynamics. We analysed the predicted signals to determine which features in the dynamics were experimen-

tally verifiable, and decomposed the signals into their constituent parts, affording a detailed understanding of both these features and the observables themselves. Finally, we suggested two experiments that would probe two separate attributes. This work, above all, demonstrated the need for multi-modal experimental studies. For the sake of an example, the ultrafast decay dynamics was well understood by (e.g.) time-resolved photo-electron spectroscopy, but the motion of the nuclei was much more clearly seen in ultrafast scattering experiments. Combining the measurements lead to an understanding of both, and a whole greater than the sum of its parts.

Chapter 8 explored the dynamics of QC after valence state excitation. These dynamics showed surprising similarities to Chapter 6, with the dynamics initially forming excited-state NBD with a significant rhombic distortion. After that, the trajectories passed through the same S_1/S_0 CI, with the trajectory outcome again principally affected by the velocity prior to passage through the conical intersection, confirming the earlier results of Chapter 6. These results also showed an intriguing ultrafast channel with coherent, NBD-forming decay within 10 fs of the initial excitation.

Finally, Chapters 9 and 10 showed two joint theoretical/experimental studies. In Chapter 9, we thoroughly analysed the static absorption and photo-electron spectra of NBD and QC, looking primarily at the Rydberg and higher-lying states. This work disentangled the entire spectrum, assigning all the important visible progressions, including reassigning the important band origins. While not directly connected to the other chapters, this work remains vital for future studies on the norbornadiene system, including any potential ultrafast experiments that initially excite the low-lying Rydberg states.

In Chapter 10, we showed the results of a combined experimental-theoretical study of the Rydberg/valence dynamics in photo-excited quadricyclane. The dynamics depended almost entirely on the initial state excited, with a very fast decay after excitation into the $3p_x$/V state, and slower, more leisurely dynamics upon excitation into the $3p_y$ and $3p_z$ manifolds. This work provided a particularly dramatic example of the importance of the initial state in photo-excited dynamics, predicting bipartite dynamics with a slower Rydberg and faster valence channel, a feature likely common in small organic molecules. This highlighted the benefit of mixed experimental/theoretical studies, with the theory providing insight and identifying general photochemical features from a complex ultrafast experiment.

The work presented in this thesis provides a holistic overview of an important model system, encompassing *state-of-the-art* experiments, potential energy surfaces and dynamics. However, the study of this system is far from complete, and therefore, we add a brief discussion of possible avenues for future research, as well as contextualising this work in the broader field of photochemistry.

It has long been known that photochemical dynamics outcomes are highly dependent on conical intersections.[68,76,79–86,217,221,222,278] Further, there are two limiting cases of dynamics: where the motion before the conical intersection is important,[68,82,217,218,222,278] and where the local topography of the potentials dictates the outcome.[80–83,85,217] The conclusion of Chapters 6 and 8 is that the NBD/QC system falls very firmly into the former camp, with the primary factor being the velocity of the wavepacket before the intersection. We posit that this feature is common in photoswitches, as it seems a relatively straightforward way to achieve efficient, multi-outcome processes.[279–281] We should thus expect photoswitches to often show peaked, bifurcating intersections, which bias the dynamical outcomes less than sloped intersections.

Although this system shows coherent dynamics from the excitation to the intersection, it is also possible to imagine a less coherent photoswitch process, where the excited dynamics is initially trapped in an excited-state minimum.[279] From there, it can gradually 'leak' out,

moving towards the intersection from a well-defined region in phase space. Alternatively, the dynamics before the intersection could allow for the wavepacket to cross at different locations on the seam, each with variable local topography.[217] Therefore, one could alter the quantum yield by controlling which intersection is accessed.

The QC/NBD system is an exciting test-bed for control and reactivity in photochemistry, especially concerning short, coherent dynamics. Focusing on this coherent limit affords higher-level simulations, as well as more clearly isolating the key factors governing the reaction outcomes, which are central to the design of practical applications. While this work concentrated on the unsubstituted isomer, exploring how substituent groups influence the potential energy surfaces and dynamics is a natural next step. This allows for further subtle changes in the dynamics, leading to both potential and inertial effects,[68,222] improving our knowledge of this system and dynamics through conical intersections as a whole.

Understanding these factors will also refine our emerging 'design rules', both increasing our theoretical understanding and potentially leading to more efficient devices. For example, many systems currently under consideration for practical applications are asymmetrically substituted[20], aligning with our predictions that breaking the symmetry could lead to a more efficient reaction (see Chapters 6 and 8). Testing our understanding by performing that substitution in this efficient, reliable and well-understood computational model is, therefore, a crucial next step. Finally, we add that solvent effects on the potentials and dynamics will be significant, and should be explored further.

Chapters 6 and 8 explore the variations in dynamics after changing two key parameters: the potential energy surface and the initial conditions. The third key ingredient in dynamics simulations is the method used to solve the nuclear equations of motion, and QC/NBD provides an excellent testing ground for comparing different dynamics methods. The system is comparatively simple, exhibiting ultrafast internal conversion via a single, well-defined conical intersection, and the CASSCF(2,2)/p-cc-(p)VDZ model is highly computationally efficient. Yet, even small changes in the potentials lead to notable discrepancies in decay times and quantum yields, and understanding how the dynamics method affects these observables is undoubtedly of interest. This is highlighted by the notably divergent ab initio multiple spawning results, confirming the value of benchmarking mixed-quantum-classical and semi-classical dynamics methods in this system.

For this, a helpful tool would be a set of parameterised potential energy surfaces. As shown in this work, the key dynamics in this system occurs in a relatively small set of internal coordinates, a feature already noticed by previous authors.[188] However, it should be noted that NBD/QC is not suitable for a description using a simple linear vibronic coupling model, and so a set of calculated potential energy surfaces in a limited subspace of selected internal degrees of freedom is the next step. Of course, this would allow for a fully-quantum simulation, and possible validation of the simple classical models we have used here to study the dynamics.

An underlying theme of this work is the connection of theoretical results to experiments. Currently, computer simulations cannot provide correct answers for anything but the most straightforward systems, and validation to experiment is the linchpin of understanding non-adiabatic dynamics. In light of this, careful consideration must be given to the calculation of experimental observables, both in terms of the correctness of the predictions and, more saliently, how we compare experiments to theoretical simulations. To what extent different experimental techniques are sensitive to changes in dynamics should be extended to other molecules, especially as this system displays such a limiting case of dynamics. We also focused only on two specific observables — photo-electron spectroscopy and x-ray scattering — but future work should branch into other experimental techniques, such as electron scattering,[46]

Coulomb explosion imaging,[282,283] core electron spectroscopy[284–288] and transient absorption spectroscopy.[289,290]

Naturally, predicting experimental variables invites a connection to actual experiments. This work, which has already been started (see Chapters 9 and 10), requires extensive collaboration with a host of groups worldwide. Ultrafast experiments are still in their infancy and rapidly improve each year, with breakthroughs in light sources, detectors and, as highlighted in this thesis, theoretical understanding. This, combined with their dependence on theoretical exposition, implies that experiments should be pre-empted by theoretical work, which can guide the experimental parameters to ensure a positive outcome. In this work, we closely looked at time- and energy-resolution, providing tangible goals for experimental work and suggesting regions and features for close analysis in experiment. Given the extreme expense, both financial and ecological, of experimental time at modern facilities, an in-depth theoretical exploration of these features, as well as a realistic discussion of what could be observed, should be standard practice before embarking on these experiments.

For the interpretation of future experiments, a set of simulations of NBD dynamics *including* Rydberg states is a necessary next step. Traditionally, this requires the explicit description of the Rydberg states in the electronic structure, as described in Chapter 10, which is computationally challenging, as the varied nature of the states often leads to one part of the system being described more correctly than another. For this, we believe that combining the results of multi-channel quantum defect theory,[56,170] an excellent way to describe Rydberg states, with standard ab initio electronic structure theory, is a promising approach for future studies.

More broadly, this system serves as an invaluable case study in photochemistry. Its short and coherent dynamics make it particularly appealing for practical applications, where efficiency and controllability are paramount, but it pushes the boundaries of currently available experimental techniques, presenting technical and theoretical challenges for measurements and their interpretation. Fully understanding this system, and how to simulate, control and modify it, offers valuable insights into ultrafast chemical reactions, pushing the boundaries for a greater influence of non-adiabatic simulations on modern chemistry. Eventually, this could lead to further advances in our general understanding of photochemical processes, a tantalising goal since the advent of *femtochemistry* more than 20 years ago.

Appendices

— A —

Calculation of Scattering Observables

Using ab initio electronic structure theory calculations (such as those covered in Chapter 3), one can calculate the properties needed for both x-ray and electron scattering (Eqs. (4.16), (4.17), (4.22) and (4.23)). These calculations, which we denote as *ab initio scattering* (AIS), are performed using an code developed in the group. The details of these calculations are unimportant to the results, as the calculations we return are essentially perfect[i]. As the wavefunction from the ab initio calculations gets better, the scattering pattern should also, as it is a direct measure of the wavefunction. Technical details of how these calculations are performed are beyond the scope of this work and can be found elsewhere.[121,291,292]

A very popular approximation of the scattering signal can be found in the *independent atom model* (IAM).[149,150] In this, we approximate the one-electron density of a molecule as the sum of atomic densities, or

$$\rho^{\mathrm{IAM}}(\boldsymbol{r}) = \sum_{\alpha}^{N_{\mathrm{at}}} \rho^{\alpha}(\boldsymbol{r}, \boldsymbol{R}_{\alpha}), \tag{A.1}$$

where $\rho^{\alpha}(\boldsymbol{r}, \boldsymbol{R}_{\alpha})$ is the density of atom α centred at position $\boldsymbol{R}_{\alpha}$. From this, one can derive equations to calculate the total scattering as

$$\Lambda_{mm}^{\mathrm{IAM}}(\boldsymbol{q}) = \underbrace{\sum_{\alpha,\beta}^{N_{\mathrm{at}}} f_{\alpha}(\boldsymbol{q})\, f_{\beta}(\boldsymbol{q})\, e^{i\boldsymbol{q}\cdot\boldsymbol{R}_{\alpha\beta}}}_{|L_{mm}^{\mathrm{IAM}}|^2(\boldsymbol{q})} + \underbrace{\sum_{\alpha}^{N_{\mathrm{at}}} S_{\alpha}(\boldsymbol{q})}_{\sum_{f\neq m} |L_{mf}^{\mathrm{IAM}}|^2(\boldsymbol{q})}, \tag{A.2}$$

where $f_{\alpha}(\boldsymbol{q})$ is the *coherent form factor* for atom α. This is the same quantity as L_{mm}, but we shall use the term form factor to distinguish the different uses. These are coherently summed, modulated by the distance between the two atoms $\boldsymbol{R}_{\alpha\beta}$, to give the elastic IAM scattering. $S_{\alpha}(\boldsymbol{q})$ is the *incoherent form factor* for atom α, calculated as $(\Lambda_{mm} - |L_{mm}|^2)$ (i.e. the inelastic scattering), and the incoherent sum of these leads to the inelastic scattering. Both of these quantities are tabulated in the International Tables of Crystallography (ITC), and we shall use these values in all calculations from here on.

Of course, we could re-frame this equation into a rotationally averaged calculation, and retrieve

$$\Lambda_{mm}^{\mathrm{IAM}}(q) = \underbrace{\sum_{\alpha,\beta}^{N_{\mathrm{at}}} f_{\alpha}(q)\, f_{\beta}(q)\ \mathrm{sinc}\left(qR_{\alpha\beta}\right)}_{|L_{mm}^{\mathrm{IAM}}|^2(q)} + \underbrace{\sum_{\alpha}^{N_{\mathrm{at}}} S_{\alpha}(q)}_{\sum_{f\neq m} |L_{mf}^{\mathrm{IAM}}|^2(q)}. \tag{A.3}$$

[i] By perfect, we mean that they are a faithful reproduction of the scattering pattern *for a given electronic wavefunction*, within the 1st Born approximation and with no relativistic effects. Of course, the calculation of the electronic wavefunction will itself also be imperfect.

The calculations for electron scattering can be found in an analogous way. For this, we use the modified formula for the coherent form factors

$$g_\alpha(q) = f_\alpha(q) - Z_\alpha. \tag{A.4}$$

This is then used in the same expression as in Eq. (A.3), giving

$$\begin{aligned}\Xi^{\mathrm{IAM}}_{mm}(q) &= \overbrace{\sum_{\alpha,\beta}^{N_{\mathrm{at}}} g_\alpha(q)\, g_\beta(q)\, \mathrm{sinc}\left(qR_{\alpha\beta}\right)}^{|\xi^{\mathrm{IAM}}_{mm}(q)|^2} + \overbrace{\sum_{f\neq m} \sum_{\alpha}^{N_{\mathrm{at}}} S_\alpha(q)}^{|\xi^{\mathrm{IAM}}_{mf}(q)|^2} \\ &= \Lambda^{\mathrm{IAM}}_{mm}(q) - 2\sum_{\alpha,\beta}^{N_{\mathrm{at}}} f_\alpha(q) Z_\beta\, \mathrm{sinc}\left(qR_{\alpha\beta}\right) + \sum_{\alpha,\beta}^{N_{\mathrm{at}}} Z_\alpha Z_\beta\, \mathrm{sinc}\left(qR_{\alpha\beta}\right).\end{aligned}$$

Again, we retrieve two additional terms related to the nuclei. The mixed term, shown here in its form factor form, and the nuclear term, which is identical in the ab initio and IAM cases.

The independent atom model is an odd method. As the density is merely the sum of the individual atomic densities, it is incapable of describing any distortions of the electron density due to the molecular environments. This includes the very significant bonding and correlation effects that are seen in all molecules, as well as the difference between different electronic states. Despite the fact that Eq. (A.1), at least on the surface, seems an extremely harsh approximation, the IAM is annoyingly accurate. To use the example of dynamics, the majority of the change in electron density is caused by the motion of nuclei and the subsequent motion of the core electrons. This is particularly stark for heavy atoms, for example iodine, where the IAM gives fantastic results. The core electrons of iodine are just not particularly affected by the chemical environment, and if they are, the effect is only a very small motion, which scattering is not sensitive enough to pick up.

— B —

Valence States

B.1 — Electronic Structure

Orbitals Images

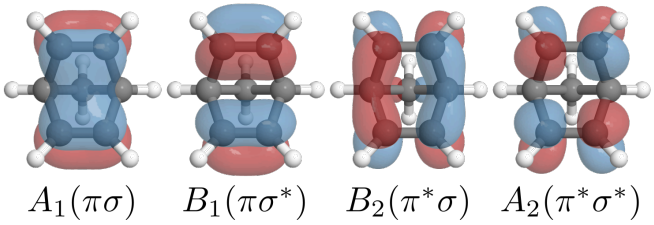

Figure B.1: Orbitals (iso-surface value of 0.05) for CASSCF(4,4)/p-cc-(p)VDZ at the NBD geometry. We use the same labelling as Fig. 5.2.

In Fig. B.1, we show the orbitals in NBD for CASSCF(4,4), matching Fig. 5.2. For the CASSCF(2,2)/p-cc-(p)VDZ calculations, as shown in Fig. B.2, the state-averaged (SA) natural orbitals do not resemble the orbitals of the (4,4) active space. This is due to the effect of the S_2 state, which is not well described, adding asymmetry. The natural orbitals for the S_0 state (or the S_1 state), show the more familiar shapes, akin to the B_1 and B_2 orbitals in the (4,4) active space. The asymmetry in the orbitals does not affect the calculations — the two sets of orbitals are simply a rotation of each other.

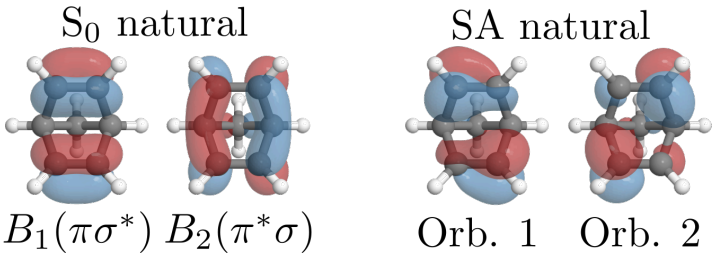

Figure B.2: Orbital (iso-surface value of 0.05) for CASSCF(2,2)/p-cc-(p)VDZ at the NBD geometry. On the right, we show the state-averaged (SA) natural orbitals, which exhibit pronounced asymmetry. The state-specific orbitals for the S_0 state (left, S_1 state gives similar results), do not show this asymmetry, and look much closer to Fig. B.1.

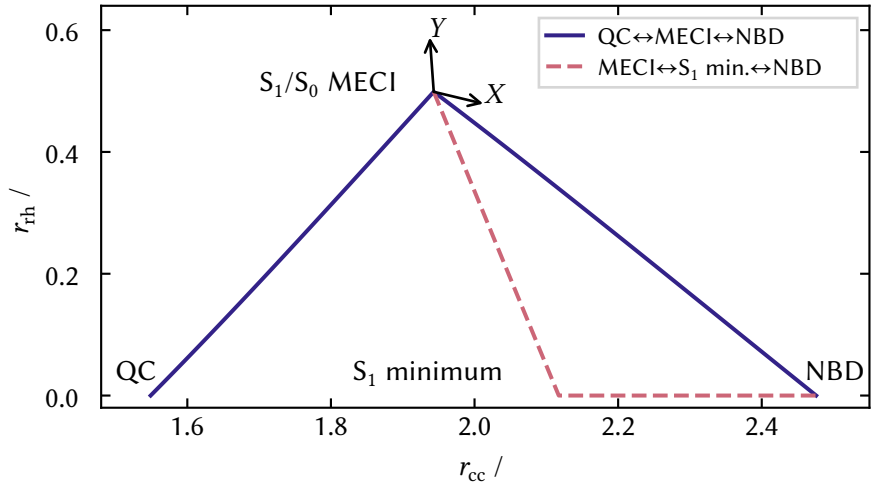

Figure B.3: Carbon-carbon distance coordinates for the two LIICs used in the (r_{cc}, r_{rh})-plane, with key geometries labelled. All geometries are calculated at CASSCF(2,2)/p-cc-(p)VDZ level. The projection of the two branching plane coordinates X and Y into the plane are also shown (cf. Fig. 5.12).

Pathway Geometries

In Fig. B.3, we show the two LIICs in the (r_{cc}, r_{rh})-plane. The QC↔S_1/S_0 MECI↔NBD LIIC (solid indigo line) travels straight between the minima and the conical intersection, conserving approximate C_2 symmetry. The S_1/S_0 MECI↔S_1 minimum↔NBD LIIC first traverses from the conical intersection to the S_1 minimum, maintaining (approximate) C_2 symmetry, and then moves to NBD, maintaining $r_{rh} = 0$ and C_{2v} symmetry. It is clear that we do not need to plot the QC↔S_1/S_0 MECI on both pathways. These pathways approximate the CASSCF(2,2) and XMS-CASPT2(2,2) dynamics, respectively (cf. Chapter 6).

Rydberg States

In Fig. B.4, we show the potential energy cuts for SA(8)-CASSCF(4,8)/aug-cc-pVDZ, a method similar to those used in previous work.[53,188] This adds a 3s and three 3p orbitals to the (4,4) active space (shown in Fig. C.2). Without CASPT2, this does not improve on the CASSCF(4,4) surface, and even predicts the Rydberg states (the flat manifold at $\approx$ 4 eV) below the valence state (the steeply sloped excited state) in NBD. Figure B.5 shows the results with XMS-CASPT2(4,8)/aug-cc-pVDZ, an improvement on CASSCF(4,8)/aug-cc-pVDZ, compared to CASSCF(2,2) and XMS-CASPT2(4,4) (both using p-cc-(p)VDZ). We can clearly see that the important S_1 valence state in NBD, on which the dynamics of Chapter 6 is based, is unaffected by including the Rydberg states, validating our model. In the QC isomer, this is less clear, and the valence state becomes close in energy to the Rydberg states. As such, our valence-only model (see Chapter 8) would not explain all of the observed experimental dynamics, as shown in Chapter 10.

MRCI

Here we show the PECs for the QC↔S_1/S_0 MECI↔NBD LIIC for CASSCF (indigo solid lines), MRCI (rose dashed) and MRCI+Q (green dotted) for the (2,2) (left panel) and (4,4) (right) active

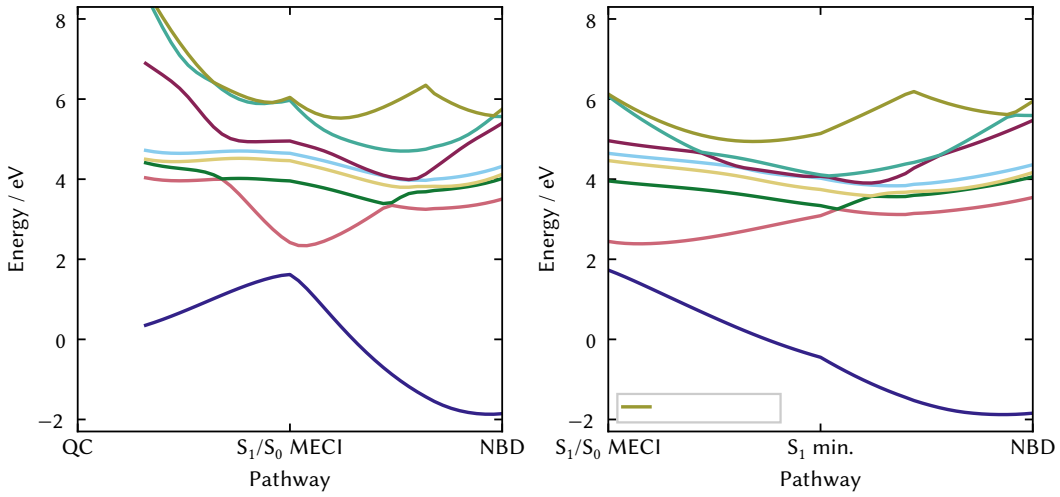

Figure B.4: Potential energy cuts for SA(8)-CASSCF(4,8)/aug-cc-pVDZ. Left: QC↔S_1/S_0 MECI↔NBD. Right: S_1/S_0 MECI↔S_1 min.↔NBD. The valence state (the strongly sloped excited state potential) is far higher in energy than the Rydberg state (the flat potentials at ≈ 4 eV, which would lead to vastly different dynamics.

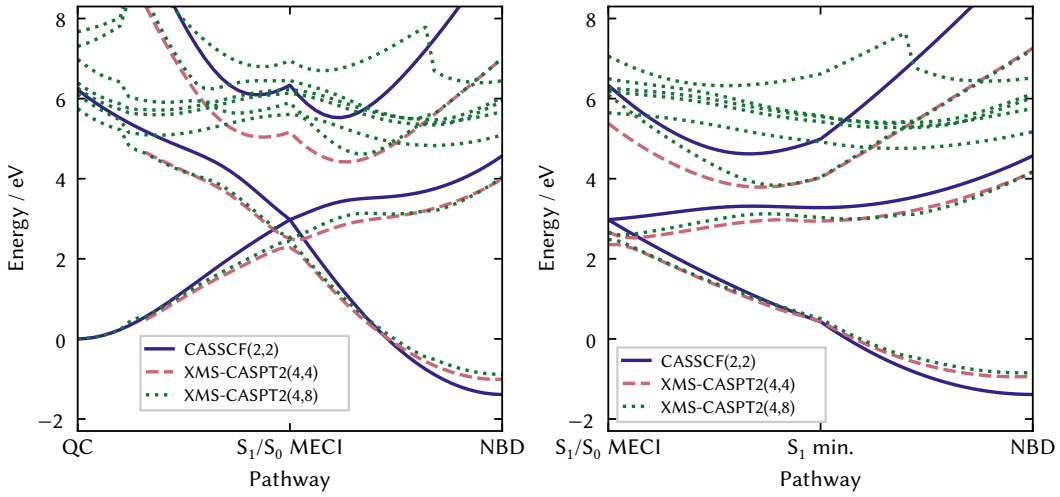

Figure B.5: Potential energy cuts for XMS(8)-CASPT2(4,8)/aug-cc-pVDZ. Left: QC↔S_1/S_0 MECI↔NBD. Right: S_1/S_0 MECI↔S_1 min.↔NBD. The CASSCF(2,2) (indigo solid), XMS-CASPT2(4,4) (rose dashed) and XMS-CASPT2(4,4) (green dotted) all show strong agreement for the lowest two states (S_0 and the valence excited state). Unlike the other two, XMS-CASPT2(4,8) shows Rydberg states at ≈ 6 eV, which do not interact with the lower valence states. As such, ignoring the Rydberg states is a valid approximation for the valence dynamics.

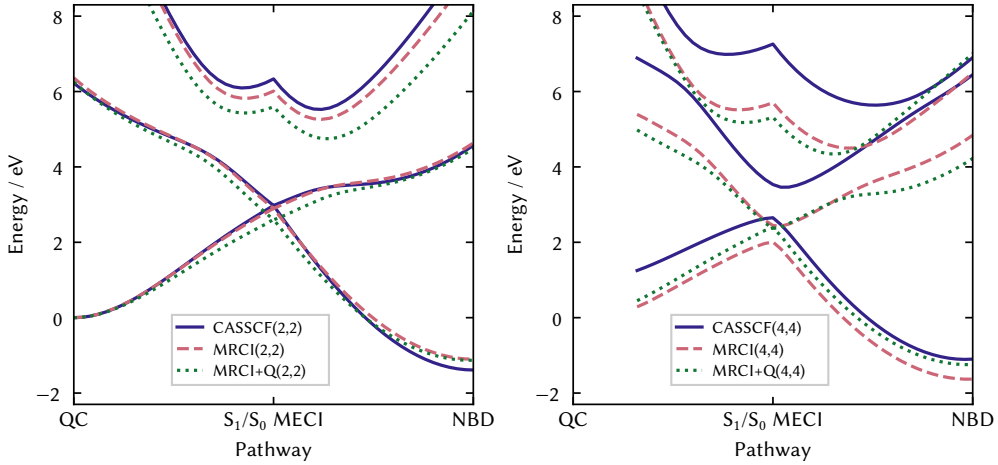

Figure B.6: MRCI on the QC↔S_1/S_0 MECI↔NBD LIIC. Left: CASSCF (solid, indigo) vs MRCI (dashed, rose) vs MRCI+Q (dotted, green), with both (2,2) (left) and (4,4) (right) active spaces. All calculations are performed with the p-cc-(p)VDZ basis set. The (2,2) active space subtly changes the description for S_0 around the NBD minimum, but qualitative agreement is seen elsewhere, even with the Davidson correction. For the (4,4) active space, the three methods do not agree even qualitatively, with a notable $\approx$ 2 eV discrepancy in excitation energy in NBD. Notably, the MRCI+Q(4,4) calculations give a similar shape to all three (2,2) active space methods.

spaces. The (2,2) case gives very close agreement for all states, whereas the (4,4) case requires the Davidson correction for the calculation to be even qualitatively correct.

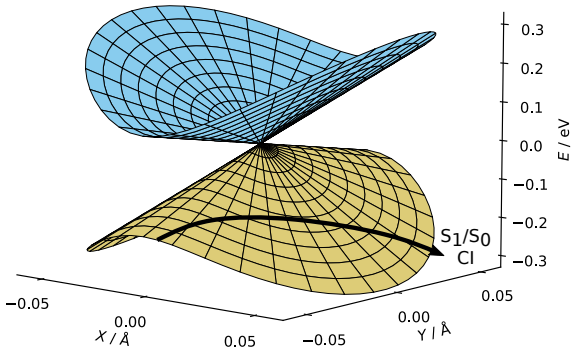

Figure B.7: Energies in the branching-plane of S_2/S_1 conical intersection, using the local linear representation[78]. This is a peaked, bifurcating intersection. The branching plane vectors are shown in Fig. B.8, with X breaking the symmetry and Y preserving it. The conical intersection was optimised using XMS-CASPT2(4,4)/p-cc-(p)VDZ. An illustrative trajectory is shown, which would travel from NBD to the S_1/S_0 conical intersection, missing the S_2/S_1 conical intersection

The S_2/S_1 Conical Intersection

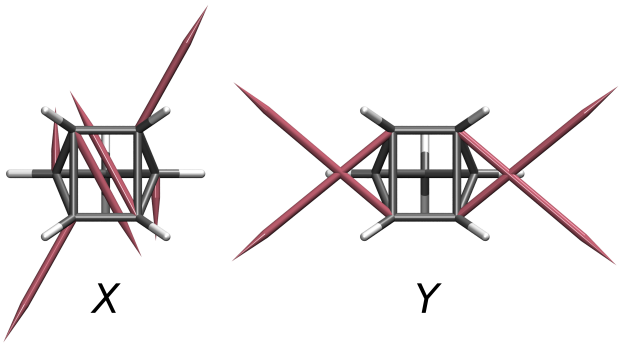

Figure B.8: Branching plane vectors for the S_2/S_1 conical intersection, optimised using XMS-CASPT2(4,4)/p-cc-(p)VDZ. The *X* vector is a rhombic displacement, which takes the molecule almost directly to the S_1/S_0 conical intersection, while the *Y* vector is very similar to the displacement vector from NBD to QC. All vectors are almost entirely within the plane of the figure.

When using XMS-CASPT2(4,4)/p-cc-(p)VDZ, the S_2/S_1 conical intersection can be found at $(r_{cc}, r_{rh}, r_{db}) \approx (2.01, 0, 1.48)$ Å, close to the S_1 minimum (it does not exist in CASSCF(2,2)). Figure B.7 shows the branching plane energies for this intersection (using the approximation in Section 2.2). It has C_{2v} symmetry, with S_2 defined as A_1 and S_1 as A_2. This is a peaked, bifurcating intersection. By looking at the vectors in the branching plane (shown in Fig. B.8), we can identify the *X* direction as breaking the symmetry with a rhombic displacement (increasing magnitude of r_{rh}), while the *Y* direction is symmetric, decreasing r_{cc} and increasing r_{db}. In short, *X* moves towards the S_1/S_0 conical intersection, while *Y* from NBD to QC. As this is a symmetric geometry and the two states have different symmetries, *X* can be identified unambiguously with the non-adiabatic coupling and *Y* with the gradient difference.

Using Fig. B.7, it is clear that any dynamics which started in NBD (i.e. coming from negative *Y* along the lower S_1 surface) would be split into two separate channels, each going to the mirror-image copies of the S_1/S_0 CI, and we expect minimal S_2 population. For clarity, we illustrate this with an example trajectory, drawn as a vector. This conical intersection is also present in the XMS-CASPT2(2,2) method, with similar energies and branching plane vectors. Notably, the conical intersection is more peaked, leading to less transfer to the S_2 state.

Basis Set Contraction

For clarity, we include a table of the basis set primitives and contractions of p-cc-(p)VDZ in Table B.1.

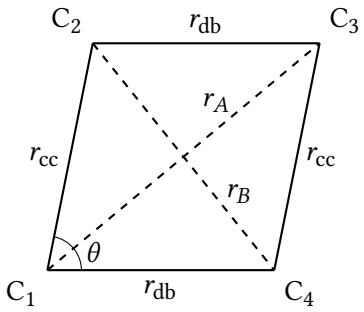

Figure B.9: Definition of four-carbon ring distances. Here it is drawn as a planar parallelogram, with the C_1C_2 and C_3C_4 distances equal (r_{cc}), as well as the C_1C_3 and C_2C_3 distances (r_{rh}). The angle θ and the two distances r_{cc} and r_{db} is sufficient to define the shape. In a non-symmetrical shape (such as a trapezium), information about all of the angles and distances is necessary.

Table B.1: Primitives and contractions for the p-cc-(p)VDZ basis set. This is a effectively a pruned aug-cc-pVDZ basis set, removing all diffuse and polarisation functions off of hydrogen atoms (a [4s|2p] contraction), and the S and D angular momentum diffuse functions off of carbon atoms (a [9s5p1d|3s3p1d] contraction). Zero values are not shown.

Atom	Ang. mom.	Primitives	Contractions		
H	**S**	13.01	0.019685		
		1.962	0.137977		
		0.4446	0.478148		
		0.122	0.50124	1	
C	**S**	6665	0.000692	-0.000146	
		1000	0.005329	-0.001154	
		228	0.027077	-0.005725	
		64.71	0.101718	-0.023312	
		21.06	0.27474	-0.063955	
		7.495	0.448564	-0.149981	
		2.797	0.285074	-0.127262	
		0.5215	0.015204	0.544529	
		0.1596	-0.003191	0.580496	1
	P	9.439	0.038109		
		2.002	0.20948		
		0.5456	0.508557		
		0.1517	0.468842	1	
		0.04041			1
	D	0.55	1		

B.2 — Dynamics

Coordinate Non-Orthogonality

In the Eqs. (5.1) to (5.3), we introduce three separate distance coordinates to measure the displacements in dynamics. These coordinates are the wing-separation coordinate $r_{cc} = 0.5(r_{12} + r_{34})$, the rhombicity coordinate $r_{rh} = r_{13} - r_{24}$ and the double-bond length $r_{db} = 0.5(r_{14} + r_{23})$, defined in figure B.9. These constitute a complete description of the geometry of the four-carbon ring in a planar C_2 symmetry — i.e. a parallelogram. Of course, in the

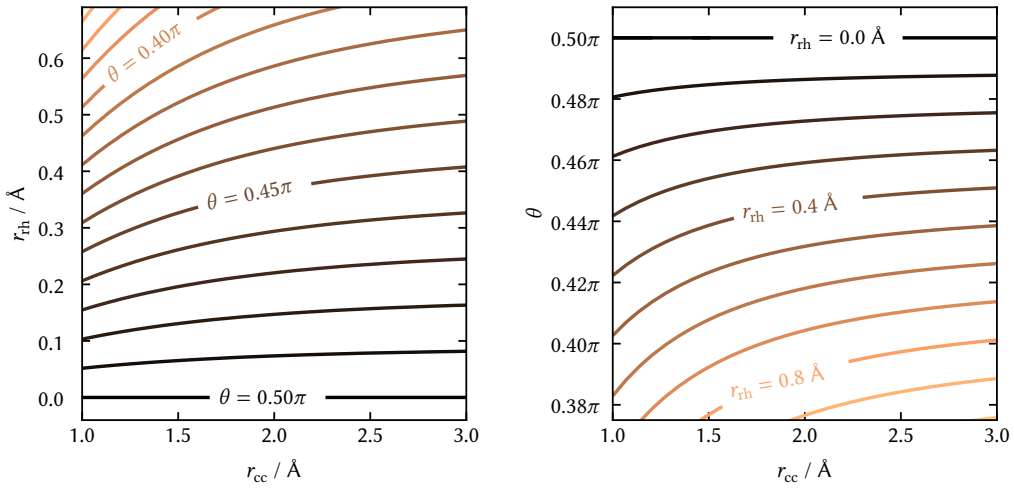

Figure B.10: Contour maps of coordinate planes. $r_{db} = 1.442$ Å, i.e. the value of the CASSCF(2,2) S_1/S_0 MECI, and the geometry is constrained to planar C_2 symmetry. Left: Constant θ values in the (r_{cc}, r_{rh})-plane. At $\theta = 0.5\pi$ there is no rhombicity. θ decreases as r_{rh} increases, with the rate decreasing as a function of r_{cc}. The same effect is seen as r_{db} increases. Right: Constant r_{rh} values for (r_{cc}, θ)-plane. At smaller values of r_{cc}, a value of r_{rh} indicates a larger value of θ.

dynamics this symmetry is broken, and there are countless geometries associated with each of the values (r_{cc}, r_{rh}, r_{db}).

r_{rh} can be related to the other distances and the angle θ (see Fig. B.9) as

$$r_{rh} = \sqrt{r_{cc}^2 + r_{db}^2 + 2r_{cc}r_{db}\cos(\theta)} - \sqrt{r_{cc}^2 + r_{db}^2 - 2r_{cc}r_{db}\cos(\theta)},$$

which can be inverted into

$$\cos(\theta) = \pm\frac{r_{rh}\sqrt{4\left(r_{cc}^2 + r_{db}^2\right) - r_{rh}^2}}{4r_{cc}r_{db}}.$$

The sign ambiguity is due to the two opposite chiralities. Here, we define that $0 \leq \theta \leq \frac{\pi}{4}$ to always return positive r_{rh}.

As r_{rh} is not simply a scaled version of θ, which is always orthogonal to r_{cc} and r_{db}, is not generically orthogonal to r_{cc} and r_{db}. As the dynamics are performed in cartesian coordinates, this *does not* affect the results.

To help understand how r_{rh} maps on to the angle θ, in figure B.10 we show lines of constant θ (left) and r_{rh} (right) in the (r_{cc}, r_{rh})- and (r_{cc}, θ)-planes, respectively. We see that as r_{cc} decreases, the value of r_{rh} for a given angle θ decreases, and vice versa. In the region we study, namely between 1.5 Å and 2.5 Å, the effect is relatively subtle, and we can approximate (quite well) the difference as distances as the rhombic angle.

We chose to use r_{rh} primarily for simplicity — it mirrors the definitions and units of the other coordinates studied in this work while capturing all of the necessary information. Additionally, it avoids complicated boundary behaviour of angles, as well as the choice of which of the angles (or which combination thereof) should be used.

Total Energy Errors

To quantify total energy errors, we use two statistics: total energy drift, defined as

$$\Delta E_{drift} = \max(E_{tot}) - \min(E_{tot})$$

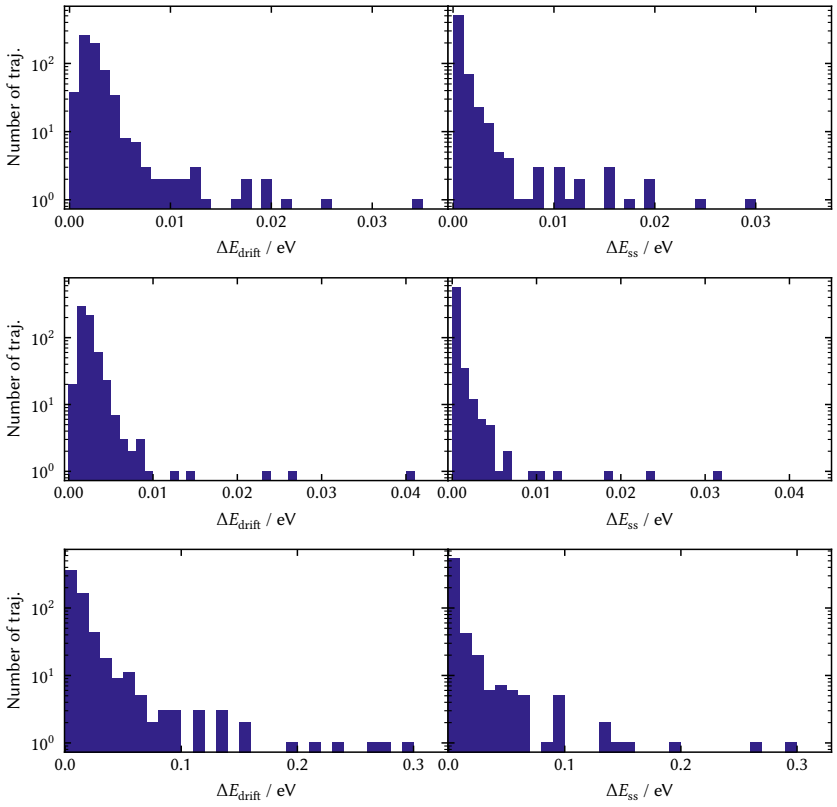

Figure B.11: Energy error histograms for the NBD-initiated dynamics. All figures have a logarithmic y-scale. Top: CASSCF(2,2). The overall error level is excellent, with only almost all trajectories (bar two) having a energy error under 0.02 eV. Middle: XMS-CASPT2(2,2). A very similar picture to CASSCF(2,2). Bottom: XMS-CASPT2(4,4). Note that the energy scale has changed by an order of magnitude. These trajectories show much worse energy conservation.

and maximum single-step energy change

$$\Delta E_{\text{ss}} = \max(|E_{\text{tot}}(t + \Delta t) - E_{\text{tot}}(t)|)$$

with $E_{\text{tot}}(t) = E_{\text{kin}}(t) + E_{\text{pot}}(t)$. Importantly, $\Delta E_{\text{ss}} \leq \Delta E_{\text{drift}}$. For both of these metrics, we are only considering dynamics *on the excited state*, as it is the focus of this work.

Histograms for the two energy errors for the CASSCF(2,2) (top), XMS-CASPT2(2,2) (middle) and XMS-CASPT2(4,4) ensembles are shown in Fig. B.11. For both the (2,2) active space calculations, there was very little energy error, with the vast majority of trajectories staying beneath a total error of 0.01 eV. The (4,4) calculations are more susceptible to CASSCF convergence issues (see Chapter 5), manifestig as significant energy deviation. Almost all trajectories conserved energy to beneath 0.02 eV, while there were some outliers with up to 1 eV of energy error. As these trajectories made up only a small fraction of the dynamics, they were kept in the analysis.

On the ground state, significant energy deviations are seen for all electronic structure methods, but these do not affect the decay pathway nor the assigned channel.

Figure B.12 shows the equivalent plot of the QC-initiated dynamics of Chapter 8. The overall conservation of energy is wose than the corresponding CASSCF(2,2) ensemble in the NBD-initiated dynamics (cf. Fig. B.11, upper panel), but is still at an acceptable level.

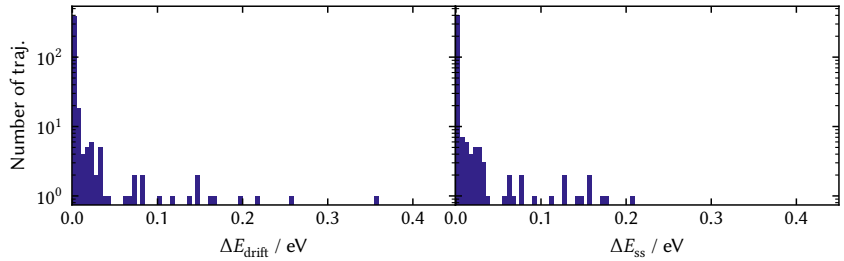

Figure B.12: Energy error histograms for the QC-initiated dynamics. The total energy of the trajectories is generally conserved to within 0.05 eV, with most trajectories below 0.2 eV, worse than in the NBD-initiated CASSCF(2,2) dynamics (cf. Fig. B.11).

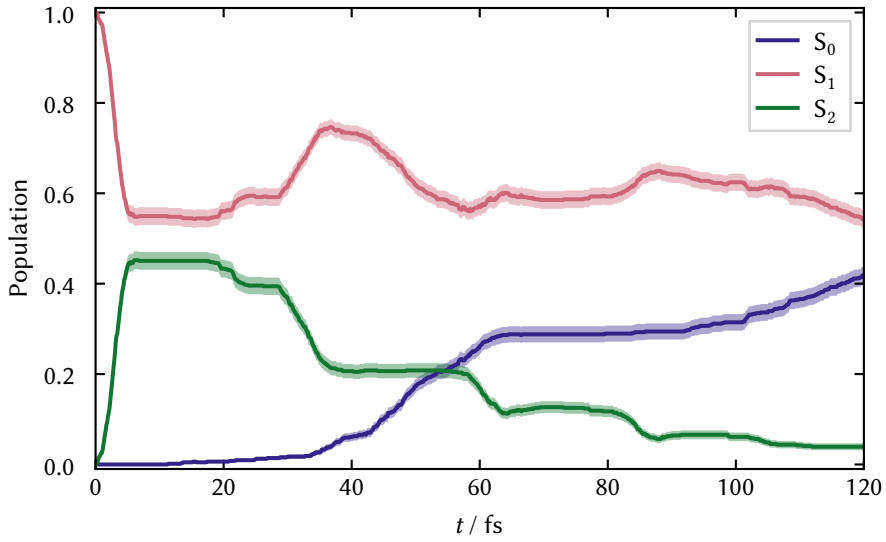

Figure B.13: Populations for CASSCF(4,4) dynamics. The immediate, large transfer to S_2 differentiates the CASSCF(4,4) dynamics from the other methods.

CASSCF(4,4) Dynamics

The CASSCF(4,4) dynamics transfers significant population onto the second excited state, due to the increased energy of S_1 relative to S_2, as discussed in Chapter 5. This can be seen clearly in Fig. B.13. The other methods only transfer $\approx 5\%$. As such, the dynamics is much slower, and leads to quite different molecular geometries. This is shown in Fig. B.14, which shows a heat-map (a population density) for the r_{cc} and r_{rh} coordinate. We do not show the same r_{cc} vs. r_{rh} plots, as the excited state dynamics is much longer and visits the same points in the $(r_{\text{cc}}, r_{\text{rh}})$-plane multiple times. The most crucial difference is the presence of some dynamics on the S_2 (with $|2\text{ud}0\rangle$ character) surface, which is described too high in energy. It therefore does not couple to the $|2020\rangle$ state, which leads to the motion towards the S_1/S_0 conical intersection, and is trapped on the $r_{\text{rh}} = 0$ line.

Example Trajectories

Here, we show some example trajectories. Figure B.15 shows an example NBD-forming trajectory for the NBD-initiated dynamics, calculated with CASSCF(2,2). Looking first at the energies (left panel), we see the three electronic states (the three non-black lines), with the

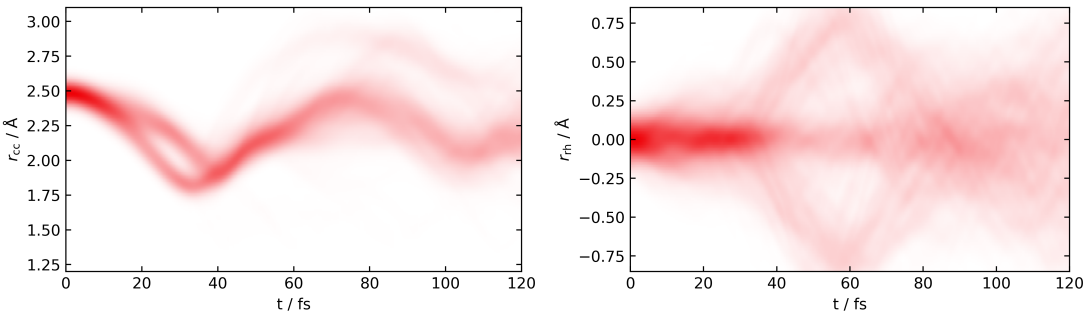

Figure B.14: Heat maps for CASSCF(4,4) dynamics. Left: r_{cc}. The dynamics exhibits two distinct channels and oscillation around the minimum of the S_2 state (of $|2ud0\rangle$ character). Right: r_{rh}. The two channels which split to $r_{cc} \pm 0.75$ Å constitute the rapid decay, similar to the other methods. Note the slightly larger r_{cc} value (cf. Fig. 6.3). The central channel is, which remains at $r_{cc} \approx 0$, is the S_2 ensemble, which is not present in the other methods.

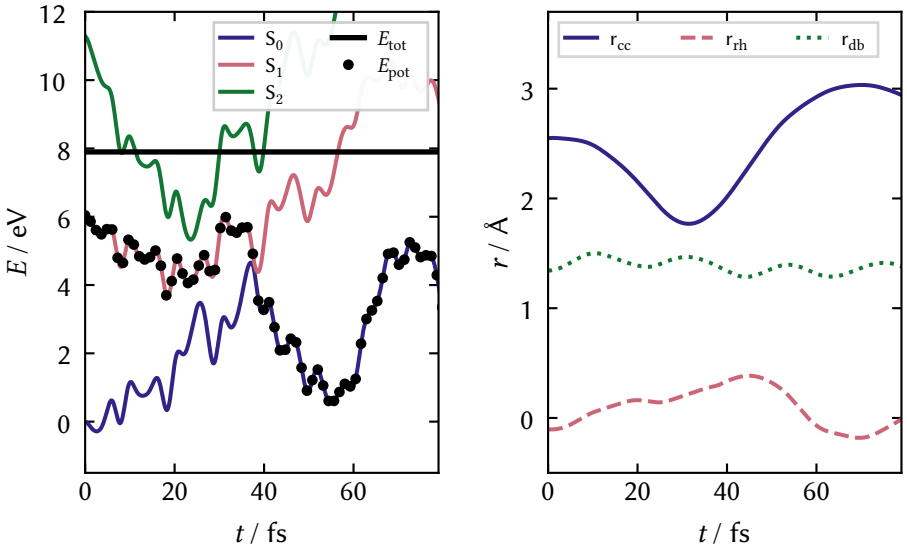

Figure B.15: Example of a NBD-initiated, NBD-ending trajectory for CASSCF(2,2). Left: Energies. The trajectory (active state, black circles) starts at 6 eV on S_1 (rose line), before rapidly moving to hit the ground state (indigo) at $\approx$ 40 fs. The S_2 state (green) comes close but does not cross the S_1 state. After that, the trajectory drops into the NBD ground state well and the other states separate. The total energy is constant at $\approx$ 8 eV. Right: Geometric parameters. The wing-separation r_{cc} (indigo solid) smoothly decreases to just under 2.0 Å, before rising back to almost 3.0 Å on the ground state. The double bond length (green dotted) oscillates around 1.4 Å, while the rhombicity r_{rh} (rose dashed) rises at the S_1/S_0 conical intersection at $\approx$ 40 fs.

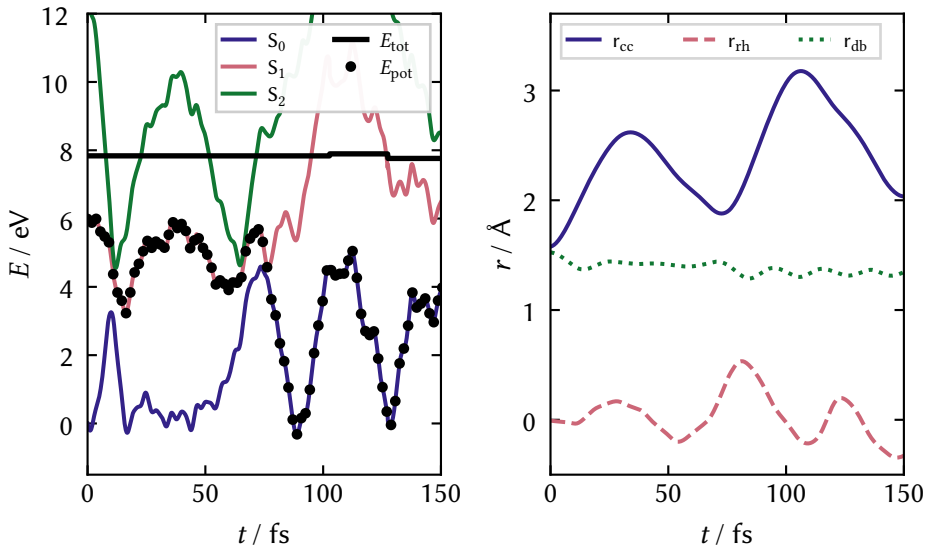

Figure B.16: Example of a QC-initiated, NBD-ending trajectory for CASSCF(2,2). Left: Energies. The trajectory again starts with S_1 (rose line) as the active state (black circles). The trajectory immediately crosses to QC, as can be seen by the avoided crossing between the S_0 (indigo) and S_2 (green) potentials. The trajectory reaches the S_1/S_0 CI at $\approx$ 80 fs, transferring to the ground state. Right: Geometric parameters. r_{cc} (solid indigo) rises with the QC to NBD motion, before dropping towards the S_1/S_0 CI, with a corresponding increase in r_{rh} (dashed rose). At longer times, r_{cc} increases as ground-state NBD is formed. Again,r_{db} oscillates around 1.4 Å, lowering with the formation of NBD.

active state depicted by the black circles. The dynamics starts at 6 eV on S_1, rapidly moving to the S_1/S_0 CI at $\approx$ 40 fs, before dropping to the NBD minimum. Just before the crossing, we see the lowering of the S_2 state, which maintains energy separation as predicted in Chapter 5. Finally, the total energy (the flat black line at $\approx$ 7.5 eV) stays constant across the pathway.

The right panel shows the three carbon-carbon distances (Eqs. (5.1) to (5.3)) across the trajectory. As seen in Fig. 6.8, r_{cc} (indigo line) lowers from 2.5 Å, increasing just before the intersection, which shows large rhombicity (rose dashed line, $r_{rh} \approx 0.4$). r_{db} (green dotted line) nutates around the value of 1.4 Å.

Fig. B.16 shows an example QC-initiated, NBD-ending trajectory, calculated with CASSCF(2,2). Looking at the energies (left panel), the first item of note is the avoided crossings of the S_0 and S_2 states (indigo and green lines, respectively). This is a characteristic feature of crossing from QC-like to NBD-like geometries, due to the change in character of the ground state. The active state (black circles) stays as S_1 (rose lines) until $\approx$ 80 fs, when it transfers to the ground state at the S_1/S_0 CI. The total energy (flat black line at $\approx$ 8 eV) is constant on the excited state, but shows some variation on the ground. Looking now at the right panel, showing distances, we see the rapid increase in r_{cc}, denoting motion from QC to NBD, before it drops to $\approx$ 2 Å at the CI. This is accompanied by a corresponding increase in r_{rh}. r_{db} again stays fairly constant, around 1.4 Å.

Separated Figures

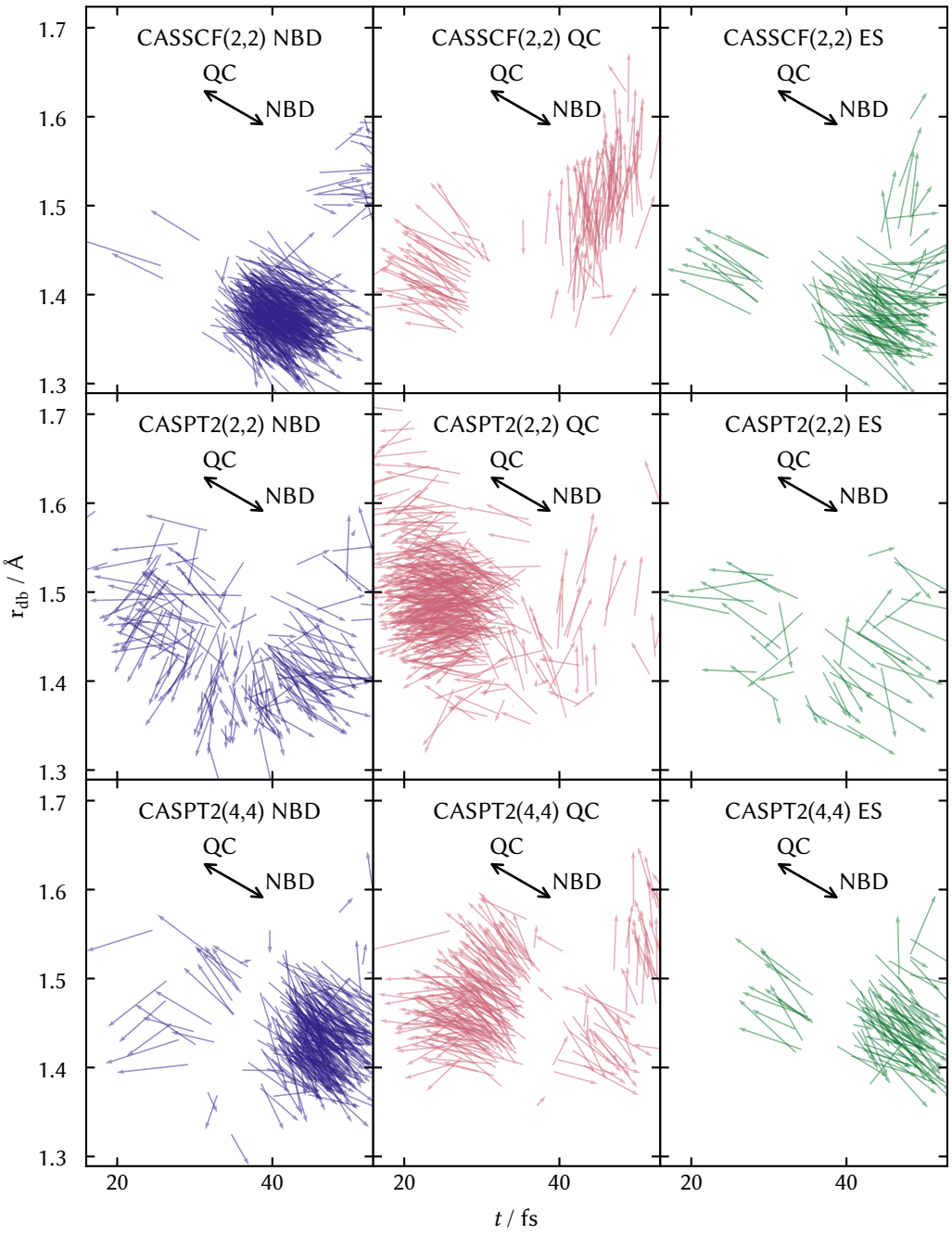

Figure B.17: Colour-blind friendlier version of Fig. 6.10, otherwise identical.

— C —

Experiments

C.1 — Absorption Spectrum

One- vs Two-Photon Processes

Electronic state	Vertical transition energy / eV	One-photon oscillator strength	Two-photon (linear) cross section / a.u.	Two-photon (circular) cross section / a.u.
1^1A_2 (V)	5.328	0.0000	0.530	0.795
1^1B_1 (3s)	5.830	0.0161	13.6	20.4
1^1B_2 (V)	6.132	0.0211	15.3	23.0
2^1A_1 ($3p_x$)	6.296	0.0218	376	271
2^1A_2 ($3p_y$)	6.358	0.0000	63.7	95.6
2^1B_1 ($3p_z$)	6.441	0.0007	4.17	6.26
2^1B_2 ($3d_{xy}$)	6.755	0.0720	14.0	21.1

Table C.1: Calculated (CC2/aug-cc-pVQZ method) vertical transition energies to the first seven excited singlet states of NBD, along with the respective oscillator strengths and two-photon cross sections (in atomic units) under both linear and circularly polarised photoexcitation.

1^1B_2 Valence State

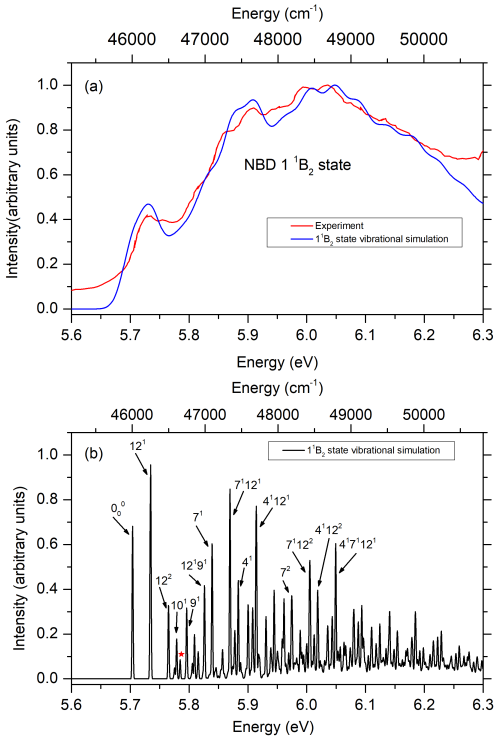

Figure C.1: (a) A comparison between the experimental[263] 1^1B_2 – 1^1A_1 absorption band of NBD and a simulation of the vibrational structure. The simulation employs the calculated 1^1B_2 state vibrational wavenumbers (Table 9.4) but the 1^1B_2 state is predicted to be unbound in one normal mode. For the purposes of this calculation, the sign of the one imaginary wavenumber has been changed to positive (see comment below). The simulated spectrum was obtained by convolving the calculated stick spectrum (not shown) with a 40 meV FWHM Gaussian function. The simulated spectrum was shifted to higher energy by 0.116 eV to align the features peaking at 5.73 eV in the simulated and experimental spectra. (b) A simulated spectrum obtained by convolving the stick spectrum with a 2 meV (FWHM) Gaussian function (comparable to the instrumental resolution in the present experiment), similarly shifted in energy. The peak marked with a * in (b) is an artefact associated with excitation to the ν_{39}=2 level that only exists after the sign change mentioned above, while other peaks associated with this mode are not distinct enough to label. The effect of these spurious transitions on the overall spectrum is minimal, for two primary reasons: Firstly, the most intense transitions (those that create the visible structure) have no excitation into this mode and would be unchanged in the simulation. Secondly, the spurious transitions lack intensity compared to the surrounding transitions, and so merely contribute to baseline 'noise'. Thus, the transitions add a small error to the simulation, but the qualitative agreement to the experimentally measured spectrum of Robin and Kuebler[263] is unaffected.

C.2 — Rydberg/Valence Dynamics in Quadricyclane

Orbital Images

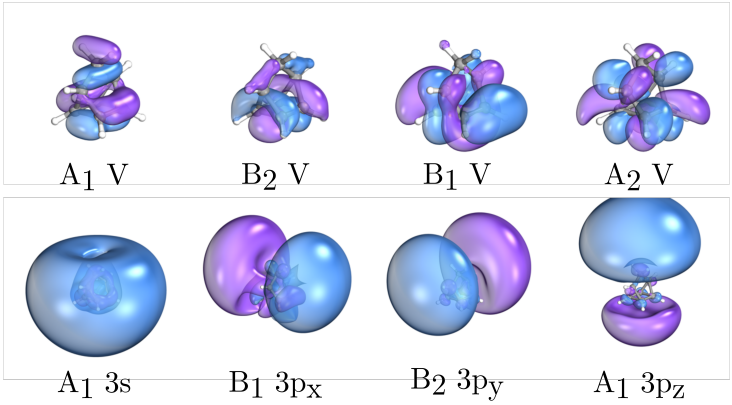

Figure C.2: The active space consists of 2 electrons in a space of 2 valence and 4 Rydberg orbitals. Extending the active space to include one additional pair of virtual and occupied orbitals creates the (4,8) active space of Valentini et al..[188] The two orbitals that extend the (2,6) active space are identified by a (4,8) in their caption. The iso-surface cutoff value has been adjusted such that 80% of the total density is shown for each orbital, and Rydberg orbitals are shown zoomed out to fully render their spatial extent.

Ionisation Channels

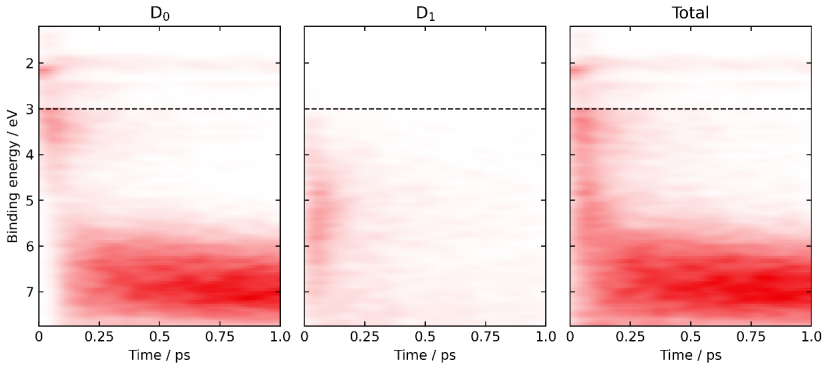

Figure C.3: Theoretical fast valence TRPES signal decomposed into ionisation to D_0 (left panel), ionisation to D_1 (center panel), and ionisation to all modelled continua (right panel). All plots are shown on identical colour bars and convolved with bi-variate Gaussians with 94 fs and 0.1 eV FWHMs.

Figure C.3 shows the contribution to the fast valence photo-electron signal from the two important ionisation channels, D_0 and D_1. Further information on the character of these states can be found in Chapter 7.

Basis Set Contraction

Table C.2: Basis sets primitives and contraction coefficients for the additional S and P basis functions placed on the bridging carbon. Primitives taken from Kaufmann et al..[293].

S		P	
Prim.	Coeff.	Prim.	Coeff.
0.24624	0.61938966	0.042335	0.095483047
0.11253	-1.6065374	0.019254	-0.21148730
0.005858	0.62877974	0.009988	-0.87477491
0.003346	-1.2909713	0.005689	0.22484356
0.002948	1.5983647	0.003476	-0.47278922
0.001324	-0.12722174	0.002242	0.40679967
0.000893	0.6792952	0.001511	-0.23103729
0.000624	-0.16767218	0.001055	0.061411951

Bibliography

[1] K. D. Borne, J. C. Cooper, M. N. R. Ashfold, J. Bachmann, S. Bhattacharyya, R. Boll, M. Bonanomi, M. Bosch, C. Callegari, M. Centurion, M. Coreno, B. F. E. Curchod, M. B. Danailov, A. Demidovich, M. Di Fraia, B. Erk, D. Faccialà, R. Feifel, R. J. G. Forbes, C. S. Hansen, D. M. P. Holland, R. A. Ingle, R. Lindh, L. Ma, H. G. McGhee, S. B. Muvva, J. P. F. Nunes, A. Odate, S. Pathak, O. Plekan, K. C. Prince, P. Rebernik, A. Rouzée, A. Rudenko, A. Simoncig, R. J. Squibb, A. S. Venkatachalam, C. Vozzi, P. M. Weber, A. Kirrander and D. Rolles, *Nat. Chem.*, 2024, 1–7.

[2] J. C. Cooper, D. M. P. Holland, R. A. Ingle, M. Bonanomi, D. Faccialà, N. De Oliveira, A. R. Abid, J. Bachmann, S. Bhattacharyya, K. Borne, M. Bosch, M. Centurion, K. Chen, R. J. G. Forbes, H. V. S. Lam, A. Odate, A. Rudenko, A. S. Venkatachalam, C. Vozzi, E. Wang, P. M. Weber, M. N. R. Ashfold, A. Kirrander and D. Rolles, *J. Chem. Phys.*, 2024, **160**, 064305.

[3] N. Goff, M. Simmermacher, E. Fasshauer, T. Northey, A. Moreno Carrascosa, L. Ma, H. Yong, B. Stankus, A. Odate, X. Xu, W. Du, K. Acheson, J. C. Cooper, D. Ratner, M. Liang, R. Forbes, M. Minitti, A. Kirrander and P. Weber, Under review.

[4] J. C. Cooper and A. Kirrander, Under review.

[5] J. C. Cooper, C. Brown, J. Kára and A. Kirrander, In submission.

[6] J. C. Cooper and A. Kirrander, In preparation.

[7] J. C. Cooper and A. Kirrander, In preparation.

[8] P. J. M. Johnson, M. H. Farag, A. Halpin, T. Morizumi, V. I. Prokhorenko, J. Knoester, T. L. C. Jansen, O. P. Ernst and R. J. D. Miller, *J. Phys. Chem. B*, 2017, **121**, 4040–4047.

[9] P. J. M. Johnson, A. Halpin, T. Morizumi, V. I. Prokhorenko, O. P. Ernst and R. J. D. Miller, *Nat. Chem.*, 2015, **7**, 980–986.

[10] L. Hutton and B. F. E. Curchod, *ChemPhotoChem*, 2022, **6**, e202200151.

[11] B. F. E. Curchod and A. J. Orr-Ewing, *J. Phys. Chem. A*, 2024, **128**, 6613–6635.

[12] M. Vacher, I. Fdez. Galván, B.-W. Ding, S. Schramm, R. Berraud-Pache, P. Naumov, N. Ferré, Y.-J. Liu, I. Navizet, D. Roca-Sanjuán, W. J. Baader and R. Lindh, *Chem. Rev.*, 2018, **118**, 6927–6974.

[13] M. Melchionna and P. Fornasiero, *ACS Catal.*, 2020, **10**, 5493–5501.

[14] X. Yang and D. Wang, *ACS Appl. Energy Mater.*, 2018, **1**, 6657–6693.

[15] L. Candish, K. D. Collins, G. C. Cook, J. J. Douglas, A. Gómez-Suárez, A. Jolit and S. Keess, *Chem. Rev.*, 2022, **122**, 2907–2980.

[16] R. B. Woodward and R. Hoffmann, *Angewandte Chemie Int. Ed. Engl.*, 1969, **8**, 781–853.

[17] R. G. W. Norrish and G. Porter, *Nature*, 1949, **164**, 658–658.

[18] K. Jorner, A. Dreos, R. Emanuelsson, O. E. Bakouri, I. Fdez. Galván, K. Börjesson, F. Feixas, R. Lindh, B. Zietz, K. Moth-Poulsen and H. Ottosson, *J. Mater. Chem. A*, 2017, **5**, 12369–12378.

[19] A. Dreos, K. Börjesson, Z. Wang, A. Roffey, Z. Norwood, D. Kushnir and K. Moth-Poulsen, *Energy & Environ. Sci.*, 2017, **10**, 728–734.
[20] J. Orrego-Hernández, A. Dreos and K. Moth-Poulsen, *Accounts Chem. Res.*, 2020, **53**, 1478–1487.
[21] D. Roke, M. Sen, W. Danowski, S. J. Wezenberg and B. L. Feringa, *J. Am. Chem. Soc.*, 2019, **141**, 7622–7627.
[22] M. Paolino, T. Giovannini, M. Manathunga, L. Latterini, G. Zampini, R. Pierron, J. Léonard, S. Fusi, G. Giorgi, G. Giuliani, A. Cappelli, C. Cappelli and M. Olivucci, *J. Phys. Chem. Lett.*, 2021, **12**, 3875–3884.
[23] A. Kazaryan, J. C. M. Kistemaker, L. V. Schäfer, W. R. Browne, B. L. Feringa and M. Filatov, *J. Phys. Chem. A*, 2010, **114**, 5058–5067.
[24] W. A. Velema, W. Szymanski and B. L. Feringa, *J. Am. Chem. Soc.*, 2014, **136**, 2178–2191.
[25] K. Hüll, J. Morstein and D. Trauner, *Chem. Rev.*, 2018, **118**, 10710–10747.
[26] A. Dreos, Z. Wang, B. E. Tebikachew, K. Moth-Poulsen and J. Andréasson, *J. Phys. Chem. Lett.*, 2018, **9**, 6174–6178.
[27] A. Kunz and H. A. Wegner, *ChemSystemsChem*, 2021, **3**, e2000035.
[28] B. Ergette Tebikachew, F. Edhborg, N. Kann, B. Albinsson and K. Moth-Poulsen, *Phys. Chem. Chem. Phys.*, 2018, **20**, 23195–23201.
[29] R. J. D. Miller, R. Ernstorfer, M. Harb, M. Gao, C. T. Hebeisen, H. Jean-Ruel, C. Lu, G. Moriena and G. Sciaini, *Acta Crystallogr. Sect. A Found. Crystallogr.*, 2010, **66**, 137–156.
[30] P. M. Weber, B. Stankus and A. Kirrander, *arXiv:2003.02839 [physics]*, 2020.
[31] S. Pathak, L. M. Ibele, R. Boll, C. Callegari, A. Demidovich, B. Erk, R. Feifel, R. Forbes, M. Di Fraia, L. Giannessi, C. S. Hansen, D. M. P. Holland, R. A. Ingle, R. Mason, O. Plekan, K. C. Prince, A. Rouzée, R. J. Squibb, J. Tross, M. N. R. Ashfold, B. F. E. Curchod and D. Rolles, *Nat. Chem.*, 2020, **12**, 795–800.
[32] F. M. Raymo and S. Giordani, *J. Am. Chem. Soc.*, 2001, **123**, 4651–4652.
[33] P. Hong, J. Liu, K.-X. Qin, R. Tian, L.-Y. Peng, Y.-S. Su, Z. Gan, X.-X. Yu, L. Ye, M.-Q. Zhu and C. Li, *Angewandte Chemie Int. Ed.*, 2024, **63**, e202316706.
[34] S. Wang, M.-S. Choi and S.-H. Kim, *J. Photochem. Photobiol. A: Chem.*, 2008, **198**, 150–155.
[35] S. W. Hell, *Science*, 2007, **316**, 1153–1158.
[36] W. Jahr, P. Velicky and J. G. Danzl, *Methods (San Diego, Calif.)*, 2019, **174**, 27–41.
[37] M. J. Fuchter, *J. Med. Chem.*, 2020, **63**, 11436–11447.
[38] A. A. Beharry and G. A. Woolley, *Chem. Soc. Rev.*, 2011, **40**, 4422–4437.
[39] M. J. Kuisma, A. M. Lundin, K. Moth-Poulsen, P. Hyldgaard and P. Erhart, *J. Phys. Chem. C*, 2016, **120**, 3635–3645.
[40] R. Eschenbacher, F. Hemauer, E. Franz, A. Leng, V. Schwaab, N. J. Waleska-Wellnhofer, E. M. Freiberger, L. Fromm, T. Xu, A. Görling, A. Hirsch, H.-P. Steinrück, C. Papp, O. Brummel and J. Libuda, *ChemPhotoChem*, 2024, **8**, e202300155.
[41] R. Nichols, T. A. McKelvey and S. L. Rodgers, 1997.
[42] E. J. Wucherer and A. Wilson, *Chemical, Physical and Hazards Properties of Quadricyclane*, Air Force Research Laboratory Technical Report PL-TR-97-3053, 1998.
[43] X.-t.-f. E, L. Pan, X. Zhang and J.-J. Zou, *Fuel*, 2020, **276**, 118047.
[44] F. Bernardi, S. De, M. Olivucci and M. A. Robb, *J. Am. Chem. Soc.*, 1990, **112**, 1737–1744.
[45] M. J. Bearpark and M. A. Robb, *Rev. React. Intermed. Chem.*, 2007, 379–414.
[46] M. Centurion, T. J. A. Wolf and J. Yang, *Annu. Rev. Phys. Chem.*, 2022, **73**, 21–42.
[47] D. Rolles, *Adv. Physics: X*, 2023, **8**, 2132182.
[48] F. Rudakov and P. M. Weber, *J. Chem. Phys.*, 2012, **136**, 134303.
[49] J. P. Doering and R. McDiarmid, *J. Chem. Phys.*, 1981, **75**, 87–91.

[50] X. Xing, A. Gedanken, A.-H. Sheybani and R. McDiarmid, *J. Phys. Chem.*, 1994, **98**, 8302–8309.
[51] M. D. Kilde, L. Broløs, M. Mansø, J. Mogensen, C. G. Tortzen and M. B. Nielsen, *Chem. – A Eur. J.*, 2020, **26**, 13429–13435.
[52] W. Alex, P. Lorenz, C. Henkel, T. Clark, A. Hirsch and D. M. Guldi, *J. Am. Chem. Soc.*, 2022, **144**, 153–162.
[53] F. J. Hernández, J. M. Cox, J. Li, R. Crespo-Otero and S. A. Lopez, *J. Org. Chem.*, 2023, **88**, 5311–5320.
[54] E. Vessally, *Phosphorus, Sulfur, Silicon Relat. Elem.*, 2009, **184**, 2307–2313.
[55] E. Vessally, *Bull. Chem. Soc. Ethiop.*, 2009, **23**, 303–308.
[56] M. S. Child, *Theory of Molecular Rydberg States*, Cambridge University Press, Cambridge, 2011.
[57] M. J. Paterson and D. Townsend, *Int. Rev. Phys. Chem.*, 2020, **39**, 517–567.
[58] A. Kirrander, *J. Chem. Phys.*, 2012, **137**, 154310.
[59] S. Reiter, D. Keefer and R. de Vivie-Riedle, *Quantum Chemistry and Dynamics of Excited States*, John Wiley & Sons, Ltd, 2020, pp. 355–381.
[60] M. Bonfanti, G. A. Worth and I. Burghardt, *Quantum Chemistry and Dynamics of Excited States*, John Wiley & Sons, Ltd, 2020, pp. 383–411.
[61] J. C. Tully, *Faraday Discuss.*, 1998, **110**, 407–419.
[62] J. C. Tully, *J. Chem. Phys.*, 1990, **93**, 1061–1071.
[63] J. E. Subotnik and N. Shenvi, *J. Chem. Phys.*, 2011, **134**, 244114.
[64] E. Schrödinger, *Phys. Rev.*, 1926, **28**, 1049–1070.
[65] C. Cohen-Tannoudji, B. Diu and F. Laloë, *Quantum Mechanics, Volume 1: Basic Concepts, Tools, and Applications*, John Wiley & Sons, 2019.
[66] M. Born and K. Huang, *Dynamical theory of crystal lattices*, 1954.
[67] L. S. Cederbaum, *Conical Intersections*, WORLD SCIENTIFIC, 2004, vol. 15, pp. 3–40.
[68] M. S. Schuurman and A. Stolow, *Annu. Rev. Phys. Chem.*, 2018, **69**, 427–450.
[69] D. V. Makhov, W. J. Glover, T. J. Martinez and D. V. Shalashilin, *J. Chem. Phys.*, 2014, **141**, 054110.
[70] D. R. Yarkony, *Rev. Mod. Phys.*, 1996, **68**, 985–1013.
[71] J. Jankunas, M. Sneha, R. N. Zare, F. Bouakline, S. C. Althorpe, D. Herráez-Aguilar and F. J. Aoiz, *Proc. National Acad. Sci.*, 2014, **111**, 15–20.
[72] S. C. Althorpe, T. Stecher and F. Bouakline, *J. Chem. Phys.*, 2008, **129**, 214117.
[73] B. K. Kendrick, *J. Chem. Phys.*, 2000, **112**, 5679–5704.
[74] G. J. Atchity, S. S. Xantheas and K. Ruedenberg, *J. Chem. Phys.*, 1991, **95**, 1862–1876.
[75] F. Sicilia, L. Blancafort, M. J. Bearpark and M. A. Robb, *J. Phys. Chem. A*, 2007, **111**, 2182–2192.
[76] M. J. Paterson, M. J. Bearpark, M. A. Robb and L. Blancafort, *J. Chem. Phys.*, 2004, **121**, 11562–11571.
[77] M. J. Paterson, M. J. Bearpark, M. A. Robb, L. Blancafort and G. A. Worth, *Phys. Chem. Chem. Phys.*, 2005, **7**, 2100–2115.
[78] I. Fdez. Galván, M. G. Delcey, T. B. Pedersen, F. Aquilante and R. Lindh, *J. Chem. Theory Comput.*, 2016, **12**, 3636–3653.
[79] S. Matsika, *Chem. Rev.*, 2021, **121**, 9407–9449.
[80] D. R. Yarkony, *J. Chem. Phys.*, 2001, **114**, 2601–2613.
[81] M. Ben-Nun, F. Molnar, K. Schulten and T. J. Martínez, *Proc. National Acad. Sci.*, 2002, **99**, 1769–1773.
[82] J. P. Malhado and J. T. Hynes, *J. Chem. Phys.*, 2016, **145**, 194104.
[83] C. A. Farfan and D. B. Turner, *Phys. Chem. Chem. Phys.*, 2020, **22**, 20265–20283.

[84] D. Asturiol, B. Lasorne, G. A. Worth, M. A. Robb and L. Blancafort, *Phys. Chem. Chem. Phys.*, 2010, **12**, 4949–4958.
[85] I. Fdez. Galván, A. Brakestad and M. Vacher, *Phys. Chem. Chem. Phys.*, 2022, **24**, 1638–1653.
[86] M. Garavelli, P. Celani, M. Fato, M. J. Bearpark, B. R. Smith, M. Olivucci and M. A. Robb, *J. Phys. Chem. A*, 1997, **101**, 2023–2032.
[87] A. Kirrander and M. Vacher, *Quantum Chemistry and Dynamics of Excited States*, John Wiley & Sons, Ltd, 2020, pp. 469–497.
[88] G. Granucci and M. Persico, *J. Chem. Phys.*, 2007, **126**, 134114.
[89] C. Zhu, S. Nangia, A. W. Jasper and D. G. Truhlar, *J. Chem. Phys.*, 2004, **121**, 7658–7670.
[90] C. Zhu, A. W. Jasper and D. G. Truhlar, *J. Chem. Theory Comput.*, 2005, **1**, 527–540.
[91] J. E. Subotnik, A. Jain, B. Landry, A. Petit, W. Ouyang and N. Bellonzi, *Annu. Rev. Phys. Chem.*, 2016, **67**, 387–417.
[92] J. R. Mannouch and J. O. Richardson, *J. Chem. Phys.*, 2023, **158**, 104111.
[93] J. E. Runeson and D. E. Manolopoulos, *J. Chem. Phys.*, 2023, **159**, 094115.
[94] J. E. Lawrence, J. R. Mannouch and J. O. Richardson, *J. Chem. Phys.*, 2024, **160**, 244112.
[95] E. J. Heller, *Accounts Chem. Res.*, 1981, **14**, 368–375.
[96] G. A. Worth and B. Lasorne, *Quantum Chemistry and Dynamics of Excited States*, John Wiley & Sons, Ltd, 2020, pp. 413–433.
[97] B. F. E. Curchod, *Quantum Chemistry and Dynamics of Excited States*, John Wiley & Sons, Ltd, 2020, pp. 435–467.
[98] M. Ben-Nun, J. Quenneville and T. J. Martínez, *J. Phys. Chem. A*, 2000, **104**, 5161–5175.
[99] J. Suchan, D. Hollas, B. F. E. Curchod and P. Slavíček, *Faraday Discuss.*, 2018, **212**, 307–330.
[100] M. Barbatti and K. Sen, *Int. J. Quantum Chem.*, 2016, **116**, 762–771.
[101] M. Ceriotti, G. Bussi and M. Parrinello, *Phys. Rev. Lett.*, 2009, **103**, 030603.
[102] A. Prlj, D. Hollas and B. F. E. Curchod, *J. Phys. Chem. A*, 2023, **127**, 7400–7409.
[103] A. Prlj, L. M. Ibele, E. Marsili and B. F. E. Curchod, *J. Phys. Chem. Lett.*, 2020, **11**, 5418–5425.
[104] R. Crespo-Otero and M. Barbatti, *Theor. Chem. Accounts*, 2012, **131**, 1237.
[105] T. Helgaker, P. Jørgensen and J. Olsen, *Molecular Electronic-Structure Theory*, 2013.
[106] D. R. Hartree, *Math. Proc. Camb. Philos. Soc.*, 1928, **24**, 89–110.
[107] V. Fock, *Z. Physik*, 1930, **62**, 795–805.
[108] A. Szabo and N. S. Ostlund, *Modern Quantum Chemistry Introduction to Advanced Electronic Structure Theory*, Macmillan, 1st edn, 1982.
[109] P. G. Szalay, T. Müller, G. Gidofalvi, H. Lischka and R. Shepard, *Chem. Rev.*, 2012, **112**, 108–181.
[110] E. R. Davidson and D. W. Silver, *Chem. Phys. Lett.*, 1977, **52**, 403–406.
[111] J. A. Pople, R. Seeger and R. Krishnan, *Int. J. Quantum Chem.*, 1977, **12**, 149–163.
[112] P. E. M. Siegbahn, *Chem. Phys. Lett.*, 1978, **55**, 386–394.
[113] D. I. Lyakh, M. Musiał, V. F. Lotrich and R. J. Bartlett, *Chem. Rev.*, 2012, **112**, 182–243.
[114] F. A. Evangelista, *J. Chem. Phys.*, 2018, **149**, 030901.
[115] B. O. Roos, P. R. Taylor and P. E. M. Sigbahn, *Chem. Phys.*, 1980, **48**, 157–173.
[116] B. O. Roos, *Advances in Chemical Physics*, John Wiley & Sons, Ltd, 1987, pp. 399–445.
[117] J. Olsen, *Int. J. Quantum Chem.*, 2011, **111**, 3267–3272.
[118] V. Veryazov, P. A. Malmqvist and B. O. Roos, *Int. J. Quantum Chem.*, 2011, **111**, 3329–3338.
[119] L. Serrano-Andrés, M. Merchán, I. Nebot-Gil, R. Lindh and B. O. Roos, *J. Chem. Phys.*, 1993, **98**, 3151–3162.
[120] B. O. Roos, K. Andersson and M. P. Fülscher, *Chem. Phys. Lett.*, 1992, **192**, 5–13.

[121] A. Moreno Carrascosa, H. Yong, D. L. Crittenden, P. M. Weber and A. Kirrander, *J. Chem. Theory Comput.*, 2019, **15**, 2836–2846.
[122] J. Finley, P.-A. Malmqvist, B. O. Roos and L. Serrano-Andrés, *Chem. Phys. Lett.*, 1998, **288**, 299–306.
[123] T. Shiozaki, W. Győrffy, P. Celani and H.-J. Werner, *J. Chem. Phys.*, 2011, **135**, 081106.
[124] S. Battaglia and R. Lindh, *J. Chem. Theory Comput.*, 2020.
[125] S. Battaglia and R. Lindh, *J. Chem. Phys.*, 2021, **154**, 034102.
[126] A. A. Granovsky, *J. Chem. Phys.*, 2011, **134**, 214113.
[127] R. Lindh and I. Fdez. Galván, *Quantum Chemistry and Dynamics of Excited States*, John Wiley & Sons, Ltd, 2020, pp. 299–353.
[128] S. Battaglia, I. Fdez. Galván and R. Lindh, *Theoretical and Computational Photochemistry*, Elsevier, 2023, pp. 135–162.
[129] Y. Nishimoto, S. Battaglia and R. Lindh, *J. Chem. Theory Comput.*, 2022, **18**, 4269–4281.
[130] A. A. Ischenko, P. M. Weber and R. J. D. Miller, *Chem. Rev.*, 2017, **117**, 11066–11124.
[131] B. Stankus, H. Yong, N. Zotev, J. M. Ruddock, D. Bellshaw, T. J. Lane, M. Liang, S. Boutet, S. Carbajo, J. S. Robinson, W. Du, N. Goff, Y. Chang, J. E. Koglin, M. P. Minitti, A. Kirrander and P. M. Weber, *Nat. Chem.*, 2019, **11**, 716–721.
[132] J. M. Ruddock, H. Yong, B. Stankus, W. Du, N. Goff, Y. Chang, A. Odate, A. M. Carrascosa, D. Bellshaw, N. Zotev, M. Liang, S. Carbajo, J. Koglin, J. S. Robinson, S. Boutet, A. Kirrander, M. P. Minitti and P. M. Weber, *Sci. Adv.*, 2019, **5**, eaax6625.
[133] J. Yang, O. Zandi, P. Zhang and M. Centurion, Ultrafast Nonlinear Imaging and Spectroscopy II, 2014, pp. 100–110.
[134] T. J. A. Wolf, D. M. Sanchez, J. Yang, R. M. Parrish, J. P. F. Nunes, M. Centurion, R. Coffee, J. P. Cryan, M. Gühr, K. Hegazy, A. Kirrander, R. K. Li, J. Ruddock, X. Shen, T. Vecchione, S. P. Weathersby, P. M. Weber, K. Wilkin, H. Yong, Q. Zheng, X. J. Wang, M. P. Minitti and T. J. Martínez, *Nat. Chem.*, 2019, **11**, 504–509.
[135] R. J. Squibb, M. Sapunar, A. Ponzi, R. Richter, A. Kivimäki, O. Plekan, P. Finetti, N. Sisourat, V. Zhaunerchyk, T. Marchenko, L. Journel, R. Guillemin, R. Cucini, M. Coreno, C. Grazioli, M. D. Fraia, C. Callegari, K. C. Prince, P. Decleva, M. Simon, J. H. D. Eland, N. Došlić, R. Feifel and M. N. Piancastelli, *Nat. Commun.*, 2018, **9**, 1–7.
[136] V. Blanchet and A. Stolow, *J. Chem. Phys.*, 1998, **108**, 4371–4374.
[137] N. Kotsina, F. Belli, S.-f. Gao, Y.-y. Wang, P. Wang, J. C. Travers and D. Townsend, *J. Phys. Chem. Lett.*, 2019, **10**, 715–720.
[138] K. Wang, V. McKoy, P. Hockett, A. Stolow and M. S. Schuurman, *Chem. Phys. Lett.*, 2017, **683**, 579–585.
[139] S. Adachi, M. Sato and T. Suzuki, *J. Phys. Chem. Lett.*, 2015, **6**, 343–346.
[140] S. Karashima, Y.-I. Suzuki and T. Suzuki, *J. Phys. Chem. Lett.*, 2021, **12**, 3755–3761.
[141] R. Srinivasan, V. A. Lobastov, C.-Y. Ruan and A. H. Zewail, *Helvetica chimica acta*, 2003, **86**, 1761–1799.
[142] A. Rudenko and D. Rolles, *J. Electron Spectrosc. Relat. Phenom.*, 2015, **204**, 228–236.
[143] H. Yong, A. M. Carrascosa, L. Ma, B. Stankus, M. P. Minitti, A. Kirrander and P. M. Weber, *Faraday Discuss.*, 2021, **228**, 104–122.
[144] I. Gabalski, M. A. Sere, K. Acheson, F. Allum, S. Boutet, G. Dixit, R. Forbes, J. M. Glownia, N. Goff, K. Hegazy, A. J. Howard, M. Liang, M. P. Minitti, R. S. Minns, A. Natan, N. Peard, W. O. Razmus, R. J. Sension, M. R. Ware, P. M. Weber, N. Werby, T. J. A. Wolf, A. Kirrander and P. Bucksbaum, *J. Chem. Phys.*, 2022.
[145] S. Serkez, G. Geloni, S. Tomin, G. Feng, E. V. Gryzlova, A. N. Grum-Grzhimailo and M. Meyer, *J. Opt.*, 2018, **20**, 024005.
[146] A.-T. Le, T. Morishita, R. Lucchese and C. Lin, *Phys. Rev. Lett.*, 2012, **109**, 203004.

[147] Z. Chang and P. Corkum, *J. Opt. Soc. Am. B*, 2010, **27**, B9.
[148] M. Nisoli, P. Decleva, F. Calegari, A. Palacios and F. Martín, *Chem. Rev.*, 2017, **117**, 10760–10825.
[149] M. Simmermacher, P. M. Weber and A. Kirrander, *Structural Dynamics with X-ray and Electron Scattering*, Royal Society of Chemistry, London, 2023, vol. 25, pp. 85–125.
[150] C. Tavard, *Cahiers de Physique*, 1965, **20**, 397–500.
[151] M. Born, *Zeitschrift für Physik*, 1926, **37**, 863–867.
[152] I. Waller and D. R. Hartree, *Proc. Royal Soc. A: Math. Phys. Eng. Sci.*, 1929, **124**, 119–142.
[153] M. Simmermacher, A. Moreno Carrascosa, N. E. Henriksen, K. B. Møller and A. Kirrander, *J. Chem. Phys.*, 2019, **151**, 174302.
[154] M. Simmermacher, N. E. Henriksen, K. B. Møller, A. Moreno Carrascosa and A. Kirrander, *Phys. Rev. Lett.*, 2019, **122**, 073003.
[155] M. Breitenstein, H. Meyer and A. Schweig, *Chem. Phys.*, 1988, **124**, 47–54.
[156] A. M. Carrascosa, J. P. Coe, M. Simmermacher, M. J. Paterson and A. Kirrander, *Phys. Chem. Chem. Phys.*, 2022, **24**, 24542–24552.
[157] N. Watanabe, K. Yamauchi, Y. Kamata, Y. Udagawa and T. Müller, *Mol. Phys.*, 2002, **100**, 2839–2847.
[158] K. M. Ziems, M. Simmermacher, S. Gräfe and A. Kirrander, *J. Chem. Phys.*, 2023, **159**, 044108.
[159] A. Natan, A. Schori, G. Owolabi, J. P. Cryan, J. M. Glownia and P. H. Bucksbaum, *Faraday Discuss.*, 2021, **228**, 123–138.
[160] M. Simmermacher, A. Kirrander and N. E. Henriksen, *Phys. Rev. A*, 2020, **102**, 052825.
[161] N. Zotev, A. Moreno Carrascosa, M. Simmermacher and A. Kirrander, *J. Chem. Theory Comput.*, 2020, **16**, 2594–2605.
[162] A. M. Carrascosa, T. Northey and A. Kirrander, *Phys. Chem. Chem. Phys.*, 2017, **19**, 7853–7863.
[163] J. Wang and V. H. Smith, *Int. J. Quantum Chem.*, 1994, **52**, 1145–1151.
[164] A. J. Thakkar and B. S. Sharma, *Int. J. Quantum Chem.*, 2001, **85**, 258–262.
[165] A. Einstein, *Ann. der Physik*, 1905, **322**, 132–148.
[166] A. Stolow, *Annu. review physical chemistry*, 2003, **54**, 89–119.
[167] G. Stock and W. Domcke, *Conical Intersections*, WORLD SCIENTIFIC, 2004, vol. 15, pp. 739–801.
[168] C. Melania Oana and A. I. Krylov, *J. Chem. Phys.*, 2007, **127**, 234106.
[169] C. M. Oana and A. I. Krylov, *J. Chem. Phys.*, 2009, **131**, 124114.
[170] C. Jungen, *Handb. High-resolution Spectrosc.*, 2011, 471–510.
[171] M. Spanner, S. Patchkovskii, C. Zhou, S. Matsika, M. Kotur and T. C. Weinacht, *Phys. Rev. A*, 2012, **86**, 053406.
[172] S. Gozem, A. O. Gunina, T. Ichino, D. L. Osborn, J. F. Stanton and A. I. Krylov, *J. Phys. Chem. Lett.*, 2015, **6**, 4532–4540.
[173] J. Tennyson, *Phys. Reports*, 2010, **491**, 29–76.
[174] D. S. Brambila, A. G. Harvey, Z. Mašín, J. D. Gorfinkiel and O. Smirnova, *J. Phys. B: At. Mol. Opt. Phys.*, 2015, **48**, 245101.
[175] G. Herzberg, *Molecular Spectra and Molecular Structure: II. Infrared and Raman Spectra of Polyatomic Molecules*, Krieger, 1991, vol. 2.
[176] T. E. Sharp and H. M. Rosenstock, *J. Chem. Phys.*, 1964, **41**, 3453–3463.
[177] D. Tripathi and A. K. Dutta, *Int. J. Quantum Chem.*, 2022, **122**, e26918.
[178] A. I. Krylov, *Annu. Rev. Phys. Chem.*, 2008, **59**, 433–462.
[179] A. I. Krylov, *Reviews in Computational Chemistry*, John Wiley & Sons, Ltd, 2017, pp. 151–224.

[180] A. Dreuw, *Quantum Chemistry and Dynamics of Excited States*, John Wiley & Sons, Ltd, 2020, pp. 109–131.
[181] M. Musiał, *Quantum Chemistry and Dynamics of Excited States*, John Wiley & Sons, Ltd, 2020, pp. 77–108.
[182] J. J. Szymczak, M. Barbatti and H. Lischka, *Int. J. Quantum Chem.*, 2011, **111**, 3307–3315.
[183] J. Janoš and P. Slavíček, *J. Chem. Theory Comput.*, 2023, **19**, 8273–8284.
[184] T. V. Papineau, D. Jacquemin and M. Vacher, *J. Phys. Chem. Lett.*, 2024, **15**, 636–643.
[185] D. Bellshaw, R. S. Minns and A. Kirrander, *Phys. Chem. Chem. Phys.*, 2019, **21**, 14226–14237.
[186] I. Antol, *J. Comput. Chem.*, 2013, **34**, 1439–1445.
[187] F. Coppola, M. Nucci, M. Marazzi, D. Rocca and M. Pastore, *ChemPhotoChem*, 2023, **7**, e202200214.
[188] A. Valentini, S. v. d. Wildenberg and F. Remacle, *Phys. Chem. Chem. Phys.*, 2020, **22**, 22302–22313.
[189] P. Celani, M. A. Robb, M. Garavelli, F. Bernardi and M. Olivucci, *Chem. Phys. Lett.*, 1995, **243**, 1–8.
[190] J. J. Serrano-Pérez, M. J. Bearpark and M. A. Robb, *Mol. Phys.*, 2012, **110**, 2493–2501.
[191] F. Aquilante, J. Autschbach, A. Baiardi, S. Battaglia, V. A. Borin, L. F. Chibotaru, I. Conti, L. De Vico, M. Delcey, I. Fdez. Galván, N. Ferré, L. Freitag, M. Garavelli, X. Gong, S. Knecht, E. D. Larsson, R. Lindh, M. Lundberg, P. A. Malmqvist, A. Nenov, J. Norell, M. Odelius, M. Olivucci, T. B. Pedersen, L. Pedraza-González, Q. M. Phung, K. Pierloot, M. Reiher, I. Schapiro, J. Segarra-Martí, F. Segatta, L. Seijo, S. Sen, D.-C. Sergentu, C. J. Stein, L. Ungur, M. Vacher, A. Valentini and V. Veryazov, *J. Chem. Phys.*, 2020, **152**, 214117.
[192] H. Lischka, R. Shepard, T. Müller, P. G. Szalay, R. M. Pitzer, A. J. A. Aquino, M. M. Araújo Do Nascimento, M. Barbatti, L. T. Belcher, J.-P. Blaudeau, I. Borges, S. R. Brozell, E. A. Carter, A. Das, G. Gidofalvi, L. González, W. L. Hase, G. Kedziora, M. Kertesz, F. Kossoski, F. B. C. Machado, S. Matsika, S. A. Do Monte, D. Nachtigallová, R. Nieman, M. Oppel, C. A. Parish, F. Plasser, R. F. K. Spada, E. A. Stahlberg, E. Ventura, D. R. Yarkony and Z. Zhang, *J. Chem. Phys.*, 2020, **152**, 134110.
[193] S. D. Folkestad, E. F. Kjønstad, R. H. Myhre, J. H. Andersen, A. Balbi, S. Coriani, T. Giovannini, L. Goletto, T. S. Haugland, A. Hutcheson, I.-M. Høyvik, T. Moitra, A. C. Paul, M. Scavino, A. S. Skeidsvoll, A. H. Tveten and H. Koch, *J. Chem. Phys.*, 2020, **152**, 184103.
[194] T. H. Dunning, *J. Chem. Phys.*, 1989, **90**, 1007–1023.
[195] R. A. Kendall, T. H. Dunning and R. J. Harrison, *J. Chem. Phys.*, 1992, **96**, 6796–6806.
[196] L. Bertram, P. M. Weber and A. Kirrander, *Faraday Discuss.*, 2023, **244**, 269–293.
[197] I. Polyak, L. Hutton, R. Crespo-Otero, M. Barbatti and P. J. Knowles, *J. Chem. Theory Comput.*, 2019, **15**, 3929–3940.
[198] B. O. Roos, M. Merchan, R. McDiarmid and X. Xing, *J. Am. Chem. Soc.*, 1994, **116**, 5927–5936.
[199] M. H. Palmer, S. V. Hoffmann, N. C. Jones, M. Coreno, M. de Simone, C. Grazioli and R. A. Aitken, *J. Chem. Phys.*, 2021, **155**, 034308.
[200] R. P. Frueholz, W. M. Flicker, O. A. Mosher and A. Kuppermann, *J. Chem. Phys.*, 1979, **70**, 1986–1993.
[201] M. Allan, *J. Electron Spectrosc. Relat. Phenom.*, 1989, **48**, 219–351.
[202] M. Z. Zgierski and F. Zerbetto, *J. Chem. Phys.*, 1993, **98**, 14–20.
[203] D. A. Lightner, J. K. Gawronski and T. D. Bouman, *J. Am. Chem. Soc.*, 1980, **102**, 5749–5754.
[204] S. Sen and I. Schapiro, *Mol. Phys.*, 2018, **116**, 2571–2582.

[205] J. W. Park, *J. Chem. Theory Comput.*, 2019, **15**, 3960–3973.
[206] T. Shiozaki, *WIREs Comput. Mol. Sci.*, 2018, **8**, e1331.
[207] A. C. Paul, R. H. Myhre and H. Koch, *J. Chem. Theory Comput.*, 2021, **17**, 117–126.
[208] P.-F. Loos, A. Scemama, A. Blondel, Y. Garniron, M. Caffarel and D. Jacquemin, *J. Chem. Theory Comput.*, 2018, **14**, 4360–4379.
[209] G. Li Manni, K. Guther, D. Ma and W. Dobrautz, *Quantum Chemistry and Dynamics of Excited States*, John Wiley & Sons, Ltd, 2020, pp. 133–203.
[210] L. Verlet, *Phys. Rev.*, 1967, **159**, 98–103.
[211] S. Fatehi and J. E. Subotnik, *J. Phys. Chem. Lett.*, 2012, **3**, 2039–2043.
[212] H.-J. Werner, P. J. Knowles, F. R. Manby, J. A. Black, K. Doll, A. Heßelmann, D. Kats, A. Köhn, T. Korona, D. A. Kreplin, Q. Ma, T. F. Miller, III, A. Mitrushchenkov, K. A. Peterson, I. Polyak, G. Rauhut and M. Sibaev, *J. Chem. Phys.*, 2020, **152**, 144107.
[213] B. G. Levine, J. D. Coe, A. M. Virshup and T. J. Martínez, *Chem. Phys.*, 2008, **347**, 3–16.
[214] B. Mignolet and B. F. E. Curchod, *J. Chem. Phys.*, 2018, **148**, 134110.
[215] M. Barbatti, M. Ruckenbauer, F. Plasser, J. Pittner, G. Granucci, M. Persico and H. Lischka, *WIREs Comput. Mol. Sci.*, 2014, **4**, 26–33.
[216] Y. Lassmann and B. F. E. Curchod, *Theor. Chem. Accounts*, 2023, **142**, 66.
[217] D. Mendive-Tapia, B. Lasorne, G. A. Worth, M. J. Bearpark and M. A. Robb, *Phys. Chem. Chem. Phys.*, 2010, **12**, 15725–15733.
[218] C. S. M. Allan, B. Lasorne, G. A. Worth and M. A. Robb, *J. Phys. Chem. A*, 2010, **114**, 8713–8729.
[219] K. Ohmori, *Annu. Rev. Phys. Chem.*, 2009, **60**, 487–511.
[220] T. Buckup, M. Motzkus and J. Hauer, *Extreme Photonics & Applications*, Springer, 2010, pp. 37–55.
[221] D. Geppert, A. Hofmann and R. de Vivie-Riedle, *J. Chem. Phys.*, 2003, **119**, 5901–5906.
[222] A. M. D. Lee, J. D. Coe, S. Ullrich, M.-L. Ho, S.-J. Lee, B.-M. Cheng, M. Z. Zgierski, I.-C. Chen, T. J. Martinez and A. Stolow, *J. Phys. Chem. A*, 2007, **111**, 11948–11960.
[223] A. D. Smith, E. M. Warne, D. Bellshaw, D. A. Horke, M. Tudorovskya, E. Springate, A. J. H. Jones, C. Cacho, R. T. Chapman, A. Kirrander and R. S. Minns, *Phys. Rev. Lett.*, 2018, **120**, 183003.
[224] M. Tudorovskaya, R. S. Minns and A. Kirrander, *Phys. Chem. Chem. Phys.*, 2018, **20**, 17714–17726.
[225] W. O. Razmus, K. Acheson, P. Bucksbaum, M. Centurion, E. Champenois, I. Gabalski, M. C. Hoffman, A. Howard, M.-F. Lin, Y. Liu, P. Nunes, S. Saha, X. Shen, M. Ware, E. M. Warne, T. Weinacht, K. Wilkin, J. Yang, T. J. A. Wolf, A. Kirrander, R. S. Minns and R. Forbes, *Phys. Chem. Chem. Phys.*, 2022, **24**, 15416–15427.
[226] L. Ma, H. Yong, J. D. Geiser, A. Moreno Carrascosa, N. Goff and P. M. Weber, *Struct. Dyn.*, 2020, **7**, 034102.
[227] K. Acheson and A. Kirrander, *J. Chem. Theory Comput.*, 2023, **19**, 2721–2734.
[228] J. Yang, X. Zhu, J. P. F. Nunes, J. K. Yu, R. M. Parrish, T. J. A. Wolf, M. Centurion, M. Gühr, R. Li, Y. Liu, B. Moore, M. Niebuhr, S. Park, X. Shen, S. Weathersby, T. Weinacht, T. J. Martinez and X. Wang, *Science*, 2020, **368**, 885–889.
[229] K. J. Wilkin, R. M. Parrish, J. Yang, T. J. A. Wolf, J. P. F. Nunes, M. Guehr, R. Li, X. Shen, Q. Zheng, X. Wang, T. J. Martinez and M. Centurion, *Phys. Rev. A*, 2019, **100**, 023402.
[230] J. Yang, M. Guehr, X. Shen, R. Li, T. Vecchione, R. Coffee, J. Corbett, A. Fry, N. Hartmann, C. Hast, K. Hegazy, K. Jobe, I. Makasyuk, J. Robinson, M. S. Robinson, S. Vetter, S. Weathersby, C. Yoneda, X. Wang and M. Centurion, *Phys. Rev. Lett.*, 2016, **117**, 153002.
[231] M. Stefanou, K. Saita, D. V. Shalashilin and A. Kirrander, *Chem. Phys. Lett.*, 2017, **683**, 300–305.

[232] P. J. Brown, A. G. Fox, E. N. Maslen, M. A. O'Keefe and B. T. M. Willis, *International Tables for Crystallography Volume C: Mathematical, physical and chemical tables*, Springer Netherlands, Dordrecht, 2004, pp. 554–595.
[233] T. Piteša, M. Sapunar, A. Ponzi, M. F. Gelin, N. Došlić, W. Domcke and P. Decleva, *J. Chem. Theory Comput.*, 2021, **17**, 5098–5109.
[234] M. Schreiber, M. R. Silva-Junior, S. P. A. Sauer and W. Thiel, *J. Chem. Phys.*, 2008, **128**, 134110.
[235] *CXI Specifications | Linac Coherent Light Source*, `https://lcls.slac.stanford.edu/instruments/cxi/specifications`.
[236] N. Hartmann, G. Hartmann, R. Heider, M. S. Wagner, M. Ilchen, J. Buck, A. O. Lindahl, C. Benko, J. Grünert, J. Krzywinski, J. Liu, A. A. Lutman, A. Marinelli, T. Maxwell, A. A. Miahnahri, S. P. Moeller, M. Planas, J. Robinson, A. K. Kazansky, N. M. Kabachnik, J. Viefhaus, T. Feurer, R. Kienberger, R. N. Coffee and W. Helml, *Nat. Photonics*, 2018, **12**, 215–220.
[237] J. Duris, S. Li, T. Driver, E. G. Champenois, J. P. MacArthur, A. A. Lutman, Z. Zhang, P. Rosenberger, J. W. Aldrich, R. Coffee, G. Coslovich, F.-J. Decker, J. M. Glownia, G. Hartmann, W. Helml, A. Kamalov, J. Knurr, J. Krzywinski, M.-F. Lin, J. P. Marangos, M. Nantel, A. Natan, J. T. O'Neal, N. Shivaram, P. Walter, A. L. Wang, J. J. Welch, T. J. A. Wolf, J. Z. Xu, M. F. Kling, P. H. Bucksbaum, A. Zholents, Z. Huang, J. P. Cryan and A. Marinelli, *Nat. Photonics*, 2020, **14**, 30–36.
[238] A. F. Habib, G. G. Manahan, P. Scherkl, T. Heinemann, A. Sutherland, R. Altuiri, B. M. Alotaibi, M. Litos, J. Cary, T. Raubenheimer, E. Hemsing, M. J. Hogan, J. B. Rosenzweig, P. H. Williams, B. W. J. McNeil and B. Hidding, *Nat. Commun.*, 2023, **14**, 1054.
[239] B. Stankus, H. Yong, J. Ruddock, L. Ma, A. M. Carrascosa, N. Goff, S. Boutet, X. Xu, N. Zotev, A. Kirrander, M. Minitti and P. M. Weber, *J. Phys. B: At. Mol. Opt. Phys.*, 2020.
[240] J. M. Ruddock, N. Zotev, B. Stankus, H. Yong, D. Bellshaw, S. Boutet, T. J. Lane, M. Liang, S. Carbajo, W. Du, A. Kirrander, M. Minitti and P. M. Weber, *Angewandte Chemie Int. Ed.*, 2019, **58**, 6371–6375.
[241] S. Karashima, A. Humeniuk, R. Uenishi, T. Horio, M. Kanno, T. Ohta, J. Nishitani, R. Mitrić and T. Suzuki, *J. Am. Chem. Soc.*, 2021, **143**, 8034–8045.
[242] M. H. Palmer, M. Coreno, M. de Simone, C. Grazioli, R. A. Aitken, S. V. Hoffmann, N. C. Jones and C. Peureux, *J. Chem. Phys.*, 2020, **153**, 204303.
[243] A. J. Jenkins, M. Vacher, R. M. Twidale, M. J. Bearpark and M. A. Robb, *J. Chem. Phys.*, 2016, **145**, 164103.
[244] M. P. Minitti, J. M. Budarz, A. Kirrander, J. S. Robinson, D. Ratner, T. J. Lane, D. Zhu, J. M. Glownia, M. Kozina, H. T. Lemke, M. Sikorski, Y. Feng, S. Nelson, K. Saita, B. Stankus, T. Northey, J. B. Hastings and P. M. Weber, *Phys. Rev. Lett.*, 2015, **114**, 255501.
[245] M. Lingyu, *Ultrafast X-ray Scattering of the Photoinduced Reaction Kinetics of the 1,2-Dithiane*, 2020, Presenters: _:n30272.
[246] N. Kotsina, C. Brahms, S. L. Jackson, J. C. Travers and D. Townsend, *Chem. Sci.*, 2022, **13**, 9586–9594.
[247] J. Claydon, N. Greeves and S. Warren, *Organic Chemistry*, Oxford University Press, Oxford, UK, 2nd edn, 2012.
[248] J. Cerezo and F. Santoro, *J. Comput. Chem.*, 2023, **44**, 626–643.
[249] C. Møller and M. S. Plesset, *Phys. Rev.*, 1934, **46**, 618–622.
[250] C. Hättig, *Advances in Quantum Chemistry*, Academic Press, 2005, vol. 50, pp. 37–60.
[251] L. Nahon, N. de Oliveira, G. A. Garcia, J.-F. Gil, B. Pilette, O. Marcouillé, B. Lagarde and F. Polack, *J. Synchrotron Radiat.*, 2012, **19**, 508–520.

[252] N. de Oliveira, M. Roudjane, D. Joyeux, D. Phalippou, J.-C. Rodier and L. Nahon, *Nat. Photonics*, 2011, **5**, 149–153.
[253] S. G. Balasubramani, G. P. Chen, S. Coriani, M. Diedenhofen, M. S. Frank, Y. J. Franzke, F. Furche, R. Grotjahn, M. E. Harding, C. Hättig, A. Hellweg, B. Helmich-Paris, C. Holzer, U. Huniar, M. Kaupp, A. Marefat Khah, S. Karbalaei Khani, T. Müller, F. Mack, B. D. Nguyen, S. M. Parker, E. Perlt, D. Rappoport, K. Reiter, S. Roy, M. Rückert, G. Schmitz, M. Sierka, E. Tapavicza, D. P. Tew, C. van Wüllen, V. K. Voora, F. Weigend, A. Wodynski and J. M. Yu, *J. Chem. Phys.*, 2020, **152**, 184107.
[254] M. B. Robin and N. A. Kuebler, *J. Chem. Phys.*, 1966, **44**, 2664–2671.
[255] A. V. Luzanov, A. A. Sukhorukov and V. E. Umanskii, *Theor. Exp. Chem.*, 1976, **10**, 354–361.
[256] R. L. Martin, *J. Chem. Phys.*, 2003, **118**, 4775–4777.
[257] F. Plasser, M. Wormit and A. Dreuw, *J. Chem. Phys.*, 2014, **141**, 024106.
[258] F. Plasser, S. A. Bäppler, M. Wormit and A. Dreuw, *J. Chem. Phys.*, 2014, **141**, 024107.
[259] F. Plasser, *J. Chem. Phys.*, 2020, **152**, 084108.
[260] F. J. A. Ferrer and F. Santoro, *Phys. Chem. Chem. Phys.*, 2012, **14**, 13549–13563.
[261] R. A. Shaw, C. Castro, R. Dutler, A. Rauk and H. Wieser, *J. Chem. Phys.*, 1988, **89**, 716–731.
[262] X. Zhou and R. Liu, *Vib. Spectrosc.*, 1996, **12**, 65–71.
[263] M. B. Robin and N. A. Kuebler, *J. Mol. Spectrosc.*, 1970, **33**, 274–291.
[264] M. N. R. Ashfold, S. G. Clement, J. D. Howe and C. M. Western, *J. Chem. Soc. Faraday Trans.*, 1993, **89**, 1153–1172.
[265] M. H. Palmer, S. V. Hoffmann, N. C. Jones, M. Coreno, M. de Simone, C. Grazioli, R. A. Aitken and C. Peureux, *J. Chem. Phys.*, 2023, **158**, 234303.
[266] W. Fuß, K. K. Pushpa, W. E. Schmid and S. A. Trushin, *Photochem. & Photobiol. Sci.*, 2002, **1**, 60–66.
[267] E. Allaria, R. Appio, L. Badano, W. A. Barletta, S. Bassanese, S. G. Biedron, A. Borga, E. Busetto, D. Castronovo, P. Cinquegrana, S. Cleva, D. Cocco, M. Cornacchia, P. Craievich, I. Cudin, G. D'Auria, M. Dal Forno, M. B. Danailov, R. De Monte, G. De Ninno, P. Delgiusto, A. Demidovich, S. Di Mitri, B. Diviacco, A. Fabris, R. Fabris, W. Fawley, M. Ferianis, E. Ferrari, S. Ferry, L. Froehlich, P. Furlan, G. Gaio, F. Gelmetti, L. Giannessi, M. Giannini, R. Gobessi, R. Ivanov, E. Karantzoulis, M. Lonza, A. Lutman, B. Mahieu, M. Milloch, S. V. Milton, M. Musardo, I. Nikolov, S. Noe, F. Parmigiani, G. Penco, M. Petronio, L. Pivetta, M. Predonzani, F. Rossi, L. Rumiz, A. Salom, C. Scafuri, C. Serpico, P. Sigalotti, S. Spampinati, C. Spezzani, M. Svandrlik, C. Svetina, S. Tazzari, M. Trovo, R. Umer, A. Vascotto, M. Veronese, R. Visintini, M. Zaccaria, D. Zangrando and M. Zangrando, *Nat. Photonics*, 2012, **6**, 699–704.
[268] C. Svetina, C. Grazioli, N. Mahne, L. Raimondi, C. Fava, M. Zangrando, S. Gerusina, M. Alagia, L. Avaldi, G. Cautero, M. de Simone, M. Devetta, M. Di Fraia, M. Drabbels, V. Feyer, P. Finetti, R. Katzy, A. Kivimäki, V. Lyamayev, T. Mazza, A. Moise, T. Möller, P. O'Keeffe, Y. Ovcharenko, P. Piseri, O. Plekan, K. C. Prince, R. Sergo, F. Stienkemeier, S. Stranges, M. Coreno and C. Callegari, *J. Synchrotron Radiat.*, 2015, **22**, 538–543.
[269] V. Lyamayev, Y. Ovcharenko, R. Katzy, M. Devetta, L. Bruder, A. LaForge, M. Mudrich, U. Person, F. Stienkemeier, M. Krikunova, T. Möller, P. Piseri, L. Avaldi, M. Coreno, P. O'Keeffe, P. Bolognesi, M. Alagia, A. Kivimäki, M. D. Fraia, N. B. Brauer, M. Drabbels, T. Mazza, S. Stranges, P. Finetti, C. Grazioli, O. Plekan, R. Richter, K. C. Prince and C. Callegari, *J. Phys. B: At. Mol. Opt. Phys.*, 2013, **46**, 164007.
[270] S. Mai, M. Richter, M. Heindl, M. F. S. J. Menger, A. Atkins, M. Ruckenbauer, F. Plasser, L. M. Ibele, S. Kropf, M. Oppel, P. Marquetand and L. Gonzalez, *SHARC2.1: Surface*

Hopping Including Arbitrary Couplings — Program Package for Non-Adiabatic Dynamics, 2019, Published: sharc-md.org.
[271] U. Jacovella, E. Carrascosa, J. T. Buntine, N. Ree, K. V. Mikkelsen, M. Jevric, K. Moth-Poulsen and E. J. Bieske, *J. Phys. Chem. Lett.*, 2020, **11**, 6045–6050.
[272] M. B. Robin, *Higher Excited States of Polyatomic Molecules*, Academic Press, 1974, vol. 1.
[273] M. B. Robin, *Higher Excited States of Polyatomic Molecules*, Academic Press, 1985, vol. 3.
[274] R. Forbes, S. P. Neville, M. A. B. Larsen, A. Röder, A. E. Boguslavskiy, R. Lausten, M. S. Schuurman and A. Stolow, *J. Phys. Chem. Lett.*, 2021, **12**, 8541–8547.
[275] H. Weir, M. Williams, R. M. Parrish, E. G. Hohenstein and T. J. Martínez, *J. Phys. Chem. B*, 2020, **124**, 5476–5487.
[276] A. Lietard, G. Piani, L. Poisson, B. Soep, J.-M. Mestdagh, S. Aloïse, A. Perrier, D. Jacquemin and M. Takeshita, *Phys. Chem. Chem. Phys.*, 2014, **16**, 22262–22272.
[277] F. Sicilia, M. J. Bearpark, L. Blancafort and M. A. Robb, *Theor. Chem. Accounts*, 2007, **118**, 241–251.
[278] B. Lasorne, M. A. Robb and G. A. Worth, *Phys. Chem. Chem. Phys.*, 2007, **9**, 3210–3227.
[279] K. Kuntze, J. Isokuortti, J. J. v. d. Wal, T. Laaksonen, S. Crespi, N. A. Durandin and A. Priimagi, *Chem. Sci.*, 2024, **15**, 11684–11698.
[280] J. Calbo, C. E. Weston, A. J. P. White, H. S. Rzepa, J. Contreras-García and M. J. Fuchter, *J. Am. Chem. Soc.*, 2017, **139**, 1261–1274.
[281] J. Briand, O. Bräm, J. Réhault, J. Léonard, A. Cannizzo, M. Chergui, V. Zanirato, M. Olivucci, J. Helbing and S. Haacke, *Phys. Chem. Chem. Phys.*, 2010, **12**, 3178–3187.
[282] A. D. Bandrauk, S. Chelkowski and P. B. Corkum, *Int. J. Quantum Chem.*, 1999, **75**, 951–959.
[283] W. Zhou, L. Ge, G. A. Cooper, S. W. Crane, M. H. Evans, M. N. R. Ashfold and C. Vallance, *J. Chem. Phys.*, 2020, **153**, 184201.
[284] M. Ochmann, A. Hussain, I. von Ahnen, A. A. Cordones, K. Hong, J. H. Lee, R. Ma, K. Adamczyk, T. K. Kim, R. W. Schoenlein, O. Vendrell and N. Huse, *J. Am. Chem. Soc.*, 2018, **140**, 6554–6561.
[285] M. Saes, C. Bressler, R. Abela, D. Grolimund, S. L. Johnson, P. A. Heimann and M. Chergui, *Phys. Rev. Lett.*, 2003, **90**, 047403.
[286] L. X. Chen, X. Zhang, J. V. Lockard, A. B. Stickrath, K. Attenkofer, G. Jennings and D.-J. Liu, *Acta Crystallogr. Sect. A Found. Crystallogr.*, 2010, **66**, 240–251.
[287] P. M. Kraus, M. Zürch, S. K. Cushing, D. M. Neumark and S. R. Leone, *Nat. Rev. Chem.*, 2018, **2**, 82–94.
[288] R. Geneaux, H. J. B. Marroux, A. Guggenmos, D. M. Neumark and S. R. Leone, *Philos. Trans. Royal Soc. A: Math. Phys. Eng. Sci.*, 2019, **377**, 20170463.
[289] S. W. Crane, M. Garrow, P. D. Lane, K. Robertson, A. Waugh, J. M. Woolley, V. G. Stavros, M. J. Paterson, S. J. Greaves and D. Townsend, *J. Phys. Chem. A*, 2023, **127**, 6425–6436.
[290] C. M. Cheatum, M. M. Heckscher, D. Bingemann and F. F. Crim, *J. Chem. Phys.*, 2001, **115**, 7086–7093.
[291] A. M. Carrascosa, *PhD*, University of Edinburgh, Edinburgh, UK, 2018.
[292] A. Moreno Carrascosa and A. Kirrander, *Phys. Chem. Chem. Phys.*, 2017, **19**, 19545–19553.
[293] K. Kaufmann, W. Baumeister and M. Jungen, *J. Phys. B: At. Mol. Opt. Phys.*, 1989, **22**, 2223.